Research in CO_2 reduction by carbonation

William Carter

A thesis submitted for the partial fulfilment of the requirements of the University of Greenwich for the degree of Doctor of Philosophy

November 2018

DECLARATION

I certify that this work contained in this thesis, or any part of it, has not been accepted in substance for any previous degree awarded to me, and is not concurrently being submitted for any degree other than that of Doctor of Philosophy being studied at the University of Greenwich. I also declare that this work is the result of my own investigations except where otherwise identified by references and that the contents are nor the outcome of any form of research misconduct.

.....
William Carter (PhD Student)
Date:

.....
Professor Koulis Pericleous (Supervisor)
Date:

.....
Professor Mayur Patel (Supervisor)
Date:

.....
Professor Mike Bradley (Supervisor)
Date:

ACKNOWLEDGEMENTS

I wish to thank my parents for their consistent support; my supervisors Koulis Pericleous and Mayur Patel for their limitless patience, guidance and encouragement during the research process, particularly when I was working remotely; Mike Bradley for advice and for letting me use the fluidisation columns in Medway; and staff and students at the Universities of Greenwich and Swansea for their friendliness and hospitality.

ABSTRACT

An algebraic slip model has been developed and tested in the CFD software suite PHYSICA, for the simulation of gas-solid flow. It has been combined with reaction code and used to simulate a carbonator and a calciner as part of a carbonation cycle for carbon capture in two and three dimensions.

Carbon capture technologies show promise and many countries are developing or planning power plants incorporating carbon capture and storage (CCS) as a means of reducing their CO_2 outputs. Carbon capture using Calcium oxide is a cost-effective alternative to the current more popular methods such as monoethylamine, which suffer from high regenerative costs and corrosion.

The algebraic slip model offers an alternative to other, more complicated methods of multiphase flow simulation, and allows for the modelling of systems containing a distribution of phases and material properties. In the past it has been used for modelling cyclones where there are a range of particles sizes to account for, but it has not been commonly applied to fluidisation, except for simulating continuous phases in some Lagrangian studies.

This thesis presents an investigation into the applicability of the model as a means of quantifying the behaviour of a fluidised bed and compares its performance to physical experiments and an earlier Lagrangian model developed in the in-house code PHYSICA.

The model's performance has been found to compare well in terms of the behaviour of the reaction in the carbonator, and to approximate the performance of both a real-world plant and a Lagrangian simulation, albeit under modified conditions.

CONTENTS

FIGURES

TABLES

NOMENCLATURE

C: Number of reaction and regeneration cycles a particle has been through

c: generic variable

c_P: Specific heat kJ kg^{-1} K^{-1}

C_D: Drag coefficient

d: Diameter (m)

e: Particle porosity

E_A: Activation energy (kJ mol^{-1})

g: Gravitational constant (9.81 m s^{-2})

H: Height (m)

ΔH_R: Heat of reaction (kJ mol^{-1})

k_s: Reaction constant from Arrhenius (mol m^{-2} s^{-1})

K: Reaction constant (varies)

M: Molar mass (kg mol^{-1})

N: Molar concentration (kmol m^{-3})

P: Pressure (varies)

Q: Enthalpy (kJ kg^{-1})

R: Specific reaction rate (s^{-1})

r_0: Initial reaction rate (s^{-1})

R_g: Gas constant (8.314 kJ mol^{-1} K^{-1})

s: Specific surface area (m^2 g^{-1})

S_i: Source term for variable *i*

t: Time (s)

u: Velocity (m s^{-1})

u_t: Terminal particle velocity (m s^{-1})

U_0: Superficial gas velocity (m s^{-1})

X: Conversion (kmol product / (kmol reactant + kmol product))

Latin

Γ: Diffusion coefficient

Ψ: Sphericity

ε: Volumetric concentration ($m^3\ m^{-3}$)

μ: Dynamic viscosity (Pa s)

ν: Kinematic viscosity ($m^2\ s^{-1}$)

ρ: Density ($kg\ m^{-3}$)

τ: Shear stress ($N\ m^{-2}$)

τ_s: Space time (time unit)

φ: Structural parameter for carbonation from [1]

Subscripts

g: Gas phase

i: Solid phase

INTRODUCTION

1.1 Climate change

Climate change is one of the major issues facing the world today and is contributing to the current surge in destructive weather patterns, as well as having more long-term effects, including global increases in temperature, melting ice in the Arctic and rising sea levels.

The increasing concentrations of greenhouse gases in the atmosphere are one of the major factors in anthropogenic climate change and carbon dioxide (CO_2) is the most common of these greenhouse gases. It makes up around 50% of the total greenhouse gas in the atmosphere, and is the largest contributor to man-made climate change [2].

The greatest source of man-made CO_2 is the power industry, which has contributed roughly 80% of recent increases in fossil fuel emissions [3]. The power sector's current contribution to man-made emissions is shown in Figure 1.

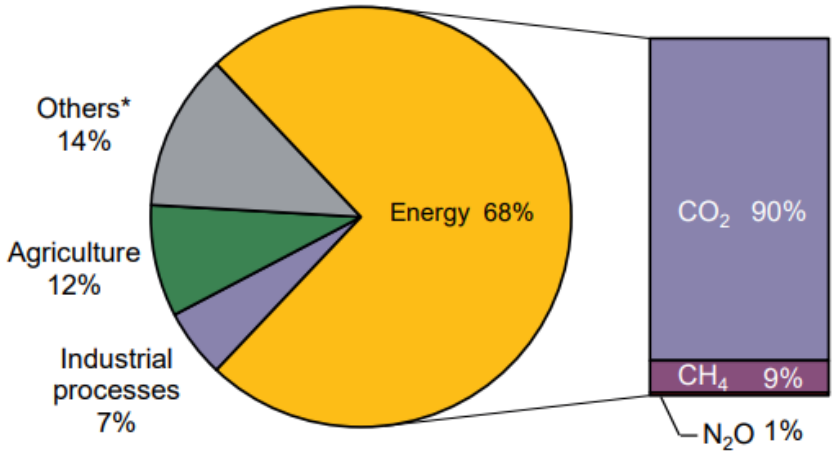

Figure 1: Estimated shares of anthropogenic greenhouse gases from I.E.A. [4]

Internationally, efforts are focussing on the power sector, with governments and industries setting targets for CO_2 reduction and providing incentives for alternative fuel supplies. These include agreements such as:

a) The United Nations Framework Convention on Climate Change of 1992, which committed governments to a reduction in greenhouse gas emissions
b) the Kyoto Protocol of 1997, in which countries made further pledges to keep to targets for emission reductions
c) the Paris Climate Agreement of 2015, which set CO_2 emission and renewable financing targets

Even with these targets, the world is currently reliant on fossil fuels and will be for some time, with estimates of CO_2 emissions at around 28 Gt per year [5]. This, combined with increasing energy demand in developing economies could lead to an increased energy demand of more than 45% by 2030 [5]. The International Energy Agency estimate that fossil fuels will still provide us with the majority of our energy by 2050 [6].

Progress is being made in the increased use of renewable technologies, such as wind, tidal and solar, which have minimal, if any, net negative environmental impact. These energy sources are improving with time, but in their current form are not capable of satisfying the world's energy requirements [7].

To meet the targets, countries are developing their own initiatives, such as in Scandinavia [8] and China where they are building more fossil-fuel power plants, but are incorporating CCS and carbon efficiency into them as standard [9, 10]. Recent developments, including the United States' withdrawal from the Paris Climate Agreement potentially threaten this progress.

1.2 Carbon capture

Carbon capture and sequestration (CCS) offers the prospect of continuing to use reliable energy sources like oil and gas, while being carbon neutral. It allows the production of energy from fossil fuels, while preventing the negative impact of their associated greenhouse gases. If properly utilised it could provide a stepping stone towards a fully renewable infrastructure, without damaging economic growth [11]. Figure 2 shows the potential for CCS if applied to various industries.

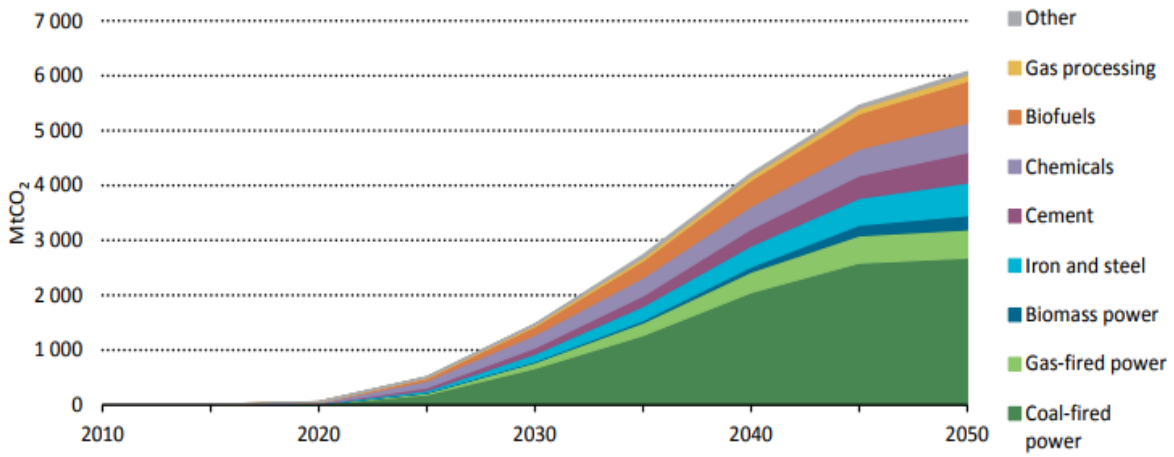

Figure 2: Potential CO_2 captured from different industries from I.E.A [12]

Carbon Capture is the application of a process to remove carbon dioxide from the output gases of facilities using fossil fuels, either through preventing its production by treating the fuel before combustion, or removing it from the flue gas afterwards, before releasing it to atmosphere.

There are already several treatments applied to flue gas from fossil-fuel power plants, both pre- and post-combustion, before it can be released to atmosphere [13], without including CCS. Some pollutants, such as NOx and SOx are screened before entry to the combustion process to reduce the risk of corrosion.

Most carbon capture is currently performed using monoethylamine (MEA) in a stripping and regeneration cycle, wherein the CO_2 is removed via contact with the MEA in an absorption column, before being regenerated at higher temperatures in a second reactor. The CO_2 is separated and sent to storage. Problems with using MEA include the high temperature and cost of regeneration and it corrosive nature [14].

The calcium looping cycle is a promising alternative for carbon capture with a number of advantages over MEA: It uses a mature technology in circulating fluidised beds, a cheap feedstock in limestone, has a small energy penalty of 6-8% [15], and has the potential for integration with other industries such as cement manufacture. As a post-

combustion system, it comes with the advantage of an uncomplicated retrofit for older plants as it can simply be added to the end of the process, thereby saving in costs.

Calcium looping was originally used in hydrogen production. It is a process consisting of two vessels: in the carbonator CO_2 is consumed in reaction with CaO to form $CaCO_3$, which is then passed to a calciner where the CO_2 is removed, before the CaO is returned to the carbonator [16]. As CaO is denatured or spent, it is replaced by fresh sorbent.

Carbonation is exothermic and calcination endothermic so the two processes can be integrated for better fuel efficiency [17], with heat from the carbonator heating the calciner feed stream. Temperature promotes reaction in the carbonator but hinders conversion. In the calciner, higher temperatures are better for conversion.

Calcium looping systems are increasingly being deployed, although only at an early stage. Some examples include the Norwegian Institute for Energy Technology who are developing a solid oxide fuel cell, using a calcium loop attached to a combined heat and power (CHP) plant, and the European Union's CaOling project which aims to provide CCS to a 20 MWt plant. Following lab-scale tests in Spain, Germany and Canada, there has been a 1.7 MWt scale investigation in Spain, which performed satisfactorily [18].

Table 1 shows some plants around the world currently implementing carbon capture. There are also some plants operating in the UK including the Drax biomass plant in North Yorkshire, which is the largest biomass plant in the UK and is looking to sell its CO_2 to breweries [19]. Using carbon dioxide for enhanced oil recovery has been used by companies in the USA including Petra Nova and the Great Plains Synfuels plant in North Dakota. Collectively, plants in the USA capture 25 million tons of CO_2 per year [20].

Table 1: Currently operating plants for CCS adapted from Rubin [21]

Project name and location	Fuel type	Year of start-up	Capture capacity	Capture system	CO_2 captured (t/yr)
Soda Ash Botswana Sua Pan Plant (Botswana)	Coal-fired	1991	17 MW	Amine	0.11
Statoil Sleipner West Gas Field (Norway)	Natural gas separation	1996	N/A	Amine	1
Petronas Gas Processing Plant (Malaysia)	Natural gas-fired	1999	10 MW	Amine	0.07
BP Gas Processing Plant (Algeria)	Natural gas separation	2004	N/A	Amine	1
Mitsubishi Chemical Kurosaki Plant (Japan)	Natural gas-fired	2005	18 MW	Amine	0.12

1.3 Research objectives

The objectives of this thesis are the following:

1) To develop a numerical model of the carbonation process based on fluidised bed technology using the PHYSICA multi-physics code developed at Greenwich
2) To test the model against other models and experiments in the literature
3) To assess the capability of the proposed model to adequately describe the carbonation cycle

In this work, an algebraic slip model has been created in the CFD software PHYSICA, to simulate a gas-solid multiphase flow. This code calculates the local mixture properties based on the solid phase concentrations to calculate overall mixture behaviour and uses differences in solid-phase slip velocities to determine how the various solid phases move relative to the mixture.

Reaction modules have been written based on a shrinking core model, to account for both carbonation and calcination. These modules have been linked with the PHYSICA heat module to model heat transfer within the system.

The algebraic slip model has not often been the model of choice for gas-solid fluidisation, with authors generally preferring Eulerian or Lagrangian models, although it has been used for the simulation of cyclones [22, 23], and combined with the Lagrangian model for the simulation of dilute columns [24], where it offers a simpler relation for the continuous phase than an Eulerian setup. This thesis will investigate the application of the algebraic slip model to a fluidisation column and compare these results with those obtained in Eulerian and Lagrangian models.

1.4 Thesis outline

The thesis is organised as follows:

1) The introduction gives a brief overview of the motivation behind the project and the methods used in its solution
2) The research background explains the current scientific understanding of the problem of carbon capture and storage and the behaviour of multiphase flow and its simulation in more detail
3) The modelling section details how this science was applied to the problem to provide a solution
4) The results section shows the model applied to simulating columns in both two- and three-dimensions
5) The conclusion and future work section summarise what has been learnt and how this work can be taken forward

RESEARCH BACKGROUND AND THEORETICAL STUDY

2.1 Introduction

The aim of this study was to develop code to simulate a carbonation cycle in the computational fluid dynamics software PHYSICA. The project implemented an algebraic slip model to account for the behaviour of the solid phases, and developed new code for reaction routines, which were integrated with the existing PHYSICA modules.

PHYSICA is an in-house finite-volume type computational fluid dynamics and structural mechanics code, which has been developed at the University of Greenwich [25]. It is coded in FORTRAN, and is made up of modules with different functions, each of which can set by the user and turned on or off. PHYSICA retains the facility for the addition of user-derived functions which allows for new code to tackle novel problems and situations.

Molaei [26] used PHYSICA to develop and test a Lagrangian technique to simulate steady-state gas-solid flow in a carbonator, and tested the performance of the reactor under different conditions and geometries. PHYSICA has also been used in many other applications, e.g. in phase-change problems for the modelling of metal solidification [25] and this PhD further develops PHYSICA's use as a tool for multiphase simulation.

The algebraic slip model is a method of simulating multiphase flows, which assumes local equilibrium is attained on a small scale. It is valid in situations where mixtures reach their terminal velocities quickly. It treats the mixture as a homogeneous fluid with properties depending on local concentrations, but accounts for the spread of each phase separately. One momentum equation is solved for the whole mixture, but each phase has its own transport equation which tracks the spread of the phase relative to the mixture, by means of a slip velocity based on the local drag coefficient [27, 28].

The routine developed can account for the fluidisation of a powder containing a distribution of solid phases, with reaction codes for both carbonation based on a shrinking core and calcination, based on a random core mechanism [29, 30].

Simulations were performed for carbonators and calciners individually in two and three dimensions.

The code was based on an original drift-flux model for the upward flow of particles in air or bubbles in a water continuum [22, 31], which has been adapted to accommodate varying densities and viscosities by the modification of the advection module and the creation of user routines to define mixture properties. It has been tested against real-world studies of fluidisation columns and various reactors in the literature to provide an accurate reflection of flow behaviour.

The Gas And Liquid Algorithm, (GALA) , a volume-conservation technique, was used to accommodate changing densities within the flow and pressure modules [32, 33]. Turbulence was modelled through a k-ε relation [34].

2.2 Types of CO_2 capture

Carbon capture offers great potential as a weapon in the fight against climate change. It provides a stopgap, allowing us to move towards a fully renewable future while weaning ourselves off fossil fuels. By using carbon capture and installing it on new plants, or retrofitting older plants, the environmental impact of energy generation can be reduced without a need for overly large-scale investment in yet unproven technologies.

There is a growing array of carbon capture techniques, and each has its own advantages and disadvantages that favour application in different industry sectors. This section introduces some of these.

Figure 3 shows how carbon capture and storage can be categorised into three main types of application, based on when and how they are used in the energy generation process. These are pre- and post-combustion and oxyfuel.

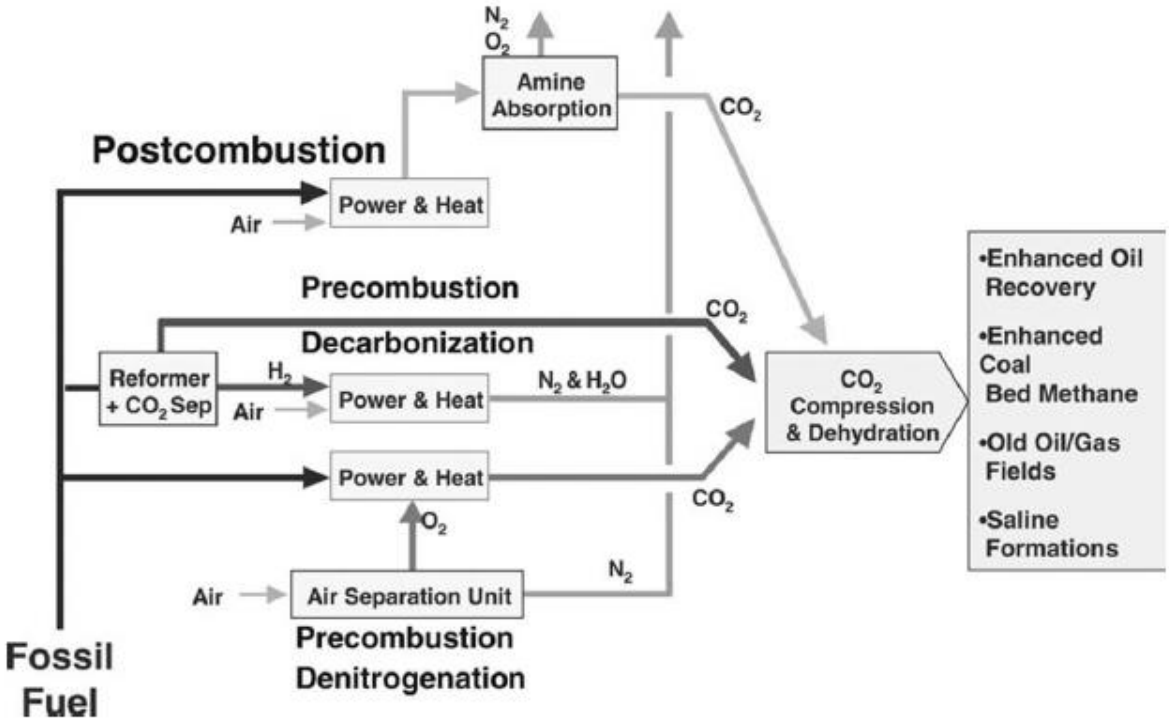

Figure 3: Main CO_2 capture routes from Steeneveldt [35]

In pre-combustion carbon dioxide is removed from the flue gas before the combustion process, through a process such as gasification. This results in a mixture of CO_2 and H_2, with CO_2 being removed and H_2 being used as the fuel, resulting in a much smaller output stream and capture equipment.

Oxy-fuel combustion uses standard equipment, but with a stream of pure oxygen. This is generated via an air separation unit, which is expensive, and requires a much larger flow of oxygen than a regular plant. The output from combustion is solely a mixture of water vapour and CO_2, which can be separated through cooling and there is no need for a complicated capture mechanism [21].

In post-combustion, CO_2 is captured after combustion in an additional facility. This method has to cope with the largest gas-flows and suffers from the greatest operational costs [36], but can be easily retrofitted to existing plants, as there is no need for modification of processes or pre-treatment facilities.

The most economically efficient option available is the construction of integrated Gas Combined Cycle (IGCC) powerplants, as these are more fuel-efficient, with oxy-fuel or pre-combustion, but where this option is not available, a benefit can still be derived from retrofitting older, less efficient plants [37].

Figure 4 shows a selection of CCS technologies which can be applied to different industries. This project is based on power generation, so discussion will focus on chemical absorption and adsorption, as these have already been applied to industrial applications. Many decades of research have been made into increasing the capacity and efficiencies of these technologies, as well as ways of reducing regeneration and equipment costs.

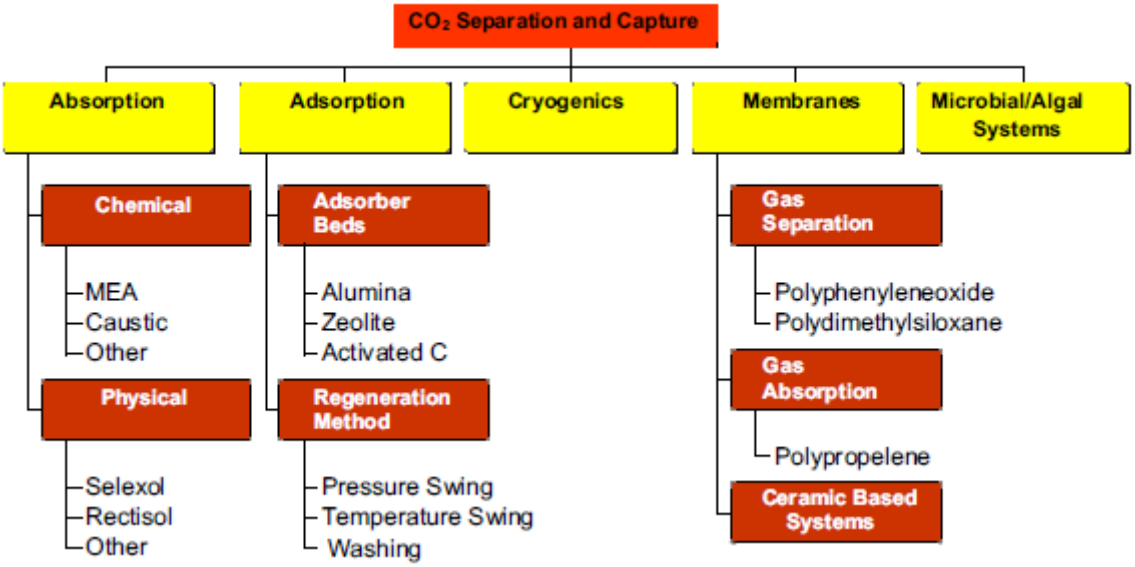

Figure 4: Technical options available for carbon capture from Rubin [21]

The other technologies here are limited with regards to large-scale application: membranes have only limited capacity, cryogenics are prohibitively expensive on a large scale, and microbial systems are comparatively slow. All have potential within different industries, however, for example:

a) Membranes can be used on a lab-scale for drug production as a cheap separation method, requiring little maintenance

b) Cryogenics can be used in the manufacture of high value products on a small scale where a very high purity is desired
c) Microbial systems are used as a biofuel in some rural communities thereby combining waste processing with energy generation

2.2.1 Pre-combustion

Pre-combustion is the process whereby carbon dioxide is removed before combustion occurs. With solid fuel, such as coal, this is achieved by combusting in the absence of air, which is known as gasification, or with high pressure oxygen and steam [37]. Both methods produce gases containing mostly CO and H_2, which can be easily separated, via adsorption, absorption, chemical reaction or membranes, and the H_2 then used as a fuel [8, 21, 35].

The main aim of pre-combustion is the conversion of the carbon fuel into a clean hydrogen fuel. The biggest advantage it brings is the smaller equipment needed for treatment, as only small gas-flows are incurred [38]. An example of a pre-combustion plant with water-gas shift reaction is shown in Figure 5.

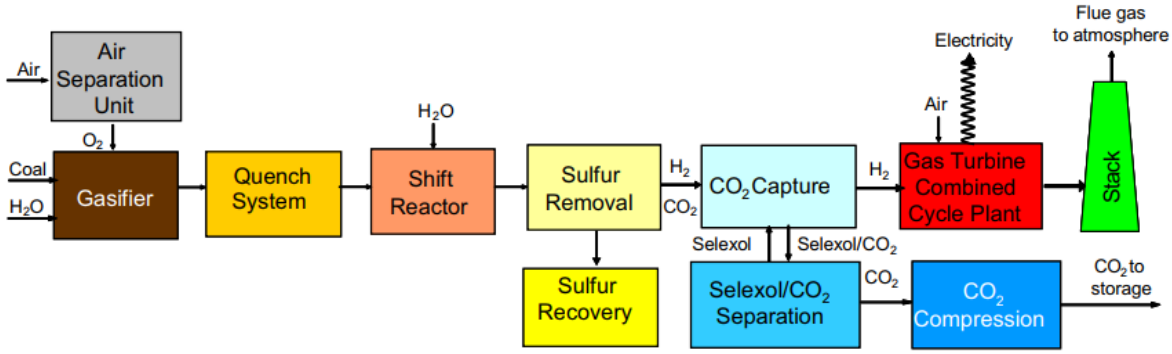

Figure 5: Schematic of an integrated gasification combined cycle with pre-combustion from Rubin [39]

2.2.2 Post combustion

Post-combustion systems capture the CO_2 from the flue gas at the end of the combustion process. Most of the flue gas is nitrogen, with water vapour, CO_2 and various impurities.

They must deal with a large gas-flow, at a relatively low CO_2 concentration and suffer the greatest operating costs [21].

One of the advantages, is the lack of retrofitting required, enabling post-combustion systems to be added to plants more easily and economically. Post-combustion systems can be added after required pollutant clean-up sections, which will also help maintain their operation.

The current most used technology is chemical reaction with the solvent monoethylamine (MEA). This takes place in a dual column cycle, with MEA cycling between a scrubber and a regenerator. Roughly 80-90% of the CO_2 is removed in the scrubber, before the MEA is heated in a regenerator, releasing the CO_2, before the solvent is returned to the scrubber. To capture the CO_2 from dilute streams, powerful reagents are required which have a high binding energy and incur high regeneration costs at high temperatures or pressures [8].

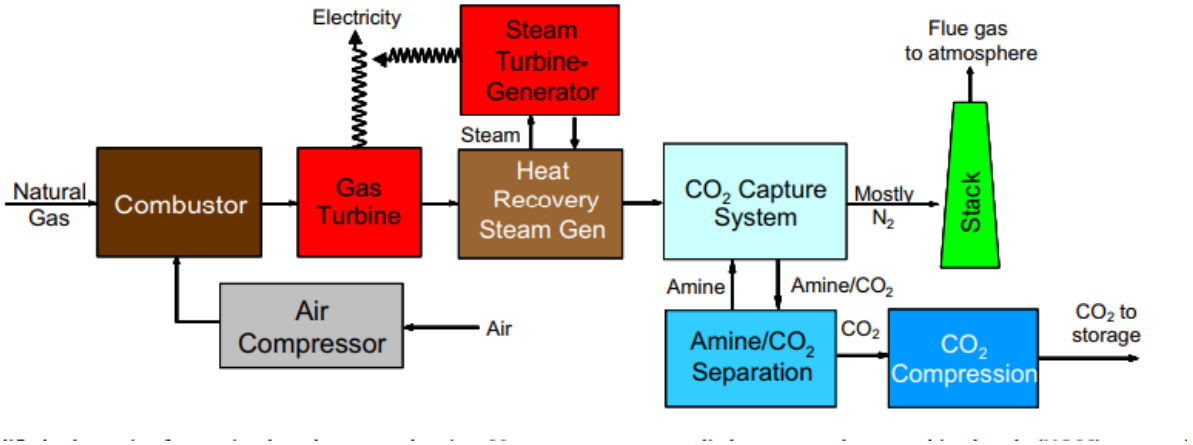

Figure 6: Simplified schematic of an IGCC plant with post-combustion carbon capture with MEA from Rubin [39]

2.2.3 Oxy-fuel combustion

Oxy-fuel systems are a special type of post-combustion. Here, pure oxygen is used rather than air. This greatly reduces the flow of the flue stream, due to the elimination of nitrogen and simplifies the separation process, as the flue stream should consist of CO_2, water vapour and small quantities of impurities. These can be removed to leave a

strong CO_2 stream by simple condensation [40]. The initial separation will rely on a strong membrane or possibly cryogenics to remove the nitrogen, which will be expensive due to either the high capital outlay on a strong membrane or the high energy consumption of a cryogenic system [41].

The great advantage of oxy fuel is that it reduces the size of the post-combustion treatment. No NOx is formed, and standard processing units are all that will be required to make pollutant levels comply with environmental standards [13].

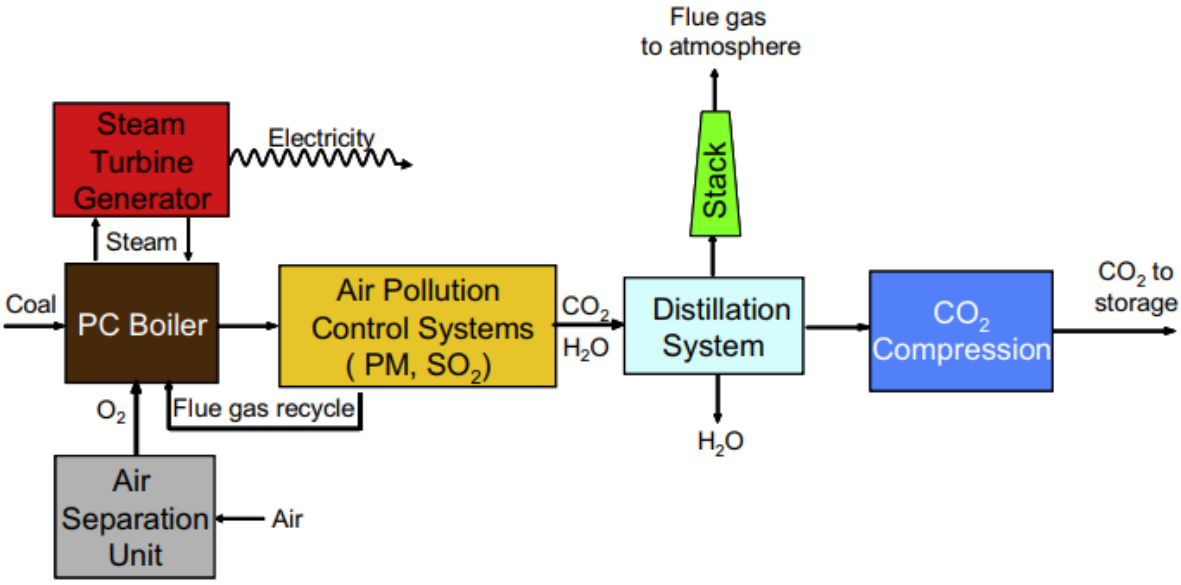

Figure 7: Simplified schematic of a coal-fired power station with oxy-fuel combustion from Rubin [39]

2.3 Methods of CO_2 capture

2.3.1 Solvent scrubbing

Solvent scrubbing, or absorption, with monoethylamine (MEA) is the current most commonly deployed form of carbon capture. It is employed in a number of industries [8] and is being studied at pilot-plant and smaller industrial scales across the world: a one ton CO_2 per hour plant was tested to assess the potential for application to a coal plant in Denmark [8] and attained 90 % carbon capture over 4000 h of operation with MEA and other solvents [42].

Solvent scrubbing is a cyclical system with two stages: 85-90 % of the CO_2 is stripped from the flue gas in contact with the solvent in an absorption column [21] before being regenerated either at a higher temperature or pressure in a stripper or regenerator.

These systems lend themselves well to post-combustion carbon capture due to the ability to capture CO_2 at low partial pressures and simple integration within the plant, although they can be used in pre-combustion as well [21].

Advantages of solvent scrubbing include fast kinetics, which allows capture from streams with lower partial pressures; and good heat integration. Disadvantages include the high power required for steam generation and energy for the heating, cooling and pumping of the solvent [21], the high cost of production of the solvent [43], and its degradation and waste disposal, as a toxic, hazardous material [36].

Efforts are being made to increase the CO_2 loading potential, reduce the regeneration temperatures and pressures and reduce the corrosive potential, volatility and degradation rate of MEA, amongst other things [21].

Another potential method is the chilled ammonia process (CAP), which uses ammonia as a solvent between 0-20 °C and runs a desorber at 100-200 °C [44]. These lower temperatures offer a great potential for energy saving compared to MEA.

2.3.2 Membrane separation

In membrane separation, a selective membrane, over which only certain gases can pass, is used to remove CO_2 from the flue gas stream. They make use of pressure differences between the sides of the membrane to force material across, and the relative sizes of the gas particles and the pores in the membrane to selectively choose which constituent parts pass [8].

The two most important qualities of a membrane are its selectivity and its permeability. The selectivity determines which gases pass over the membrane and which are retained, and the permeability how much of these gasses pass over [21]. An ideal membrane will have a high selectivity for CO_2, allowing a concentrated stream with few contaminants,

and a high permeability, maximising this amount. Unfortunately, there is a trade-off between selectivity and permeability in membranes – the more material that can pass over, the lower in concentration the product stream will be.

The advantages of membranes include cheap maintenance and a lack of utilisation costs in most cases. Problems include the necessary trade-off between purity and recovery rate, a requirement for pre-treatment to avoid damaging the membrane which can even offset the cost advantages, the need for multiple stages and recycling for difficult separations, and a poor economy of scale.

However, membranes are increasingly being used in coordination with other carbon capture methods: In Mexico, work is being done incorporating amine groups that can capture the CO_2 into the membrane itself, while other researchers have employed an amine stream on the other side of the membrane, to strip away the CO_2 as soon as it transfers through [21], maximising the pressure difference driving force.

Membranes are not currently economically competitive with amines [21] on an industrial scale, although there is a likelihood that they could compete in lower intensity industries which produce highly concentrated CO_2 streams.

Due to a high initial and maintenance cost and the low capacity, membrane separation is only suitable for small scale carbon capture.

2.3.3 Adsorption

Adsorption over a solid sorbent is a promising carbon capture alternative currently attracting interest [45]. In adsorption, molecules in a gas or liquid mixture are stripped by contact with a solid surface, in a similar manner to absorption. It is possible to select for different species, and the temperature and pressure can also be varied to maximise or vary the quality and quantity of the materials adsorbed.

Pressure and temperature swing adsorption systems are units where a single column operates as both a stripper and a regenerator. The temperature and pressure are set to maximise the attachment of certain particles and the gas inlet opened, then, once the

adsorbent is saturated, the inlet is closed, and an outlet opened, and the conditions changed to promote dissociation of the gas from the solid particles and the column cleansed by gas flow. Desorption usually takes place in atmospheric conditions, but can be enhanced by operating within a vacuum [46]. Vacuum adsorption has comparable costs to MEA absorption, but normal adsorption is cheaper due to lower energy costs, as the cycle is driven primarily by pressure, rather than temperature.

In post-combustion, either TSA or PSA can be applied to CO_2 capture, or the system can be used for pre-combustion and combined with reaction in the same reactor to reduce costs [47].

Important things to consider in adsorption are selectivity, capacity, regeneration and the lifetime of the adsorbent. The regeneration step, be it temperature or pressure based will reduce the capacity of the adsorbent [48].

Authors such as Su [49] have tested carbon nanotubes for use as an adsorbent in CO_2 capture and found it to be successful. Various adsorbents have been proposed and some tested including carbon fibre monolithic adsorbents [50] and activated carbon fibre phenolic resin composites [51].

2.3.4 Accelerated carbonation treatment

Carbonation is a natural process undergone by silicates and calcinates over time, and results in their being made harder and more resilient following exposure to CO_2 [52]. This natural carbonation is slow and uneven [53], but by applying accelerated carbonation the overall application can be much more rapid, taking minutes instead of years, as well as bringing a consistent boost to the strength over the whole structure. This results in hardened mortars and cements, which are less prone to erosion.

Accelerated carbonation can also be applied to landfill, where it can be used to solidify toxic wastes, thereby reducing the capacity for leeching.

Accelerated carbonation works by subjecting the calcites and silicates to an excess of CO_2 in the presence of water. The CO_2 permeates through the solids and is dissolved in

the water, before being hydrated to H_2CO_3. The cementitious phases then dissolve and are ionised and $CaCO_3$ is formed very quickly [52], and precipitates out of the solution. This is followed by further carbonation.

2.4 Fluidisation

Fluidisation is the suspension of particles by the upward flow of a gas or liquid. It is used in the process industries in reactors and separators, to promote reaction and phase separation due to the high surface area to volume ratio that particles possess.

When an upward flow of fluid through a bed of particles is equal to the apparent weight minus the buoyancy force, the particles will become suspended: the bed will expand and the voidage will increase. This will remain the case with increasing velocity until the loosest form of packing is attained. If velocity is increased further, the particles will separate, and the bed will be fluidised. The superficial gas velocity at the point that the drag force on the upward flowing particles is equal to their weight is known as the minimum fluidising velocity [54].

In gas/solid systems a uniform fluidisation occurs at low velocities, where the gas/particle mixture is generally homogeneous. At higher velocities, the two phases will separate into a continuous, or dense, phase at the bottom with a discrete, bubbly phase above. At higher velocities, turbulence will occur and the bed will begin to resemble a boiling liquid [55].

As the gas velocity is further increased transportation of the solid phase out of the column will begin to occur. The stages of fluidisation are shown in Figures 8 and 9.

To calculate the minimum fluidising velocity, the Ergun equation can be used to give the pressure difference required to fluidise a column at minimum conditions [56, 57]:

$$\frac{\Delta p}{\Delta x} = 150\frac{(\sum \varepsilon_i)^2}{\varepsilon_g^3}\frac{\mu_g U_0}{(\Psi_i d_i)^2} + 1.75\frac{\sum \varepsilon_i \rho_g U_0^2}{\varepsilon_g^3 \Psi_i d_i} \quad (1)$$

ρ_g and ρ_s are the gas and solid densities (kg m^{-3}); ε_g and ε_s are the gas and solid voidages; μ_g is the gas viscosity (Pa s), U_0 is the superficial gas velocity (i.e. the volumetric gas flowrate divided by column area) (m s^{-1}); Ψ is the sphericity (the relative roundness of the particles); and d_i is the particle diameter for the phase i (m).

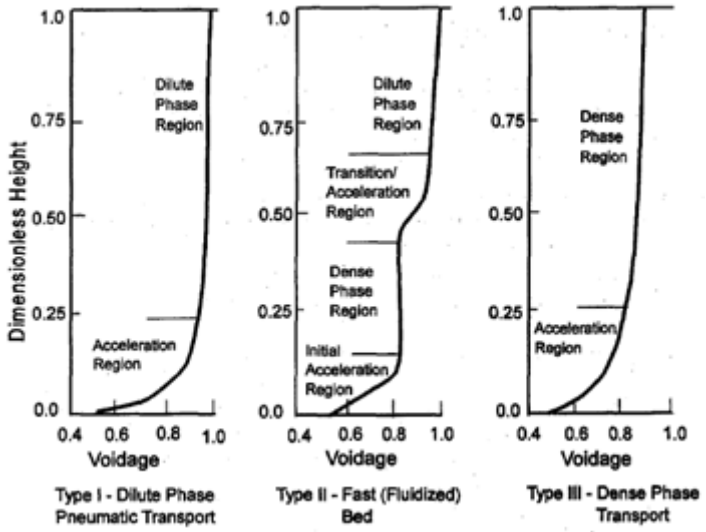

Figure 8: Void profiles in the riser of a circulating bed from Yang [58]

An estimate of the particle velocity necessary in the above equation can be derived from the Archimedes number, which is a ratio of the gravitational forces to the viscous forces [54].

$$Ar = \frac{\rho_g(\rho_i - \rho_g)gd_i^3}{\mu_g^2} = 150\frac{(1-\varepsilon_{mf})}{\Psi_i^2\varepsilon_{mf}^2}Re_{mf} + \frac{1.75}{\Psi_i\varepsilon_{mf}}Re_{mf}^2 \quad (2)$$

g is the acceleration due to gravity (m s^{-2}) and R_{emf} is the Reynolds number at the minimum fluidisation velocity.

$$Re_{mf} = \frac{\rho_g u_{mf} d_i}{\mu_g} \quad (3)$$

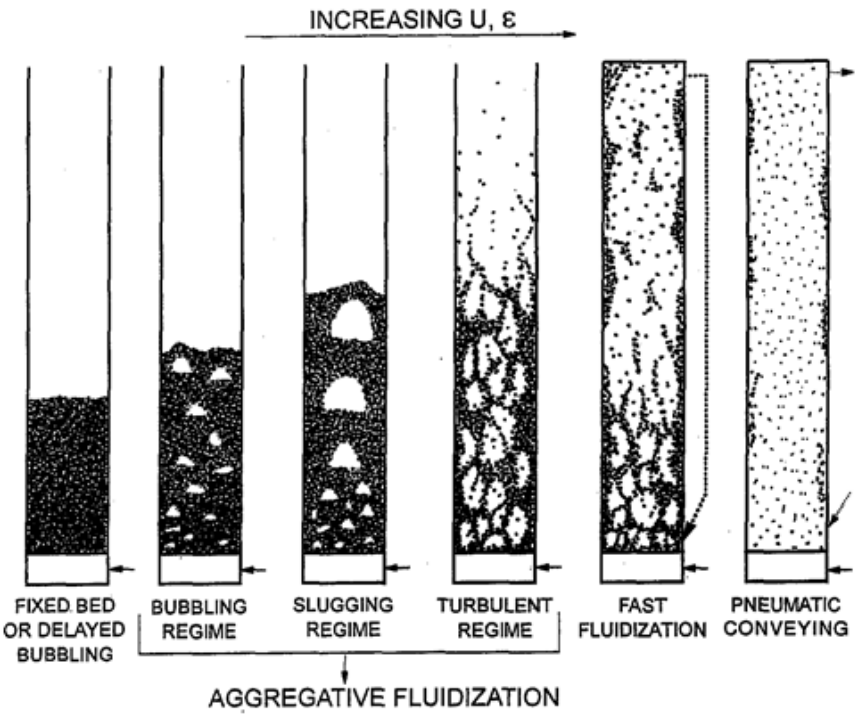

Figure 9: Schematic diagram showing hydrodynamic regimes of fluidisation from Grace [59]

Theoretically, if the voidage at minimum fluidisation were known, it would be possible to calculate u_{mf} from the above, however it is complicated to determine ε_{mf}, as it varies with temperature and the dimensions of the particles in a complex manner [60]. It is usually best to assume a value of ε_{mf}, based on empirical correlations.

An estimate for the voidage at minimum fluidisation velocity can be obtained from Eqn. (4) [61]

$$\varepsilon_{mf} = 0.586\Psi^{-0.72}\frac{\mu_g^2}{\rho_g\left(\left(\rho_i-\rho_g\right)g\right)^2 d_i^3}\left(\frac{\rho_g}{\rho_i}\right)^{0.021} \qquad (4)$$

Another simple way of calculating the fluidisation velocity is to use the slip velocity of the heaviest or largest particle – as any velocity above this will cause the powder to be carried upwards. In the case of the algebraic slip model, this is given by:

$$u_i^* = -\left[\frac{4}{3}\left(\frac{\rho_i}{\rho_g} - \frac{\rho}{\rho_g}\right) g \frac{d_i}{C_D}\right]^{1/2} \quad (5)$$

The fluidisation behaviour in the bed will be dependent on the type of powder that is used. Geldart [57] suggested a classification system whereby powders were defined as one of four types [56], which is shown in Figure 10.

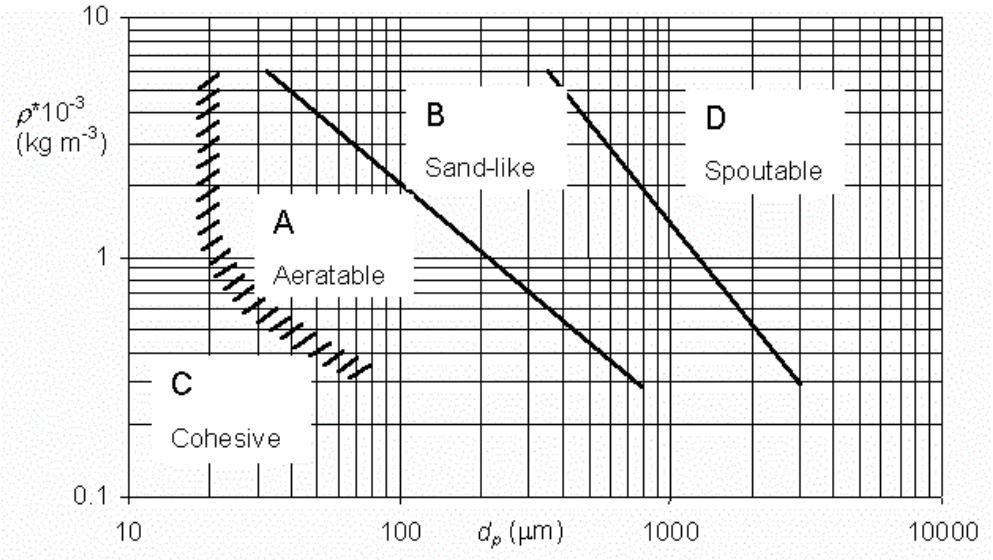

Figure 10: Powder classification diagram from Geldart [57]

A) Particles with a diameter between 20-100 μm diameter and a density less than 1400 kg m^{-3}. These are called powders and fluidise in a stable manner. As velocity is increased, it eventually reaches fluidisation velocity, and the bed will rise. Thereafter any increases in velocity will lead to an increase in bed height up until about three times u_{mf}. Any velocities higher than this will result in the stable bed collapsing to its minimum fluidisation while a chaotic, turbulent, bubbling behaviour will be observed above this.
B) Category B particles are between 40-500 μm diameter with densities between 1400-4500 kg m^{-3}. These beds are much less stable than those with category A particles. Free bubbling typically occurs as soon as u_{mf} is reached.
C) Category C particles are very small (<30 μm) and light and are difficult to fluidise as the intraparticle forces have a much larger force than gravity. Upward

air flow will form channels which through which air will subsequently flow, never leading to the fluidisation of the bed.

D) Category D particles are too big and heavy to fluidise effectively. They require a higher u_{mf}, and a much higher gas flow, so that very little mixing will occur due to the large distances between particles.

The first step in reactor design is to calculate the residence time needed to obtain the desired extent of reaction. The gas velocity can then be chosen to allow for this residence time based on the properties of the average phase.

A typical process for a fluidised bed system comprises a number of elements, including [56]:

Feed of gas to/from the reactor;

Separation of entrained particles from the exhaust gas

Recycle of particles to the reactor

Heating and cooling of input/output streams and the reactor

Fans and compressors for pumps to pump feed/output

Instrumentation and controls

To design the above features, the following properties must be determined or predicted [56]:

Behaviour of fluidised solids

Rates of heat/mass transfer

Chemical reaction rates

Distribution of reactant concentrations

2.5 Multiphase flow simulation

There are a number of factors complicating the simulation multiphase flow, having to capture the behaviour of each phase, the interactions between phases, and turbulent effects which may not all be known [62].

Many methods for the simulation of multiphase flow have been developed over the years to account for different scenarios. These can range from very definite separations of two distinct phases, such as the interaction between the water and air on a lake on a cold day, to the turbulent flow of bubbles in a reactor intensified through agitation.

The FLUENT 12 manual [62] has some recommendations for the choice of multiphase models for each flow pattern. It recommends the use of the mixture, or algebraic slip model for pneumatic transport or the simulation of dispersed phases, but not a fluidised bed. The carbonator in a carbonation cycle is operated as a fast-fluidised bed, so this may be appropriate here, but often the calciner is simulated as a bubbling bed, for which Fluent recommends Eulerian flow. These flow types will be explained in more detail below.

Upward gas-liquid flows, which are the most often studied, range from, with increasing velocity:

a) Discrete bubbly flows, with bubbles widely dispersed in a liquid
b) Slug flows where a bubble will travel upwards occupying the entire width of the channel with the liquid flowing around it
c) Churn flows where the two phases are chaotically mixed
d) Annular flows where the heavier phase is concentrated at the edge and the lighter phase flows up the middle in a continuous stream [55].

In gas-solid flow, the mixture's behaviour also follows displays certain regimes, which include, with increasing solids flow:

a) Particle laden flows, where a few discrete particles are suspended by the gas
b) Fluidised beds where large inventories of solids are suspended
c) Pneumatic transport, where the solids particles are moved upwards by the flow of gas.

Within these gas-solid mixtures, mixing and turbulence will occur, and bubbles will be formed, similarly to the behaviour of gas-liquid flows.

It is possible to formulate a multiphase flow in terms of local instant variables pertaining to each phase and the boundary conditions at all phase interfaces by solving the Navier-Stokes equations directly, which is known as direct numerical simulation. Unfortunately, this is still confined to micro-scale flows where the geometry is of similar scale to the particles under consideration [63] and very small time steps , as the scale of operations required to complete simulations is related to the cube of the Reynolds number.

There are three main approaches to multiphase flow modelling which will be covered here. These are the Volume of Fluid (VOF), Eulerian and Lagrangian models.

In VOF both fluids are continua represented with the same momentum equation while continuity equations for each volume fraction are solved individually. Each cell has its own properties based on the mixture volume fractions [64]. VOF is generally used where there is a definite boundary between the phases and is really designed to cope with interpenetrating mixtures. There is often a degree of surface tension, which can be important. The Capillary number can be used to determine if this is significant and the method appropriate.

There are various relations to model the interface between fluids which depend on the relative concentrations within each cell at the boundary and the interface. VOF is generally applicable to situations such as free-surface flow and stratified flow [38].

Eulerian flow can use both mass and volume conservation depending on the problem in question, but solves momentum and conservation equations for each phase, which are then coupled via momentum, heat and mass transfer coefficients and a shared pressure field. The transfer coefficients represent the interfacial interactions and depend upon the arrangement of phases within the cell, i.e. whether the phases are discrete or continuous and the extent to which they are dispersed within each other.

The Eulerian model is the most complex and computationally expensive model and is used for systems such as fluidised beds and suspensions. It first appeared as the Inter-

Phase Slip Algorithm (IPSA) [65]. An extension of IPSA, call MIPSA (Multi-InterPhase Slip-Algorithm) was used within a two-dimensional Computational Fluid Dynamics (CFD) code to model a lean phase circulating fluidized bed [66]. The different phase concentrations are tracked as volume fractions, and closure relations are employed to describe the interface transfer between the phases. These can be complicated and are often derived from empirical relationships [55].

The Lagrangian approach tracks the motion of a discrete phase within a continuous one. Many particles are simulated, and their averaged values are used to get a representation of the system [39]. The gases are modelled using the Navier-Stokes equations and the solids are tracked via Newton's second law and angular momentum. Molaei [26] used a Lagrangian method to simulate the lean-phase carbonation in a variety of different reactors.

Instead of tracking the flow of material through a given space, in Lagrangian models the of the individual particles are tracked based on balances of their material properties as they pass through the fluid [67]. This method has generally been used for dispersed flows, as it can become expensive when many pieces are tracked.

With increasing computational power, Lagrangian models such as the discrete element method (DEM), are being used increasingly for modelling processes such as pneumatic conveying [68]. Like other Lagrangian codes, DEM models the gas via an Eulerian model and tracks the solids, but includes a large mass of particles, making it suitable for fluidisation, but computationally expensive [69].

The algebraic slip model is a variant on the mixture method which is based on Eulerian flow. It boasts the advantage over other multiphase methods in that it can model suspensions containing wide distributions of sizes and densities of particles with relatively high computational efficiency. It is like the VOF method in that it solves one continuity equation with separate momentum equations for each phase, with mixture properties dependent on their local concentrations, but is applicable in situations where equilibrium has occurred.

This method simplifies the interaction of the discrete and continuous phases somewhat by assuming homogeneity, but despite this reduction in the accuracy; it also removes

complicated closure relations and greatly reduces the simulation time and computational expense.

THE CALCIUM LOOPING CYCLE

3.1 Introduction

Solid sorbents are one of the most promising technologies currently being investigated for carbon capture. A range of lab-scale and pilot plant studies into the performance of various metal oxides have been performed, including calcium, potassium and lithium [70-73].

The carbonation cycle was first proposed by Shimizu [16] and comprises two steps:

1) carbonation, where the CO_2 is "captured" from the flue gas of a power plant through reaction with calcium oxide, or lime, to form calcium carbonate at 600-700 °C
2) Calcination, where the calcium carbonate and carbon dioxide are regenerated into concentrated streams at 750-900 °C, and the CO_2 is removed from the cycle [74].

The CO_2 is then sent for containment or re-use while the regenerated lime is returned to the carbonator and the remaining flue gas released to the atmosphere, possibly after undergoing further treatment.

Post-combustion carbon capture using limestone in a calcination-carbonation cycle is a promising technology for the removal of CO_2 from the flue gases of fossil fuel power plants. It only leads to a small reduction in the thermal efficiency of the power station (6-8%), makes use of an already established technology in fluidised beds; uses a cheap and readily available reactant in limestone; produces a very pure CO_2 output stream (95 vol% plus) [15]; has the potential for integration with other industries such as cement manufacture and is simple to install without affecting the operation of the plant, as it is added at the end before release of waste gas.

Abanades estimated an increase of the cost of electricity by around 50% from 0.04 € $(kW\ h)^{-1}$ without CO_2 capture to 0.06 € $(kW\ h)^{-1}$ for a carbonation plant using calcium oxide, which corresponds to a cost of 15 € t^{-1} of CO_2 captured [75]. An oxyfuel carbonator was found to be more effective with cost increases from 0.025 \$ $(kw\ h)^{-1}$ to 0.031 \$ $(kW\ h)^{-1}$, at around 8.30 \$ t^{-1} of CO_2 captured [76].

David and Herzog studied a range of plants including integrated coal gasification combined cycle, pulverised coal, and a natural gas combined cycle and compared the costs of operating MEA or adsorption. They found that between 2000 and 2012 the costs of carbon capture had reduced significantly, lowering by around 25% (natural gas) to 40 % (IGCC) [77].

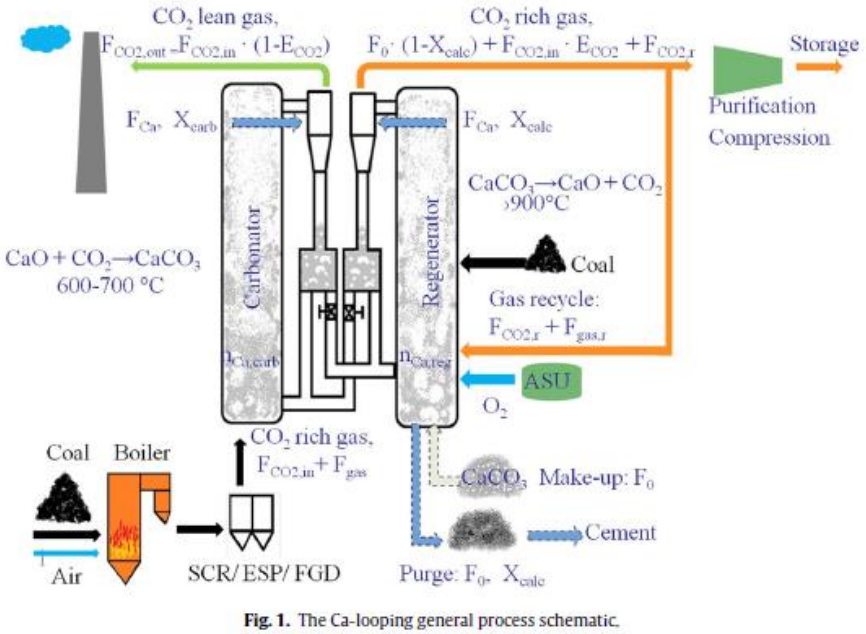

Fig. 1. The Ca-looping general process schematic.

Figure 11: Typical combustion scheme for Ca-looping post-combustion CO_2 capture from Duelli [78]

Figure 11 shows a typical system for carbon capture via a carbonation/calcination cycle from Duelli [78]. It includes standard operating conditions and temperatures.

1) The flue gas from the power plant enters the carbonator where it contacts the Calcium Oxide powder. The high surface area of the powder and the temperature promote the rate of reaction from CaO and CO_2 to $CaCO_3$. The now CO_2-lean flue gas is released to the atmosphere.
2) Once enough CO_2 has been removed from the gas stream the gas/powder mixture is sent to a calciner. Here, at temperatures around 900 °C, the CaO and CO_2 are regenerated. The CaO is recycled to the carbonator and the CO_2 purified and compressed and sent to storage.

The high temperatures used in carbonation and calcination promote a rapid reaction rate and high conversion (80%) and hence reduce potential reactor and inventory size compared to colder processes [79]. The process uses a lot of energy in heating and reacting the components, but the higher temperatures can be used for steam generation to recycle energy back into the system [70].

Carbonation is usually modelled via a grain method, where a layer of product forms around an unreacted core. It has been observed that carbonation initially follows a rapid reaction rate, but after enough of the product layer has formed, this is followed by a much slower diffusion-controlled stage as CO_2 must first penetrate the outer layer [30, 70].

Repeated use of a carbonation/calcination cycle results in the lowering of the efficiency of the reagents, through processes such as sintering and collision. Abanades [83] reports that after 13 cycles, the conversion limit will drop to around 24%. Hydration has been put forward as a technique to limit the rate of degradation, as this has been found to keep CaO capacity above 50% after 20 cycles, whereas without it the capacity of the CaO is reduced to less than 20% in dry cycles [83, 84].

Other factors which affect the particles include [74]:

1) Sulphation due to incomplete removal of sulphur dioxide from the feed stream
2) Sintering due to heat
3) Attrition due to collisions between particles

These will all lead to a loss of efficiency in the reactor with time and repeated cycles, meaning reagents will need to be replaced.

A complete reactor system to carry out chemical processes comprises a whole system of units, including heat exchangers, filtration and separation devices for pre- and post-treatment etc. This study will focus on the reactor and the other equipment will be ignored. Figure 12 shows the flow process for a CO_2 capture pilot plant facility, including the extra processes.

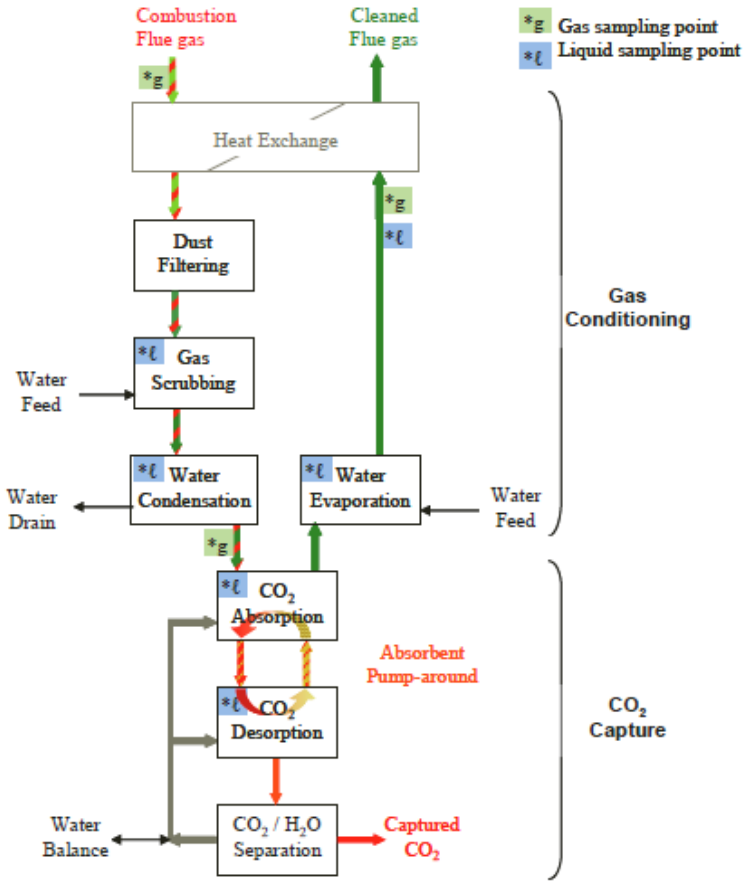

Figure 12: Flow chart for a coal-fired CHP pilot plant from Bryngelsson and Wester [85]

3.2 Carbonation kinetics

Carbonation is a gas-solid reaction between calcium oxide and carbon dioxide [86]. It is exothermic with a ΔH_R of -178 kJ mol^{-1} and occurs at two general rates: an initial fast stage (reaction controlled), and a slower (diffusion controlled) stage. Calcination is the opposite reaction and is endothermic.

The carbonation reaction is given by:

$$CaO_{(s)} + O_{2(g)} \rightarrow CaCO_{3(s)} \quad (6)$$

Carbonation is commonly described by grain models employing a shrinking core or random pore mechanism [1, 87]. It can be simplified as:

$$\frac{dN}{dt} = Ks \tag{7}$$

Where N is the molar concentration, K is the reaction constant and s is the available surface area. The reaction constant is made up of various parameters including particle concentrations, temperature and pressure.

In a standard grain model, there is a central, unreacted core around which a layer of product develops as reaction occurs. Initially, the available surface for reaction is the particle surface area and the reaction will occur at its maximum rate [87]. As the reaction proceeds the outer perimeter of the unreacted particle will reduce, and the area available for reaction will be reduced, thus diminishing the rate. Above a critical diameter, the diffusion step will become dominant. This process is shown in Figure 13.

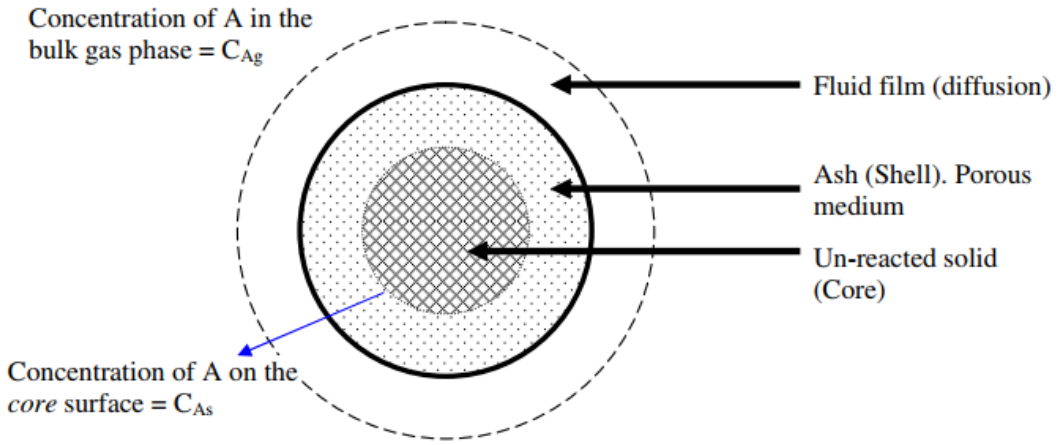

Figure 13: Shrinking core model from Madras [88]

This leads to two reaction regimes: the reaction-controlled regime and the diffusion-controlled regime, with separate equations describing the behaviour of each. Kunii and Levenspiel [87] proposed the following equations for these mechanisms:

Reaction control

$$\frac{t}{\tau} = 1 - (1 - X)^{1/3} \tag{8}$$

Diffusion control

$$\frac{t}{\tau} = 1 - (1 - X)^{2/3} + 2(1 - X) \tag{9}$$

Where t is the time, τ is the time for total conversion and X is the conversion.

These relations offer a good approximation to the problem, but they do not take internal pore structures into account, and could theoretically lead to total conversion, so they cannot be used to fully explain the carbonation reaction.

Lee [86] found that the initial kinetic controlled rates were rapid until the conversion approached an ultimate conversion, whereupon they slowed as the reaction entered the diffusion controlled regime. They found this initial rate to be zero order, represented by a rate constant, but as the conversion grew higher, this rate reduced. To capture this, they put forward a relationship between the conversion, a rate constant and this so-called ultimate conversion, after which the rate is reduced. This is shown in Equation (10).

$$\frac{dX}{dt} = k\left(1 - \frac{X}{X_u}\right)^n \tag{10}$$

Where n is 1 and X_u is the ultimate conversion of CaO, given by

$$X_u = kb \tag{11}$$

This relation was found to be valid for various limestones for the kinetic controlled stage, with conversions up to 0.5. The values found for k and b are shown in Table 2.

Table 2: Kinetic parameters for the carbonation model from Lee [86]

Temperature (°C)	Chemical reaction control regime			Diffusion control regime		
	k (min^{-1})	b (min)	X_u	k (min^{-1})	b (min)	X_u
585[a]	0.406	0.587	0.24	0.049	14.875	0.73
615[a]	0.600	0.489	0.29	0.110	6.821	0.75
655[a]	0.925	0.506	0.47	0.344	2.241	0.77
690[a]	1.070	0.637	0.68	0.759	1.001	0.76
725[a]	1.855	0.404	0.75	2.111	0.352	0.74
550[b]	0.273	1.435	0.39	0.074	9.167	0.68
600[b]	0.563	0.967	0.54	0.165	4.581	0.76
650[b]	0.858	0.863	0.74	0.375	2.325	0.87

[a] Data of Bhatia and Perlmutter [6].
[b] Data of Gupta and Fan [1].

Symonds et al. [30] conducted experiments carbonating limestone in a thermogravimetric analyser with and without hydration. They used particles between 250 to 425 μm diameter at temperatures of 620 °C. They used their results to develop a model using a shrinking core mechanism which represented the rate of carbonation (R) under kinetic control as a power law depending on the concentration of carbon dioxide, with zero order based on the calcium carbonate.

$$R = M_{CaO} k_s s\left(P_{CO_2} - P_{CO_2,eq}\right) \tag{12}$$

where M_{CaO} is the molar mass of CaO, k_s is the reaction constant, s is the specific surface area and $P_{CO2,eq}$ is the partial pressure of CO_2 at equilibrium in atm.

R is a specific rate (s^{-1}) which was expressed in terms of conversion by

$$R = \frac{dX}{dt(1-X)} \tag{13}$$

The reaction constant k_s was given by the Arrhenius expression

$$k_s = k_0 \exp\left(-\frac{EA}{RT}\right) \tag{14}$$

where k_0 is the exponential factor at initial conditions and EA the activation energy.

The specific surface area, *s*, for a sphere is:

$$s = \frac{6}{\rho d_i} \tag{15}$$

They found that the behaviour of carbonation at the initial kinetic controlled step was well explained by a zero-order rate based on the temperature and carbon dioxide concentrations.

3.2.1 1D Carbonation module

A one dimensional carbonation module was constructed in Excel and PHYSICA based on the above work by Lee [86], using an Arrhenius expression to define the constants k and b for a range of temperatures via a regression analysis. The first-order mechanism gave a rate of conversion based on the concentration of CaO, assuming an excess of CO_2.

$$r = -k_r N_{CaO} \tag{16}$$

The constants used in the Arrhenius expression are given in Table 3.

Table 3: Kinetic data for carbonation from [79, 89]

Regime	Source	E_a (kJ mol^{-1})	K ($minl^{-1}$)
Rate controlled	Bhatia/Perlmutter	72200	1.03E+04
	Gupta/Fan	72.7	1.16E+04
Diffusion controlled	Bhatia/Perlmutter	189.3	1.57E+10
	Gupta/Fan	102.5	2.33E+05

k_r comes from a relationship between conversion, half-life and first order reaction rate:

$$k_r = \frac{\ln 2}{t_{1/2}} \tag{17}$$

The half-life was calculated from Equation (18).

$$t = \frac{Xb}{kb - X} \tag{18}$$

where equations for k and b come from the following regression analyses, which is applicable between 873 and 973 K:

$$k = -2.94533T_n + 4.520333 \tag{19}$$

$$b = 0.00585T_n - 0.00572 \tag{20}$$

Figure 14 shows the effect of temperature on the conversion rate of calcium oxide based on Bhatia and Perlmutter [89]. The maximum attainable conversion, before the rate-limiting diffusion-controlled phase is entered, is roughly 0.45, and that this will occur at 900-925 K. This should reach the higher conversion limit at around 3 minutes, although the rate begins to drop at around 2 minutes.

For a temperature of 900 K, the half-life of the reaction for CaO to be half-converted to $CaCO_3$, is 0.75 minutes, or 45 s. This corresponds to a reaction rate constant, for a first order stoichiometric reaction for CaO of 0.015 kmol min^{-1}.

The target maximum conversion for the calcium oxide was set to 0.5, and the temperature of the reactants entering the reactor to 900 K.

The initial design for the system was performed on Excel, while assuming constant temperatures and pressures. It used a first order Euler scheme and tracked the molar, mass and volumetric concentrations. Only the kinetically controlled regime was modelled.

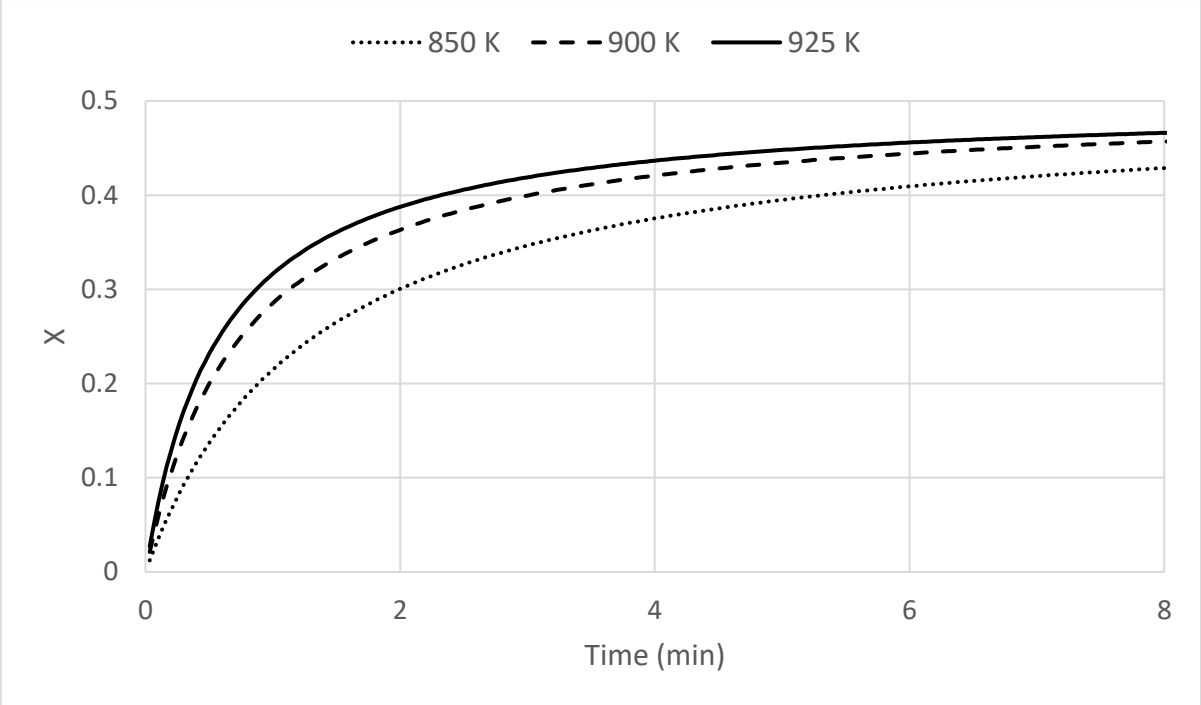

Figure 14: Conversion of CaO to $CaCO_3$ at different temperatures

3.3 Calcination kinetics

In calcination the carbon dioxide and calcium oxide consumed in carbonation are regenerated. It occurs at temperatures around 900 °C and is endothermic. Much like carbonation, it is usually described by grain models such as the shrinking core mechanism.

$$CaCO_{3(s)} \rightarrow CaO_{(s)} + CO_{2(g)} \quad (21)$$

Unlike carbonation, which is often performed in circulating fluidised beds, calcination is often run in smaller reactors at a lower velocity as a bubbling fluidised bed, due to the longer residence times required [90, 91].

The rate of calcination is dependent on many factors as it is a complicated process and many factors have been considered to contribute to this rate.

Various stages have been proposed as rate-determining including reaction rate at the interface [92, 93] , gas-film diffusion and product diffusion and even the rate of heat transfer at the surface of the particle [94].

It has been found that resistance to heat transfer and pore diffusion as well as the presence of impurities can also have a significant impact on the reaction rate [95].

Shen and Smith [96] theorised that kinetic control, product diffusion control and gas-film diffusion control could all be factors.

Borgwardt [97] explained the kinetics via a shrinking core with an initial reaction controlled step, followed by a slower diffusion controlled phase, while Ohme [98] used a similar model and found the kinetic controlled stage to be active below 1000 °C.

Bhatia and Perlmutter proposed the random pore model [1], whereby the internal structure of the particles affects the conversion rate and capacity.

The random pore model is like the shrinking core but features spherical or cylindrical pores through which the gas can disperse until it reaches a surface to react with. As the reaction proceeds these pores are filled with reactant and are blocked, thereby reducing the surface area available for reaction and increasing the limits to the rate of diffusion. Above a certain conversion, the rate will be severely limited, which is the diffusion-controlled stage. This is shown in Figure 15, where there is an inner core of $CaCO_3$ which has reacted to form CaO and CO_2 on its outer surface.

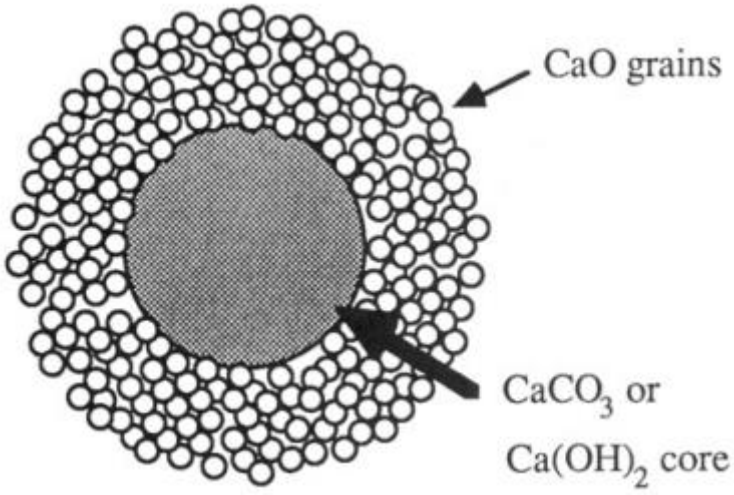

Figure 15: Illustration of the shrinking core calcination model from Milne [99]

Bhatia and Perlmutter described the two phases in the model by:

Reaction control

$$\frac{1}{\varphi}\left[\sqrt{1-\varphi\ln(1-X)}-1\right]=k't \tag{22}$$

Diffusion control

$$\frac{1}{\varphi}\left[\sqrt{1-\varphi\ln(1-X)}-1\right]=k''\sqrt{t} \tag{23}$$

Where φ is a structural parameter depending on surface area, porosity and initial length of the pore system per unit volume and k' and k'' are rate constants.

Milne [99] looked at the calcination rates of particles with sizes between 1 and 90 μm, which had been treated with water. They used a shrinking core mechanism based on the assumption that the grain was comprised of smaller $CaCO_3$ grains which all calcined at the same rate:

$$\frac{k'}{r_0} = \frac{1-(1-X)^{1/3}}{t} \tag{24}$$

They found an initial rate given by:

$$r_0 = \frac{3}{\rho s} \tag{25}$$

Where *s* is the specific surface area. This leads to a relation between conversion, time and particle size:

$$X = 1 - \left(1 - \frac{k}{d_{\mathrm{i}}^{0.6}} t\right)^3 \tag{26}$$

Khinast [29] performed studies on the rate of calcination by varying the temperature and pressure with different limestones. They proposed a random pore model, in which the pore structure evolved based on the extent of reaction similar to the carbonation model of Bhatia and Perlmutter explored in the carbonation section [1].

$$\frac{dN_{CaCO_3}}{dt} = -\frac{\rho_{CaCO_3}}{M_{CaCO_3}} \frac{\partial X}{\partial t} = -R \tag{27}$$

Where ρ_{CaCO3} is the density of $CaCO_3$, M_{CaCO3} is its molecular mass, k_s is the reaction coefficient and *X* is the conversion.

They described the porosity as being proportional to the conversion, to represent the receding available surface area of the particles as the reaction proceeds.

$$\frac{\varepsilon}{\varepsilon_0} = 1 + X\left(\frac{\varepsilon_e}{\varepsilon_0} - 1\right) \tag{28}$$

Where ε_e is the final porosity and ε_0 the initial.

The rate of the initial, kinetically controlled stage is given by:

$$R = \frac{\rho_{CaCO_3}}{M_{CaCO_3}} \frac{\partial X}{\partial t} = K s_v \tag{29}$$

Where *K* is an empirically derived exponential function describing the equilibrium driving force behind the reaction and s_v is a relation describing the specific surface area:

$$K = kf(CO_2) = k\exp\left(-a_1 \frac{P_{CO_2}}{P^0_{CO_2}}\right) \tag{30}$$

P is the partial pressure in bar, the effect of which on reaction rate is displayed in Figure 16:

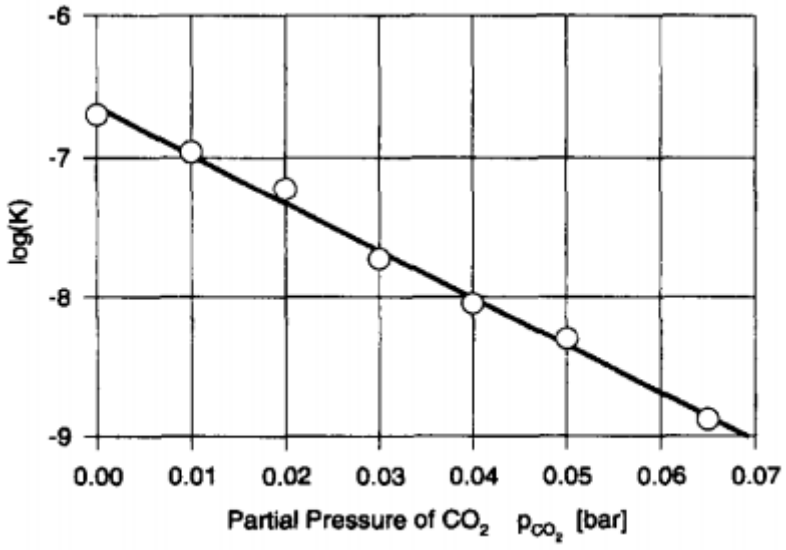

Figure 16: Influence of the CO_2 partial pressure on the reaction rate from Khinast [29]

The surface area was calculated as a function of the conversion and some variable used to explain the inner shape of the particle.

$$\frac{S_v}{S_{v,0}} = (1 - X)[1 - \varphi \ln(1 - X)]^{1/2} \tag{31}$$

The parameters were fitted by the least squares to data from experiments by Khinast as well as Bhatia and Perlmutter [100].

Figure 17 shows how the model applies to the particle itself and the changes in the various properties as the CO_2 permeates the outer gas layer into the solid.

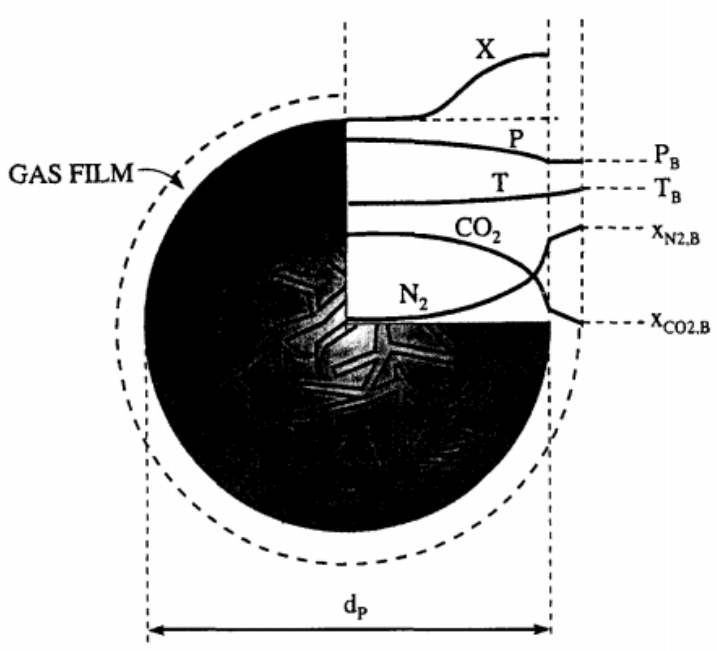

Figure 17: The variables considered in the random core model of Khinast [19]

3.4 Costs of CO_2 capture

Combustion with carbon capture requires additional sources of energy for both the capture and regeneration processes. This 'energy penalty' is in addition to costs for transport and storage.

These energy penalties are generally ten to a hundred times greater than other environmental penalties at modern power plants [21]. This reduces plant efficiency, which leads to a higher fuel requirement and produces more waste which requires more treatment. Some typical energy penalties are shown in Table 4.

The four major costs which need to be considered when analysing the potential of carbon capture are for the capture itself, the transport, the storage and the monitoring [35]. Examples of these are shown in Table 5.

Table 4: Energy penalty for post-combustion CO_2 capture from Steeneveldt [35]

	Natural Gas Derived Flue Gas (GJ/tonne CO_2)	Coal Derived Flue Gas (GJ/tonne CO_2)
Fuel Efficiency without CO_2 capture	58% (Combined Cycle, 0.04 bar condenser pressure 400 MW)	45% (Pulverized Bituminous Coal 600 MW)
Captured CO_2 Compression to 100 bar (g)	0.4	0.4
Blower (overcome pressure drop in absorber)	0.1–0.34	0.04–0.1
Pumps	0.21–0.33	0.06–0.11
Sub Total Power	Power: 0.71–1.07	Power: 0.51–0.61
Regeneration Heat (Equivalent Power)	2.7–3.3 (0.62–0.76)	2.7–3.3 (0.62–0.76)
Fuel Efficiency (%) with CO_2 capture	~47–50%	~34–36%

Table 5: Overview of indicative costs in a CO_2 capture and storage value chain from Steeneveldt [35]

	USD/tonne CO_2	Common cost drivers	Specific cost drivers
Capture and compression	5–90	Volume of CO_2 Location	CO_2 partial pressure in source
Transport	0–20		Existing infrastructure
			Transport distance
Storage	2–12		Existing infrastructure
			Storage capacity
			Monitoring requirements

High temperature processes such as carbonation offer the prospect of heat recovery from the gas, and potential steam generation to power plant facilities [70], but there is still an additional requirement for energy: the regeneration step is endothermic and requires a source of heat.

Some of the different potential technologies for carbon capture, with their estimated costs are outlined in Table 6. This presents the post-combustion plants as notably more cost-effective than the alternatives.

Table 6: Cost comparisons of the main technology options from Steeneveldt [35]

Reference	Fuel cost ($/kg)	Estimated cost of CO_2 avoided USD/tonne	Estimated capital cost (USD/kW)	Estimated capital (USD/kW)
Post-combustion natural gas combined cycle				
Parsons, 2002, 508 MW NG	2.82	74	0.949	1099
NETL, 2002, 379 MW NG	3.55	45	0.875	911
IEA GHG, 2004, MEA, 776 MW NG	3	41	1.844	938
Melien, 2005, 392 MW NG	2.96	57	1.09	1261
Rubin *et al.*, 2005, 507 MW NG	4.44	49	1.099	909
Rubin *et al.*, 2005, 507 MW NG	4.44	68	0.733	909
Post-combustion pulverized coal sub-critical boilers				
Simbeck, 2001, 294 MW	0.98	45	2.09	1059
Alstom *et al.*, 2001, 255 MW 96% capture	1.3	73	2.228	1941
Chen *et al.*, 2003, 140 MW	1.2	56	1.48	837
Chen *et al.*, 2003, 282 MW	1.2	48	1.48	647
Post-combustion pulverized coal super and ultracritical boilers				
Parsons, 2002b, 329 MW PC	1.29	51	1.83	2219
Parsons, 2002b, ultracritical boiler, 367 MW PC	1.29	49	2.35	1943
IEA GHG, 2004, MEA, 666 MW PC	1.5	29	4.061	1894
Rubin *et al.*, 2005, 492 MW PC	1.25	40	3.102	1936
Oxyfuel boiler				
Dillon *et al.*, 2005, 532 MW	1.5	27		1857
Oxyfuel natural gas cycle				
Dillon *et al.*, 2005, 440 MW	3	47	—	1034
Pre-combustion NG combined cycle				
Jacobs, 2003, 392 MW NG	3.52	68.4	1.329	1076
Melien, 2005, 358 MW NG	2.96	76		
IGCC GE oxygen-fired, bituminous coal				
Simbeck, 2002, 455 MW BC	0.98	22	2.151	2067
IEA GHG, 2003, 730 BC	1.5	16	4.682	1495
Rubin *et al.*, 2005, 492 BC	1.25	20	2.749	1748
Melien, 2005, 699 MW BC	0.3	14.5	6.8	1919
Melien, 2005, 424 MW	2.96	34.4	1.47	1089

Porter et. al. [101] performed a techno-economic assessment of potential carbon capture technologies, and found similarly that post-combustion treatment without further gas treatment offered the cheapest solution, albeit one which became more expensive following post-process treatment to bring flue gas within environmental limitations. This is shown in Figure 18, where pre-combustion is overall cheaper, but the capture process itself is highlighted as being lower in cost impact.

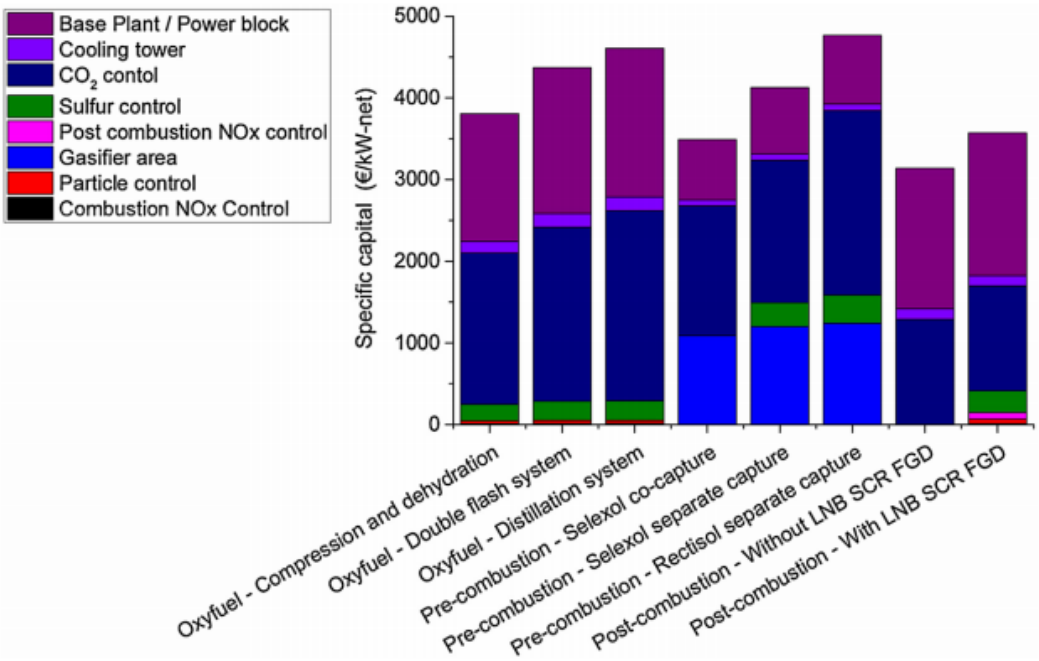

Figure 18: Specific capital required for the different CO_2 capture technologies and purification processes from Porter et. al. [101]

Wang [102] ran a series of simulations of the carbonation process for carbon capture and found that the greatest indicator of the energy penalty of a plant with CCS facilities was the efficiency of the original combustion process, and that the greatest contributor to the energy penalty was the CO_2 compression step.

Han et al [103] analysed various techno-economic assessments of CCS plants in the literature, before studying economic feasibility of three large-scale CCS plants, together with risk assessments for all three. They found a great variability between different assessments of costing and risk, based on the different input conditions. Transport and storage costs were always much less than capture costs, with depleted oil fields one of the more economically feasible locations.

3.5 Carbon storage

The three most likely locations for CO_2 storage are [104]:

1) Oil and gas reservoirs. This could be done either after, or as part of enhanced oil recovery.
2) Saline aquifers
3) Inaccessible coal seams. This could be done as part of methane recovery.

Integration of carbon storage with existing technologies, such as enhanced oil or methane recovery offers potential for savings in these industries as well.

To be an appropriate location for carbon storage, potential facilities must be large enough, safe enough to not allow leakage, accessible enough to access, and economical. There is currently some uncertainty regarding capacity, with global reserves estimated to be from 475-5880 Gt CO_2 [104]. With current emission estimates around 28 Gt CO_2 per year [5], this offers some respite, assuming much of the CO_2 can be captured and securely held. Table 7 shows some options and how much space there is available in each. Annex 1 refers to storage within the country of production whereas non-annex 1 is for storage in another country.

It may be possible to use temporary storage, whereby leakage is designed and accounted for [104].

Table 7: Estimated storage potential (Gt CO_2) from Bode [104]

	Remaining oil fields	Depleted oil fields	Remaining gas fields	Depleted gas fields	Enhanced coal bed methane
Onshore					
Total Annex 1[a]	2.6–186.2	8.4–16.8	91.2–382	2.5–156.7	0–401.7
Total non-Annex 1[a]	6.4–547.8	13.6–27.2	127.8–543	1.5–234.3	0–1,078.3
Total	9–734	22–44	219–925	4–391	0–1,480
Offshore					
Total Annex 1[a]	0.6–67.2	6.1–32.6	38.3–412.3	13.6–20.5	10.4–374.1
Total non-Annex 1[a]	2.4–240.8	13.9–74.4	110.7–365.7	6.4–11.5	19.6–706.9
Total	3–308	20–107	149–778	20–32	30–1,081

MODELLING DESCRIPTION

4.1 Introduction

The focus of this work has been the simulation of a carbonation cycle for the purposes of post-combustion carbon capture. The cycle consists of two reactors: a carbonator to capture CO_2 using CaO and a calciner to regenerate the CaO in a dual-reactor system. This work has been performed with the in-house software PHYSICA employing an algebraic slip model for the multiphase flow hydrodynamics and a variation of the shrinking core mechanism for the reaction. The performance of the reactor system with regards to carbon capture was investigated and the potential for using the algebraic slip model in lieu of a more complicated computational fluid dynamic model was evaluated.

The algebraic slip model is applicable in situations where convection is dominant. It assumes there is negligible acceleration due to gravity and the solid particles are already travelling at their terminal velocity determined by the balance between drag and acting forces, in this case gravity. The difference in terminal velocity between each phase and the mixture is known as the slip velocity. This governs the rate of transport of each solid phase in the mixture.

The algebraic slip model boasts the advantage over other multiphase methods in that it can model suspensions containing a wide distribution of sizes and densities of particles. The method simplifies the interaction of the discrete and continuous phases by assuming homogeneity, but despite this reduction in the accuracy; it also removes complicated closure relations and greatly reduces the simulation time and computational expense.

4.2 Gas-solid multiphase flow model description

4.2.1 Continuity and momentum equations

The mixture [34] is modelled as a continuous fluid, with a continuity equation given by:

$$\frac{(\partial \rho u)}{\partial t} + \nabla \cdot (\rho u) = S \tag{32}$$

The momentum equation for the mixture is solved for an overall mixture velocity u_i:

$$\frac{(\partial \rho u_i)}{\partial t} + \nabla \cdot \left(\rho \underline{u} u_i\right) = -\frac{\partial p}{\partial x} + \nabla \cdot \left(\Gamma \nabla (u_i)\right) + S_{u_i} \tag{33}$$

PHYSICA solves for the following general conservation equation for any variable *c*.

$$\frac{(\partial \rho c)}{\partial t} + \nabla \cdot (\rho u c) = \nabla \cdot \left(\Gamma \nabla (c)\right) + S_c \tag{34}$$

4.2.2 Material properties

The components under consideration in this work are air, carbon dioxide, calcium carbonate and calcium oxide. The properties of these pure components at standard conditions are summarised in Table 8. Initial simulations assumed density did not change, but later tests had a density which varied with temperature.

Table 8: Material properties

Component	RMM (kg kmol^{-1})	Density (kg m^{-3})	Viscosity (Pa s)
Air	28	1.2	0.000018
CO_2	44	1.98	n/a
CaO	56	3340	n/a
$CaCO_3$	100	2710	n/a

The most important local properties to determine mixture behaviour are the density and viscosity. As the particle concentrations are in volume fraction, the local density can be derived from Equation (35).

$$\rho = \sum_{i=1}^{n} \varepsilon_i \rho_i \tag{35}$$

Ishii and Zuber's viscosity correlation was used [105]:

$$\mu = \mu_g \left(1 - \frac{\sum \varepsilon_i}{(\sum \varepsilon_i)_{max}}\right)^{-2.5(\sum \varepsilon_i)_{max}} \tag{36}$$

The momentum equation for the mixture, summed over the phases, can be written as [106]

$$\frac{\partial}{\partial t} \sum_{i=1}^{n} \varepsilon_i \rho_i u_i + \nabla \cdot \left(\sum_{i=1}^{n} \varepsilon_i \rho_i u_i u_i \right) = -\sum_{i=1}^{n} \varepsilon_i \nabla p_i + \nabla \cdot \sum_{i=1}^{n} \varepsilon_i \left(\tau_i + \tau_{T,i}\right) + \sum_{i=1}^{n} \varepsilon_i \rho_i g + \sum_{i=1}^{n} M_i \tag{37}$$

Using the definitions of mixture velocity and density from Equations (33) and (35), the advection term in Equation (37) can be rewritten as:

$$\nabla \cdot \sum_{i=1}^{n} \varepsilon_i \rho_i u_i u_i = \nabla \cdot (\rho u u) + \nabla \cdot \sum_{i=1}^{n} \varepsilon_i \rho_i u_i^* u_i^* \tag{38}$$

u_i^* here is the 'slip velocity' of the phase *i*.

The thermal conductivity and expansion coefficient of the mixture were assumed to be equal to that of the gas phase, while the specific heat capacity varied proportional to local phase concentrations [107]:

$$c_P = \sum_{i=1}^{n} \varepsilon_i c_{P,i} \tag{39}$$

4.2.3 Algebraic slip model

The algebraic slip model was used to represent the system's hydrodynamics. This model treats the fluid as a homogeneous mixture with local properties dependant on the local concentrations of phases within each cell. An overall transport equation for the mixture is solved for continuity and momentum, as if it were a single fluid phase, and the flow of the solid species are individually solved with their own transport equations.

In cases where the algebraic slip is valid, the gravitational forces are equal to the drag forces:

$$(\rho_i - \rho) g \frac{\pi d_i^3}{6} = \frac{1}{2} \rho_g u_i^{*2} \frac{\pi d_i^2}{4} C_D \tag{40}$$

The local concentrations in each cell are used to calculate densities and viscosities which are then used to calculate the local momentum and mixture velocities. In real terms, this is only a representative velocity of the mixture, and is not true in a physical sense, in that none of its components are travelling at this rate in this direction, only that the mixture is moving in this way. The gas phase in the mixture is assumed to be travelling at the mixture velocity, slowed by its interaction with the solid phases, which all move at their own individual speeds.

The algebraic slip model has not traditionally been applied to fluidisation columns, as a rapid acceleration of particles is required when they enter the column to overcome the gravitational acceleration and initiate fluidisation, which requires a very short relaxation time. This relaxation time is described by:

$$t_i = \begin{cases} \dfrac{\rho_i d_i^2}{18\mu} & \text{if Re} < 1 \\ \dfrac{2\rho_i d_i}{3\rho_g C_D u_t} & \text{if Re} > 1000 \end{cases} \tag{41}$$

This relaxation time gives values too short for the application of the mixture model from an initial static condition. If particles are introduced from a side stream, the downward acceleration from gravity needs to be counteracted by an upward acceleration from the gas velocity combined with a sideways push to spread the

particles so they will be captured and pushed upwards, otherwise they would fall in earlier tests.

To accomplish this, a lower boundary over which the slip velocity was relaxed was employed. Below a certain height, at a theoretical lower barrier, no slip velocity was applied to the solid phases, and above this, over an increase of 0.1 m the slip velocity was gradually introduced. The gas velocity prevented the downward flow of particles as it was set above the highest slip velocity present in the column. This is shown in Figure 19, where the slip velocity is introduced gradually in the shaded section.

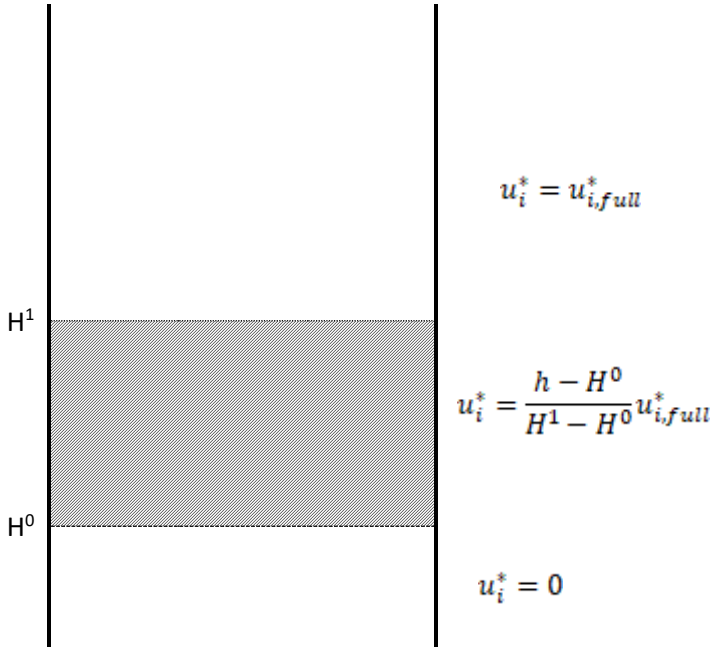

Figure 19: The lower barrier

An additional limit to the slip velocity was applied to prevent flow into overly concentrated cells:

$$u_i^* = u_i^* \left(\frac{0.62 - \sum \varepsilon_{i,n+1}}{0.62} \right)^4 \tag{42}$$

Where, $\sum \varepsilon_{i,n+1}$ is the sum of the volumetric concentrations of the solid phases in the cell to which the phase is moving and 0.62 is the maximum volumetric concentration of spheres, which is also used in the viscosity relationship [105].

The transport of phases in PHYSICA is given by:

$$\frac{(\partial \rho \varepsilon_i)}{\partial t} + \nabla \cdot (\rho u \varepsilon_i) - \nabla \cdot \left(\Gamma \nabla(\varepsilon_i)\right) = S_i \tag{43}$$

Where Γ is the exchange coefficient of i and S_i the sum of the other sources.

There are two main source terms in the concentration equation:

1) Change in concentration due to slip velocity
2) Change in concentration due to carbonation or calcination

To simplify the separation of these sources, the slip velocity can be written separately, and the transport equation rewritten as:

$$\frac{\partial(\rho \varepsilon_i)}{\partial t} + \nabla \cdot \left(\rho(u - u_i^*)\varepsilon_i - \Gamma_i \nabla(\varepsilon_i)\right) = S_i \tag{44}$$

The values of the u^* term in the transport equation were calculated at the faces between the cells, by extrapolating the cell properties from the centre, where *p* refers to the face, *e* refers to the cell below the face and *w* to the cell above it:

$$\rho_p = \frac{\rho_e + \rho_w}{2} \tag{45}$$

$$\nu_p = 2\frac{\nu_e \nu_w}{\nu_e + \nu_w} \tag{46}$$

Using these interfacial values, Equation (40) can be rearranged to give an expression for an individual phase's slip velocity.

$$u_i^* = -\left[\frac{4}{3}\left(\frac{\rho_i}{\rho_g} - \frac{\rho}{\rho_g}\right) g \frac{d_i}{C_D}\right]^{1/2} \quad (47)$$

Where ρ_i and ρ_g are the solid phase and gas densities (kg m^{-3}), g is the gravitational acceleration (m s^{-2}), u_i^* is the slip velocity of phase i (m s^{-1}), d_i is the particle diameter of phase i (m) and C_D is the drag coefficient.

The drag coefficient was evaluated iteratively [108]:

$$C_D = \begin{cases} 24\,(1 + 0.15Re^{0.687})/Re & \text{for } Re < 1000 \\ 0.44 & \text{for } Re \geq 1000 \end{cases} \quad (48)$$

Where Re is the particle Reynolds number:

$$Re = \left(\frac{\rho_g u_i^* d_i}{\mu_g}\right) \quad (49)$$

The flux is then calculated, and a source term S_i added or subtracted from the cells either side of the face.

$$S_i = \begin{cases} u_{i,f}^* A_f \varepsilon_{i,\mathrm{f}-1} \rho_f & \text{if } u_{i,f}^* \geq 0 \\ u_{i,f}^* A_f \varepsilon_{i,\mathrm{f}+1} \rho_f & \text{if } u_{i,f}^* < 0 \end{cases} \quad (50)$$

4.2.4 Gas And Liquid Algorithm

The Gas And Liquid Algorithm (GALA) [109] was used to ease the convergence of the pressure correction routine in the flow module.

GALA is a routine in PHYSICA whereby volume is conserved, rather than mass. This allows for the simulation of compressible flow as the density can vary, without putting too great a stress on the pressure differential.

The variations in concentration within a fluidised bed can lead to large differences in local properties from region to region, causing large density variations and pressure differentials which can cause problems for convergence and accuracy, even when using

relaxation. The lower barrier which prevents the downward flow of particles in this system is an example of this, as the highest particle concentrations are immediately above it, while below there is nothing but pure gas.

GALA was developed as part of the solidification functions in PHYSICA to allow for varying densities. It has previously been used in Volume of Fluid simulations, where it employs a free surface marker to track the boundary between the liquid and the solid metal.

By using GALA, the standard continuity equation can be rewritten in a volumetric form:

$$\frac{D\rho}{Dt} = -\rho(\nabla.\underline{u}) \tag{51}$$

For the algebraic slip model, no solidification occurred, and the free surface marker was set to 0, so the mixture was considered totally fluid, but with varying material properties.

Due to its design for use in solidification, the GALA implementation does not allow for steady-state simulations. As such it was necessary to run transient experiments until a pseudo steady state had been achieved.

4.2.5 Turbulence

Turbulence in multiphase flow is very complicated, as it depends not just on the local concentrations, but also the contact pattern between the phases. To get good values for simulating turbulence in multiphase flow, very specific experiments would have to be performed, and it is not always possible to find appropriate empirical research for the application at hand.

Some researchers have ignored turbulence [27], others such as Johansen et al. [110] and Pericleous [22] have evaluated the turbulent contributions for each solid phase and the gas phase and combined them as an overall turbulent contribution, while others have used the overall mixture properties as if it were a single phase flow [111] .

The k-ε model was employed in this work, with the properties of the continuous mixture phase used for the whole mixture, as has been done before for turbulent multiphase simulations [106]. This led to the solids affecting turbulence only through their mass contribution to the mixture, rather than through any physical effects on diffusion or mixing.

In k-ε, two turbulent properties of the flow are tracked: the fluctuating vorticity, *k*, and the rate of dissipation of kinetic energy of the fluid, *ε*. At high Reynolds numbers, these properties can be related as the rate of dissipation of energy is equal to the fluctuating vorticity multiplied by the viscosity.

PHYSICA tracks the two variables by the following equations:

$$\frac{\partial k}{\partial t} + \nabla \cdot (\rho \underline{u} k) = \nabla \cdot \left(\left[\mu_0 + \frac{\rho \nu_T}{\sigma_k} \right] \nabla k \right) + \rho \nu_t G - \rho \varepsilon \tag{52}$$

$$\frac{\partial \varepsilon}{\partial t} + \nabla \cdot (\rho \underline{u} \varepsilon) = \nabla \cdot \left(\left[\mu_0 + \frac{\rho \nu_T}{\sigma_\varepsilon} \right] \nabla \varepsilon \right) + C_{1\varepsilon} \rho \nu_t G \frac{\varepsilon}{k} - C_{2\varepsilon} \rho \frac{\varepsilon^2}{k} \tag{53}$$

G is the turbulent generation rate

$$G = 2\left(\left[\frac{\partial u}{\partial x} \right]^2 + \left[\frac{\partial v}{\partial y} \right]^2 + \left[\frac{\partial w}{\partial z} \right]^2 \right) + \left(\frac{\partial u}{\partial y} + \frac{\partial v}{\partial x} \right)^2 + \left(\frac{\partial u}{\partial z} + \frac{\partial w}{\partial x} \right)^2 + \left(\frac{\partial v}{\partial z} + \frac{\partial w}{\partial y} \right)^2 \tag{54}$$

Where ρ is the fluid density, μ_0 is the laminar viscosity, ν_T is the turbulent viscosity, given by

$$\nu_T = C_\mu \frac{k^2}{\varepsilon}$$

C_μ, $C_{1\varepsilon}$, $C_{2\varepsilon}$, σ_k, σ_ε, are all constant with the values 0.09, 1.44, 1.92, 1.0 and 1.3 respectively. The turbulent viscosity is added to the diffusivity term in the general transport equation.

The initial and boundary values of k and ε come from:

$$k_0 = \frac{3}{2}(lu)^2 \tag{55}$$

And

$$\varepsilon_0 = 0.1643\frac{k_0^{1/2}}{l} \tag{56}$$

4.2.6 Carbonation module

The carbonation module was based primarily on work by Symonds [30]. They used a shrinking core mechanism, where the reaction coefficient in the initial kinetically controlled stage was dependent on the available surface area. As reaction proceeded, a porous layer of product built up around the outside of the particle, decreasing the active radius of the pure reactant available and providing an obstacle to reaction. Above a conversion of 0.5, the product layer provided a barrier, and diffusion across this became the rate limiting step in the reaction and the rate slowed dramatically.

Only relations for the first, kinetically controlled stage were considered in this study, and the extent of solid reaction was not extended to the levels where diffusion-control would occur. It was assumed that any particles reaching these levels would be regenerated in the calciner or replaced with new feedstock.

For the kinetically controlled stage, Symonds [30] found that the rate could be written as a zero-order constant, based on time and conversion. The generic reaction order was given as:

$$R = \frac{dX}{dt(1-X)} \tag{57}$$

Where R is the specific reaction rate (s^{-1}) defined as a function of the reaction constant and the gas concentration in relation to equilibrium.

$$R = M_{CaO} k_s s\left(P_{CO_2} - P^0_{CO_2}\right) \tag{58}$$

where M_{CaO} is the molar mass of CaO (56 kg kmol^{-1}), k_s (mol m^{-2} s^{-1}) is the reaction constant, P is the partial pressure of CO_2 and $P^0_{CO_2}$ is the equilibrium partial pressure of CO_2, both in atm. As the reactor is operating at atmospheric pressure, an expression for the change in conversion in the initial stages can be written in terms of volumetric gas concentration:

$$\frac{dX}{dt} = M_{CaO} k_s s(1 - X)\left(\varepsilon_{CO_2} - \varepsilon^0_{CO_2}\right) \tag{59}$$

where X is the conversion and $\varepsilon^0_{CO_2}$ is the equilibrium volumetric concentration of CO_2. If total conversion is theoretically possible, X can be written as a function of N the local molar concentration (kmol m^{-3}):

$$X = \frac{N_{CaCO3}}{N_{CaO} + N_{CaCO3}} \tag{60}$$

The expression for the overall rate was further simplified by expressing it as a function of an overall zero order reaction coefficient K and a specific surface area s:

$$\frac{d\varepsilon_{CaO}}{dt} = Ks \tag{61}$$

The reaction coefficient here comes from:

$$K = \rho_{CaO} k_s\left(\varepsilon_{CO_2} - \varepsilon^0_{CO_2}\right) \tag{62}$$

For the reaction coefficient, an expression from Symonds [30] for Havelock limestone was used to simplify the relationship between temperature and reaction rate:

$$\ln k_s = -\frac{3575.1}{T} - 10.09 \tag{63}$$

The equilibrium partial pressure in atm for CO_2 comes from Baker [112].

$$\log_{10}\left(\varepsilon^{0}_{CO_2}\right) = 7.079 - \frac{8308}{T} \tag{64}$$

This is valid above 900 K and below 300 atm. *s* is the specific surface area:

$$s = \frac{6}{\rho_{CaO} d_0 (1 - e_0)} \tag{65}$$

Where e_p is the particle porosity, assumed to be 0.5, and the diameter came from a simple arithmetic average

$$d_0 = \sum \varepsilon_i d_i \tag{66}$$

The routine works for multiple particle sizes by first calculating the total carbon dioxide conversion based on the average diameter of CaO particles and the extent of the reaction.

The individual changes in phases concentration for the solids are then calculated based on their local molar concentrations. A side effect of this is that in any cell, all phases will react at the same rate, based on their concentration, although cells with higher concentrations of smaller particles will react quicker overall.

4.2.7 Calcination module

The calcination module was based on work by Khinast [29]. They used a random pore model, similar to the shrinking core model of Symonds [30]. Both are grain models, using an initial rate to describe the chemically controlled stage. The main difference between the two being that the random pore model accounts variation in the shape of the surface area when calculating reaction progress. Again, the diffusion-controlled stage was not considered in this study.

The rate of reaction for this model was given as:

$$\frac{dX}{dt} = M_{CaCO_3} k_s s (1 - X)^{2/3} \tag{67}$$

This was rewritten to be a function of an overall reaction coefficient and an available surface area.

$$\frac{d\varepsilon_{CaCO_3}}{dt} = Ks \tag{68}$$

Where *K* comes from this expression:

$$K = \rho_{CaCO_3}(1-X)^{2/3} k_s e^{-a\varepsilon_{CO_2}/\varepsilon^0_{CO_2}} \tag{69}$$

k_s is the reaction constant from the Arrhenius expression which was taken as 2.03 x10^{-7}, and a is a constant which was taken as 11.92, both from experimental results [29], assuming that temperature would not vary greatly when reaction occurs.

For the calculation of *s*, an additional term is applied to represent the changing available surface area and the structure of the pores in the model.

$$s = s_0(1-X)\sqrt{1 - a\ln(1-X)} \tag{70}$$

4.2.8 Heat transfer

The mixture was treated as a homogeneous fluid, with local heat transfer coefficients depending on the concentrations of the different species. The individual particles were not considered, but rather the contribution of each phase to the cell. A single value was used to represent the heat transfer coefficients within the cell for the mixture, based on the relative contributions of each phase to the cell's total population. The specific heat for each cell was calculated via an arithmetic average based on the local concentrations, while the thermal conductivity and coefficient of thermal expansion were taken to be that of the gas phase.

PHYSICA solved for the enthalpy by means of Equation (71):

$$\frac{(\partial \rho h)}{\partial t} + \nabla \cdot (\rho \underline{u} h) = \nabla \cdot \left(\left[k + \frac{\rho \nu_t}{\sigma_t} \right] \nabla [h] \right) + \nabla \left([kh] \nabla \left(\frac{1}{c_p} \right) \right) + S_h \quad (71)$$

Here, ρ is the mixture density, h is the enthalpy, u is the velocity, k is the thermal conductivity of the gas phase, c_p is the mixture specific heat capacity, ν_T is the turbulent kinematic mixture viscosity and σ_T is the heat turbulent Prandtl number.

The main sources of heat into the system consisted of the input streams and the heat generated or consumed by reaction. The entry conditions for inlet streams were given by Equation (72).

$$Q = \dot{m} c_P T \quad (72)$$

Where T is the temperature in K. Zero enthalpy was taken as enthalpy at 0 K, and all enthalpy calculations were performed in reference to this, unless specified otherwise.

The heat source due to the reaction was equal to the total molar conversion multiplied by the molar heat of reaction.

$$S_{h,r} = r \Delta H_R \quad (73)$$

Where r is the total moles reacted in the time step, given by the reaction module and ΔH_R is the heat of reaction for a mole of CaO. Zero enthalpy for the system was set to be the energy at 273 K.

4.2.9 Boundary conditions

In PHYSICA the source terms for a variable in the general equation can be represented by two terms, a coefficient (*Co*), which must be positive, and a value (*Val*).

$$S_\varphi = Co(Val - \varphi) \quad (74)$$

There are two main boundary condition specifications in PHYSICA, by which it is possible to manipulate this source term: a fixed value and a fixed flux.

A fixed value boundary condition, for example constant temperature, has a value specified by the user and a coefficient is then determined automatically to ensure that this value is the value in the boundary cell.

$$Val = \text{Temperature} \tag{75}$$

$$Co = A\frac{\Gamma_\varphi}{d} + \max\left(-C_\varphi, \underline{u} \cdot \underline{n}, 0\right) \tag{76}$$

Where A is the area of the cell face at the boundary, Γ_φ is the diffusion coefficient, C_φ is the convection coefficient, u is the mixture velocity and $\underline{u} \cdot \underline{n}$ is the normal component of velocity at the face.

This routine subtracts the maximum of either the local concentration or the latent local flux from the incoming value, so the value of the variable is that specified.

In a constant flux routine, the value is multiplied by a very large number, typically 10^{10}, and the coefficient divided by this number, so that the amount of the variable entering the system is always the same, regardless of the value of the cell at the inlet. The latent flux in the inlet cell is subtracted automatically, so as not to add to the inlet flux.

$$Val = 1 \times 10^{10} \times \text{Concentration} \tag{77}$$

$$Co = 1 \times 10^{-10} \tag{78}$$

The boundaries of the column are shown in Figure 20. The slip velocity is introduced in the shaded region.

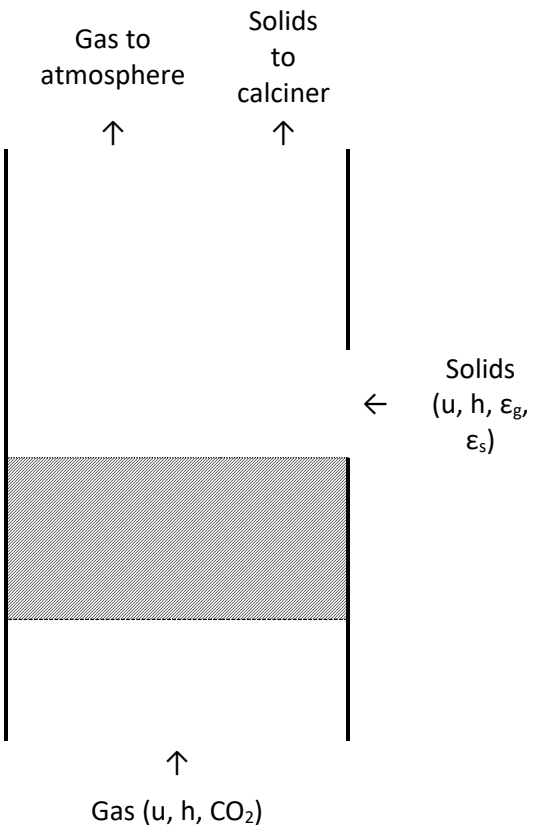

Figure 20: Inlets and outlets to the reactor

4.3 Assumptions in modelling

4.3.1 Convective forces dominate

The algebraic slip model is valid where convective forces dominate, and the relaxation time of the solid particles is low enough that terminal velocity is achieved quickly. In the case of a fluidised bed, there is a rapid acceleration of particles at the bottom, and any incoming flows will be subject to that acceleration. For fluidizable particles in the density ranges under consideration, the relaxation time is larger than would be necessary for instant fluidisation, so the behaviour of fluid entering via a side-stream is of questionable validity. Once it has attained equilibrium, however, the flow should behave in a realistic manner.

4.3.2 Sintering and attrition are neglected

Particle denaturation due to temperature effects, and damage sustained by particles due to collisions were not considered in the model. This would be necessary in a mass balance for real world design, but in this case, any material lost would be made up for by additional feed, specified by the user. If the project were extended to batch cycles of the carbonator/calciner system, this would have to be considered.

4.3.3 Particles are spherical

Particles were assumed to be spherical for practical purposes, including:

1) Reaction rates in the shrinking core mechanism
2) Limits to solids phase concentration
3) Drag force

4.4 Previous work

This work builds on an earlier study by Molaei [26] who used a Lagrangian model to simulate a carbonation process. He modelled the carbonator as a bubbling bed, with particle residence times between 10 and 30 s. Newton's laws of motion were to track the particles in the discrete phase and steady-state time-averaged conservation equations were used for the continuous phase, based on work by Kuipers et al. [113], who used a generalised form of the Navier-Stokes equations.

It was assumed that the vectors and scalars were made up of a time averaged and a fluctuating term.

$$u_i = \bar{u}_i + u_i' \quad p = \bar{p} + p' \quad h = \bar{h} + h' \tag{79}$$

The mean flow quantities for the continuous gas phase were tracked via the following equations for continuity (1), momentum conservation (2) and conservation of enthalpy (3), accounting for both time averaged and fluctuating terms:

$$\nabla \cdot (\rho \bar{u}) = \overline{S_m} \tag{80}$$

$$\frac{\partial}{\partial t}(\rho \vec{u}_i) + \nabla \cdot (\rho \bar{u} \vec{u}_i) = -\frac{\partial p}{\partial x_i} + \nabla \cdot \left(\mu_{eff} \nabla \vec{u}_i\right) - \frac{\partial}{\partial x_j}\left(\alpha \rho \overline{\acute{u}_\iota \acute{u}_j}\right) + \overline{S_{u_\iota}} \tag{81}$$

$$\frac{\partial}{\partial t}(\rho \vec{u}_i) + \nabla \cdot (\rho \bar{u} h) = \nabla \cdot \left(k \nabla \frac{h}{c_p}\right) - \frac{\partial}{\partial x_j}\left(\rho \overline{\acute{u}_\iota \eta}\right) + \overline{S_h} \tag{82}$$

Here, ρ is the gas density, u the overall gas velocity, u_i the velocity of the gas phase in the i direction, μ_{eff} the effective gas viscosity, h the gas enthalpy and c_p the gas specific heat. $\overline{S_m}$ is the overall mass transfer, $\overline{S_{u_\iota}}$ the momentum tranfer and $\overline{S_h}$ the enthalpy transfer between the gas and solid phases.

The terms $\overline{\acute{u}_\iota \acute{u}_j}$ and $\overline{\acute{u}_\iota \eta}$ represent correlations between fluctuating velocities (the Reynolds stresses) and enthalpies (the turbulent heat flux), respectively. These were resolved by means of a k-ε turbulence model.

The particle velocities at the timestep $i+1$ were solved by comparison with the gas velocities:

$$u_p^{i+1} = u - \left(u - u_p^i\right)\frac{1}{e^{\Delta t/\tau}} + g_x t\left(1 - \frac{1}{e^{\Delta t/\tau}}\right) \tag{83}$$

$$v_p^{i+1} = v - \left(v - v_p^i\right)\frac{1}{e^{\Delta t/\tau}} + g_y t\left(1 - \frac{1}{e^{\Delta t/\tau}}\right) \tag{84}$$

τ is a particle relaxation time

$$\tau = \frac{4\rho_p d_p^2}{3\rho_f \mu_f C_D Re} \tag{85}$$

A stochastic turbulence model was used to generate eddies that could capture the particles. The position of the particle was updated the gas velocities at each time step.

$$x_p^{i+1} = x_p^i + \Delta t \frac{u_p^i}{2} \tag{86}$$

$$y_p^{i+1} = y_p^i + \Delta t \frac{v_p^i}{2} \tag{87}$$

The reaction rate came from Grasa [21], who used a random core model based on the available surface area within the particle.

$$\frac{dX}{dt} = \frac{k_s S_0 C(1-X)\sqrt{1-\Psi \ln(1-X)}}{(1-\varepsilon)\left[1+\frac{\beta Z}{\Psi}\sqrt{1-\Psi \ln(1-X)}-1\right]} \tag{88}$$

The energy source term summed the enthalpy of all phases:

$$S_h = \sum_i^{N_p} S_{h,i} = \sum_i^{N_p} \int_0^{\Delta t_i} \frac{m_{p,0}}{M_{CaO}} \Delta H_r X_i(t) dt \tag{89}$$

First, the transport of the continuous gas phase was solved, and then the velocity and position of the particles were updated, based on the above relations. Particle positions were based on shape functions based on the shape of the cell in the mesh that contained them.

Results from Molaei's work will be presented in Section 8 and compared with results obtained using the algebraic slip model.

NUMERICAL METHODS

5.1 Finite volume discretisation

The continuity, momentum, turbulence, reaction and heat transfer equation were solved for this gas-solid system using a finite-volume method over a regular grid of control volumes. The finite volume method discretises the governing equations and uses local assumptions to turn them into coupled algebraic equations. They are solved over a subdivided grid for each individual cell, with each cell having an averaged value at its central node [114].

The values at each of these nodes were extrapolated to the edge of the control volume by a truncated Taylor series expansion. The cells were linked by these borders, over which the transport equations are solved.

In the finite volume method, the conservation equation was integrated over these non-overlapping control volumes and over time until the integrals are zero. The numerical integration scheme chosen for the integration was chosen based on certain assumptions and approximations to the solution.

In this scheme, the local concentrations of the individual phases were used to generate local properties for each cell. The flow of the mixture was then solved for a continuous, homogeneous fluid, albeit one whose properties varied from location to location. Conservation equations for each individual phase were then solved, for reaction within each cell and slip velocity over each boundary to generate additional sources in terms of mass and energy. This is represented by Figure 21.

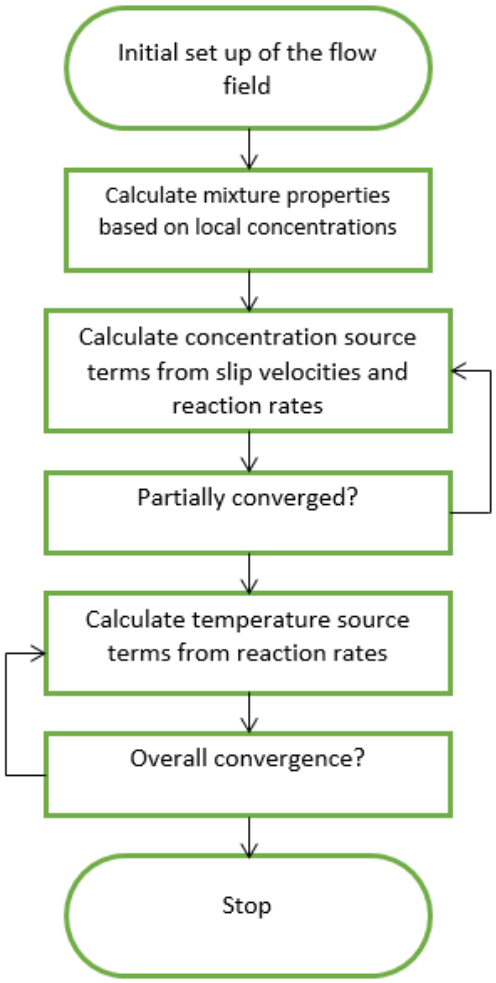

Figure 21: Schematic diagram of algebraic slip and reaction models

Due to the dominance of advection in the situations under consideration, the hybrid scheme of Spalding [115] was used, which is a combination of the upwind and central differencing schemes. It uses the upwind scheme where convection is dominant and the central differencing method when this is not the case.

In the cell centred method, the control volume is representative of the element it occupies and the node at its centre contains the values for the whole volume. The matrix produced should be diagonally dominant, to ensure convergence, and care must be taken when linearizing sources to ensure that this is maintained.

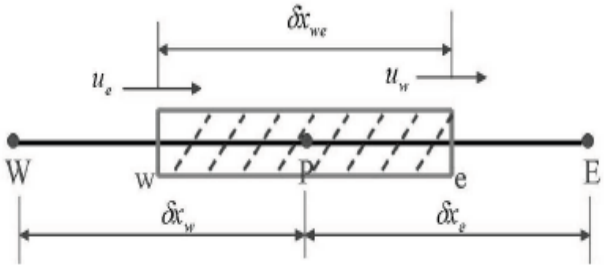

Figure 22: Discretisation scheme

$$(\rho u\varphi)_e - (\rho u\varphi)_w = (\Gamma\,(\varphi_E - \varphi_P)/\delta x_e) - (\Gamma\,(\varphi_P - \varphi_W)/\delta x_w) \qquad (90)$$

In this, $(\rho u\varphi)_w$ represents the property entering the west face and $(\rho u\varphi)_e$ the property leaving the east, as shown in Figure 22. These are approximated in central difference by:

$$\varphi_e = \frac{\varphi_E + \varphi_P}{2} \qquad (91)$$

$$\varphi_w = \frac{\varphi_W + \varphi_P}{2} \qquad (92)$$

Equation (79) can be rewritten in terms of cell-centred values as:

$$A_P\varphi_P = A_E\varphi_E + A_W\varphi_W \qquad (93)$$

Convection and diffusion fluxes are expressed by:

$$F = \rho u \qquad (94)$$

$$D = \frac{\Gamma}{\delta x} \qquad (95)$$

The coefficients in the equation are now:

$$a_E = D_E - \frac{F_e}{2} \tag{96}$$

$$a_W = D_W + \frac{F_w}{2} \tag{97}$$

$$a_P = D_E + \frac{F_E}{2} + D_W - \frac{F_W}{2} = a_E + a_W + (F_e - F_w) \tag{98}$$

In some circumstances, when flow is very powerful, and advection dominates, there is an unequal contribution to the values at the cell wall from each node. In this case, central differencing would produce an inaccurate value, and the upwind scheme was employed. This assumes that the upwind cell will provide the values at the border between the cells as all the flow will be moving in that direction. In this case, the coefficients become:

$$a_E = D_e - \max\left(\frac{F_e}{2}, 0\right) \tag{99}$$

$$a_W = D_e + \max\left(\frac{F_w}{2}, 0\right) \tag{100}$$

$$\begin{aligned} a_P &= D_E + \max\left(\frac{F_E}{2}, 0\right) + D_e - \max\left(\frac{F_e}{2}, 0\right) \\ &= a_E + a_W + (F_e - F_w) \end{aligned} \tag{101}$$

The upwind scheme can cause artificial diffusion, so in these cases the hybrid scheme was employed. This uses the Peclet number to gauge which scheme to use. The Peclet number is a dimensionless number which is the ratio of convective forces to diffusive forces. It is given by:

$$Pe = \frac{\rho u L}{\Gamma} \tag{102}$$

If the flow is significant in either direction the hybrid scheme uses the upstream values for the variable. As the Peclet number approaches more closely to 1, so the downstream

node will have a larger impact on the value at the boundary. Higher Peclet numbers correspond to smaller values of dϕ/dx.

The hybrid scheme uses central differencing if the absolute of the Peclet number is less than 2 and the upwind scheme if it is larger.

$$a_E = \max\left(-F_e, D_e - \frac{F_e}{2}, 0\right) \qquad \text{when } -2 < Pe < 2 \tag{103}$$

$$a_W = D_W + \max\left(-F_w, D_w + \frac{F_w}{2}, 0\right) \qquad \text{when } 2 \leq Pe \tag{104}$$

$$a_P = a_E + a_W + \max\big((F_e - F_w), 0\big) \qquad \text{when } -2 \geq Pe \tag{105}$$

5.2 Interphase sources and sinks

The algebraic slip model treats the mixture as a homogeneous fluid with one continuity and momentum equation for the mixture. The extent of interphase mass transfer is between the gas phase, in terms of CO_2 and the solid phases. There is also transfer within the solid phases, in terms of transfer between CaO and $CaCO_3$. There is no transfer between size groups.

Because the total mass in the system is conserved, the net sum of the interphase mass transfer (Γ) is 0.

$$\sum_{i=1}^{n} \Gamma_i = 0 \tag{106}$$

The overall balance for each phase in the system is given by:

$$\frac{(\partial \varepsilon_i)}{\partial t} + \nabla \cdot (u\varepsilon_i) = \nabla \cdot \left(\Gamma_i \nabla(\varepsilon_i)\right) + S_i \tag{107}$$

The sources come from the reaction term:

$$CaO(s) + O_2(g) \rightarrow CaCO_3(s) \quad (108)$$

PHYSICA keeps a record of the sources in each simulation, and these were checked to ensure that only the reaction contributed significantly to the net populations change for any phase, that these contributions were balanced and that any extra sources due to other modules were minimised.

5.3 Control of numerical convergence

PHYSICA employs a forward Euler mechanism

$$y_{n+1} = y_n + hf(y_n, t_n) \quad (109)$$

Due to the algebraic slip model's assumption that equilibrium has been attained, and there is no acceleration, time steps had to be small, but because a forward Euler was applied, there were no theoretical limits to the size. The use of the GALA mechanism meant that steady state was not an option, so transient runs had to be performed.

The time step was varied, based on the density of the mesh, with the standard rough meshes having default time steps of 0.01 s, to give Courant numbers below 1 as a guide to promote quick convergence, although it was not necessary for this method. The Courant number is a prerequisite in explicit codes, as it prevents material bypassing cells within one time-step.

$$C = \frac{u\Delta t}{\Delta x} \leq C_{max} \quad (110)$$

Relaxation was set to 0.1 for the pressure, to account for the large pressure brought about the by the lower boundary and the sharp division in density between the gas and solid phases.

Both two and three-dimensional meshes were created using a program called MBrick3. A comprehensive explanation of this can be found at [116] and in [117].

CODE VERIFICATION SIMULATIONS

6.1 Introduction

In this section, the results of tests on the basic operations of the model are presented.

The hydrodynamics of the system were investigated by observing the behaviour of the solid phases when subjected to an upward air velocity, either at or just above the minimum fluidisation velocity.

The carbonation and calcination modules were tested by replicating the results of practical experiments, first in Excel and then in PHYSICA. The initial Excel results were used as guidelines for the conditions and targets for the PHYSICA simulations. Initial work was done in a simple, isolated system which changed with time, while more studies of enthalpy and temperature were performed in a larger mesh with inlet and outlet flows.

The enthalpy module was integrated with the carbonation and calcination modules and was again verified by comparison with the earlier Excel work.

6.2 Convection

The performance of the algebraic slip model in PHYSICA in predicting the flow of gas-solid mixtures at low velocities was tested by subjecting a mixture of different size particles to an upward gas flow between their minimum fluidising velocities.

The powder initially occupied a space in the column at a height of between 0.2 and 0.4 m, with a barrier limiting the downward flow of particles placed between 0.1 and 0.2 m. The slip velocity module was inactive below 0.1 m, before being steadily introduced as a linear function of height above this, until the full slip was used above 0.2 m.

At gas velocities below the minimum fluidisation velocity, no upward flow of the powder should be expected. The solid phases with a lesser diameter and lower density would be expected to be transported at a lower upward velocity than those phases with higher diameters and densities. In a system of calcium oxide and calcium carbonate,

with solid phases of the same diameter, the lighter calcium carbonate particles should be fluidised at a lower velocity due to their lower density, while the heavier calcium oxide phases should remain static.

The properties of the particles used in this test are shown in Table 9. They were subjected to an upward gas velocity of 2.1 m s^{-1}. The calcium carbonate should be fluidised as it has a slip velocity of -1.99 m s^{-1}, whereas the calcium oxide should remain static due to its slip velocity of -2.21 m s^{-1} and the presence of the lower barrier.

Table 9: Particle properties for convection test

Powder	CaO	$CaCO_3$
Density (kg m^{-3})	3340	2710
Diameter (μm)	250	250
u_g (m s^{-1})	2.1	2.1
Re_p	35.00	35.00
C_D	1.87	1.87
Slip velocity (m s^{-1})	-2.21	-1.99
Net velocity (m s^{-1})	-0.11	0.11

Figure 23 shows the volumetric concentrations of the solid phases after 10 s. The grey area shows the region in which the slip velocity was developed. The red line at its base is where the reduced slip velocity was first introduced, with the red line at its top representing where the full slip velocity phase began. There is a lower peak of the solid concentrations immediately above the lower barrier, and the solid particles occupy a small volume above this.

The CaO is almost entirely contained within the lower 0.15 m above the barrier and trails off quickly above this. Very little upward transport of this phase has occurred. The $CaCO_3$ is also mostly concentrated just above the lower barrier but displays a steadier reduction over the height of the column, and has even reached to heights approaching 1 m.

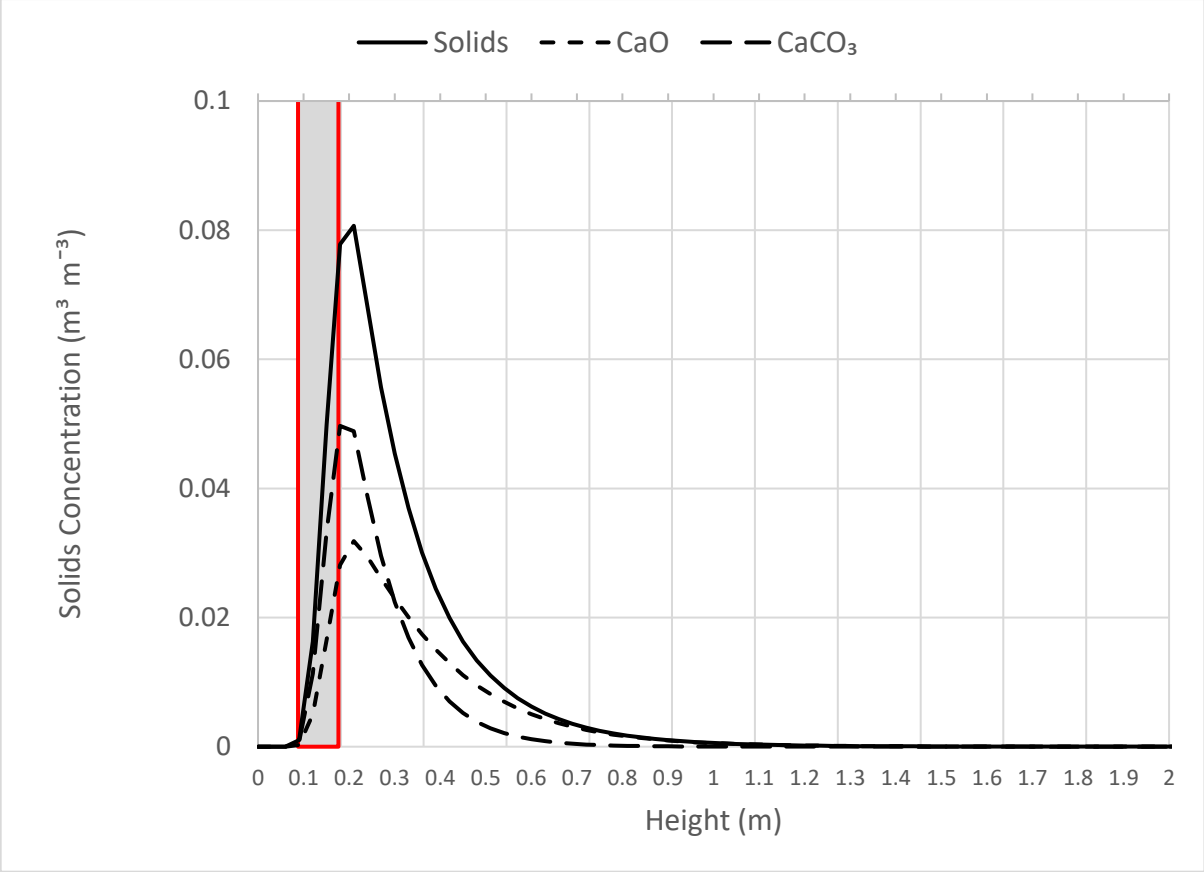

Figure 23: Volumetric concentration profile at minimum fluidisation

The calcium oxide is the principal constituent of the solid phases below 0.3 m, while above this the calcium carbonate is present in higher proportions.

Figure 24 shows the solid phases as a fraction of the total mass. Here, the values are much higher, as the solids density is much higher than the gas. The lower part of the column is mostly CaO, with the $CaCO_3$ as the dominant phase stretching out above this. Due to its much higher mass than the gas, the $CaCO_3$ phase dominates the higher parts of the column, even where it occupies a negligible volume fraction. It is easier to see the changes in the relationship between the solid phases in this diagram.

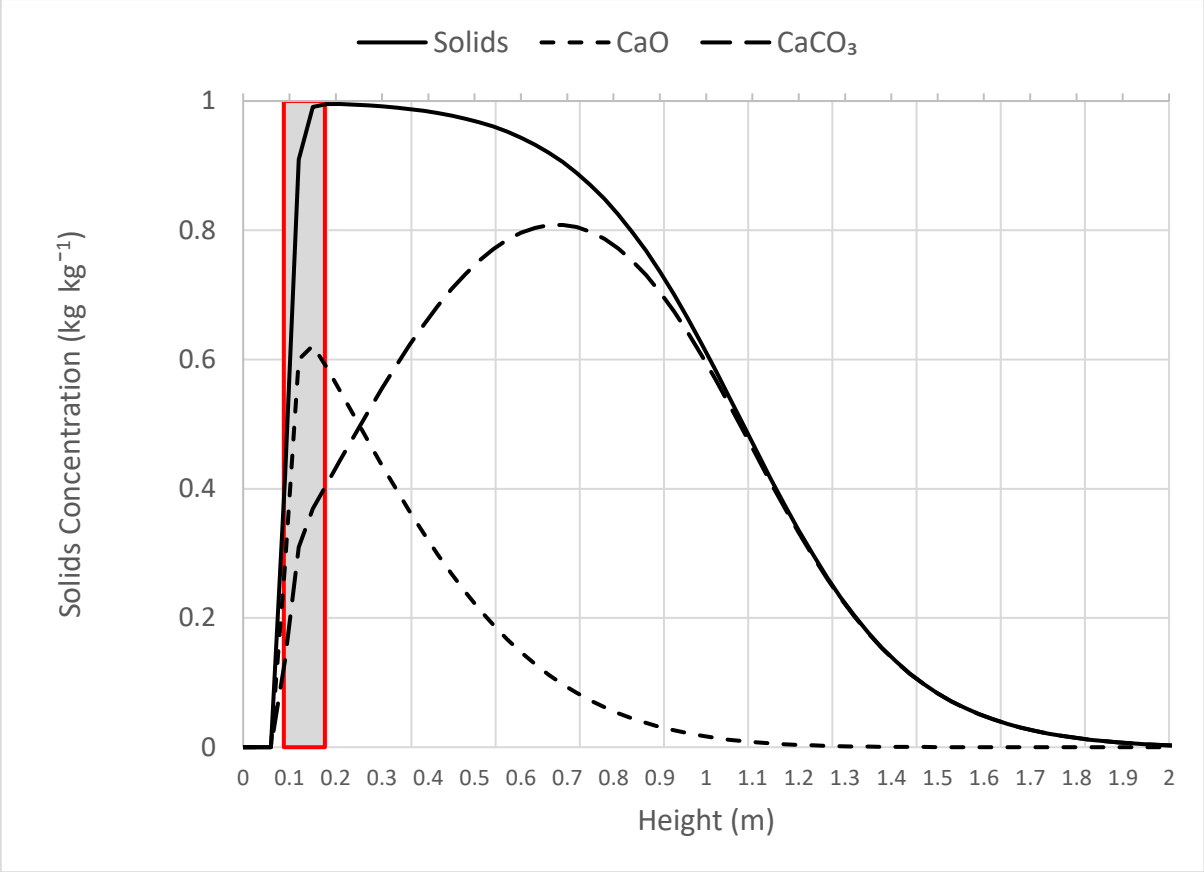

Figure 24: Mass concentration profile at minimum fluidisation

The concentrations peak around the middle of the slip velocity introduction zone, with the overall solids retaining their maximum to the end, but the proportion of CaO diminishing and $CaCO_3$ increasing as it approaches the full introduction of the slip velocity.

These results are what we would expect to see from an experiment such as this, hence the algebraic slip model incorporated here, can account for the net transport of solids.

6.3 Reaction

Carbonation and calcination routines were written for Excel and PHYSICA and their accuracy was tested. In Excel, a simple Euler method was used to calculate the change of the molar concentration of CO_2, with regards to time. Once these results were found

to compare favourably with laboratory work by Symonds [30] for carbonation and Khinast [29] for calcination, the models were adapted for PHYSICA and subjected to further testing.

In PHYSICA, a small two-dimensional mesh was used, with only the reaction module active. Once the performance of this module was satisfactory, it was extended to incorporate inlet and outlet flows, and results were compared against data from larger-scale practical work by Duelli [91] and Unterberger [90].

6.3.1 Carbonation

For carbonation and calcination models in the literature, a shrinking core mechanism is commonly used to explain the reactive behaviour of the particles [99, 118]. This assumes that the reactive solid phase initially consists of particles which are 100% pure. The particles react rapidly with gasses on their surface which causes a layer of the product to form over the outside of the particle. To maintain reaction, the gasses must now penetrate this outer layer to reach the pure, central core. This layer will grow inwards and reduce the diameter of the pure inner core, until the diffusion becomes the time limiting step in the reaction process and the rate is reduced. This divides the reaction process into two phases:

1) A kinetically controlled phase where reaction is rapid
2) A diffusion-controlled phase where reaction is slow

In a true shrinking core mechanism each particle would be part CaO and part $CaCO_3$ and the overall properties of the particle would change as the reaction proceeded [106].

There are various ways of capturing the effects of the extent of reaction in the system, including:

Model the particles together as the same phase but change their respective proportions within each cell based on the local extent of reaction – i.e. CaO core with a $CaCO_3$ layer of a certain thickness.

Assume a flat rate of conversion and base the relative concentrations in the cell on the height the particles have reached.

What was chosen was to assume that particle changed entirely from one phase to another, which increased the number of species present, but meant that no record needed to be kept of the extent of reaction. The shrinking core mechanism was used as a guide for the reaction rate, and to determine the maximum conversion, but each phase was assumed to be wholly either CaO or $CaCO_3$, and the rate determined the fraction of the phase converted.

This will have some effects on the results, as the $CaCO_3$ particles which are heavier in real life are less dense in this model, which will increase the rate at which they ascend and leave the reactor, but also decrease their residence time compared to the CaO particles, thereby effectively increasing the rate of reaction further.

The rate of reaction was expressed as a function of the rate of conversion multiplied by the molar volume [30]:

$$\frac{dN_{CaO}}{dt} = -\frac{\rho_{CaO}}{M_{CaO}}\frac{\partial X}{\partial t} \tag{111}$$

The rate of conversion can be written as a function of a reaction coefficient, specific surface area and the local CO_2 partial pressure in atm, which under atmospheric conditions is equivalent to its volumetric concentration.

$$\frac{dX}{dt} = M_{CaO}k_s s(1-X)\left(\varepsilon_{CO_2} - \varepsilon^0_{CO_2}\right)^a \tag{112}$$

The reaction coefficient *ks* is measured in mol m^{-2} s^{-1} kPa^{-n}. It is given by:

$$k_s = k_0 e^{-E/RT} \tag{113}$$

The power to which the pressure term is raised, *a*, is 1 for atmospheric pressures and below.

Abanades [119] determined a maximum conversion, based on the number of previous carbonation cycles that a particle had been subjected to:

$$X^{max} = a^N + b \tag{114}$$

Where *a* was found to be 0.782 and *b* to be 0.174 for a sample of calcium oxide, and *N* is the number of cycles.

Expanding equation (104), it can be rewritten as:

$$\frac{d\varepsilon_{CaO}}{dt} = -\frac{6}{d_0(1-e_0)}\frac{M_{CaO}}{\rho_{CaO}}k_s(X^{max}-X)\left(\varepsilon_{CO_2}-\varepsilon^0_{CO_2}\right) \quad (115)$$

The $\frac{M_{CaO}}{\rho_{Cao}}$ comes from converting the units for the equation from kmol m^{-3} s^{-1} to m^3 m^{-3} s^{-1}.

The initial conditions for the carbonation verification experiment in are shown in Table 10.

Table 10: Initial reactor conditions for carbonation

Powder	CaO	$CaCO_3$	CO_2	Air
Density (kg m^{-3})	3340	2710	0.6	0.38
Diameter (µm)	250	250	n/a	
RMM (kg $kmol^{-1}$)	56	100	44	28
Initial C (m^3 m^{-3})	0.0006	0	0.08	0.9194
Temperature (K)	923			

The behaviour of the mixture using the above described reaction kinetics was modelled first in Excel and then in PHYSICA, with the same temperature and pressure being used for both. The particles were on their first cycle and had not been reacted before. Changes in enthalpy and temperature, and how these would impact on the reaction rate were not considered.

Figure 25 shows the change the maximum rate of the reaction for the carbonation process for the first 150 s. This rate, *r**, comes from Symonds [30] as a representative of the maximum rate of reaction.

$$r^* = 1-(1-X)^{1/3} \quad (116)$$

The model used represents the maximum rate of reaction achieved by the kinetic model, so both tests may overestimate the reaction rate over the whole process, but they do not

account for any reaction in the diffusion-controlled phase [30]. Both the Excel and PHYSICA models are shown together with the experimental data.

The Excel and PHYSICA are practically identical for the first 40 s, whereupon zero values in PHYSICA begin to affect the results. These first 40 s are very close to the early behaviour of the laboratory experiments, with a rate very similar to that at peak reaction, although not for as long as was observed. As the residence time of the CaO particles in the reactor is unlikely to be beyond 20 s, the limitations of the model at the higher conversions are unlikely to have a negative impact on the results.

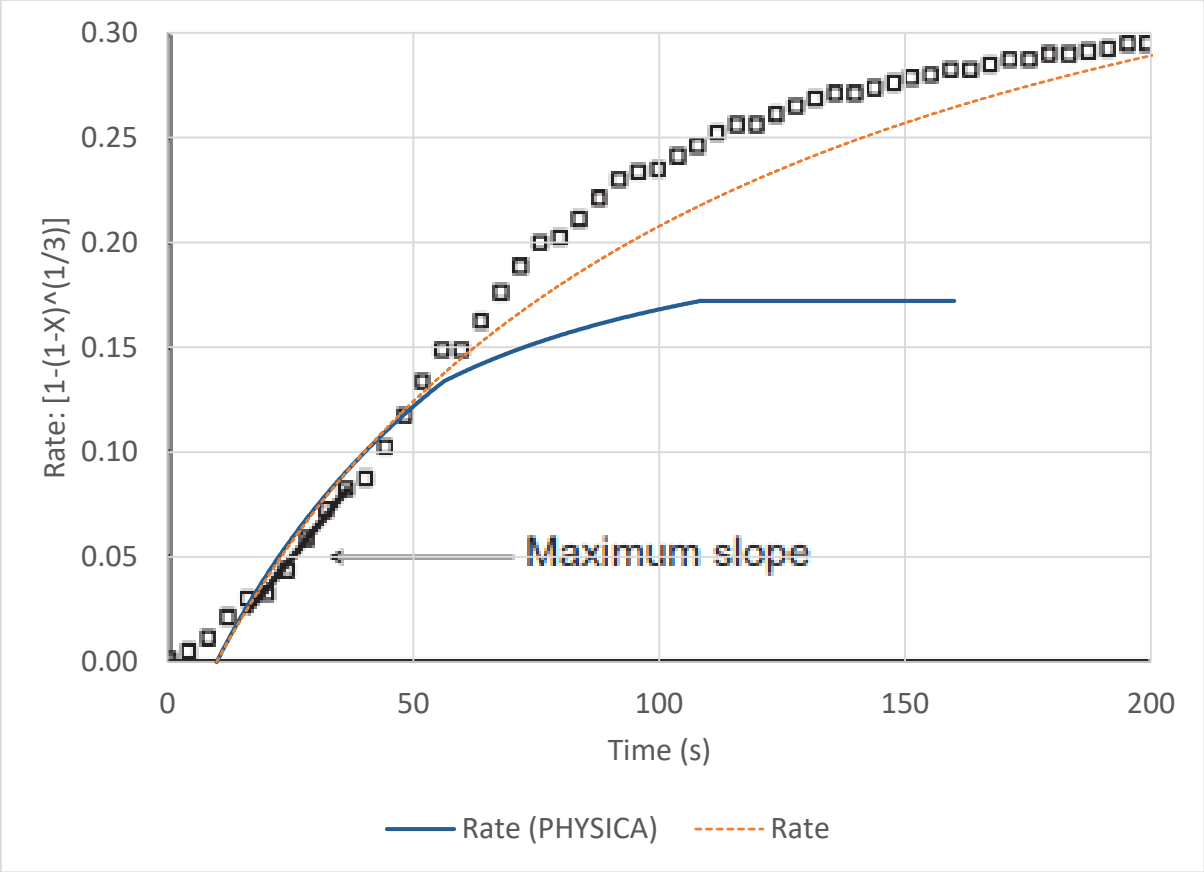

Figure 25: Slope extraction from grain-model carbonation from Symonds [30]

The reaction stops proceeding either when once the equilibrium CO_2 partial pressure has been reached and the amount of CO_2 produced is below a specified theoretical minimum, or when the maximum extent of solids reaction has occurred. Here, it is the former that limits the reaction.

6.3.2 Calcination

The calcination routine was based on a random core mechanism as shown in Section 4.2.7 [29].

$$\frac{d\varepsilon_{CaCO_3}}{dt} = -\frac{\rho_{CaCO_3}}{M_{CaCO_3}}\frac{\partial X}{\partial t} = -KS_v \tag{117}$$

Tests were performed as with carbonation, with 50 μm diameter particles at an initial concentration of $6x10^{-4}$ m^3 m^{-3}, and at a temperature of 1150 K. Initial conditions are shown in Table 11.

Figure 26 shows the conversion for the calcination model, with respect to time, for both the Excel and PHYSICA simulations compared with the experimental work by Khinast [29]. The model in Excel has a very slight delay, while that in PHYSICA responds more quickly, but both methods exhibit a similar overall pattern. Results for both models have been shifted to start at 2 s to line up better with the data on the logarithmic graph.

The lines both attain a similar slope to the maximum for the reaction, although PHYSICA begins to tail off after 10 s and does not reach the same level of conversion due to an imposed maximum concentration limit at just over 0.8.

The calciner will be operated as bubbling fluidised bed [78], hence it would not be practical to simulate it fully here, as it the diffusive forces will be too great to be disregarded. The residence times for this reactor are likely to be around 60 s, to achieve the greatest efficiency, which could be simulated in a very tall fast fluidisation column.

Table 11: Initial reactor conditions for calcination

Powder	CaO	$CaCO_3$	CO_2	Air
Density (kg m^{-3})	3340	2710	1.83	0.32
Diameter (μm)	50	50	n/a	
RMM (kg $kmol^{-1}$)	56	100	44	28
Initial C (m^3 m^{-3})	0	0.0006	0	0.0004
Temperature (K)	1150			

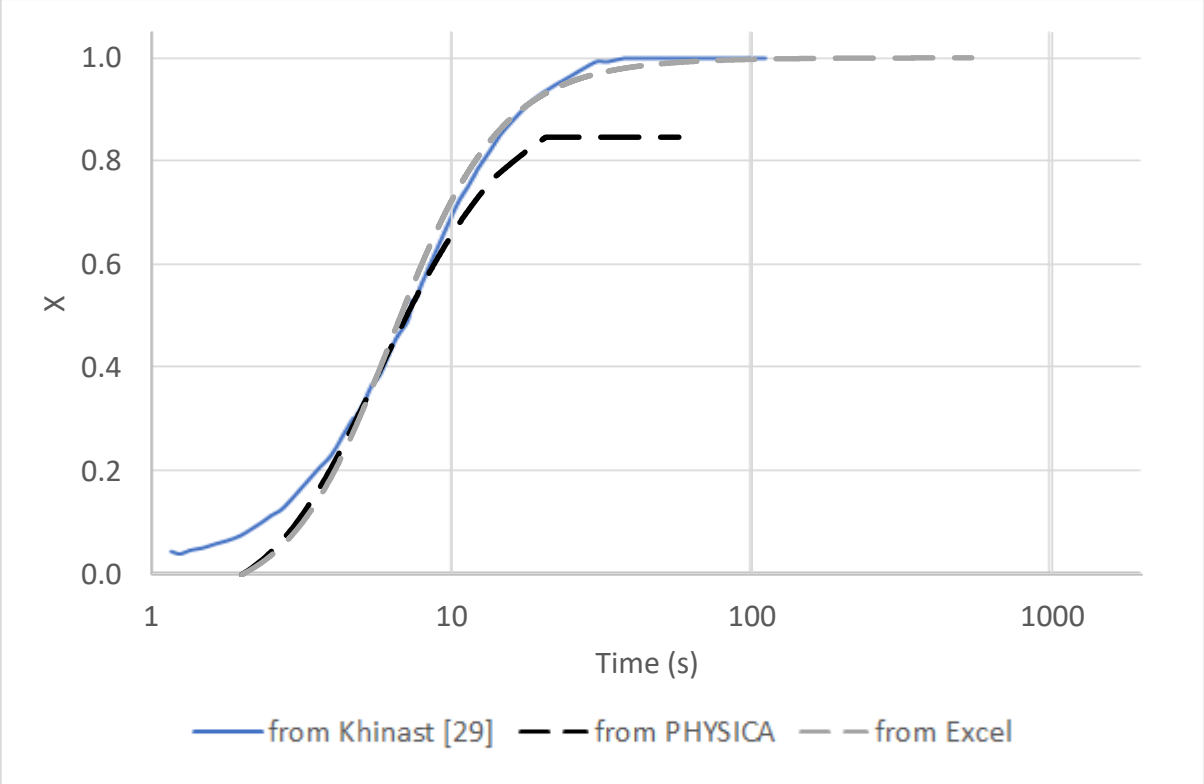

Figure 26: Experimental data and modelling results for 50 µm particles as a function of the CO_2 partial pressure from Khinast [29]

Table 12 shows a mass balance in kg for a scaled down calciner at steady state. The system is balanced and with these inlet flow rates releasing 170 kg h^{-1} of CO_2 from an input of 3900 kg h^{-1} $CaCO_3$ in a single pass.

Table 12: Mass balance for the calciner

Mass	Solids in (kg s^{-1})	Gas in (kg s^{-1})	Exit (kg s^{-1})	ΔN_R (kg s^{-1})	Sum
CaO (300 µm)	6.69E-02		-3.94E-02	2.85E-04	6.01E-04
CaO (400 µm)	6.75E-02		-3.96E-02	3.16E-04	
$CaCO_3$ (300 µm)	5.40E-03		-2.73E-03	-5.09E-04	-1.07E-03
$CaCO_3$ (400 µm)	5.44E-03		-2.69E-03	-5.65E-04	
CO_2		1.07E-03	-4.26E-04	4.73E-04	
Sum	1.45E-01	1.07E-03	-8.48E-02	0.00E+00	

6.4 Mixture Enthalpy

The enthalpy was tested in combination with the flow module. The reactor initially contained N_2 at an enthalpy equivalent to 923 K, with a mixture of air and powder entering from the bottom, also at an enthalpy equivalent to 923 K. The enthalpy routine in PHYSICA uses a reference temperature of 0 K for its zero enthalpy at standard atmospheric pressure.

A simple two-dimensional reactor, 0.1 m diameter by 10 m height was used. For the first 0.2 m both the advection and reaction modules were inactive. Tests were performed for both carbonation and calcination.

6.4.1 Carbonation

Figure 27 shows the volumetric concentrations after steady state was achieved, while Figure 28 shows the changes in enthalpy, temperature and specific heat.

With solids entering the reactor at a concentration of $3x10^{-4}$ m^3 m^{-3}, with a local CO_2 partial pressure of 0.1 and achieving a CaO conversion of 0.2, the specific heat capacity of the mixture should change from 0.96 to 0.94 kJ kg^{-1} K^{-1}, and the temperature should rise around 25 to 30 K from the release of heat during the reaction.

The solids concentration at the lower barrier comprises solely of CaO at 0.0003 m^3 m^{-3}, and over the height of the column, this steadily decreases to 0.00024, while the amount of $CaCO_3$ increases from 0 to 0.00012 and the CO_2 reduces from 0.1 to about 0.05 m^3 m^{-3} by the exit. This results in a net overall increase in the solids concentration to 0.00035 m^3 m^{-3} and a decrease in the CO_2 of 50 % on this pass.

Figure 28 shows the changes in the thermal properties of the system, including the enthalpy, specific heat capacity and temperature of the mixture. Temperature is the solid line, enthalpy the dashed. Values for temperature and enthalpy are shown on the left, and specific heat capacity on the right.

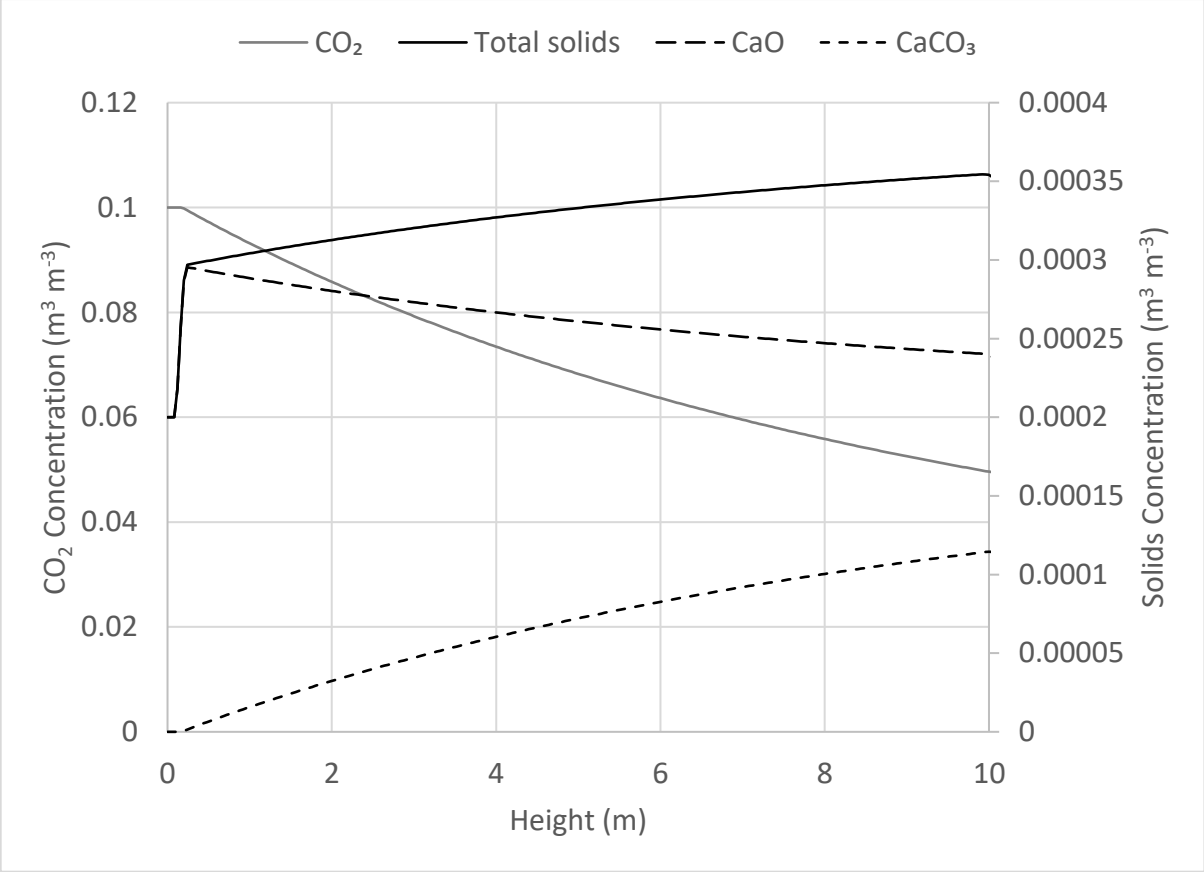

Figure 27: Changes in volumetric CO_2 and solids concentrations for carbonation

The gas enters the reactor at an enthalpy equivalent to a temperature a few degrees below that of the solids, but the mixture reaches the solids temperature quickly after they are subjected to the slip velocity at a height of 0.2 m. This section also sees a decrease in the mass-based heat capacity of the air as it is mixed with the powder.

Above this height, the enthalpy steadily increases from 860 to 862 kJ kg^{-1} over the column, while the specific heat reduces from 0.95 to 0.934 kJ kg^{-1} K^{-1}, as the pure CaO is converted to $CaCO_3$, which exhibits a lower heat capacity. This results in a net increase in the temperature of around 25 K, which is within the expected range determined from earlier calculations.

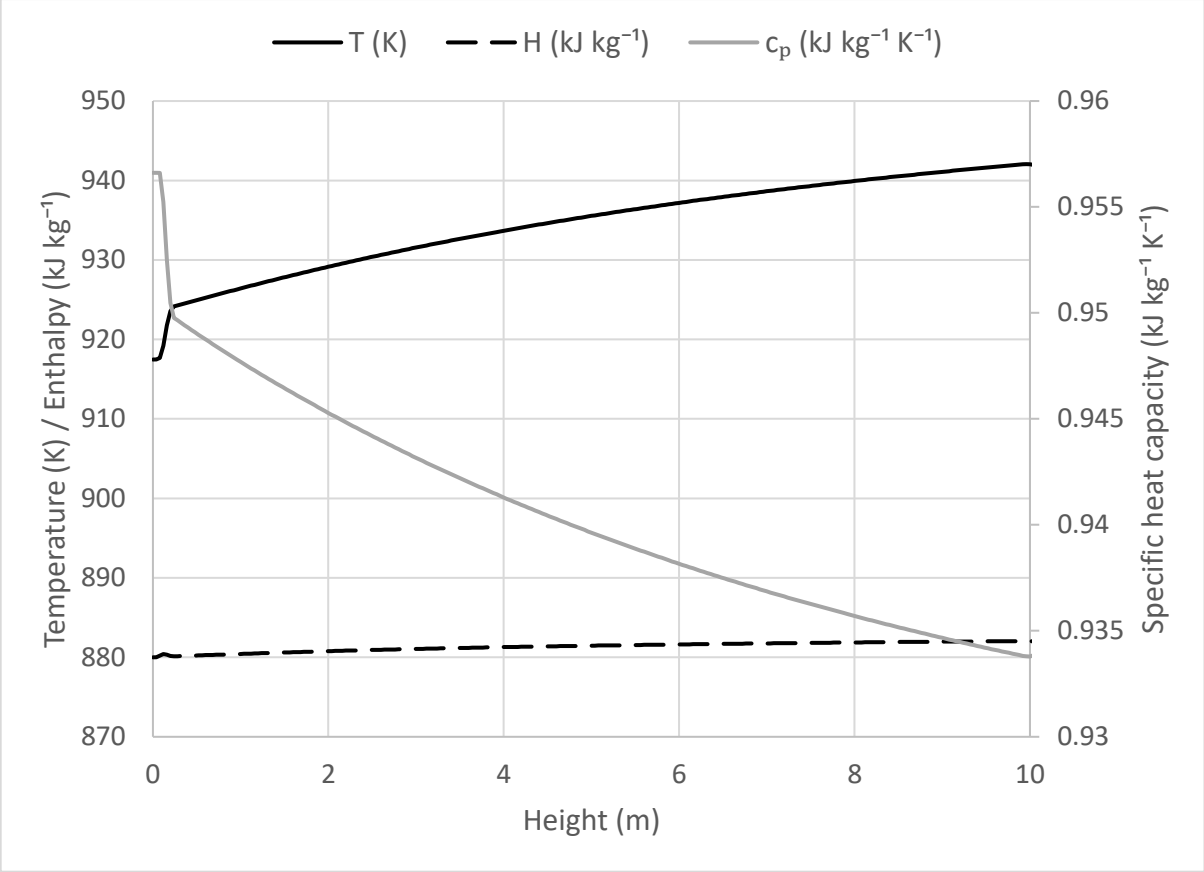

Figure 28: Temperature and enthalpy change in carbonation

6.4.2 Calcination

Figure 29 shows the changes in volumetric concentration of the solids and CO_2 phases for the calcination module, with CO_2 concentration on the left and solids on the right.

The CaO concentration decreases from around $3.5x10^{-4}$ m^3 m^{-3} to $3x10^{-4}$ m^3 m^{-3} over the height of the column, while the $CaCO_3$ increases to around $1x10^{-4}$ m^3 m^{-3} from 0. The CO_2 concentration rises from 0 to 0.035 m^3 m^{-3}.

As calcination is the opposite of carbonation, a temperature change of the same scale should be expected, with some differences allowing for the increasing concentrations of gases. These will have more of an impact, as they have higher heat capacity than the minerals. A conversion of 0.2 would be expected to result in a temperature reduction of 30 to 40 K.

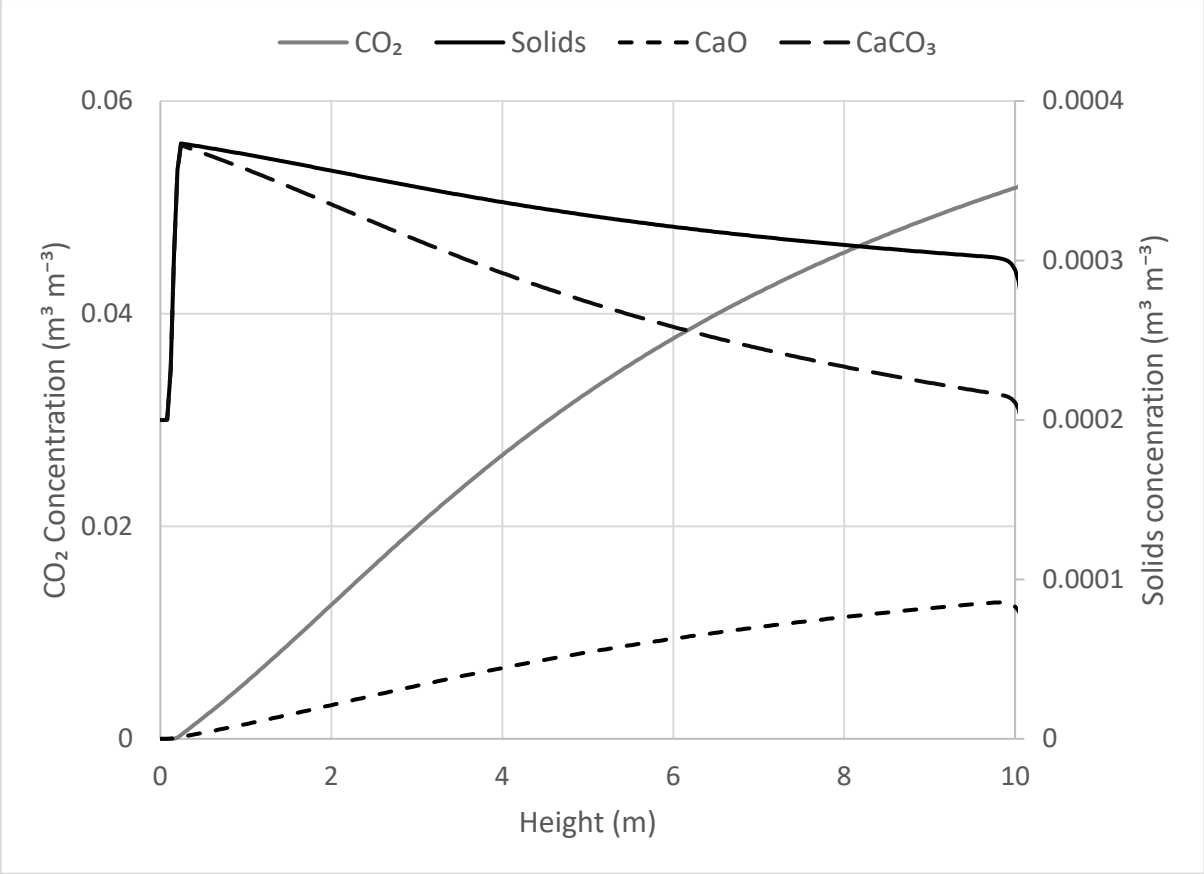

Figure 29: Changes in volumetric CO_2 and solids concentrations with height for calcination

Changes in enthalpy and specific heat of the mixture over the height of the column are shown in Figure 30. The gas enters the column at an enthalpy equivalent to a temperature of 1115 K, while the solids enter with an enthalpy equivalent to 1155 K. As the mixture moves up the column and calcination occurs, energy is consumed, and the specific heat is raised, which reduces the mixture temperature further.

The enthalpy is reduced from 895 to 893 kJ kg^{-1} and the specific heat increased from a low of 0.89 at the solids inlet to 0.93 kJ kg^{-1} K^{-1}. This resulted in a net temperature decrease of 30 K from 1155 to 1125 K for the mixture from solids inlet to solids outlet, which is within the range estimated earlier.

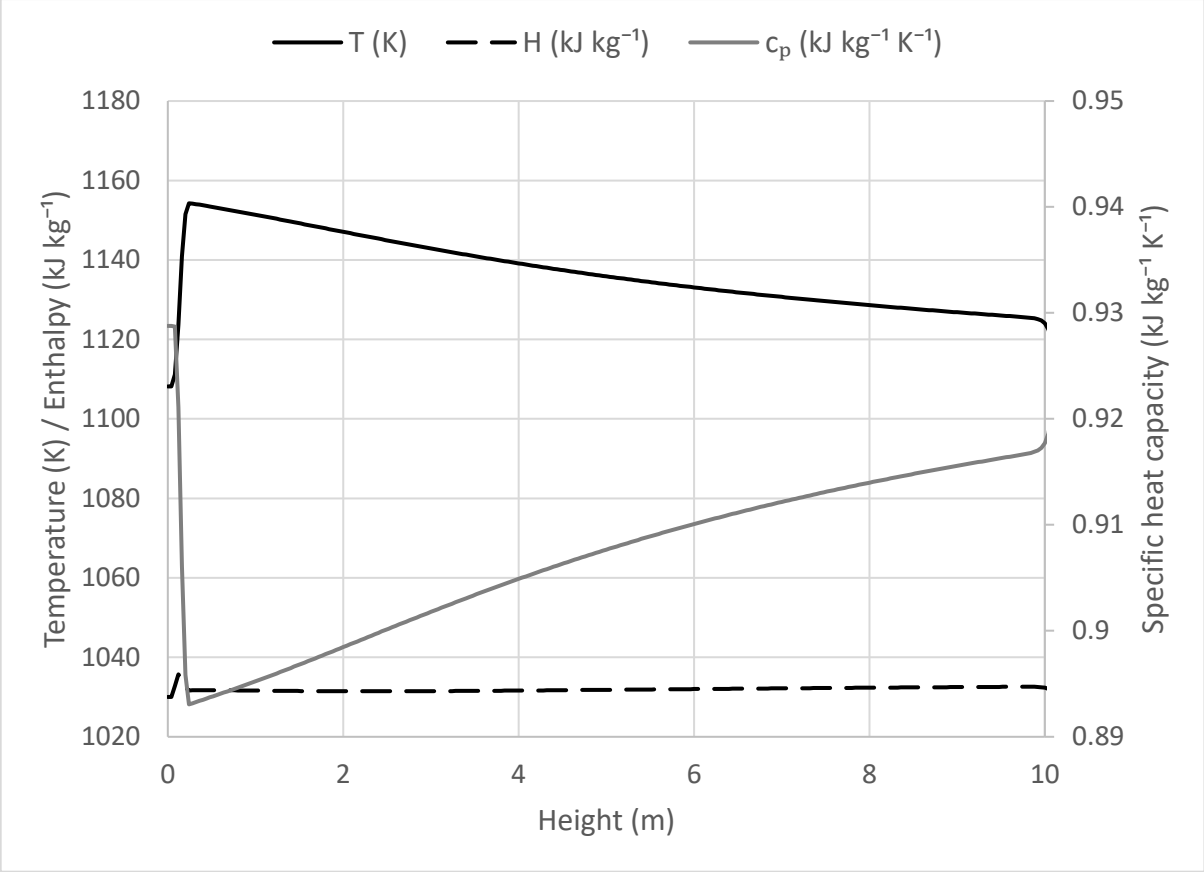

Figure 30: Changes in enthalpy and temperature in the calciner

6.5 Mass sources

In terms of mass sources, the sole contributor to interphase mass transfer in this study is the reaction step. Particles do no increase or decrease in diameter, but as reaction proceeds, mass in the form of CO_2 is transferred between the solid and gas phases as CaO is converted to $CaCO_3$ and vice versa.

It is assumed, for the sake of simplicity and to reduce the number of variables, that particles are converted entirely from CaO to $CaCO_3$, and that the ratio of these phases gives the extent of the reaction for the mixture, rather than the extent of reaction of an individual particle. As the $CaCO_3$ particles contain more mass even though they are lighter, the mass of the CO_2 will be transferred from the gas to the solid phase.

If the model is balanced, the net rate of solids generation will equal the net rate of CO_2 consumption and the rate of $CaCO_3$ production will be equal to the combined rates of CaO and CO_2 consumption. The mass within and density of each cell will stay the same, as the mass is transferred between the solid and gas phases.

The total solids production is equal to the total CO_2 consumption, so this is balanced. The total CaO consumption is 5.04×10^{-4} kg, the total CO_2 consumption 3.96×10^{-4} kg and the total $CaCO_3$ generation 9×10^{-4} kg so this also balances. These are values per time-step. A mass balance for the carbonator is shown in Table 13. On this pass 54 % of the CO_2 entering the system is captured.

Table 13: Mass balance for the carbonator

Mass	Solids in (kg s^{-1})	Gas in (kg s^{-1})	Exit (kg s^{-1})	ΔN_R (kg s^{-1})	Sum
CaO (300 µm)	8.52E-02		-4.52E-02	-2.38E-04	-5.04E-04
CaO (400 µm)	8.71E-02		-4.52E-02	-2.66E-04	
$CaCO_3$ (300 µm)	6.89E-03		-4.07E-03	4.24E-04	8.99E-04
$CaCO_3$ (400 µm)	7.02E-03		-4.10E-03	4.75E-04	
CO_2		4.99E-05	-3.43E-04	-3.96E-04	
Sum	1.86E-01	4.99E-05	-9.89E-02	0.00E+00	

In this section, the derived hydrodynamic and reaction modules were tested by comparing the results obtained in Excel and PHYSICA with observations from practical experiments, and then integrated with the heat module.

It was found that the algebraic slip model was able to capture the beginnings of fluidisation when it would be expected to occur and suspends the particles above this velocity as in pneumatic conveying. Using the shrinking core model as a guiding rate gave an adequate representation of the rate of reaction up until a point where the calculated rates and observed rates from experiment began to diverge. The timescales that this divergence occurred at are not covered in this study, as the residence times for the simulations were kept in the vicinity of 10 s, so this was not seen as a problem.

PROCESS SIMULATION RESULTS

7.1 Introduction

In this section, the behaviour of the carbonator was tested under a variety of conditions, to investigate how the model performed. The model is tested both for varying solid phase properties as well as different reactor geometries and operating conditions.

Reactant properties were varied such as

- Particle diameter – to investigate the effects of slip velocity and residence time
- The number of cycles the particles had been subjected to – how the efficiency of the reactants can affect the capture rate
- CO_2 concentration – how the volume of CO_2 in the system affects both the amount and proportion that is captured

Reactor operating conditions and design were tested, including

- Reactor height – how this affects residence time
- Gas-flow velocity – effect on residence time and reaction
- Temperature – Its effect on the reaction and capture rate
- Side inlet vs. lower inlet – How the inlet mechanism affects the model behaviour and whether this can be captured adequately with an algebraic slip model

The tests were conducted on a two-dimensional 0.1 x 10 m reactor with a mesh of 20 x 250 cells. There was a lower inlet for both the solid and gas phases at a velocity of 2.15 m s^{-1}. The default mixture properties and reactor conditions are summarised in Table 14.

Table 14: Initial and boundary conditions for testing

Powder	CaO	$CaCO_3$	CO_2	Air

Density (kg m^{-3})	3340	2710	1.98	1.2
Diameter (µm)	250	250	n/a	
RMM (kg $kmol^{-1}$)	56	100	44	28
Inlet Con (m^3 m^{-3})	0.0006	0	0.1	0.8994
Temperature (K)	923			

7.2 Standard column behaviour

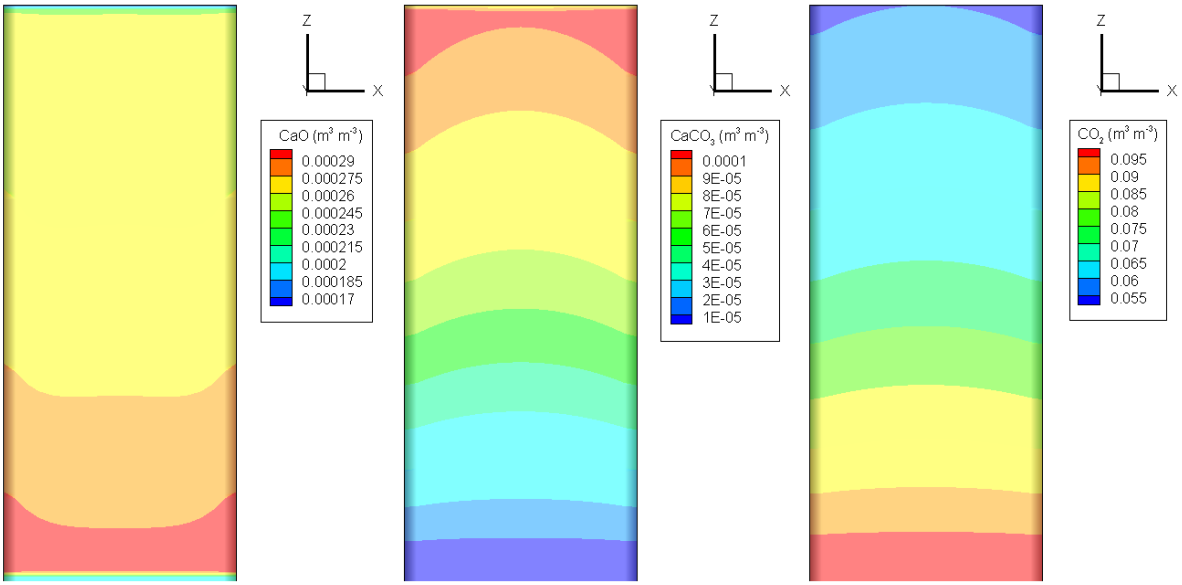

Figure 31: Behaviour of the standard carbonation model

Table 15: Material properties

Component	RMM (kg $kmol^{-1}$)	Density (kg m^{-3})	Viscosity (Pa s)
Air	28	1.2	0.000018
CO_2	44	1.98	n/a
CaO	56	3340	n/a
$CaCO_3$	100	2710	n/a

The reactor originally contained N_2 with an enthalpy specified to set the temperature to 923 K and the reactor operated adiabatically. The inlet stream had an enthalpy of 880 kJ kg s^{-1}, corresponding to a temperature of 923 K with a mixture specific heat capacity

of 0.91 kJ kg^{-1} K^{-1} with mixture properties as defined in Table 15. The reaction extent and enthalpy of the system under these conditions are shown in Figures 31 to 33.

As this is fast fluidisation the powder occupies the whole column, and Figure 31 shows how the solid phases in the column change from Calcium Oxide to Calcium Carbonate as they move upwards, together with the depletion of the Carbon Dioxide in the gas stream. The volumetric concentration of CaO reduces from $2x10^{-4}$ to $1.62x10^{-4}$ m^3 m^{-3}, while the $CaCO_3$ increases from 0 to $8.42x10^{-5}$ m^3 m^{-3} and CO_2 is reduced by over 50% from 0.1 to 0.049 m^3 m^{-3}. Figure 32 shows this information on a line graph for the centre of the column.

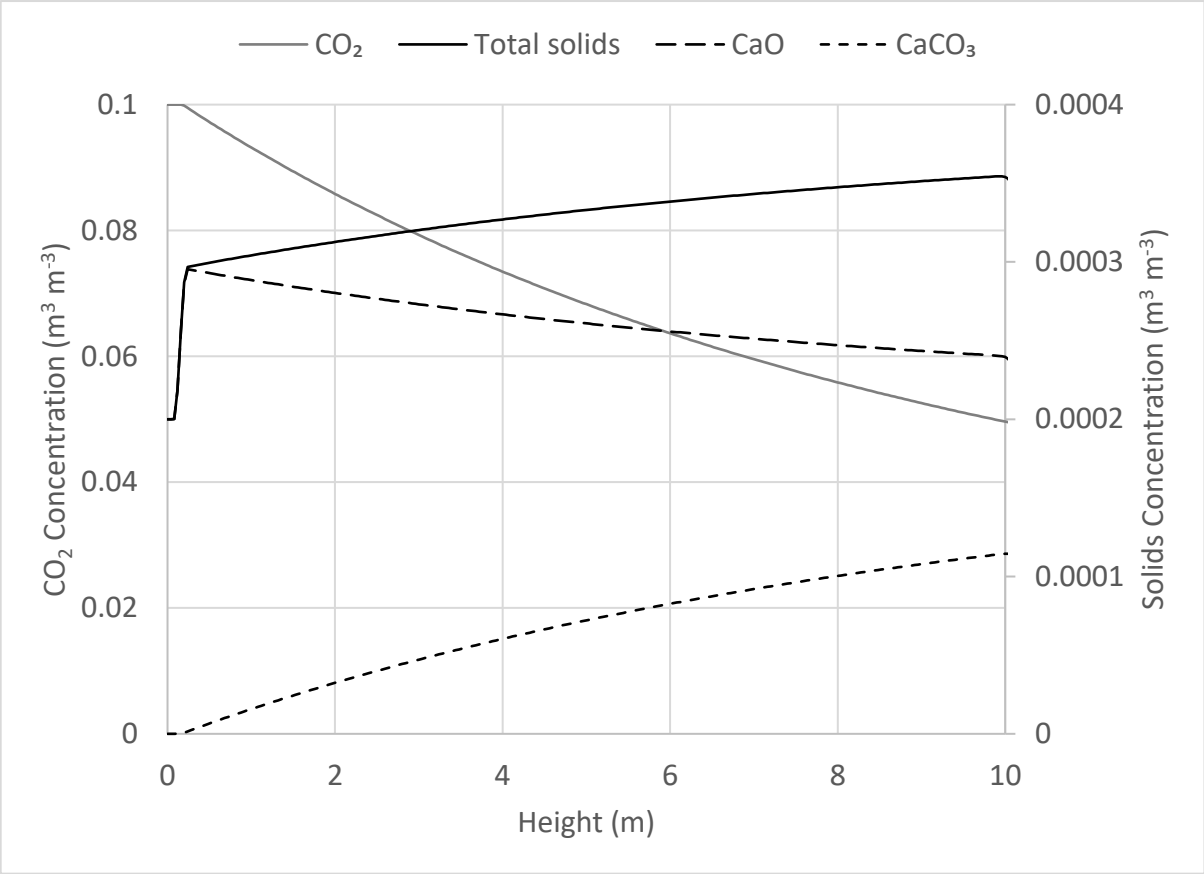

Figure 32: Standard behaviour of carbonation routine

The model predicts a steady change in the reactant and product concentrations along the reactor length. These changes in concentration release heat and lower the heat capacity of the mixture, resulting in the rise in temperature shown in Figure 33. The

enthalpy experiences a sharp leap as the solids enter, before increasing steadily along the height of the column while the heat capacity reduces as the solids are converted from one phase to another and the temperature rises.

This study provided the initial conditions, around which the following investigations were based.

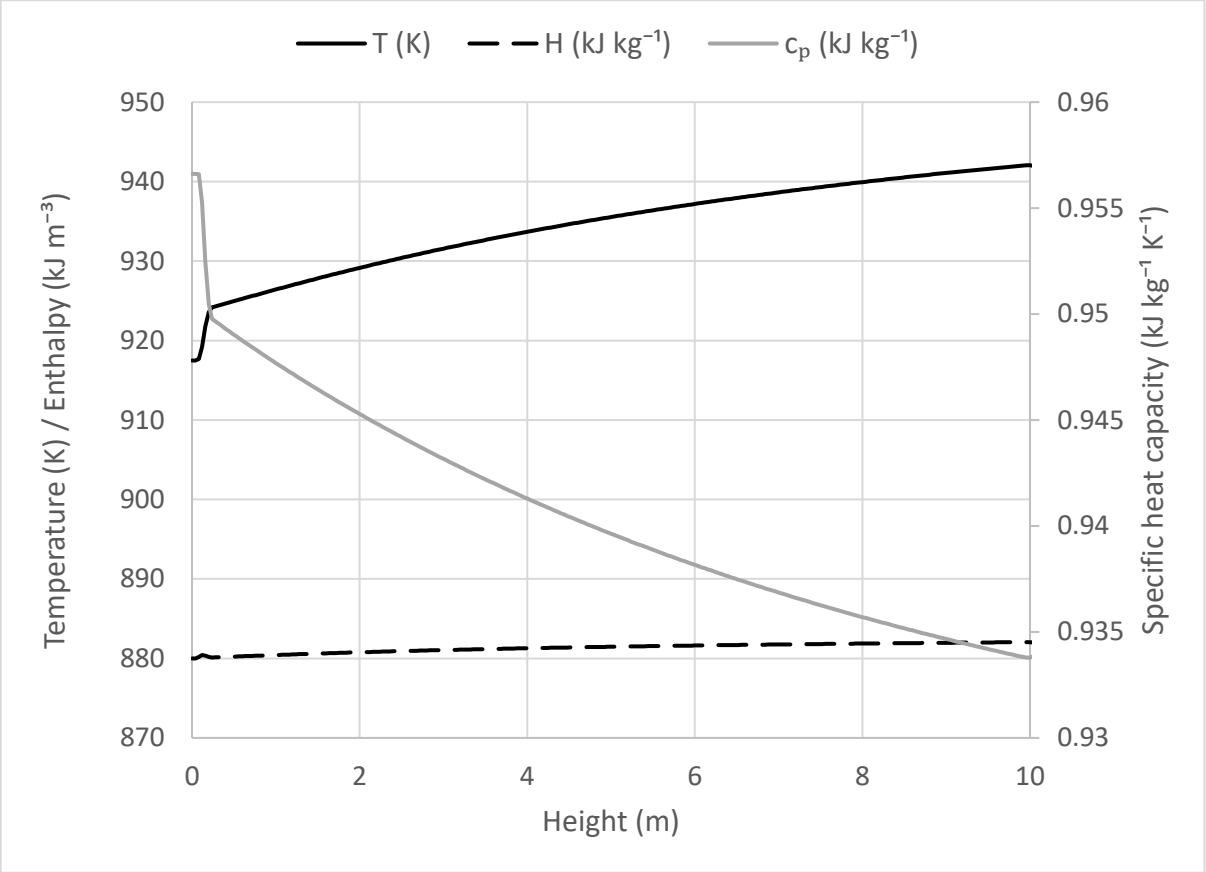

Figure 33: Temperature, enthalpy and specific heat of standard carbonation

7.3 Temperature

The operating temperature of the reactor was varied between 903 and 943 K. The reactor initially contained air (N_2) with properties of viscosity at 1.8×10^{-5} Pa s and density 1.2 kg m^{-3} and a specific heat capacity of 1.005 kJ kg^{-1} K^{-1} with an enthalpy equivalent to the set temperature. A mixture containing 3×10^{-4} m^3 m^{-3} CaO particles entered from the bottom, at an enthalpy equivalent to the same temperature as the

reactor. The effect of temperature on the carbonation reaction is twofold: the equilibrium concentration, which is favoured by lower temperatures and the rate of the reaction, which is enhanced by higher.

Figure 34 shows the CO_2 profiles for the different temperatures over the last 4 m of the reactor length.

The outlet CO_2 concentration increases only very slightly from 0.048 to 0.052 $m^3\ m^{-3}$, and less CO_2 is captured as the temperature is increased from 903 to 943 K. More than three quarters of this rise has taken place above 923 K. This has also led to a small reduction in the formation of $CaCO_3$ (8.54 to 7.92 $m^3\ m^{-3}$), and hence reduction in overall volumetric solids concentration, as would be expected.

There is little difference in the CO_2 captured between the lowest two temperatures, while the higher temperatures (933 and 943 K) are noticeably less effective.

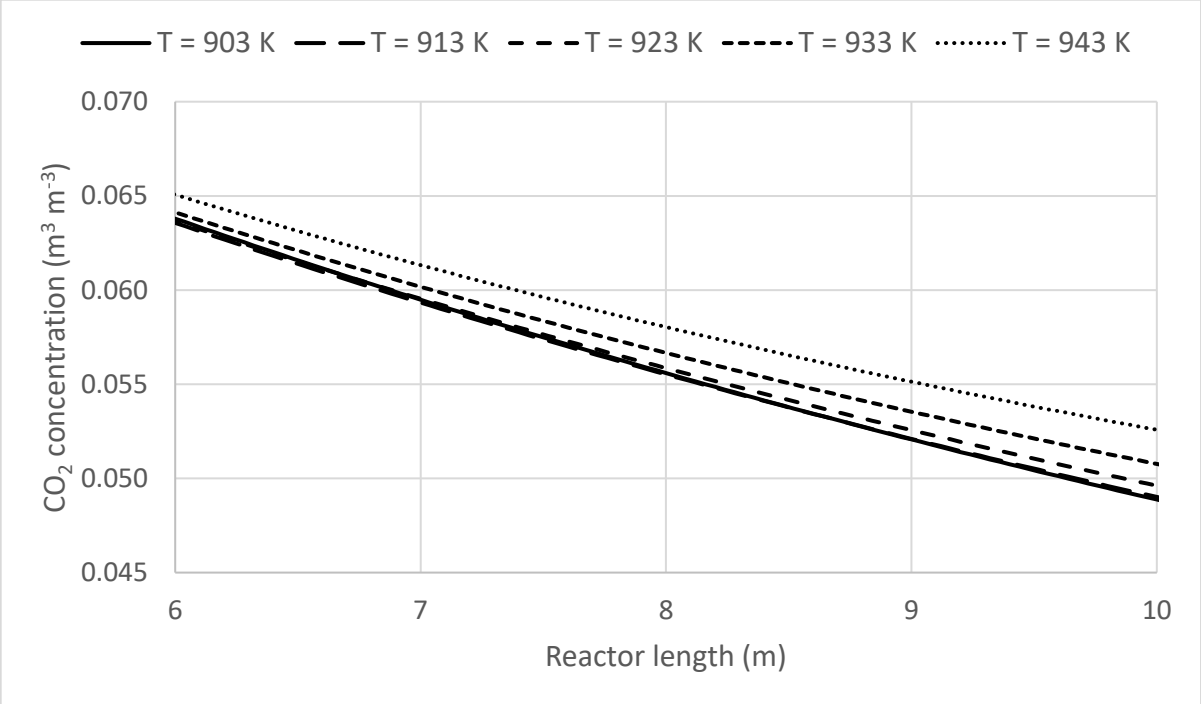

Figure 34: Effect of temperature on CO_2 concentration at top of column

7.4 Gas density

Experiments were performed varying the gas densities, based on the ideal gas law.

$$pv = nRT \tag{118}$$

Where p is the pressure in kPa, v is the volume of the gas in m^3, n is the number of kmol, R is the ideal gas constant and T is the temperature in K. If pressure is constant, then the volume occupied by the gases at 900 K is much higher than at 298 K, and so the density is reduced, which will result in lower slip velocities for the solid phases.

The density was then calculated from

$$\rho = \frac{m}{v} \tag{119}$$

Runs were completed both for reduced densities, and reduced densities with reduced mixture velocity.

As can be seen in Figure 35, a reduction in gas density due to temperature results in an increase in the capture rate. The primary reason for this is that with boundary conditions prescribed by volumetric concentration, a reduction in gas density leads to a reduction in the mass and molar quantities of CO_2 passing through the system, unless there is a corresponding reduction in the volumetric solids concentrations.

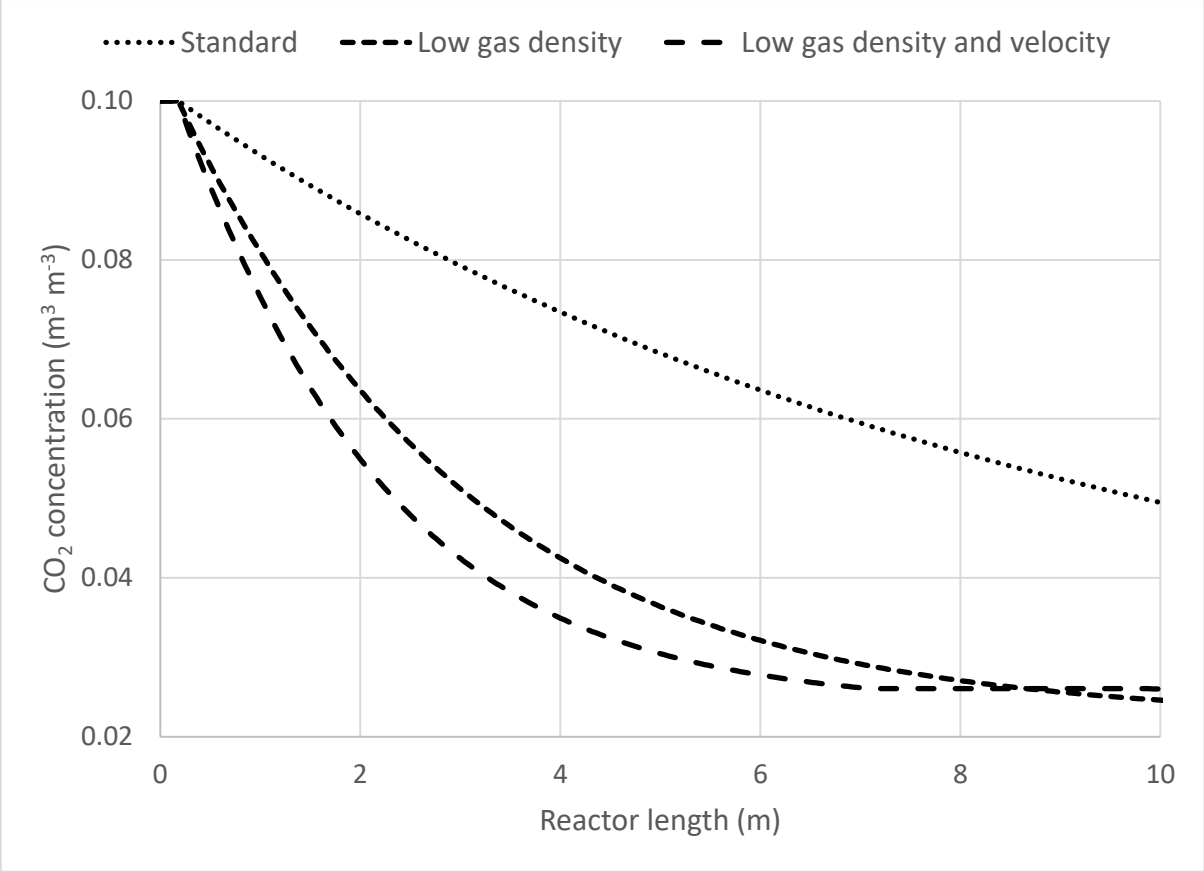

Figure 35: Effects of reducing gas density and mixture velocity

7.5 Gas-flow

The rate of gas-flow is an important factor in fluidisation, as it must be high enough to suspend the particles, while allowing a long enough residence time that sufficient reaction will occur. During the initial design of a column, the residence time required for optimum reaction is calculated, and then based upon the physical dimensions of the column and the minimum fluidisation velocity, an appropriate gas velocity can be chosen.

In mixtures, where a range of particles of varying size and density are present, it is necessary to consider the range of slip velocities and residence times to ensure that as great a fraction as possible are subject to reaction.

A series of studies were performed in the simple 2D mesh, varying the lower gas velocity from 1.95 to 2.35 m s^{-1}. The particles were 100 μm in diameter with a slip velocity of 1.04 m s^{-1}. This gave a range of residence times from 7.95 s (for 2.35 m s^{-1}) to 10.82 s for 1.95 m s^{-1}. Figure 36 shows the CO_2 concentration profiles for these runs.

As with the temperature variations, increasing the gas flow-rate lead to small decreases in the efficiency of the process, with slightly elevated CO_2 levels leaving the reactor. The volumetric concentration of CO_2 increased from 0.046 to 0.051 m^3 m^{-3} as the velocity increased from 1.95 to 2.35 m s^{-1}.

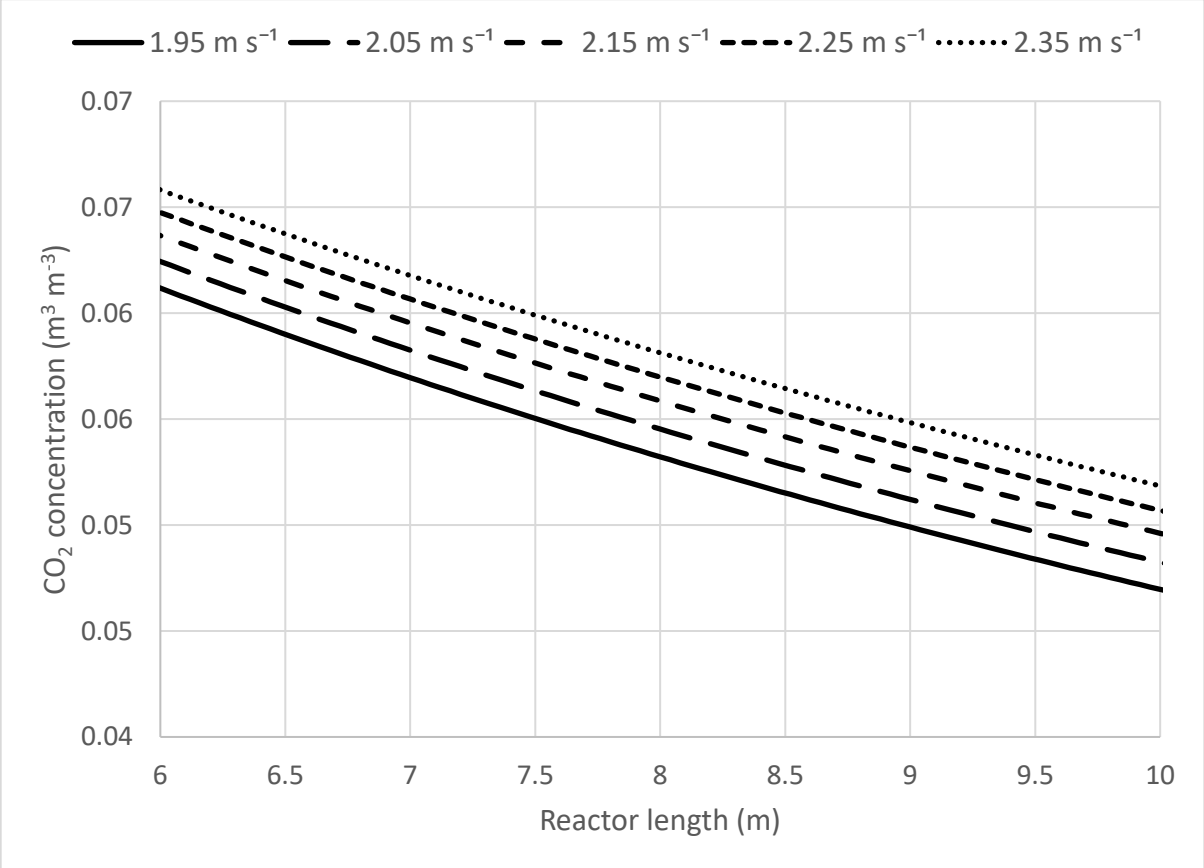

Figure 36: The effect of gas flowrate on the outlet stream CO_2 concentration

7.6 Number of cycles

As the solid reactants are subjected to multiple cycles of carbonation and subsequent regeneration, they will become denatured due to effects such as attrition from collisions

and sintering from exposure to high temperatures. This will reduce the maximum extent and rate of reaction and diminish the performance. Abanades [83] found that the maximum possible conversion for solids in a carbonation cycle (X^{max}) can be represented as a function of the number of times that a reagent has been reacted and regenerated:

$$X^{max} = a^C + b \tag{120}$$

where C is the number of cycles of reaction and regeneration that a particle has been through and a and b are empirical values for some CaO particles which were found to correlate well for a range of limestones with a as 0.782 and b as 0.174.

A series of studies were performed with different values of maximum conversion (X^{max}) to observe the behaviour of the carbonation cycle after multiple passes of the solid phases to show the impact of recycling the solid phases, rather than replacing them. For this test, it was assumed that all the solids phases had been subject to the same number of cycles and had been fully reacted, while in a real process only a small fraction will react in any given cycle [90], and the mixture will contain phases which will have been through a range of cycles.

Figure 37 shows the CO_2 concentration profiles for particles which have been through one to three cycles. The decrease in performance is very noticeable moving from C=1 to C=2, with a much smaller drop from C=2 to C=3.

On the first pass through the system, more than half the CO_2 was captured (a reduction in outlet concentration of 0.1 to 0.049 $m^3\ m^{-3}$), while the second and third passes have outlet CO_2 concentrations of 0.061 and 0.069 $m^3\ m^{-3}$, respectively. This is a reduction in capture efficiency from 51%, to 39% to 31%.

If the plant is to operate efficiently, then a regular replenishment of solid phases is needed to keep the performance high. The reduction in efficiency for higher cycles suggests it might be sensible to budget for operating with phases which had gone through multiple cycles. Mackenzie [120] investigated the costs of carbon capture plants and found that over a thirty year period, despite its relative value at $25 per ton, the costs of limestone fuel outweighed the costs of operating the plant and regenerating the fuel by a ratio of over six to one.

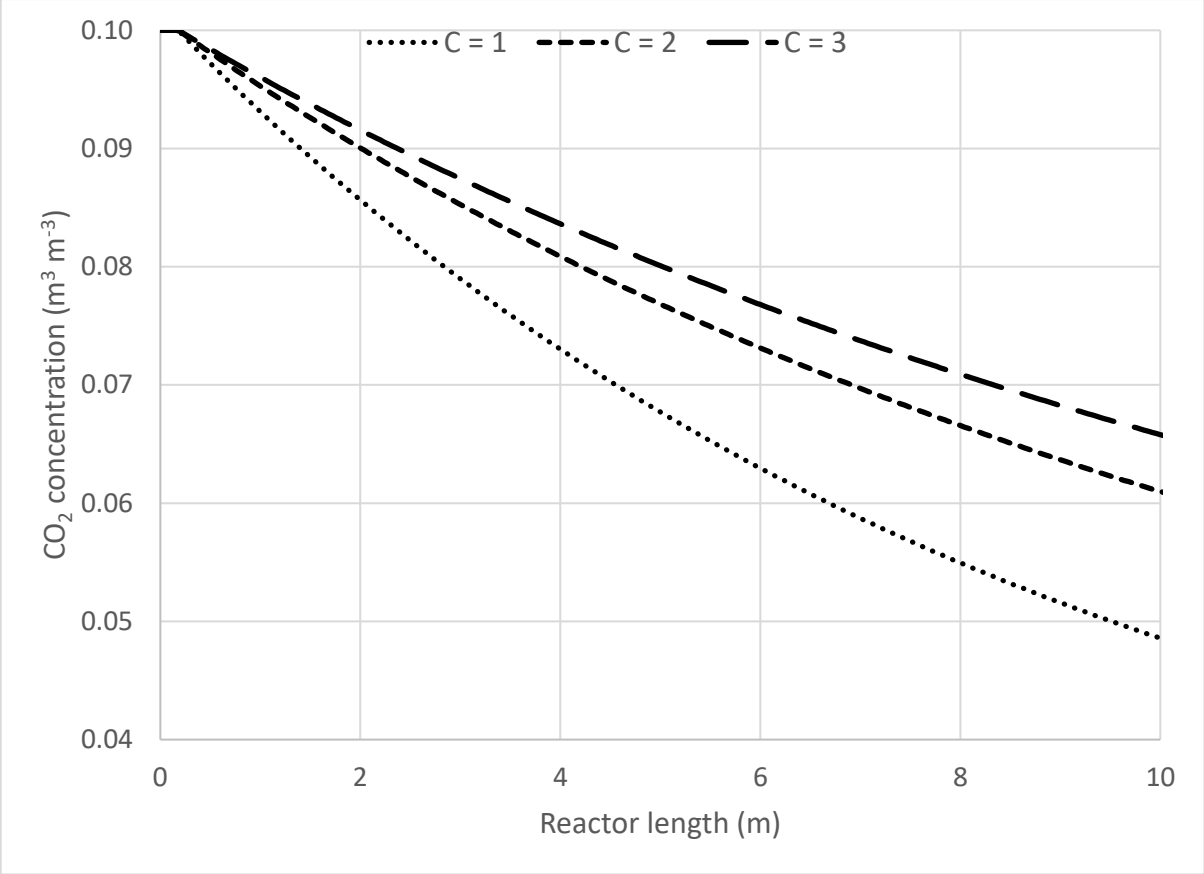

Figure 37: The effect of the number of cycles on the CO_2 concentration profile

As an example, the German energy company Energie Baden-Württemberg [90] plan to capture 88% of the 815 t/hr CO2 emissions from their demonstration plant in Stuttgart using a carbonation system. They aim to convert 33 % of the CaO fuel in each pass, while replacing 2 % of the converted $CaCO_3$ in each cycle.

7.7 Reactor height

The behaviour of the reaction was tested for different heights of reactor. The heights were varied between 6 and 12 m, and the column behaviour recorded.

Figure 38 shows the CO_2 concentration profiles in the reactor for reactors of different lengths. As expected, the longer columns capture more CO_2 as the particles have a longer residence time. The height of the reactor has no impact on the rate of reaction,

but the higher columns capture more CO_2 due to the longer residence time. The 12 m column captures 56% of the inlet CO_2, whereas the 6 m column only accounts for 37%. A doubling of the height has increased the capture total by 50%.

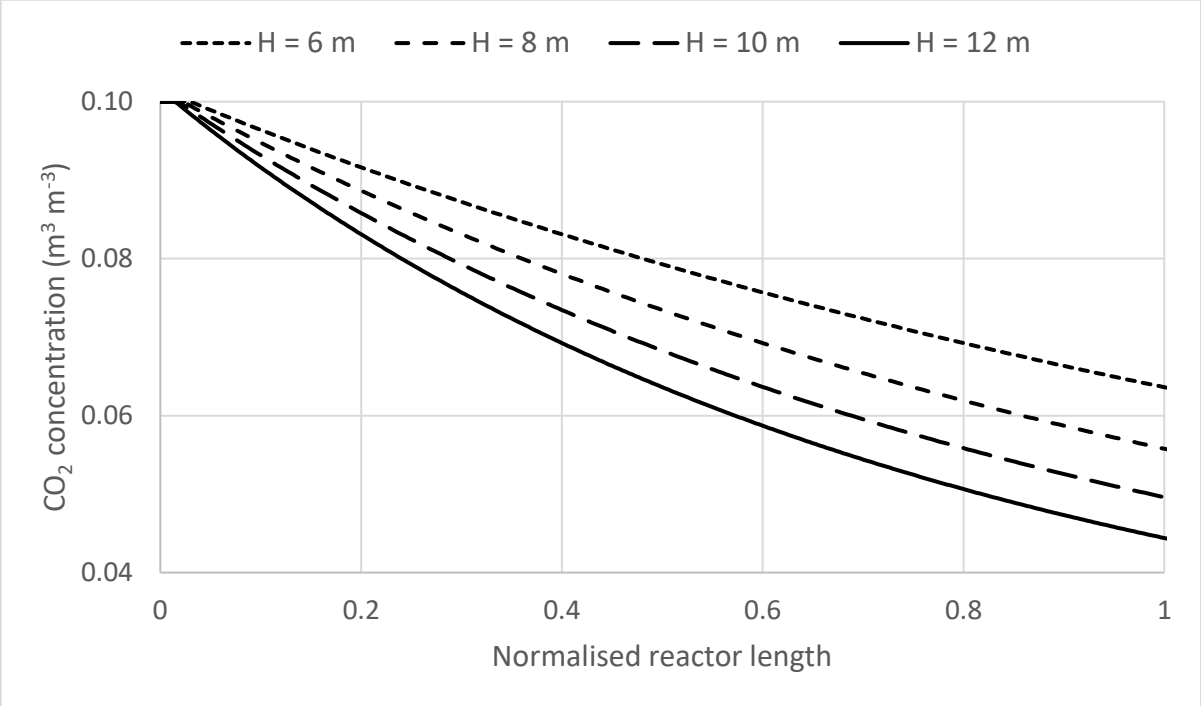

Figure 38: CO_2 concentration profiles for different height reactors

7.8 Inlet CO_2 concentration

Tests were performed with the inlet CO_2 partial pressures set to levels between 0.05 and 0.15 bar, the results of which are shown in Figure 39. As the concentration of inlet CO_2 is increased, the amount and proportion of CO_2 captured also increases, as does the quantity of $CaCO_3$ produced. For a CO_2 level of 0.05, 0.023 m^3 m^{-3} is retained by the system, or roughly 46%. This increases to 0.077 for an inlet value of 0.15, which is a capture level of 53%. Unfortunately, the gain in efficiency is offset by the larger volumes of CO_2 that pass through the system unprocessed, as the CO_2 outlet concentration has risen from 0.027 to 0.073, which is a dramatic increase.

Figures 40 and 41 show the volumetric solids concentration in the centre of the column for the Molaei's Lagrangian model and the current model, respectively. This study modelled the column as pneumatic conveying whereas Molaei simulated it as a

bubbling bed, which have very different solid profiles due to the difference in velocities and residence times. The bubbling bed consists of discrete bubbles travelling up through a slow-moving powder mixture, whereas in pneumatic conveying all the mixture is carried up the column well mixed by the gas.

As the CO_2 is removed from the gas phase and deposited on the CaO, the share of volumetric concentration occupied by the solids phase increases in the current model.

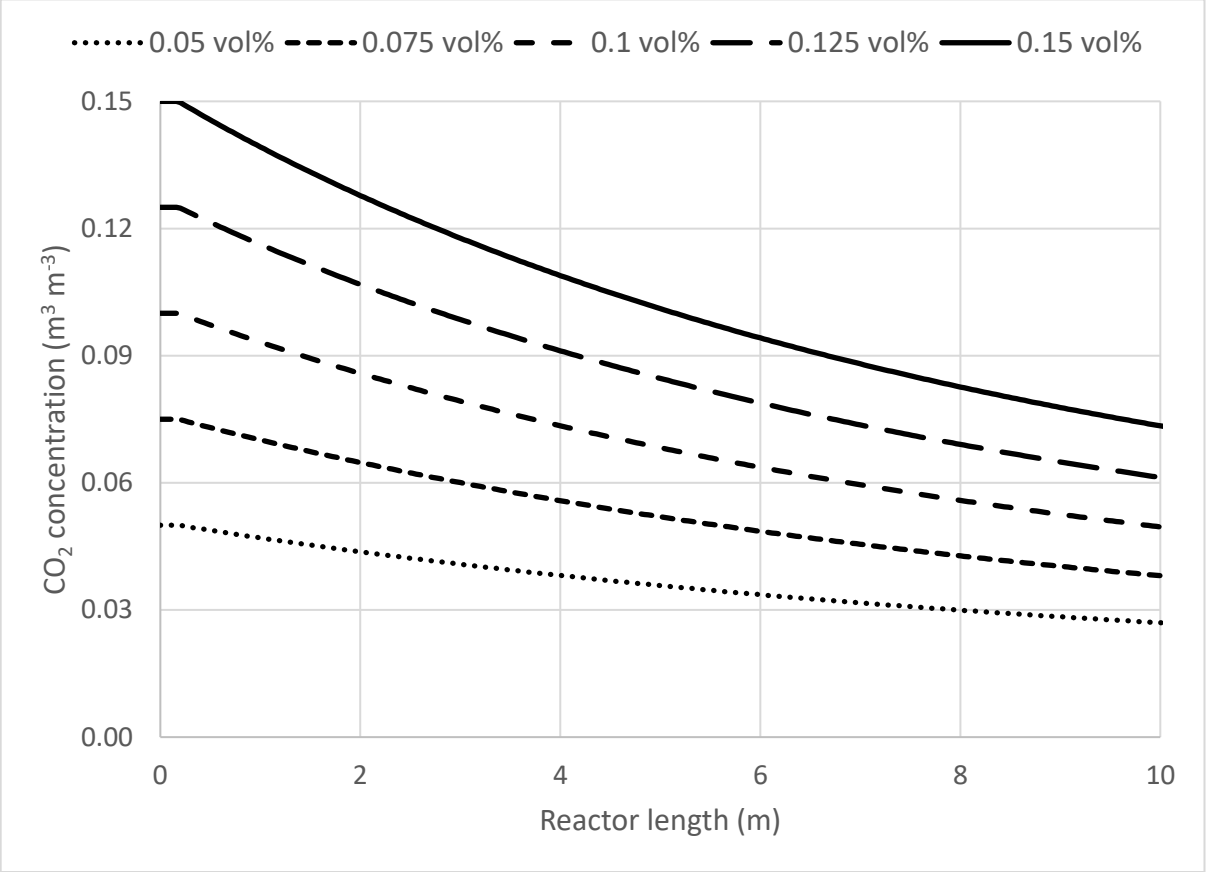

Figure 39: CO_2 profiles for different inlet CO_2 concentrations

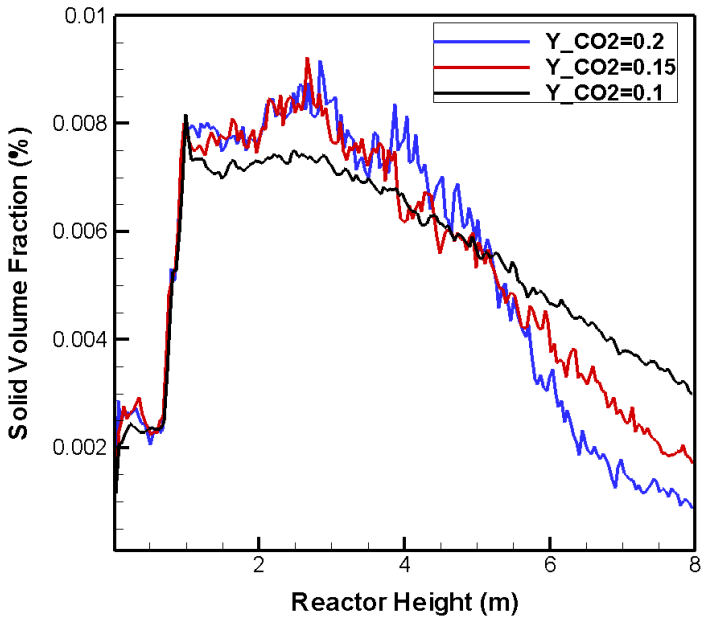

Figure 40: Solids concentrations at the centre of the column for different inlet CO2 concentrations from Molaei [26]

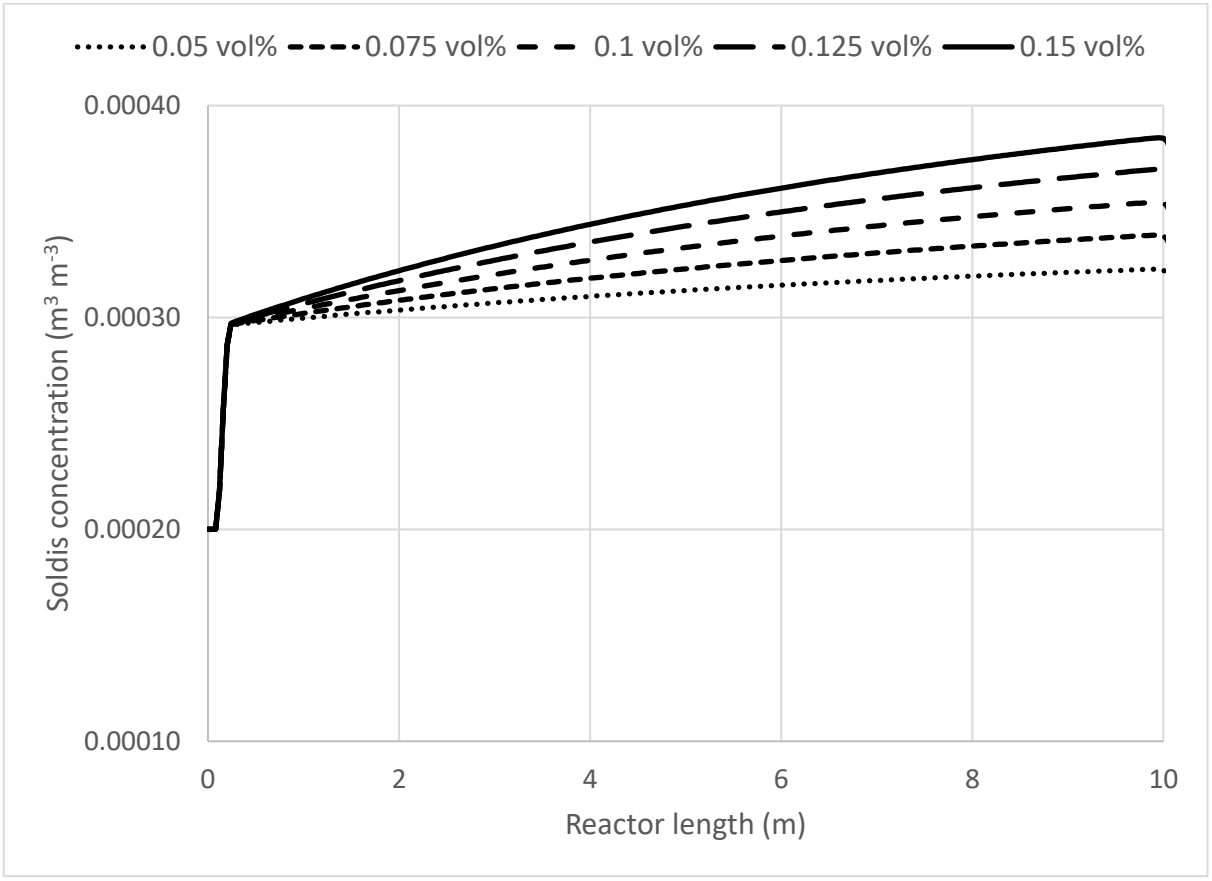

Figure 41: Solids concentrations at the centre of the column for different CO_2 inlet concentrations

7.9 Solid flow rate

The solids inlet concentration was varied between 0.0001 $m^3\ m^{-3}$ and 0.0004 $m^3\ m^{-3}$ at the lower inlet. This corresponds to a solids flowrate of between 2.15 l s^{-1} to 8.6 l s^{-1}. The effects of the flowrate on the CO_2 concentration profile over the upper half of the column is shown in Figure 42.

Increasing solids flow from 2.15 to 4.3 l s^{-1} has the largest effect on the capture capacity of the solids, as CO_2 volume fraction is reduced from 0.052 to 0.0498, which corresponds to a capture efficiency increase from 47.7 to 51%. Further flow increases to 6.45 and then 8.6 l s^{-1} only have a slight impact on the CO_2 conversion, increasing the percentage captured to 51.9% and reducing the CO_2 volume fraction to 0.048.

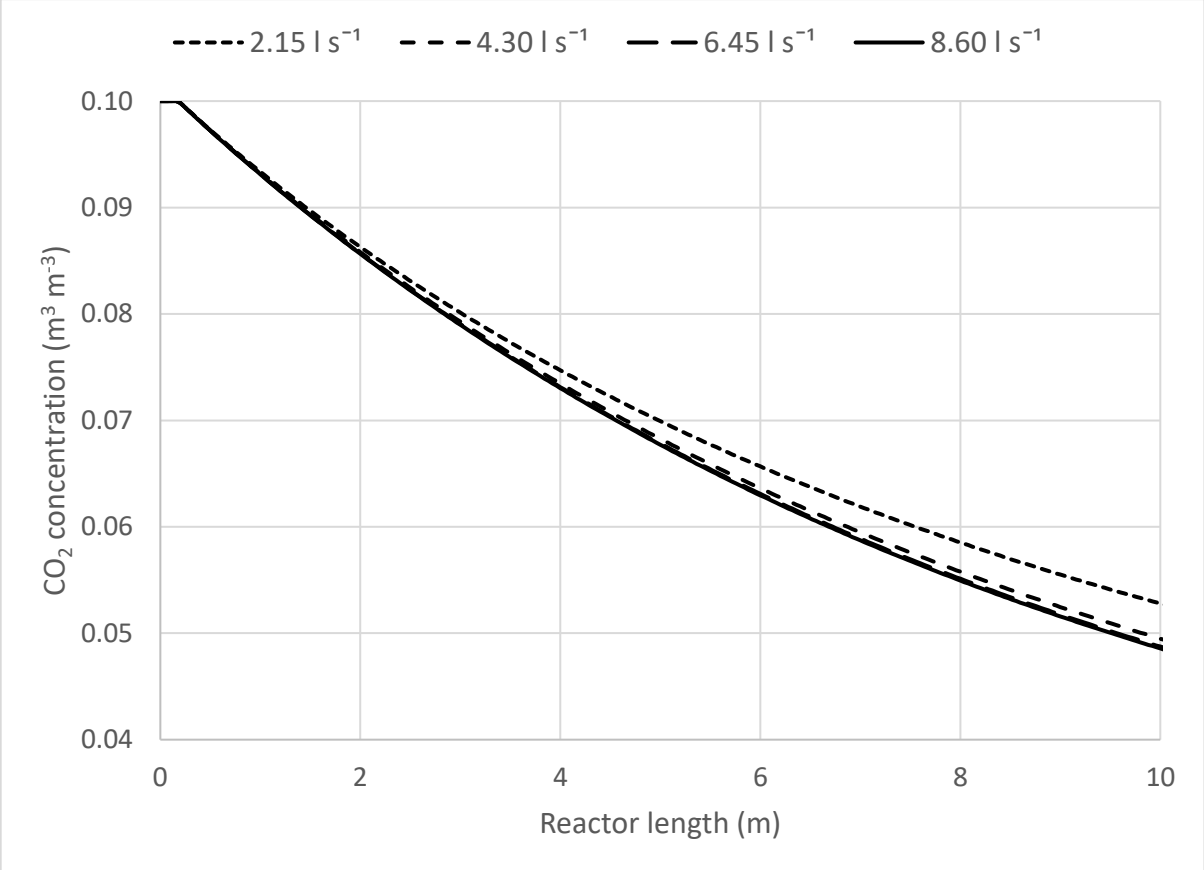

Figure 42: Effect of solids flow rate on CO_2 concentration

7.10 Particle diameter

One of the major motivations for this work and one of the prime advantages of the algebraic slip model is the ability to accommodate multiple solid phases. To capture this, the model was enhanced to allow for the simulation of several solid phases with different diameter particles of calcium carbonate and calcium oxide, as well as an inert gas phase and CO_2.

The reaction modules were modified to calculate an overall reaction rate for the gas based on the total local levels of CaO, CO_2 and $CaCO_3$, before being extrapolated for each solid phase based on their local concentration. The overall properties of the mixture were calculated at the beginning of each time-step.

The performance of different diameter particles fluidised by the same velocity air was investigated, first as a single solid phase, and then as a mixture comprising several phases. The diameters were varied between 100 and 200 μm, and the final simulation comprised the five different solid phases in two species, with CO_2 at a partial pressure of 0.1 and a temperature of 923 K. The results of the studies for each particle size as an individual phase are shown in Figures 42 and 43. Each of the phases entered the column at the same volumetric concentration.

The particles chosen are in Category B of the Geldart diagram from Section 2.4. These are easily fluidizable at minimum fluidisation velocity, but their behaviour is unsteady and their use results in unstable beds, which promotes mixing.

The increase in diameter from 100 to 200 μm has a dramatic effect on the process due to changes in the rate of both reaction and transport. The lower surface area to volume ratio has reduced the reaction rate and resulted in a rise in the outlet CO_2 partial pressure from 0.046 to 0.064, which is an increase of nearly 50%. The 200 μm particles are not fully fluidised at the velocities used here and are not being carried out of the column. There is a much lower level of reaction occurring with the larger particles.

Figure 43 shows that the halving in diameter from 200 μm to 100 μm has resulted in an increase in the capture efficiency from 31.2% to 51.5% and a reduction in CO_2 outlet concentration from 0.069 to 0.046.

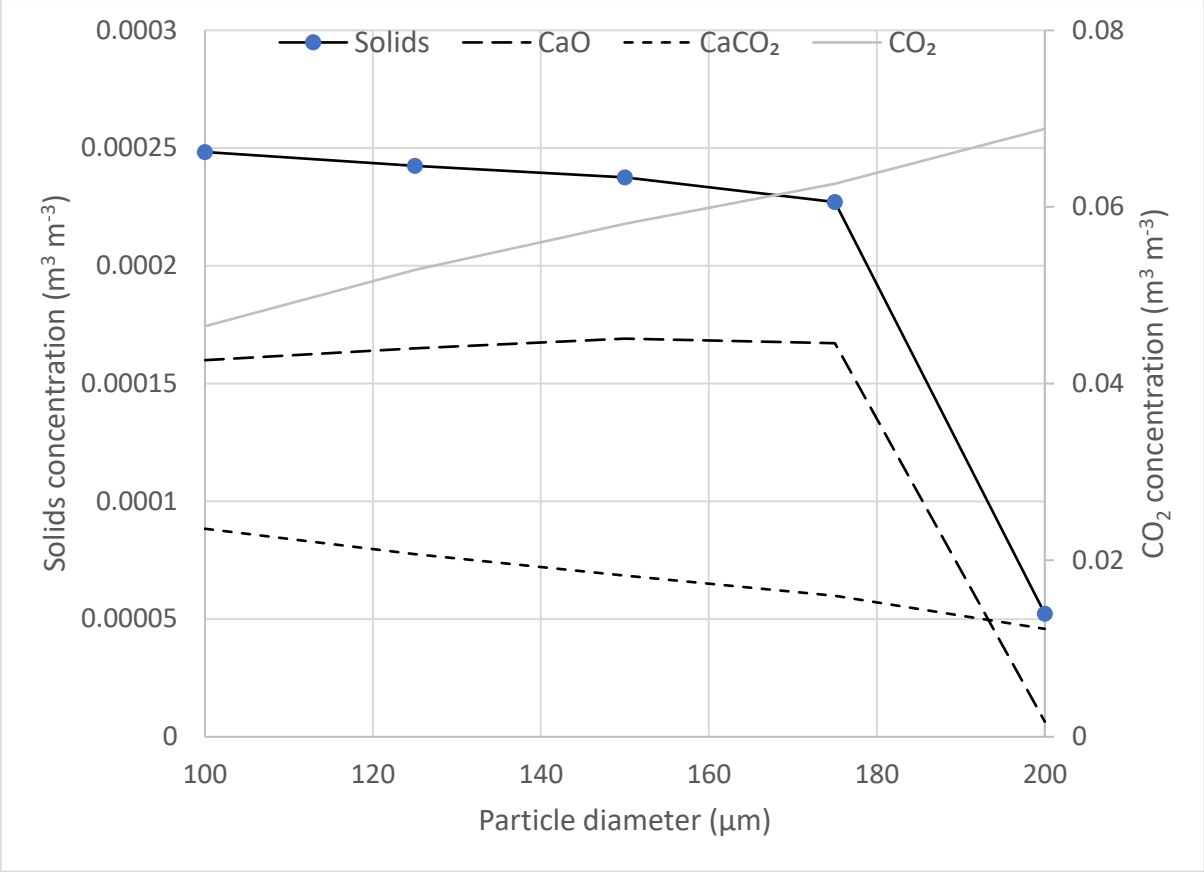

Figure 43: CO_2 and solids concentrations for different particle diameters

After being tested separately the five particles were all modelled concurrently, in a ten solid phase simulation. Vertical slices of the column for some of the CaO phases after 10 s are shown in Figure 44. The smaller particles on the left are being propelled through the column at a lower concentration, while the larger diameter phases on the right are taking longer to ascend the column and are thus at a higher concentration but have not reached the top of the column yet. They are also more concentrated towards the walls, where the upward gas velocity is set to 0, and turbulence will have a greater impact due to interactions between the powder and the eddies at the walls.

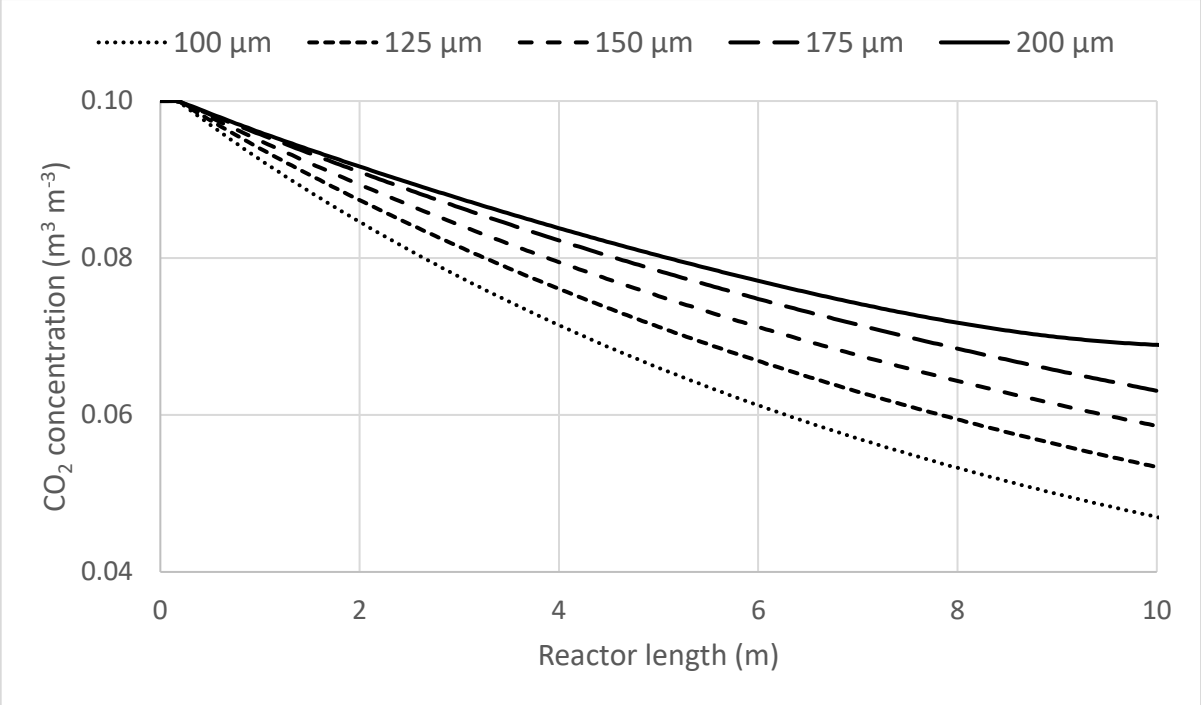

Figure 44: Effect of particle diameter on volumetric CO_2 concentration

The slow net upward velocity of the larger diameter particles is reducing the contact time between them and the gas phase, as they do not yet occupy the whole of the column. This, together with their reduced reaction rate due to their lower surface area to volume ratio further reduces their effectiveness for carbon capture purposes.

For solids to be carried upwards and fluidised by gases, their downward terminal velocity must be less than the upward velocity of the gas. This value, where the solids change from falling downwards, to being held stationary, to moving upwards with the gas, is known as the minimum fluidisation velocity (u_{mf}). The gas velocity in this simulation has not been set high enough above the u_{mf} for the larger solids.

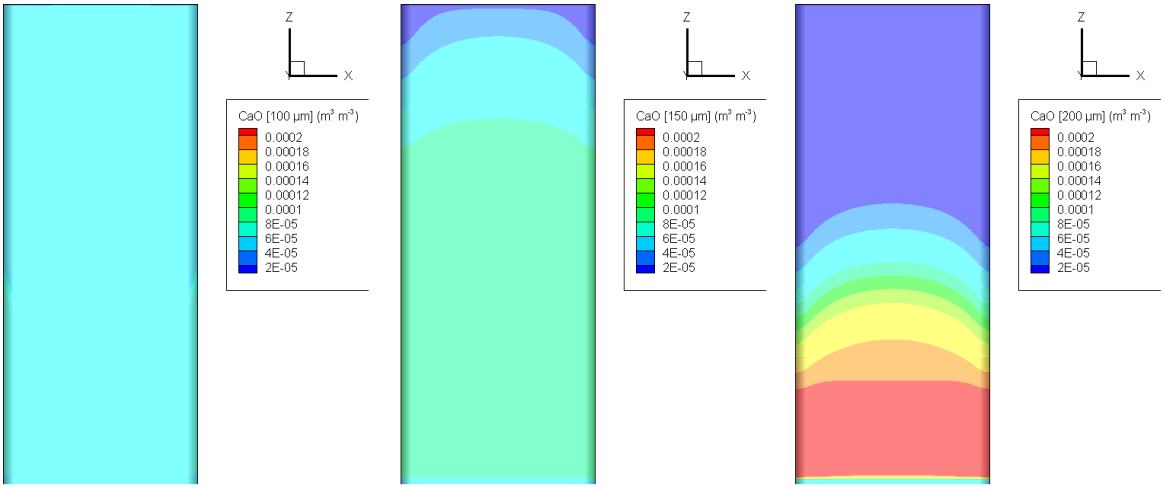

Figure 45: Vertical slices for the 100, 150 and 200 µm particles in a mixed simulation

Figures 46 and 47 show the horizontal concentration profiles for the different phases in the five-particle flow at heights of 1 m and 3 m, respectively, together with the gas velocity.

At 1 m height, the solids phases are more concentrated at the edges, whereas at 3 m the solid phases peak in the middle. The velocities at the 1 m point follow a more rounded distribution, but over a larger range of velocities, with a peak in the centre of 2.25 m s^{-1} and a low point of under 1.98 m s^{-1} at the wall, whereas the 3 m profile has a more definite peak in the centre of the column, but over a much smaller range of velocities.

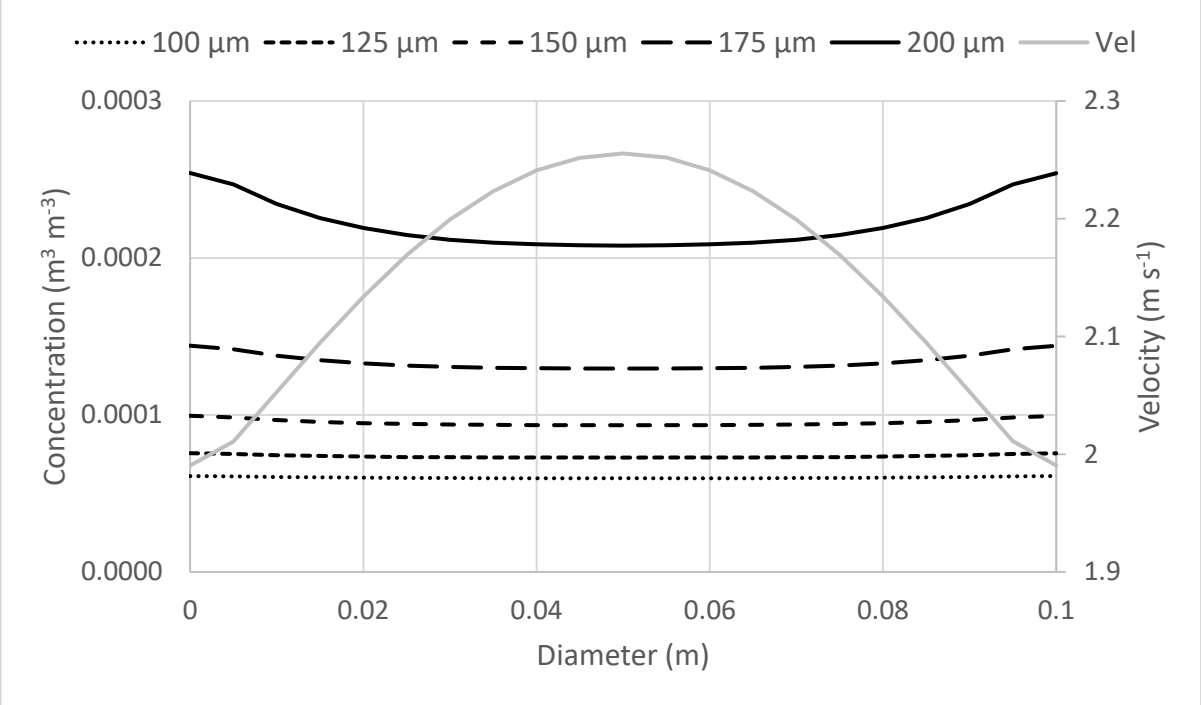

Figure 46: Horizontal concentration profiles at 1 m height

The larger diameter solid phases have the highest concentration in these experiments, a combination of their larger volumetric concentration, and the lower residence times of the smaller diameter particles due to their smaller slip velocities. These higher slip velocity phases are also present in noticeably higher concentrations at the walls, particularly further down the column.

The solids at 3 m in Figure 47 are more notably dominant in the centre, rather than at the edges as occurs at 1 m in Figure 46. The gas velocity is much reduced here, and there is a much smaller difference in velocity between the walls and the centre, although it is comparatively greater than at 1 m.

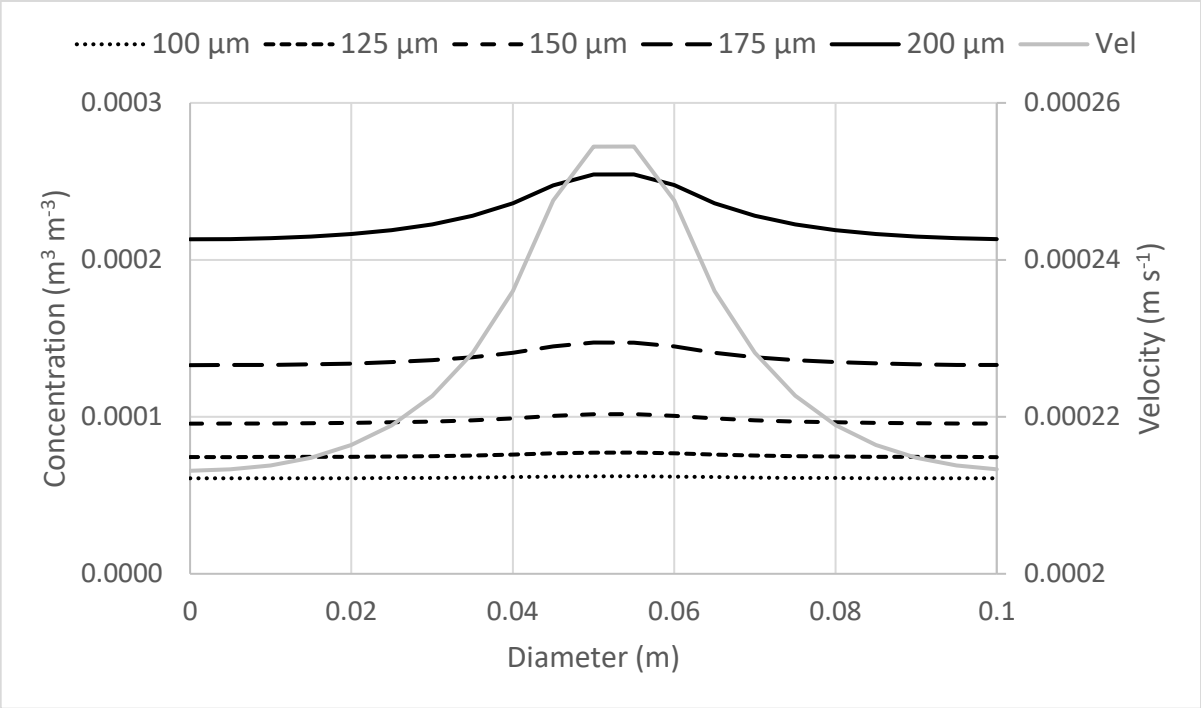

Figure 47: Horizontal concentration profiles at 3 m height

The solids profile up the centre of the column is shown in Figure 48, together with the CO_2 levels. There is nothing below the lower solid barrier at 0.2 m and above this the solids are generally present at a steady concentration which increases up the column. This is to be expected in carbonation as the contribution of the gas to the overall volume is reduced as the CO_2 is converted to $CaCO_3$.

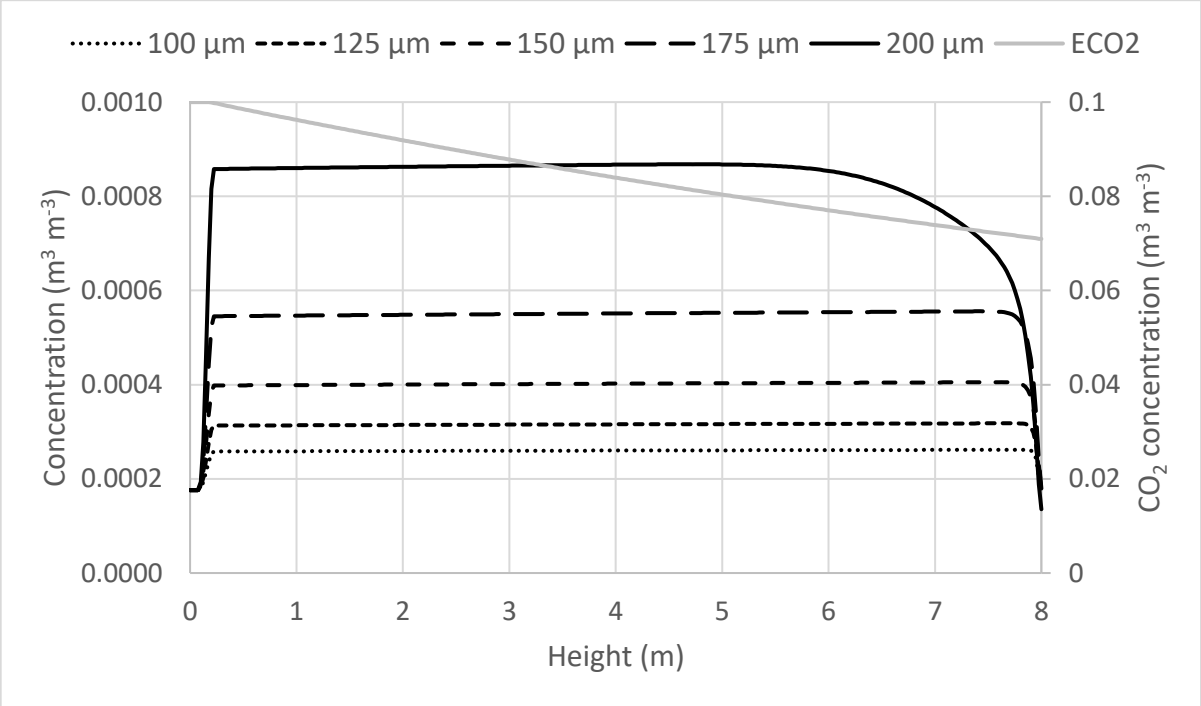

Figure 48: Concentration profiles at the centre of the column for a five-particle flow

The concentration profiles of the solids at the wall is shown in Figure 49, and it is much like that at the centre. The most notable differences are the higher solid concentrations at the walls, particularly among the higher diameter phases, which are present at a concentration of 0.00114 m^3 m^{-3} at the wall, compared to 0.00086 m^3 m^{-3} at the centre, which is roughly a ratio of 4:3. There is a much difference for the smallest phase which has a concentration of 0.000286 m^3 m^{-3} at the wall compared to 0.000277 m^3 m^{-3} in the centre.

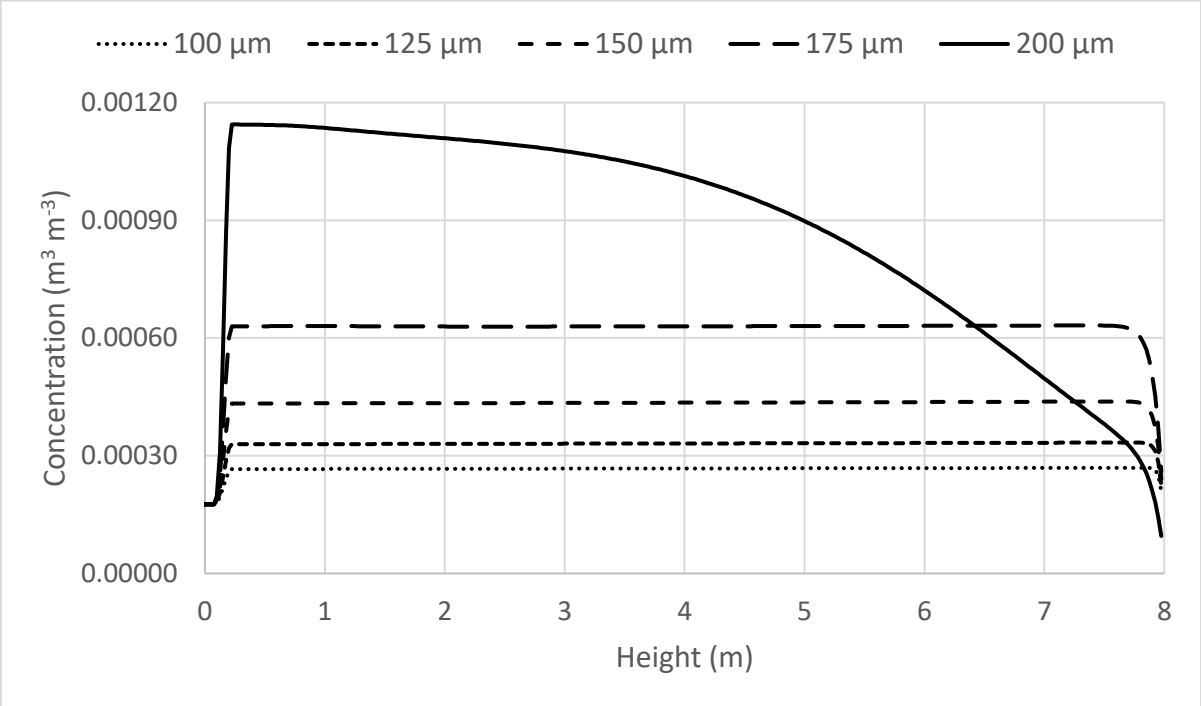

Figure 49: Concentration profiles at the wall for a five-particle flow

7.11 Side inlet

The column was modified to incorporate a side inlet for the addition of a solid phase and experimental runs were performed with the two inlets. This was an effort to see if the model developed here could adequately represent the initialisation of fluidisation for an initially unfluidized mixture.

In simulations where there was a side inlet it was necessary to account for additional velocity from the side stream. The lower gas had to be set high enough to suspend the particles, while the solid stream contained an additional flow which spread the solid phases across the column to promote mixing and add to the upward velocity of the mixture.

In a real-world scenario, the solids entry stream is usually a re-entry duct, sometimes with no significant gas-flow behind it, but in this model, to ensure dispersion of the solid phases, it was necessary to incorporate the gas velocity to move particles away from the wall. Without this input, the solids were often fluidised too quickly to spread across the column and remained close to the wall. As such, the impact of the side inlet will be overstated in these simulations.

The lower gas velocity was set to be 0.05 m s^{-1} above the minimum fluidisation velocity of the solids, and the solids phase velocity was set high enough to spread the solid phases across the column, while giving a residence time close to 10 s for the reaction. The material balance for the column considered both the lower and side inlets for calculation of upward gas velocity.

An estimate for the mixture velocity above the inlet was obtained from a volume balance, where it was assumed that all the incoming gas from the side inlet would contribute to the overall upward velocity:

$$u_{g,column} = \frac{u_{bottom}A_{column} + u_{side}A_{side}}{A_{column}} \tag{121}$$

The projected residence time for the solid particle in the column was calculated from:

$$\tau = \frac{u_{column} - u_i^*}{H_{column} - H_{side}} \quad (122)$$

Where H_{side} is the height of the side inlet.

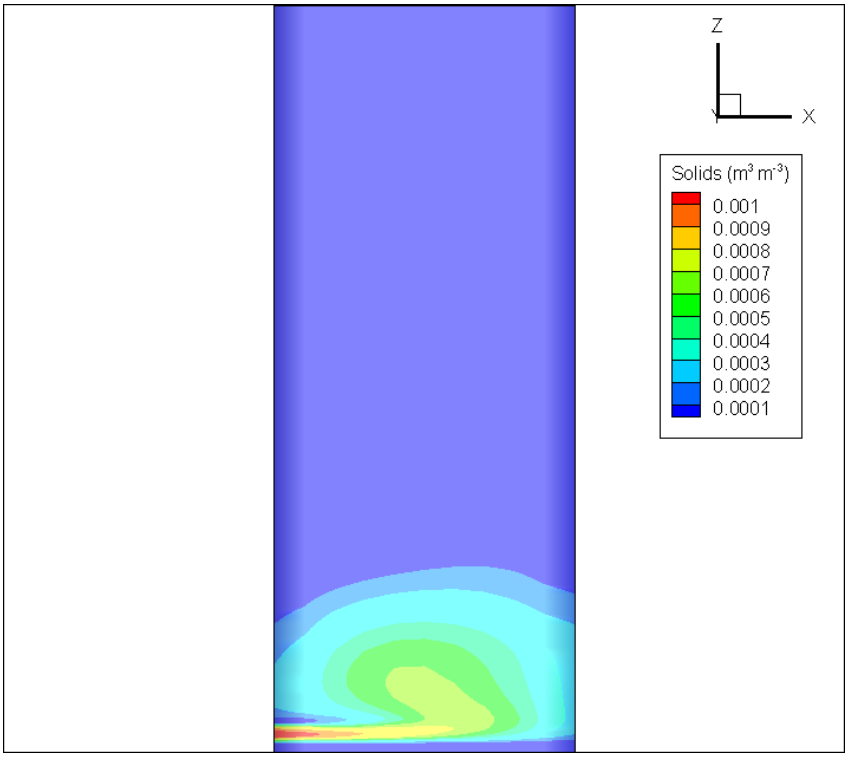

Figure 50: Solids phase development from the side inlet after 1 s

The volumetric solids concentration was set to give a molar flow-rate of CaO ten times more than CO_2 [78]. The side inlet had a specified CO_2 content of 0. To prevent the solids phases creeping up the wall, a gas stream was included above the solids stream, entering the column at the same velocity, but free of solids. An example of the solids development after 1 s is shown in Figure 50.

In the early stages of simulation, the solids particles enter the column as a jet, driven by the velocity of the side stream, before being fluidised by the incoming gas phase.

The side inlet occupies a height of 0.1 m in the column wall and is 10 cells. The spread across the whole of the column at the base of the solid flow, and the more gaseous sides of the reactor can be seen in more detail in Figure 51. The initial concentrations are high, as set by the inlet, but the overall level quickly finds a lower equilibrium which it occupies for the rest of the length of the reactor, as would be expected.

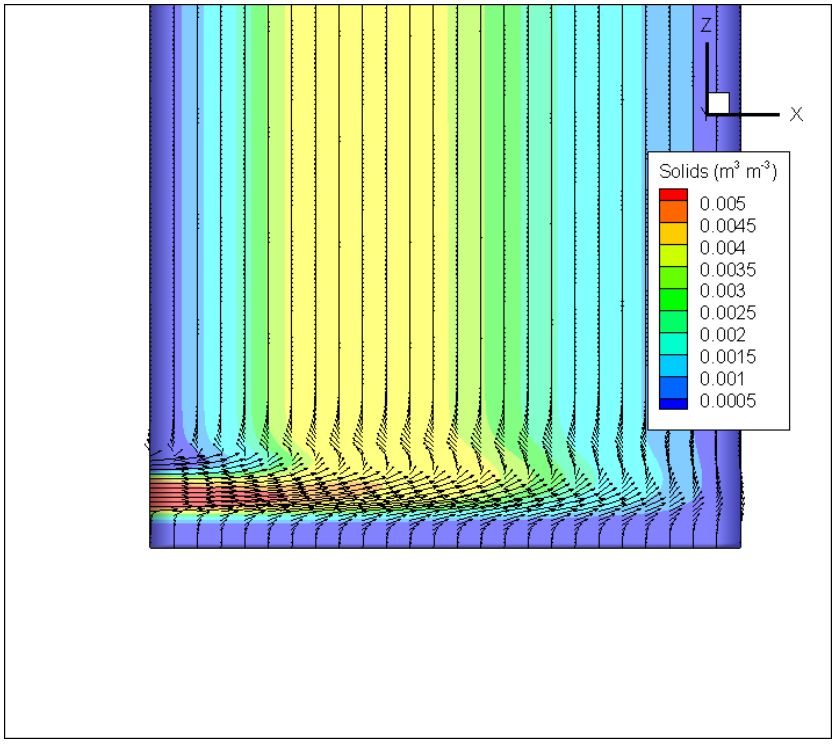

Figure 51: Solids entry from the side inlet in the lower half of the column (0-1 m)

After 10 s, steady state has been achieved. The solid and gas phases have reached the top of the column and the reaction has achieved its maximum rate and the column is displaying pneumatic transport. Figure 52 shows the solids concentrations, which are spread across the column, mostly in the centre due to conditions at the walls. A lower peak remains at the solids inlet, due to the presence of the inlet jet and limitations on downward flow here.

Initially above the jet the solid phases mostly occupy the centre of the column, but as they ascend, they spread out to cover more area and move towards the edges. Above

the jet, the solid phases are pushed back in towards the centre by the gas coming from below forcing its way up the right-hand side of the reactor.

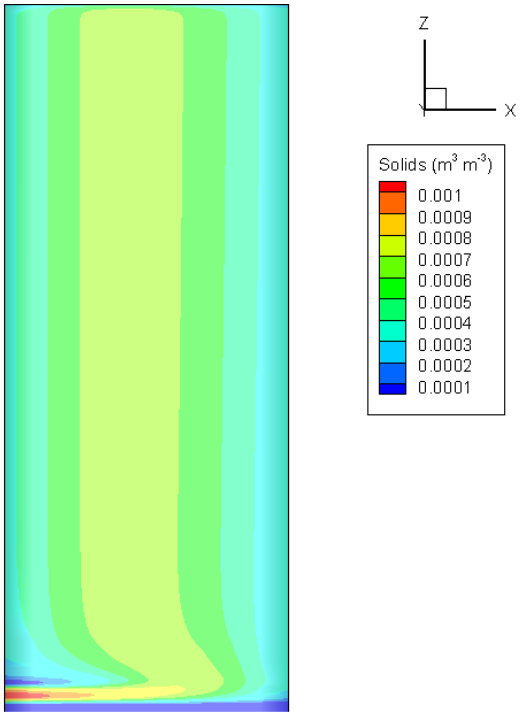

Figure 52: Solids concentration in the column after 10 s

The CO_2 concentration in the side inlet column is shown in Figure 53. Below the solids inlet the CO_2 occupies the whole of the reactor before the inlet jet of the solids steams pushes the gas over to the right-hand side. Above this jet the CO_2 begins to diffuse across the column, reacting with the CaO present to form $CaCO_3$.

The CO_2 does not reach the furthest left of the reactor, which remains CO_2 free, and the CO_2 on the right, where there is mostly gas, remains largely unreacted, however the CO_2 which has diffused towards the centre of the column has been reduced in concentration from 0.1 to around 0.065 $m^3\ m^{-3}$ at the top.

The values for CO_2 at the top of the column vary between 0.003 on the left to 0.0725 on the furthest right of the column, with a value of 0.047 $m^3\ m^{-3}$ in the centre, which is within the expected range for a reactor of this height [26].

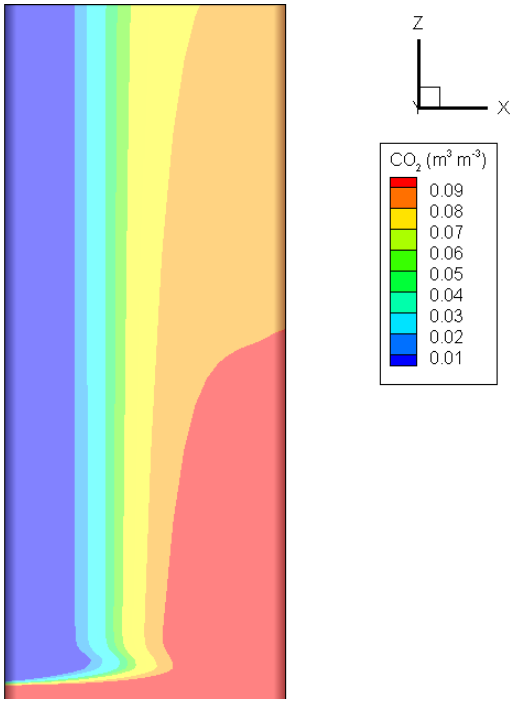

Figure 53: CO_2 concentration in the column after 10 s

A notable aspect of the CO_2 profile is the relative lack of gas penetration into the solid mixture, so the gas stream on the left which contains no CO_2, remains on the left of the solids, while the gas stream on the right, which does contain CO_2, remains on the right. This is due in part to assumptions around the dominance of convection and the minimisation of the impact of diffusion, and the differences in momentum between the gas and solid streams.

The concentration profiles for CaO and $CaCO_3$ in the column at steady state are shown in Figures 54 and 55. The CaO profile is very similar to that of the total solids, as the CaO constitutes the bulk of the solid phases. The $CaCO_3$ can be seen to increase over the height of the column, after its high concentration in the jet, from $6x10^{-5}$ to $1x10^{-4}$ m^3 m^{-3}.

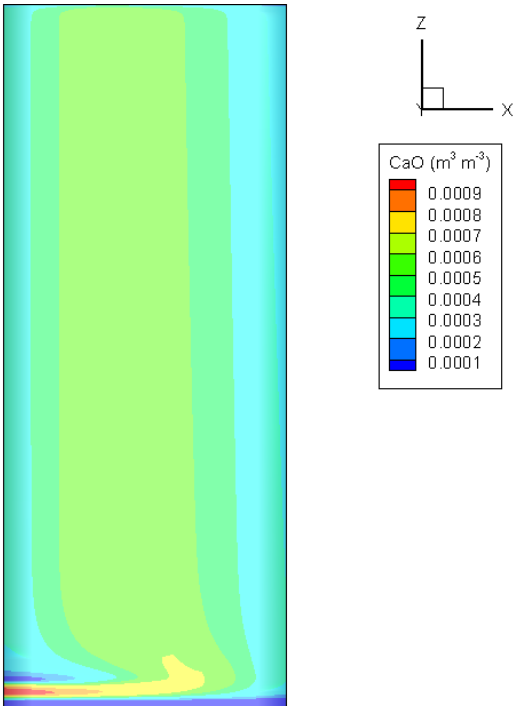

Figure 54: CaO concentration in the column after 10 s

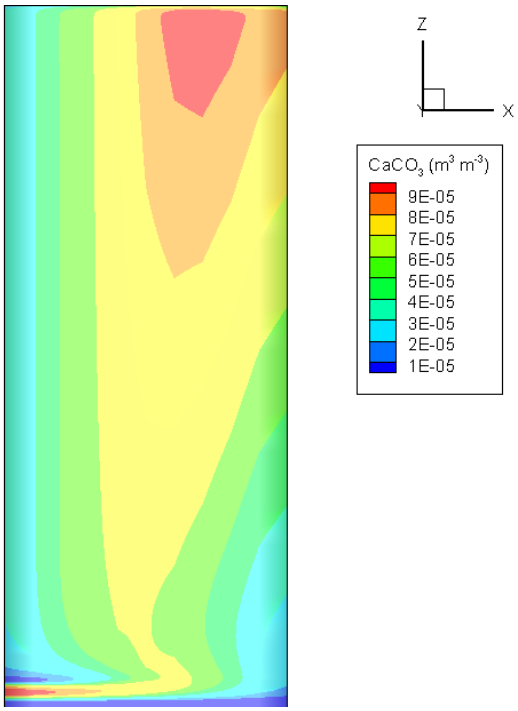

Figure 55: $CaCO_3$ concentration in the column after 10 s

7.11.1 Particle diameter with a side inlet

A simulation with the side inlet was performed with five different solid phases together, of different diameter particles, between 100 and 200 μm. Volumetric inlet concentrations were the same for each phase. The profiles for the different phases at 3s development and at steady state are shown in Figures 56 to 58.

Figure 56 shows the profiles of the different solid phases as they spread vertically up the centre of the column. There is a peak in the solids concentrations for all phases where the jet enters the column, followed by a sharp decline, particularly for the larger diameter particles. These phases have a high lower peak, followed by a large decrease to a minimum, after which the concentration increases to an equilibrium for the remainder of the column in the bulk phase.

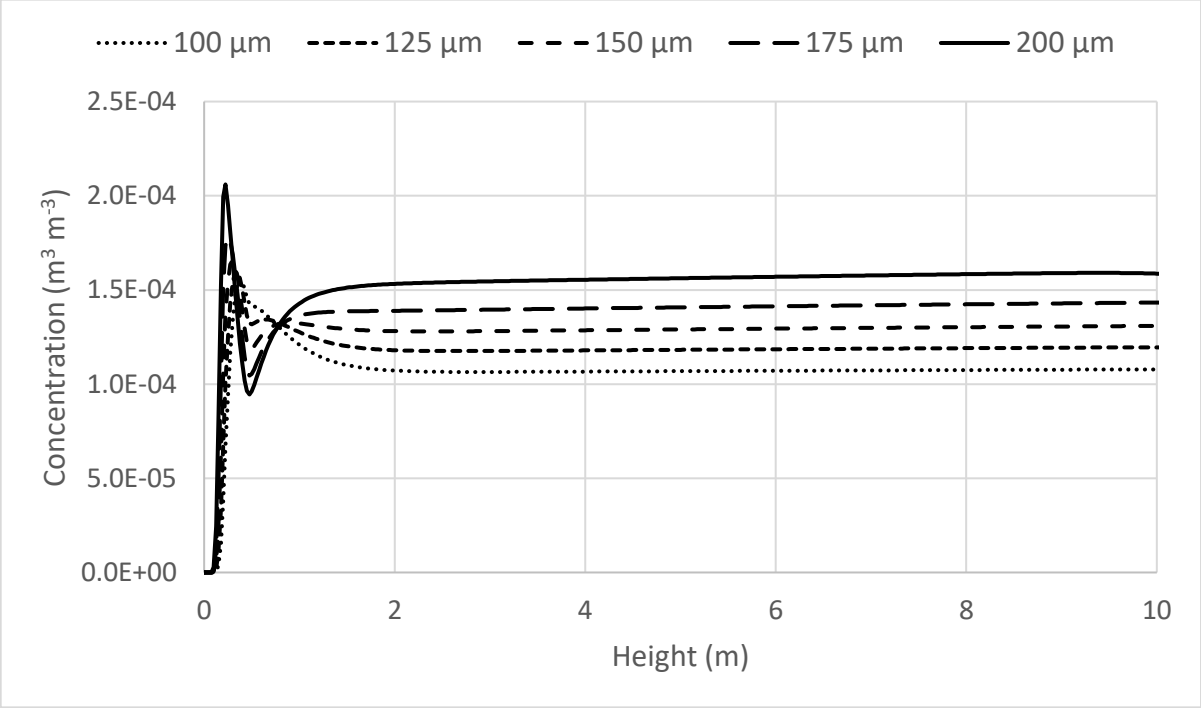

Figure 56: Concentration profiles in the centre of the column for five particle sizes from a side inlet

The smaller diameter particles have a very similar lower peak, but a smoother transition to the leaner part of the column, with the 100 μm diameter solids only displaying a maximum, with a minimum value attained in the lean section.

Figures 57 and 58 show the horizontal concentration profiles at a height of 3 m after 1 s and 10 s respectively. After 1 s, the bulk of the solids are present only on the right-hand side, with the smaller particles dominant, as the larger ones have yet to reach this height. After 10 s, steady state has been attained and the point of peak concentration has shifted to the left, and the larger particles are now dominant. The higher diameter particles are also more spread out across the column, with a peak concentration reached at 0.07 m, while the smaller particles, being fluidised earlier, have a peak concentration 0.03 m from the side inlet.

The heavier and/or higher diameter particles shoot over to the far side of the column, predominantly due to two reasons:

1) Higher momentum at the inlet due to their higher mass while entering at the same velocity as the other phases
2) Easier fluidisation of the smaller diameter particles due to their lower slip velocity, resulting in these phases being attaining a vertical velocity earlier

The mixture velocity also develops as the simulation proceeds: after 1 s, the combination of upward and side stream result in an upward velocity of 3.1 m s^{-1} on the left, from 2.91 m s^{-1} for the gas stream moving up the right-hand side with almost all the solids being low diameter particles on the right-hand side.

At steady state, with the solid flow now developed on the left-hand side, the velocity profile has shifted with the highest velocity over on the right at 3.8 m s^{-1}, while the left-hand side is now 2.5 m s^{-1}.

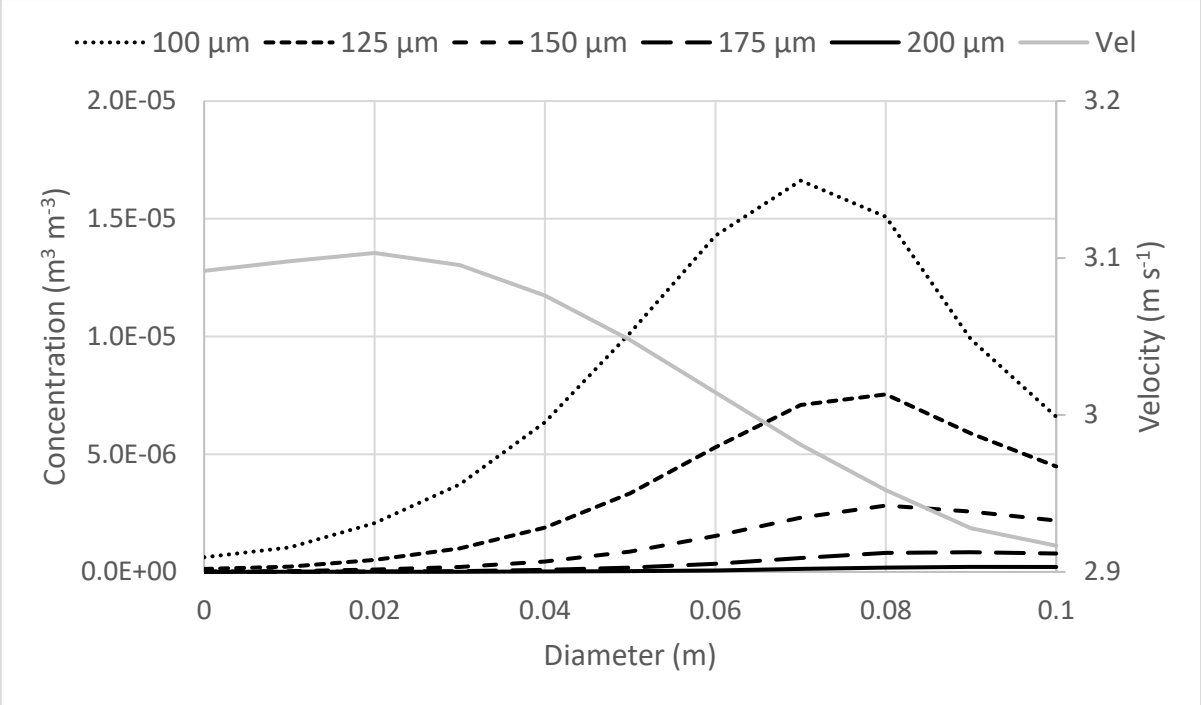

Figure 57: Concentration profiles for the solid phases at 3 m height after 1 s

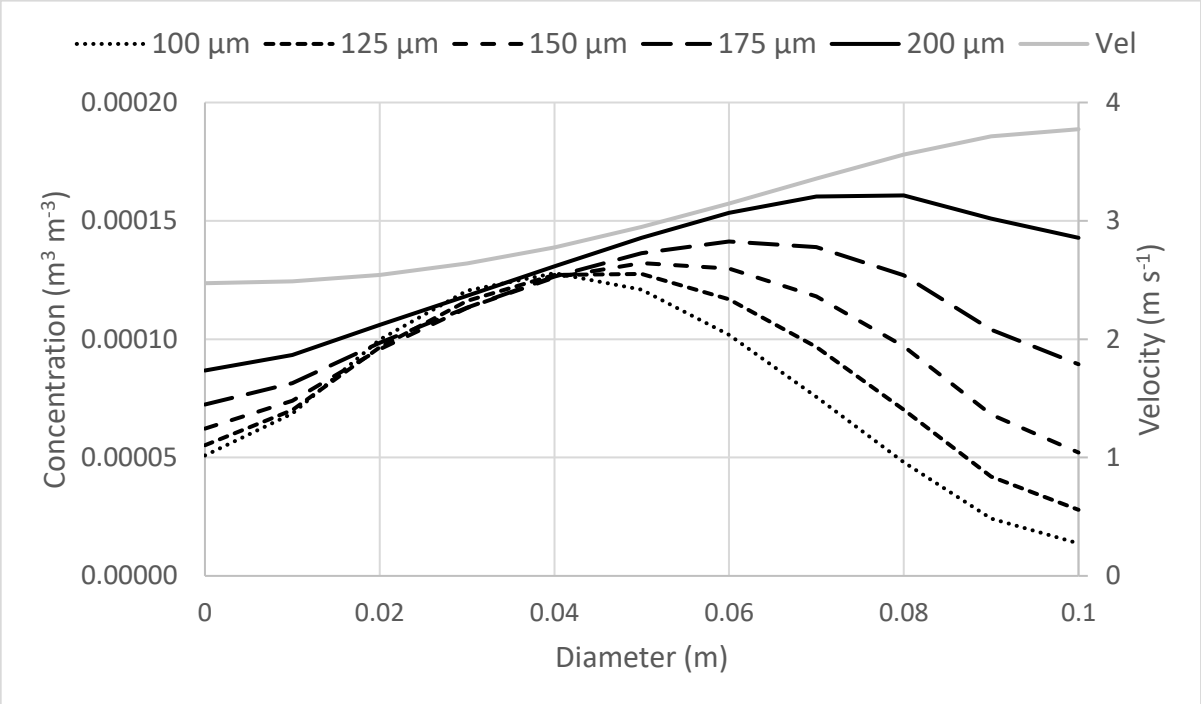

Figure 58: Concentration profiles for the solids phases at 3 m height at steady state

Figure 59 shows the concentration profiles for the solid phases and CO_2 at the centre of the column. After a lower peak at the barrier/inlet all the phases settle into a steady concentration, while the CO_2, reduced by the high solid presence, recovers at the beginning of the steady solid phase and gradually reduces along the remainder of the reactor.

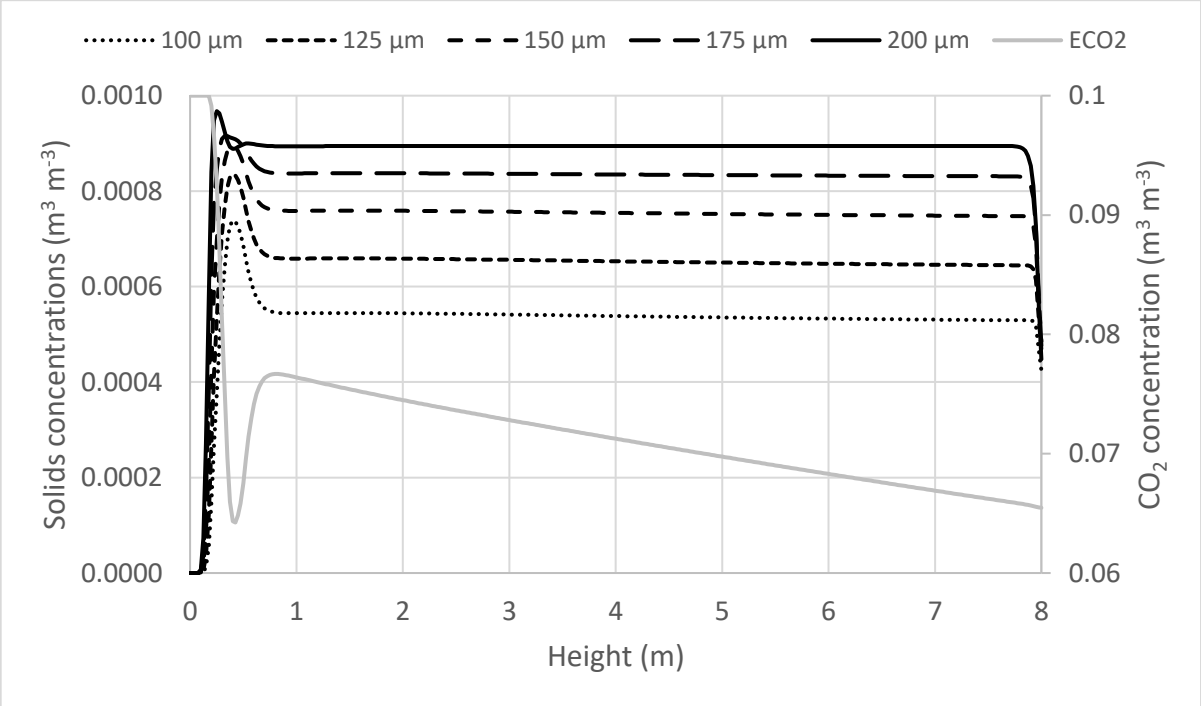

Figure 59: Solid phase and CO_2 concentration profiles for a side inlet

7.12 Mesh dependency

The performance of the model was tested at different mesh densities to see if this would have a considerable impact on the simulation results.

The mesh was varied about the default mesh (20 x 255), reducing resolution to 12 x 153 and increasing it to 28 x 357. The results of these tests are shown in Figures 60 and 61.

Figure 60 shows the velocity profiles for the differently meshed columns. The extent of meshing had its greatest effect on the velocities, with it being particularly noticeable around the lower boundary. Here, the higher density meshes have a greater velocity differential between the centre of the column and the walls, with higher mixture

velocities recorded in the centre (2.24 compared to 2.21 m s^{-1}) and lower at the walls (2 vs 2.05 m s^{-1}). It is also noticeable that the region of reduced velocity around the lower boundary does not extend as far upwards in the higher resolution simulations. The boundary layer is noticeably thinner higher up the column. This because the lower resolution meshes are incapable of capturing the full impact of the walls' effects on the flow.

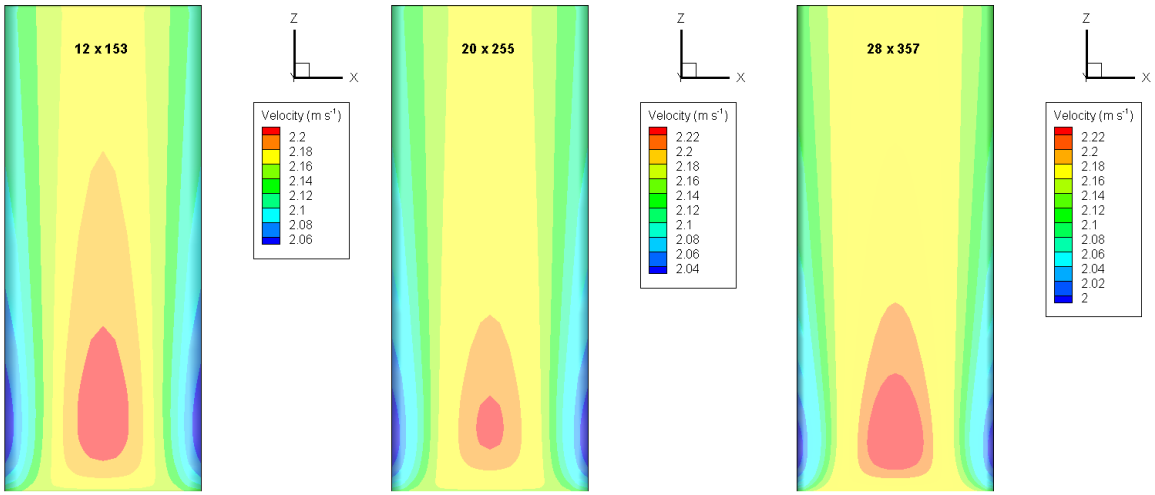

Figure 60: Mixture velocities in the column at different mesh densities

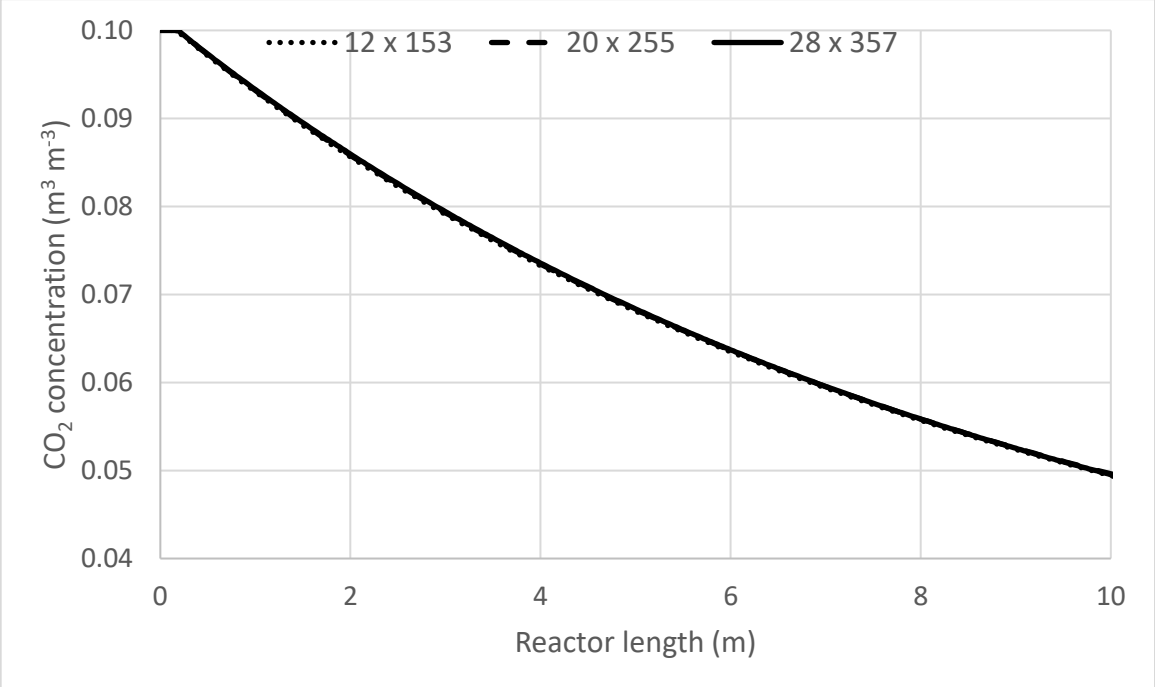

Figure 61: CO_2 concentration profiles at the centre of the column for different mesh densities

Figure 61 shows the CO_2 concentrations through the centre of the column, and the mesh has negligible influence on this, as the reaction mechanism is based on volumetric concentrations, which do not vary much in the centre of the column. These are very similar, suggesting that these mesh resolutions make little difference at this level of cell density.

7.13 Lower boundary

A lower boundary over which the slip velocity was gradually introduced was used in this work to approximate the effects of a lower mesh to prevent the downward flow of particles. It was initially so that below a height of 0.1 no slip velocity was present, and it gradually increased linearly to the standard slip velocity over the next 0.1 m.

This was necessary in some of the earlier experimental setups, and it was decided to investigate the effects of this slip velocity introduction method. As such, two tests were performed: (1) the removal of the introductory section – i.e. the slip velocity was applied instantaneously as the solids move above 0.2 m in height, and (2) the slip velocity was introduced over a longer height, in this case from 0.1 to 0.5 m. Figure 62 shows the effects of these, together with the standard boundary for the lower 3 m of the column.

The most obvious effect of these changes in the lower boundary are the onset of the high solids concentrations. With the default introduction between 0.1 and 0.2 m on the left, a low concentration of solids is observable in a semi-circular area above the lower boundary. The instant introduction of slip velocity in the centre shows a similar pattern with a more noticeable transition at the lower border. The gentle introduction between 0.1 and 0.5 m on the right has a more gradual increase, and the semi-circle is smaller in area.

All the simulations have an inlet solid phase at 0.0003 $m^3\ m^{-3}$ at the bottom, which gradually increases in concentration as the CaO reacts with the CO_2 as it moves up the column. Figures 63 and 64 show the concentration profiles of the solids at the centre of

the column and the wall, respectively, and Figure 65 shows the CO_2 profile at the column centre.

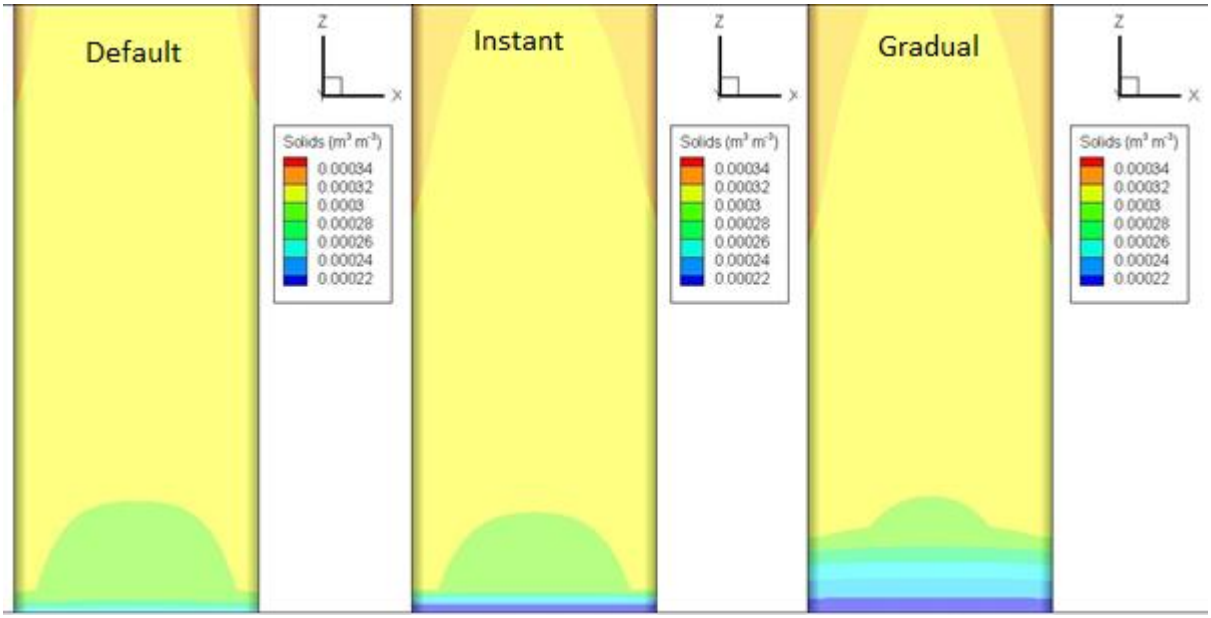

Figure 62: Effect of varying the extent of the lower boundary on the lower 3m of the column

The lower part of the profiles are different for each scenario, with the default starting first at 0.1 m height, being joined by the a vertical line from the instant slip velocity at a height of 0.2 m, with the more gradual barrier reaching the same concentration after a steady climb at 0.4 m. Both the gradual and instant barriers share a similar profile above this, while the default is lower.

At the 0.2 m point, the default column has solids at 2.87×10^{-4} m^3 m^{-3}, the instant 2.48×10^{-4} m^3 m^{-3} and the gradual 2.19×10^{-4} m^3 m^{-3}, which are reductions of 14 and 24 %, respectively.

At the top of the default column, the solids are at 2.41×10^{-4} m^3 m^{-3}, compared to 2.46 for the instant and 2.45×10^{-4} m^3 m^{-3} for the gradual introduction, a difference of 1.5-2 %.

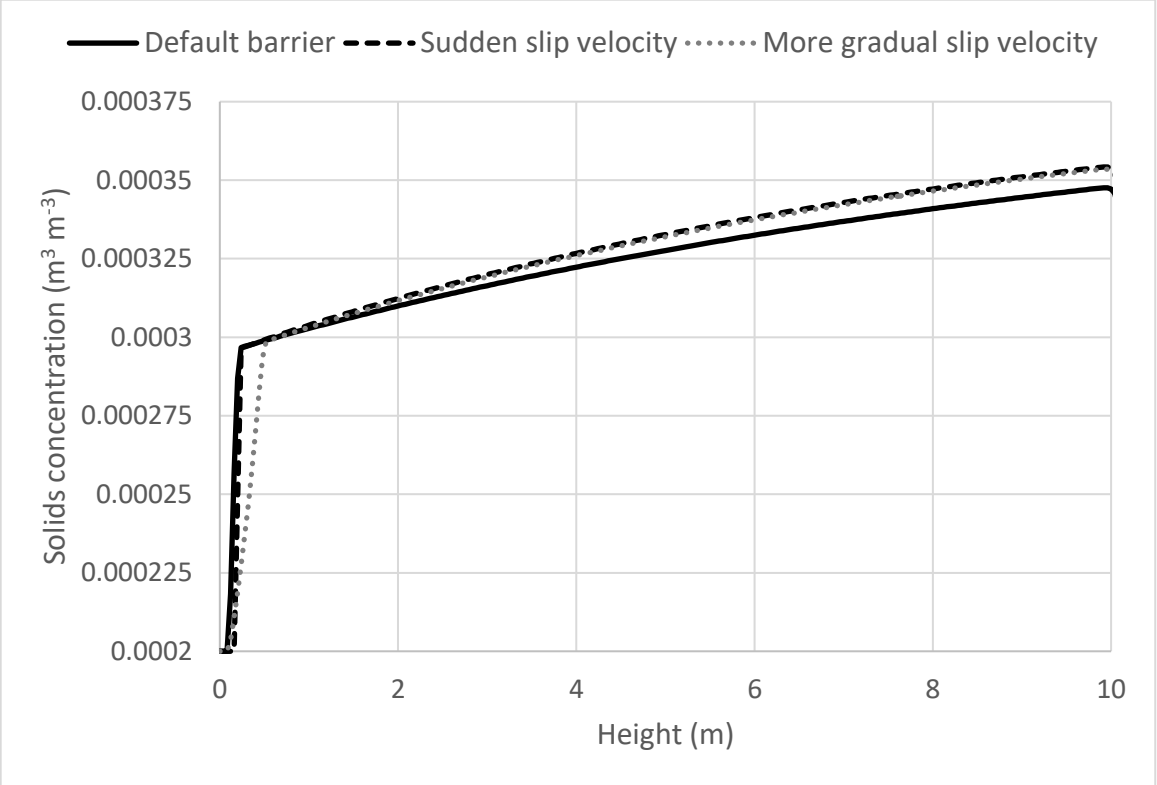

Figure 63: Solids concentration profiles at the centre of the column for the three lower barrier setups

In keeping with the higher solids concentrations, the CO_2 concentrations are lower, at 0.05 m^3 m^{-3}, compared to 0.055 at the exit for the default, which is a 10% better capture for the variants. The walls concentrations follow similar lines as the centre, being 2.43×10^{-4} m^3 m^{-3} for the default and 2.49-2.5×10^{-4} m^3 m^{-3} for the variants, a difference of around 2 %.

Overall, the different lower barriers, produced higher solids profiles up the column and less CO_2, but the standard model had a greater proportion of solids near the bottom. The variants also estimated a higher capture percentage.

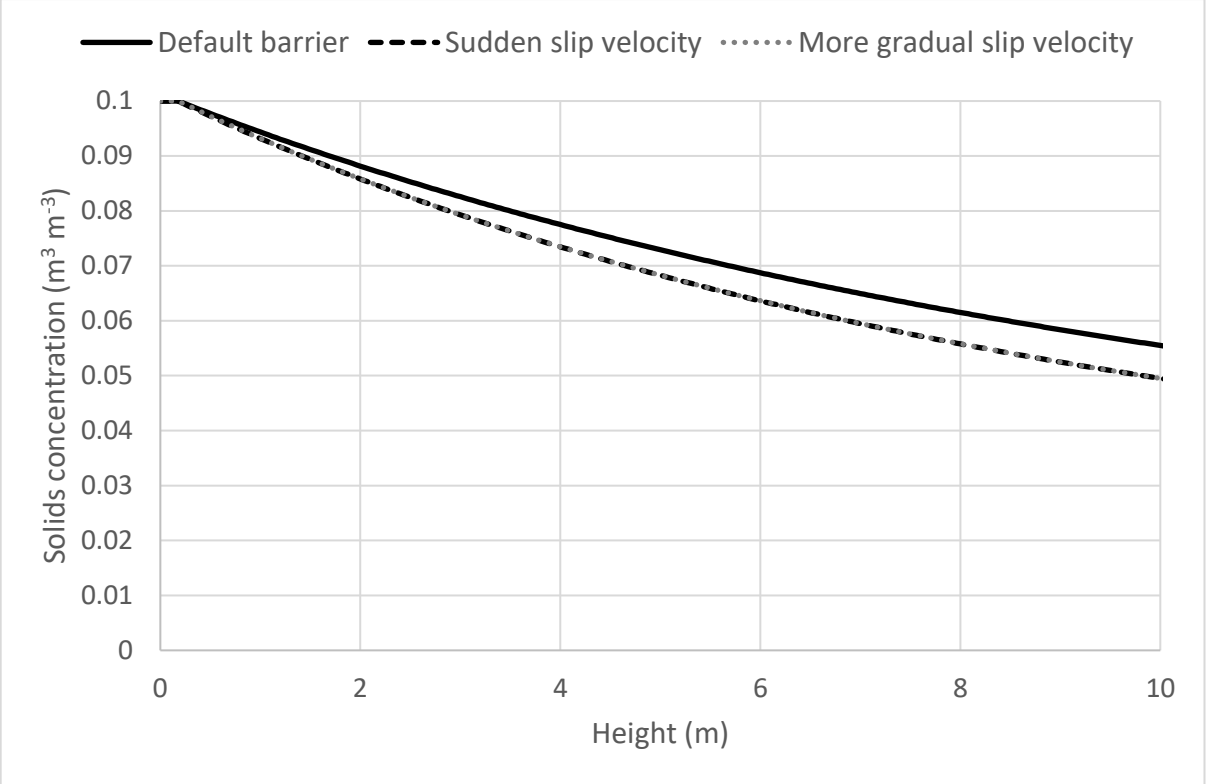

Figure 64: CO_2 profiles at the centre of the column for the three barrier types

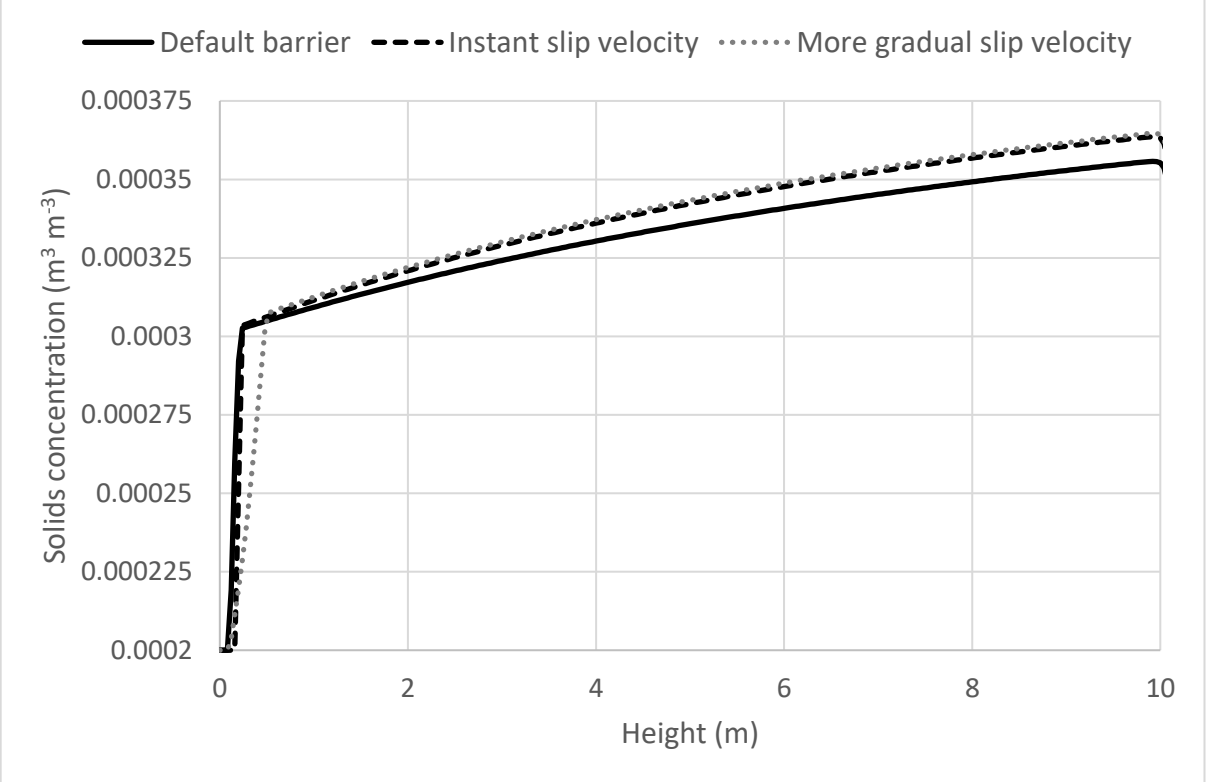

Figure 65: Solids concentrations profiles at the walls for the three lower barrier types

THREE-DIMENSIONAL SIMULATION

8.1 Introduction

After testing in two-dimensions, the model was extended to three dimensions with runs performed for solids entry from both lower and side inlets. It was then used for studies based on work by Molaei [26] for both two and three dimensions and subsequently to assess a carbonation column, based in part on work by Duelli [70, 78] and Unterberger [90] at Stuttgart.

8.2 Three dimensions

The algebraic slip model is a balance between the gravitational and drag forces experienced by solid particles in the vertical direction. As such its extension from two to three dimensions was simple.

The main concerns regarded performing new material balances as the areas and volumes under consideration were now different, and an attempt to incorporate a side inlet, to investigate the effects of the algebraic slip model on flow in other directions and whether it can account for true three-dimensional behaviour.

Simulations were run with inlet solids flow from both below and from a side inlet. This side inlet was set to occupy a 90° arc with a height of 0.2 m to allow a high enough solids flow-rate at low inlet concentrations to balance with the incoming CO_2 flow from the lower inlet, with a velocity less than half of that of the upward velocity and an average residence time of at least 10 s. The inlet concentration of the CaO was chosen so as make the inlet molar flow of CaO to be ten times that of CO_2 from the gas inlet [78].

The bulk of the column above the inlet was based on that in Unterberger [90], who used a 0.071 x 12.4 m high column for their carbonation experiments. Dimensions for the reactor are given in Table 16.

Table 16: Three-dimensional reactor dimensions and boundary conditions

Diameter (m)	0.071
Height (m)	12.4
A_{bottom} (m^2)	0.0040
A_{side} (m^2)	0.0056
u_{bottom} ($m\ s^{-1}$)	2.15
u_{side} ($m\ s^{-1}$)	0.5

To make the column, MBRICK3 was used to create two quarter cylinders, which were connected along a straight edge and then duplicated. An initialisation routine in PHYSICA was used to create an inlet patch on one of the outside faces, with another patch above this for inlet gas to push the solids away from the wall, as with the two-dimensional simulations. The xy profile of the reactor is shown in Figure 66. The location of the side inlet is shown in orange highlighting on the left.

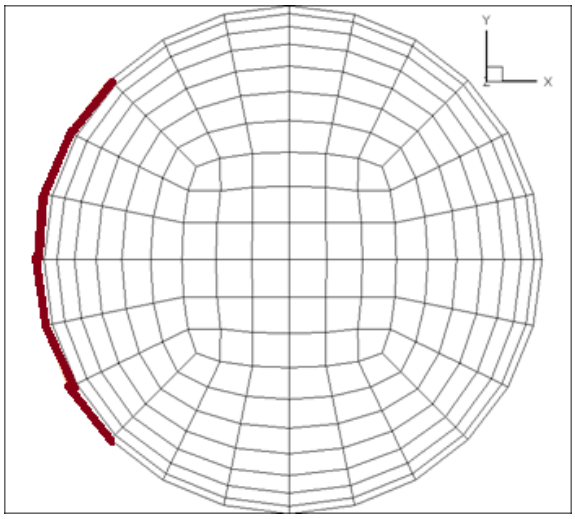

Figure 66: XY profile of the three-dimensional column

8.2.1 Lower solid inlet

For a lower solid inlet (i.e. flow from the bottom of the column), the incoming mixture velocity was set to above the minimum fluidisation velocity to give an average

residence time of around 10 s for the five solid phases. These inlet boundary conditions are shown in Table 17. The inlet enthalpy was set to give a temperature of 923 K.

Table 17: Inlet boundary conditions

Velocity (m s^{-1})	2.15
Energy (kJ)	927
Solids (m^3 m^{-3})	0.00005

The behaviour of the mixture in three dimensions is very similar to that was observed for two. The results of this test are shown in Figure 67 to 69.

Figure 67 shows the concentration profiles for the different species in the mixture. Interestingly, all solid concentrations are increasing in this simulation as they move up the centre of the column. This is because, as the CO_2 is consumed, the volume fraction consisting solely of gas is reduced. The CO_2 concentration is decreasing steadily up the column from 0.1 down to 0.04.

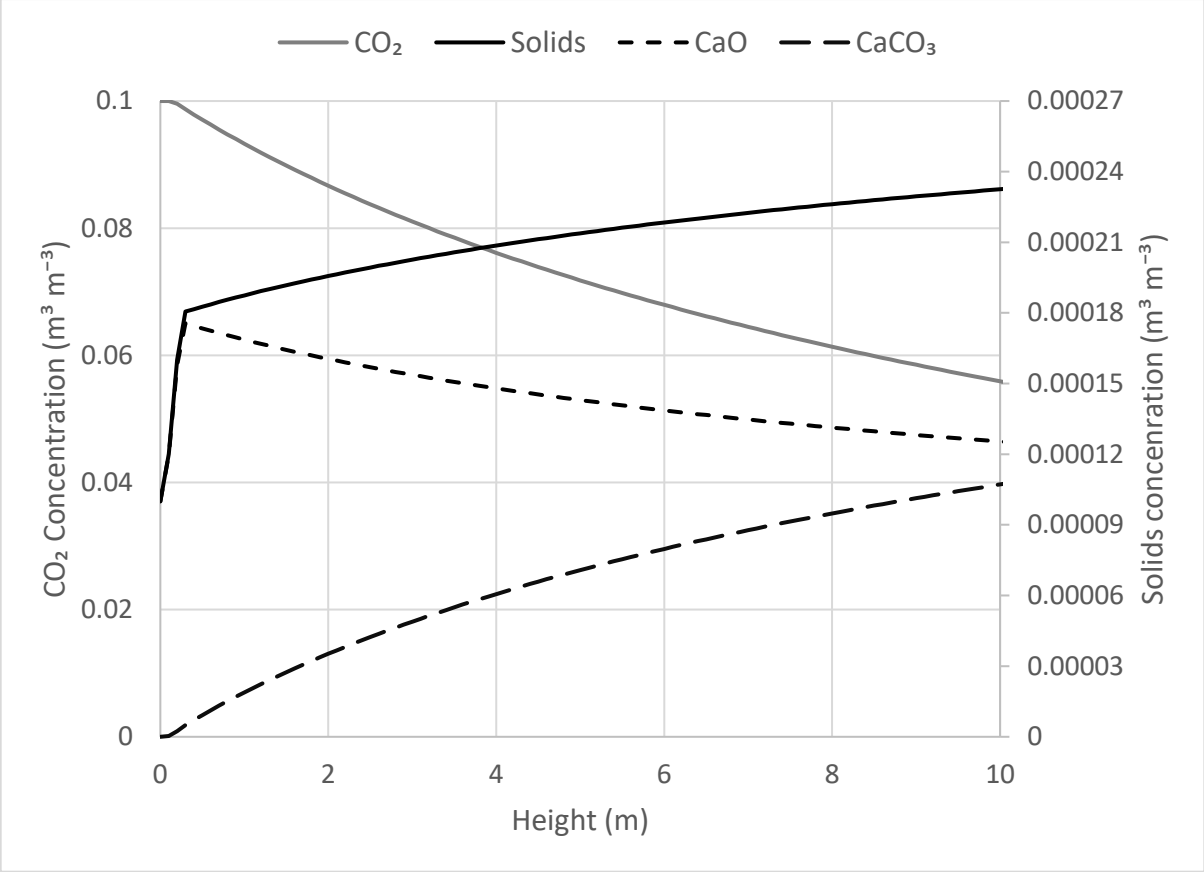

Figure 67: Concentration profiles through the centre of the 3D reactor

Figure 68 shows the concentrations profiles at a height of 3 m, which is 2.6 m above the point at which the slip velocity is activated. At this point, the velocity is greatest through the centre of the column at 3.4 m s^{-1} and is almost 0 m s^{-1} at the edge. The solids concentration is very low at the sides, peaking near the edge on both sides declining slightly and being even over the centre of the column. The smallest diameter particles are carried up more at the sides but have a lower concentration in the column overall. This suggests their slip velocity is less than the gas velocity in the boundary layer close to the wall.

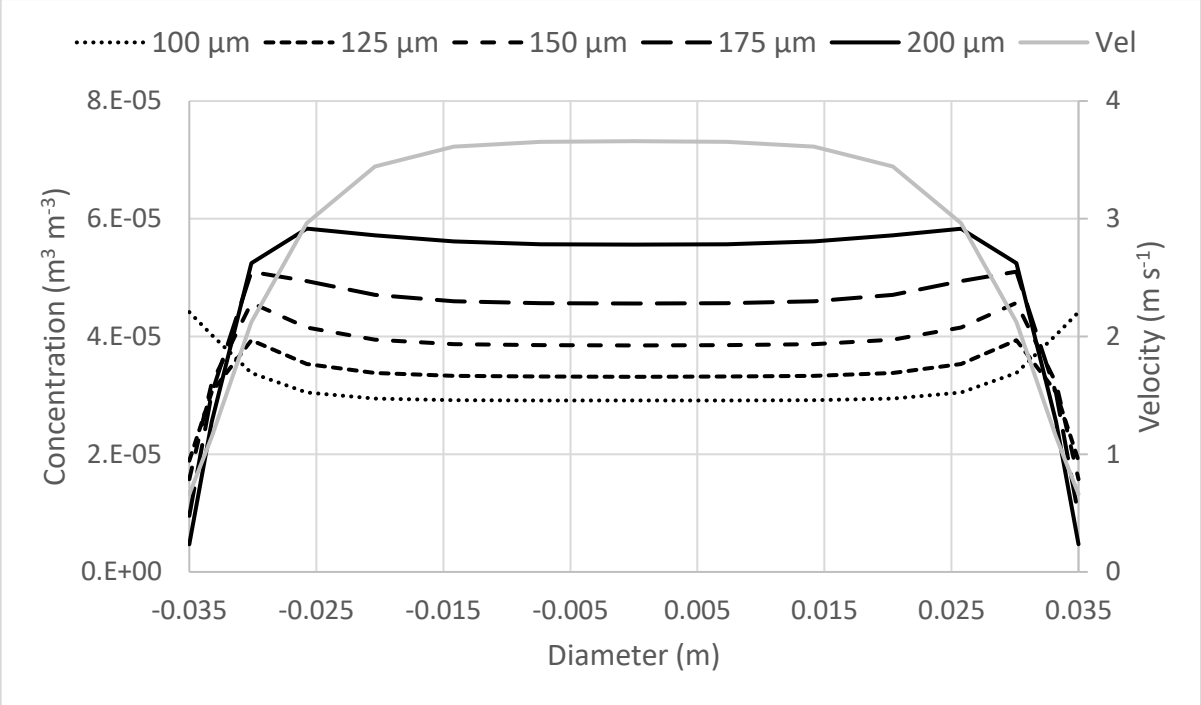

Figure 68: Concentration profile at z=3 m for a 3D column with a lower solids inlet

Figure 68 bears similarities to Figure 46, for solid concentrations and mixture velocity in two dimensions, with a rounded velocity profile, and similar centre profiles for the solids, although here most solid concentrations drop to 0 at the wall, whereas in Figure 46 these are maximised at the wall.

Figure 69 shows horizontal slices through the carbonator at different heights displaying the total of the various phase concentrations. The solids concentrate at the walls, as suggested by Figure 68 for the smaller particles, with the gas reacting more quickly near the walls, which would be expected with more small diameter particles here.

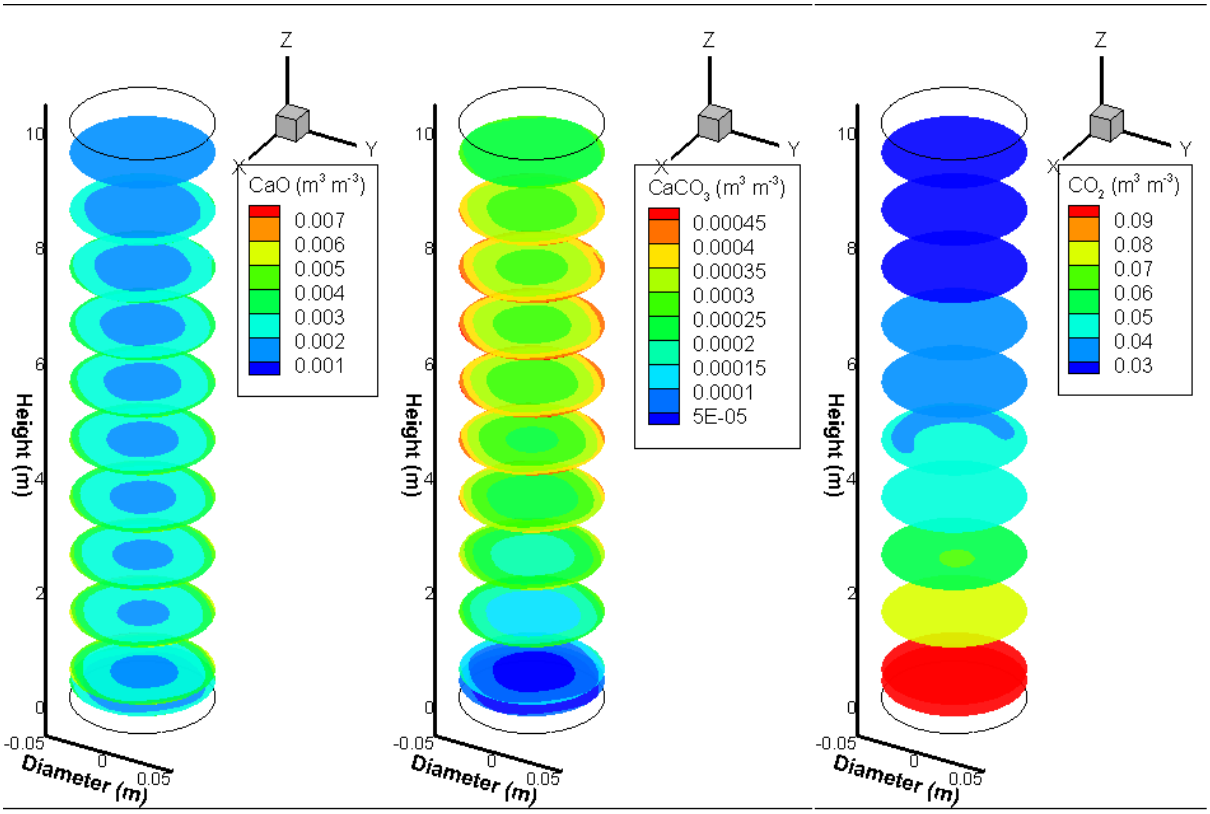

Figure 69: Slices of a 3D column with solids inlet flow from the bottom

The lowest slice in the diagrams, at 0.4 m height, that is not regularly placed, represents the lower barrier, above which the slip velocity is initiated and below which they travel at the full mixture velocity. The lower edge of the solid inlet is located at this point.

The levels of CaO decrease slightly from 1.8×10^{-4} to 6×10^{-5} m^3 m^{-3} over the centre of the column, with a reduction to closer to 1×10^{-4} m^3 m^{-3} around the edge. The CO_2 reduces steadily over the length of the reactor, but a higher level of CO_2 is retained in the centre.

8.2.2 Side inlet

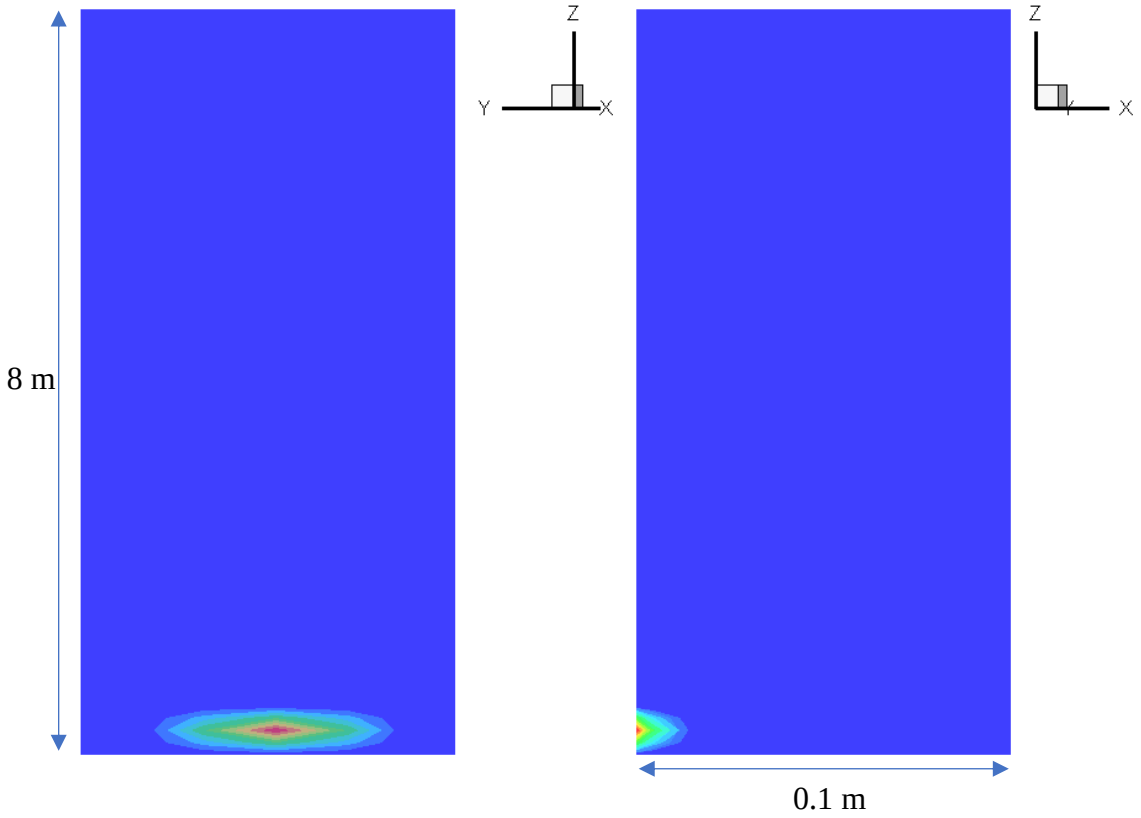

Figure 70: Typical side inlet for a three-dimensional column

A series of experiments were done with the three-dimensional mesh using a side inlet, as shown in Figure 70.

For the side inlet experiments, an incoming flow at 0.45 m s^{-1} introduced CaO solid phases with a combined concentration of $5x10^{-4}$ m^3 m^{-3} with an associated energy stream of 840 kJ kg^{-1}. The initial energy in the system was 927 kJ kg^{-1}. The solids stream entered 0.2 m above base of the column with a height of 0.1 m and an arc of 0.05 m.

As before, the solid phases take the form of a jet upon entry to the reactor, as was seen before in Figure 52, and occupy the centre of the reactor, but are not present in high concentrations at the edges. This leads to the higher concentrations up the side of the reactor above the inlet shown in Figure 71 in contrast to the lower more uniform levels in Figure 68 where the powder and gas are all fully mixed upon entry to the reactor. The CO_2 capture is also reduced due to this reduction in mixing, entering the column at

a volume fraction of 0.1, but leaving to be recycled back to the column or released to atmosphere at a volume fraction of 0.056 m^3 m^{-3}, which is a 44% reduction.

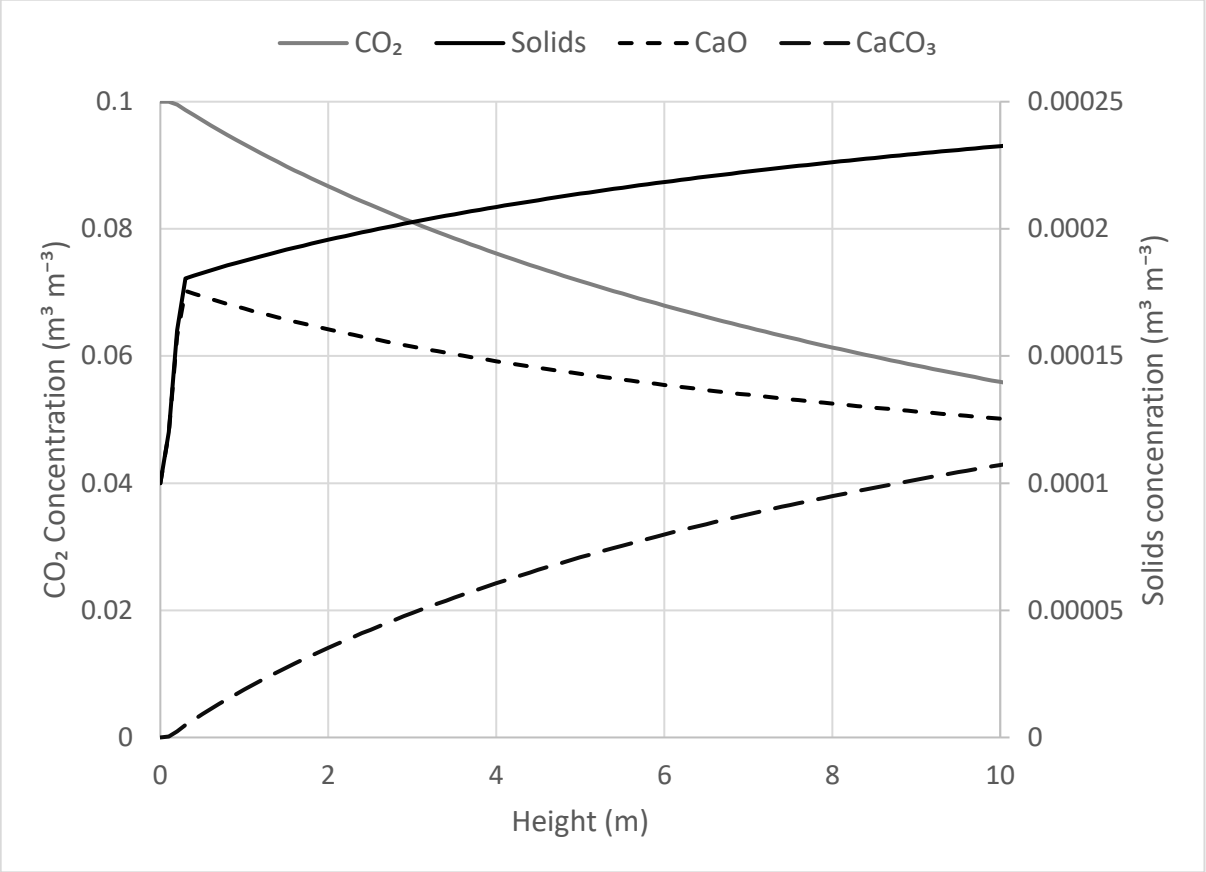

Figure 71: Concentration profiles at the centre of a 3D column with a solids side inlet

A concentration profile at 3 m is shown in Figure 72. The velocity overall is much greater away from the solids inlet, being closer to almost 7 m s^{-1} on the right, where the solids concentrations is low. The solid peak on the left is less than a third of the lower inlet, at $1.8x10^{-5}$, rather than $6x10^{-5}$ m^3 m^{-3}, despite being balanced to be the same at the inlet. The levels of all but the smallest diameter particles at the wall are very low, with only the 100 μm phase fluidised at the wall, despite the high velocities over the rest of the column, much as with the two-dimensional simulations and with the lower solids inlet.

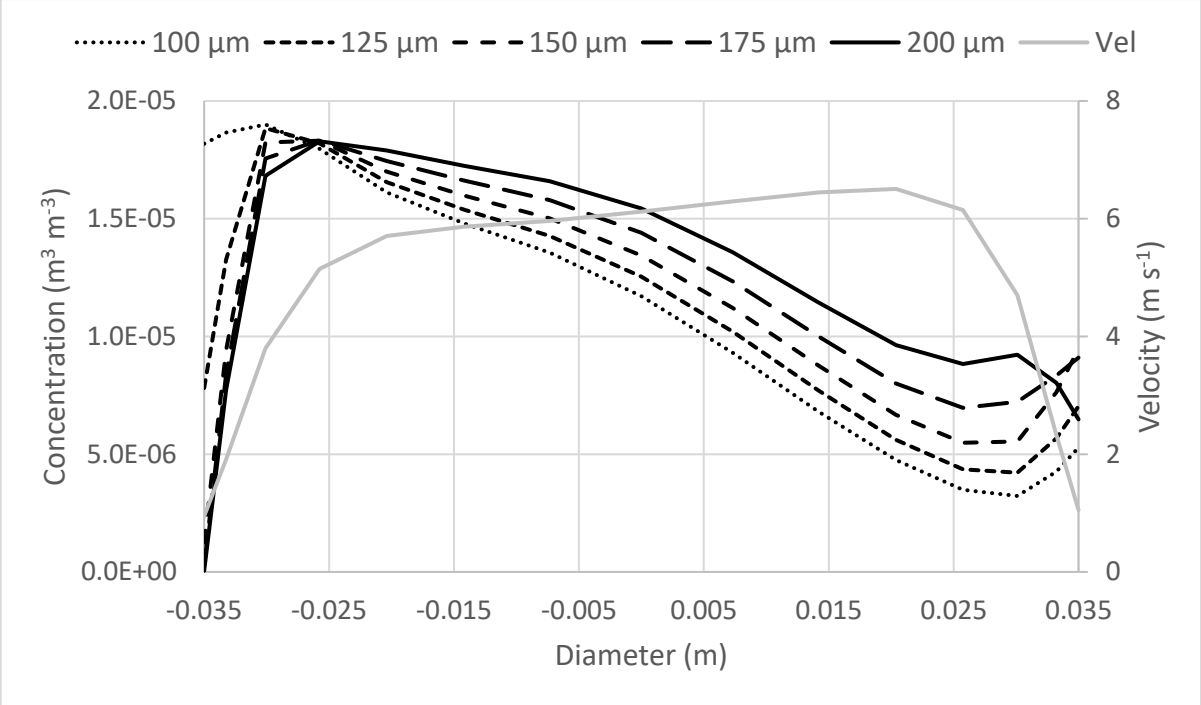

Figure 72: Concentration profiles and mixture velocity at 3m height at steady state

The three-dimensional slices in Figure 73 show the inlet CaO occupying nearly half of the column at the solids inlet, with the other half containing CO_2, with no $CaCO_3$ present. The CaO moves up the column, while a ring of $CaCO_3$ forms around a central core of CaO. The CO_2 spreads across the column and reduces in concentration without ever penetrating the strong CaO core, whilst the $CaCO_3$ forms mostly around the edges of the reactor, encroaching inwards as it is pushed upwards.

As before, the lowest slice is at the lower boundary at 0.4 m, above which the solids enter.

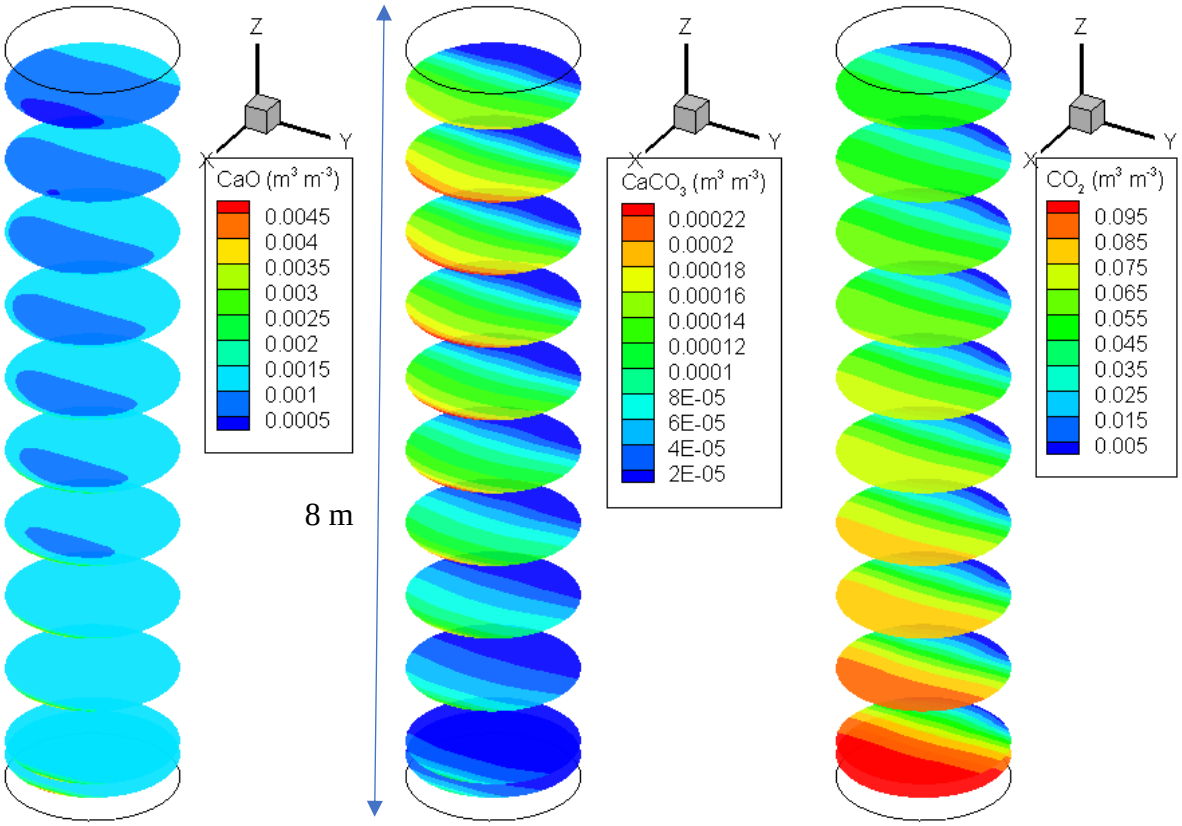

Figure 73: Slices of a three-dimensional column with solids flow from a side inlet

8.3 Molaei

A similar, three dimensional column was used to replicate work by Molaei [26]. He used a Lagrangian model to simulate a dilute flow of Calcium Oxide particles between 100 and 200 μm diameter in number of scenarios, including an expanding column. In this case, work with a cylindrical 0.1 x 8 m column was chosen, due to its relative simplicity and the ease of extending the work to three-dimensions. Molaei's methodology is explained in more detail in Section 4.4.

The reactor and solid phase properties used by Molaei are shown in Table 18.

Table 18: Initial and boundary conditions for tests based on Molaei [26]

Description	Value
Particles	
Particle density (kg m^{-3})	3340
Particle diameter (μm)	$\mathbf{100-200}$
Particles sphericity	1.0
Fluxes	
Gs: Solid mass flux (kg.m^{-2} s^{-1})	0.064-1.0
Gg: Gas inlet mass flux (kg.m^{-2} s^{-1})	0.84-1.3
Initial Parameters	
CO_2 volume fraction	0.1
Gas initial temperature (°C)	650
Geometry	
Diameter of the reactor (m)	0.1
Height of the reactor (m)	8.0
Operating Conditions	
Carbonator Temperature (°C)	650-660
Gas inlet velocity (m s^{-1})	2.15-3.3
Outlet pressure (kPa)	101.03

8.3.1 Experiments with a lower inlet

Simulations were first performed with a lower inlet mixture velocity of 2.15 m s^{-1} with solids and gases both entering from below at uniform concentrations across the column. The highest slip velocity of the phases present here is for CaO at 200 μm diameter which is -1.76 m s^{-1} in a dilute flow. The column initially contained only air at 923 K. The solids flows were converted to equivalent volume fractions of $3x10^{-4}$ m^3 m^{-3} by assuming a uniform distribution at their regular densities (3340 kg m^{-3} of CaO powder, 2710 kg m^{-3} of $CaCO_3$ powder).

After 5 s, the solids concentration profiles can be seen in Figure 74. At this early stage of fluidisation, the solid phases are all being suspended, but the higher diameter

particles have yet to reach as high as the smaller. They are also present in larger concentrations in due to their higher residence times.

At this stage, there is the appearance of a dense phase at the bottom of the column, which is full of the heavy solids, and a lighter phase higher up, where those with a shorter residence time are more spread out.

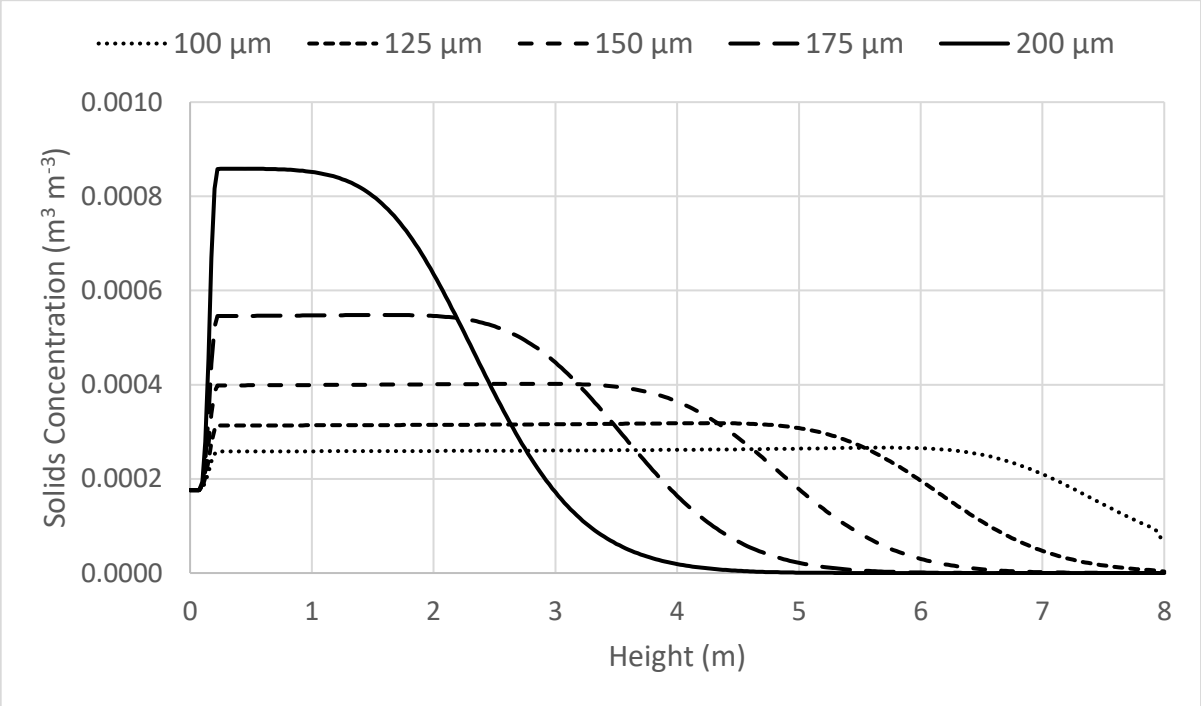

Figure 74: Molaei reactor after 5 s

After 20 s all the phases are fluidised and are being transported from the column. Those with a longer residence time are present at higher concentrations throughout the reactor.

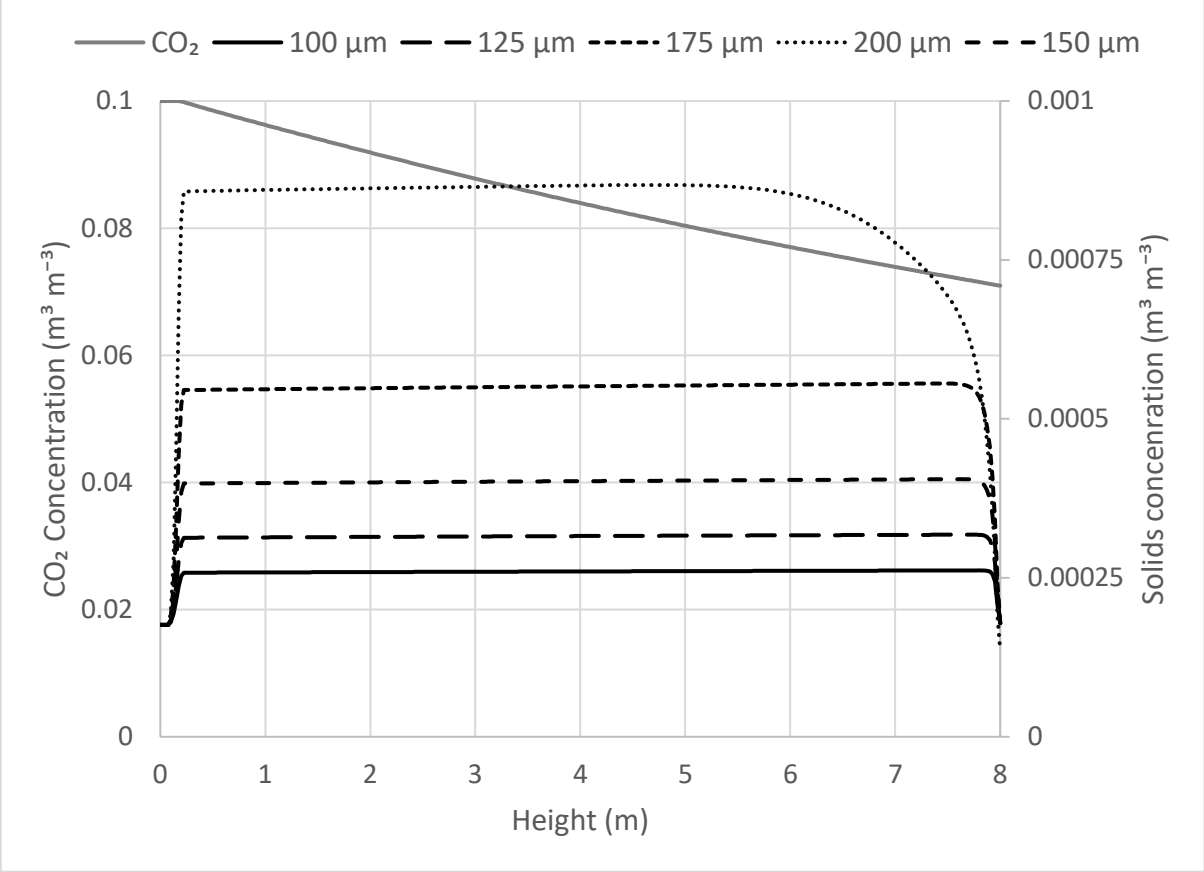

Figure 75: Solid phase concentration in the centre of the column

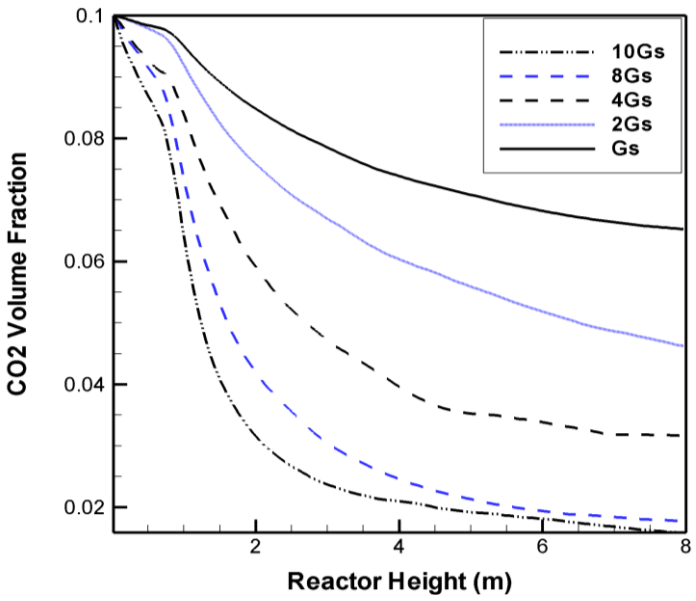

Figure 76: CO_2 removal from Molaei

When comparing the CO_2 removal rate from these experiments with those of Molaei [26] in Figure 76, one finds an overall similarity with the least effective flow-rate (Gs), which is the direct equivalent, although the curve here is much flatter, in keeping with the much flatter solids concentration profiles observed in this study.

Due to the lack of upward gas velocity at the walls, the solid concentrations at the edge of the column are higher in the lower echelons. The solid phases with higher slip velocity are also present here in higher concentrations at almost 4:3 times that of the centre for the largest. This is shown in Figure 77.

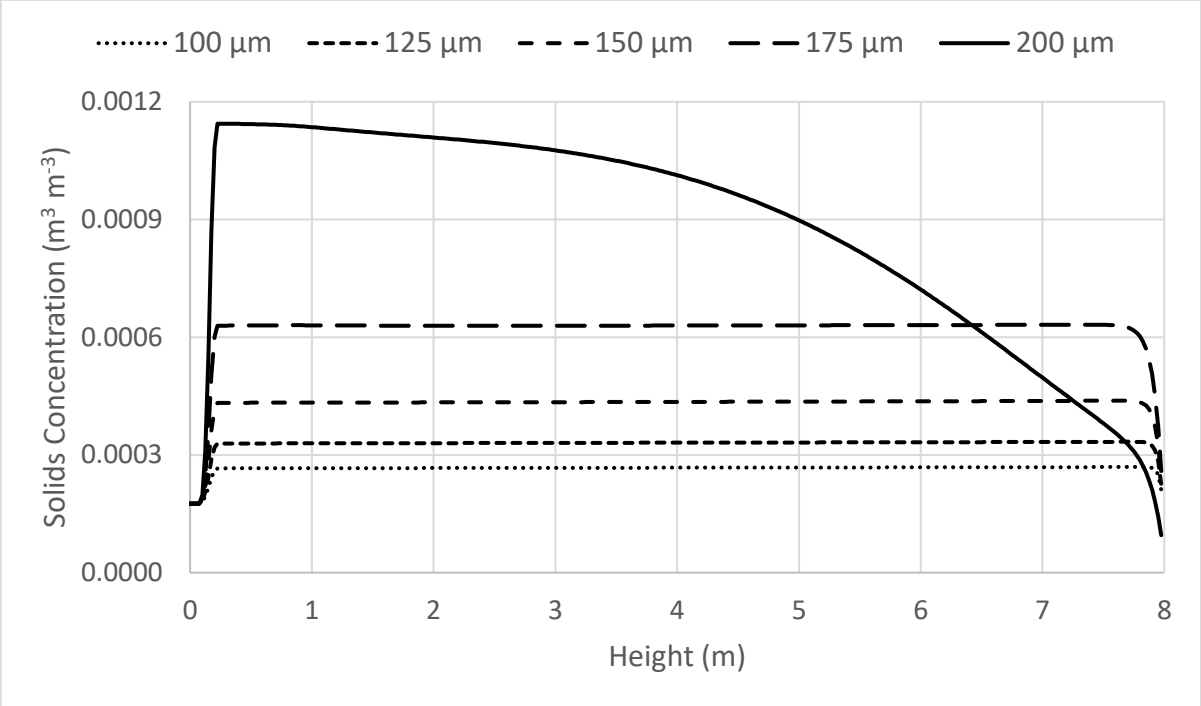

Figure 77: Solid phase concentrations at the walls

A comparison of solid concentration profiles through the centre of the reactor is shown in Figure 78. There are several differences in the central solid profiles, the main one being the lack of a comparative lower peak for the algebraic slip model. The Lagrangian model has a very definite lower peak at the mesh, a reduction and then an increase at the solids inlet before a decrease to an equilibrium level which it remains at for the remainder of the column. The algebraic slip model has a less noticeable lower peak

with a steady reduction. Both models have higher concentrations of the higher diameter particles due to their higher slip velocity and increased residence time.

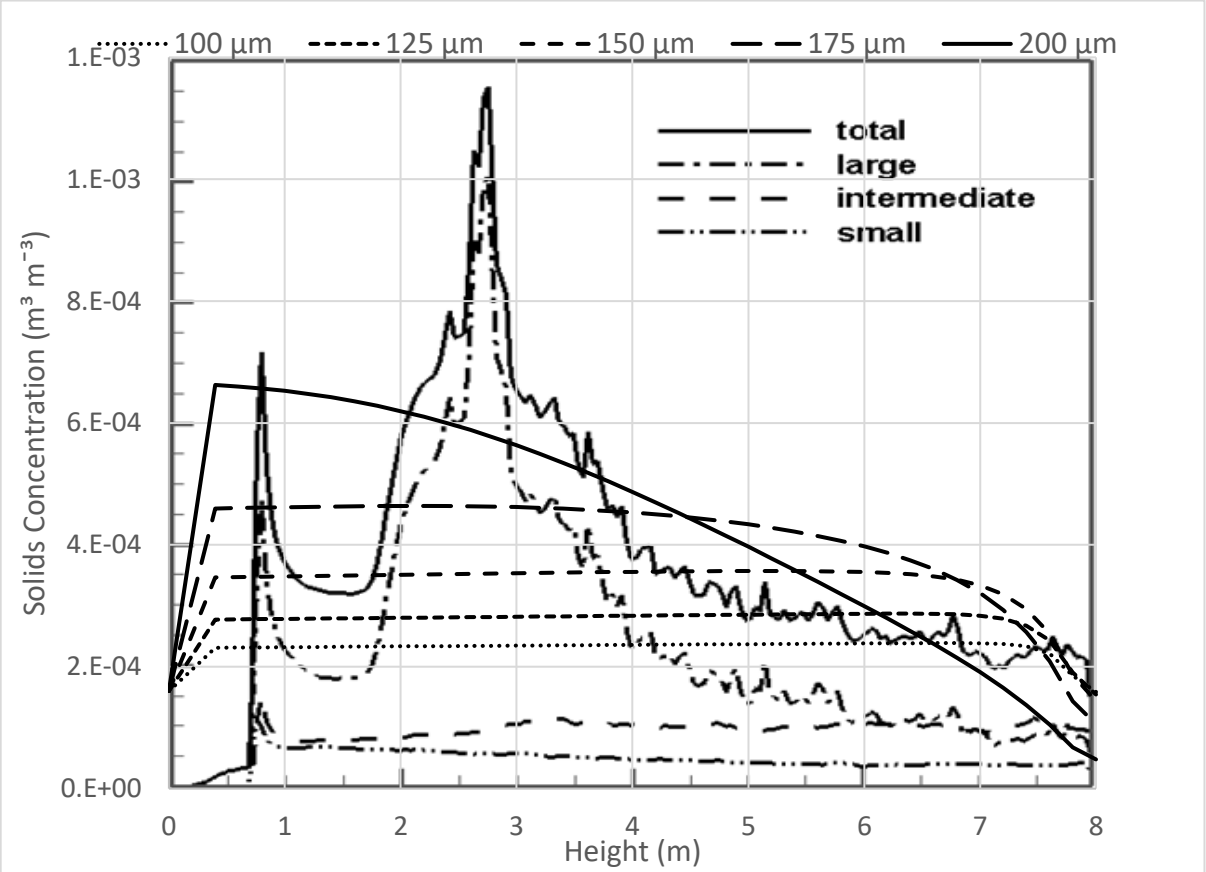

Figure 78: Comparison of solids concentrations in Molaei [26] and algebraic slip model

Molaei modelled the reactor as a bubbling bed, so most of the solids are at higher concentrations nearer the bottom, reducing as they bubble up to the top. The process in this study used a higher velocity - more like pneumatic conveying, so the solids phases follow a more uniform concentration profile as they ascend the reactor.

The location of the inlet is also important. Molaei placed his between 2 and 3 m, whereas in this work, the lower boundary was activated after 0.2 m, and any side inlet was located here also. The inlet/lower barrier locations have higher solids concentrations for both models.

8.3.2 Side inlet

Molaei's [26] column was also simulated using a lower gas inlet with an upward flow of 2.15 m s^{-1} and a side solid phase inlet flow of 0.45 m s^{-1} in the x direction and -0.225 m s^{-1} in the z direction at $1x10^{-3}$ m^3 m^{-3} per phase to see how the algebraic slip model represented initial fluidisation for a three dimensional system.

The solid concentrations along the centre of the column after 5 seconds are shown in Figure 79. This is very similar to the results for Figure 74, for the column with the lower inlet. The phases with the lower slip velocity have reached further up the column in an overall lower concentration than those with higher slip velocities, which have remained closer to the lower barrier. The concentrations at the base of the column will be the overall concentration up the centre of the column once equilibrium has been achieved.

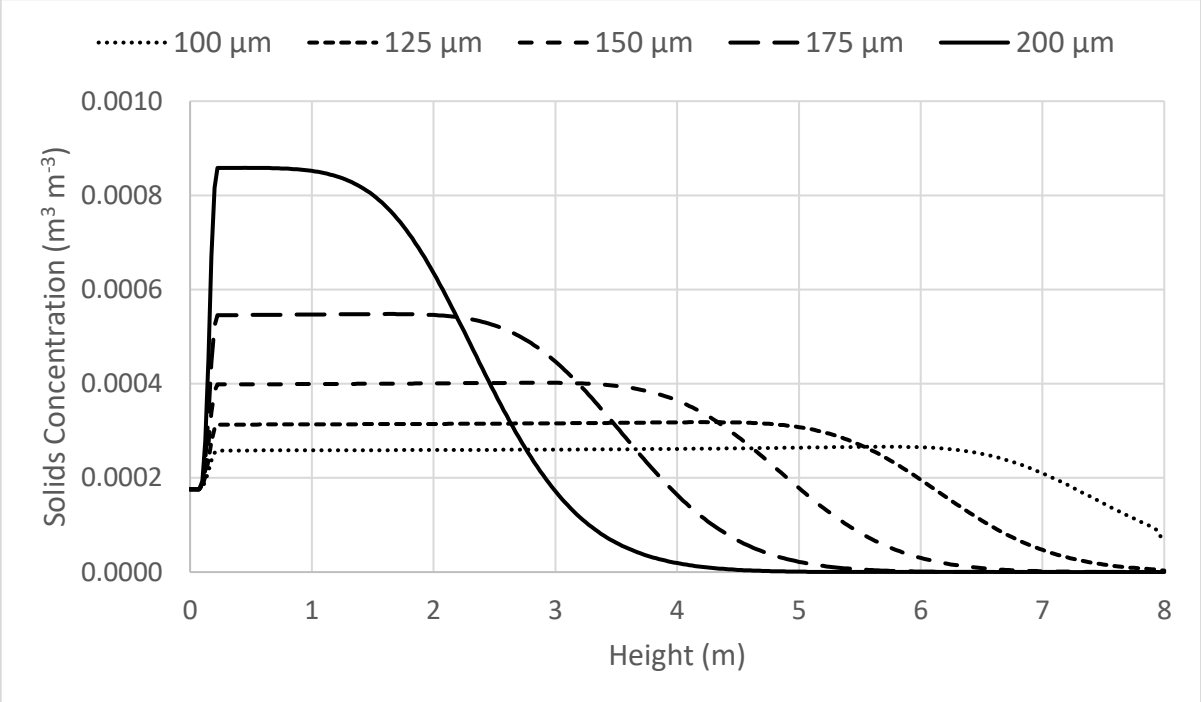

Figure 79: Volumetric solid phase concentrations in the column centre after 5 s

Figure 80 shows the concentrations in the centre after 20 s. Equilibrium has been achieved, and all phases have reached the top of the reactor through the centre. In contrast to Figure 75 for solid flow from below, there remains a peak at the centre

corresponding to the solid inlet jet, where the solid phases collect as they are fired into the column and cannot move downwards. This ‘dense’ phase lasts only for a fraction of a metre before the concentrations lower to a steady level, related to the residence time and slip velocity, which is consistent along the remainder of the column length.

The CO_2 concentration drops off from 0.1 to 0.065 as the gas encounters the side inlet jet, before recovering to 0.076 and then decreasing steadily across the remainder of the column to 0.065. Comparison to Figure 75 and 76 shows a similar beginning and end, but a different profile. The dramatic reduction in CO_2 concentration at the solid inlet corresponds with the higher solid flow rates in Figure 76, but the subsequent recovery and steadier reduction in CO_2 levels and uniform solid profiles is in keeping with Figure 75.

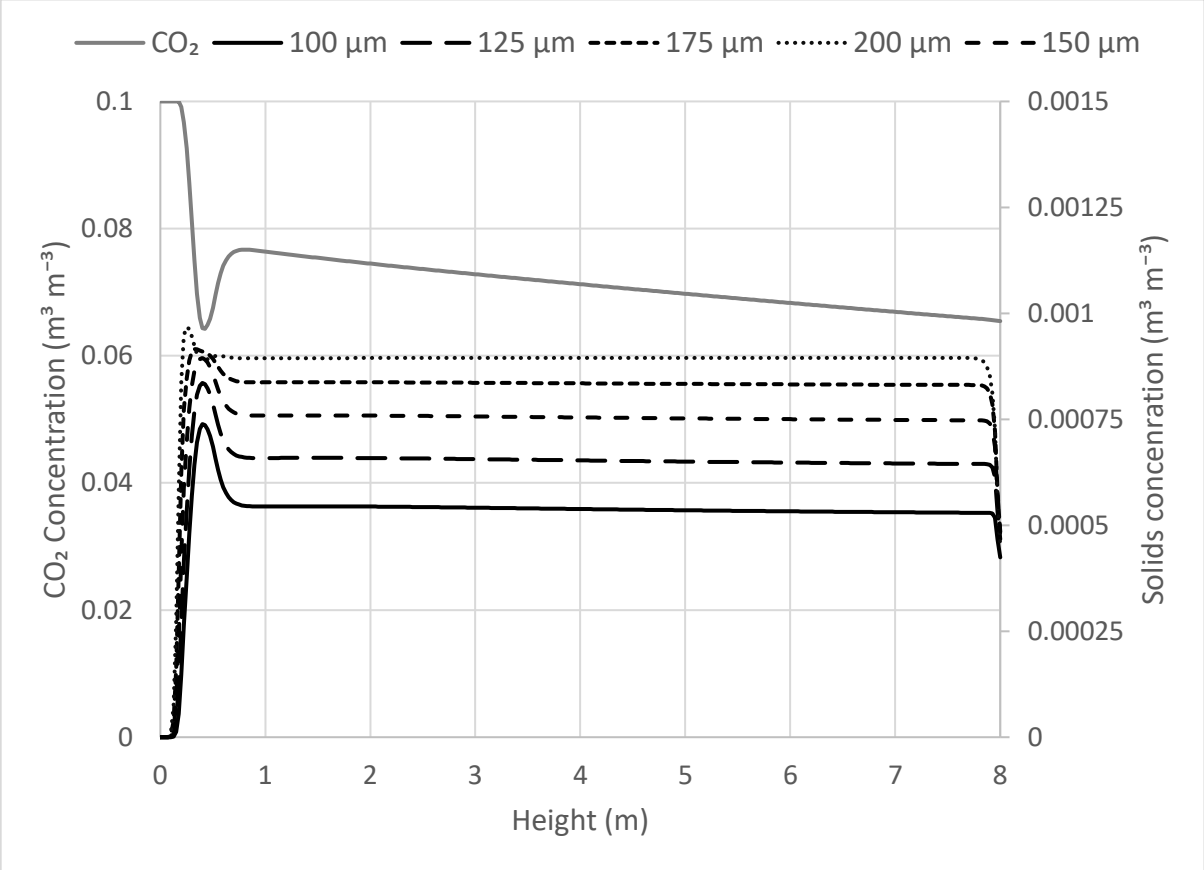

Figure 80: Volumetric solid phase concentrations in the column centre after 20 s

The concentration profiles at the near wall in Figure 81 consist almost solely of the high-density jet as it enters, and above this there is an area of low concentration section next to the wall. All phases are 0.011 m^3 m^{-3} at the jet and 3.5x10^{-5} m^3 m^{-3} above this. This is an artefact of the boundary conditions and the assumption that convection will dominate over diffusion.

In comparison to the solids profile from Molaei [26] in Figure 82, where there is a steady reduction in concentrations as the solids ascend the column, in this work there is a lower peak concentration and then a uniform level above this. In this, the powder has been fully transported by pneumatic conveying. This will lead to a more rapid reduction in CO_2 concentration for Molaei as the gases pass through the concentrated section, before reaching the uniform end value, whereas in this model the reduction should be more steady, as the CO_2 will be exposed to a lower CaO concentration, but for longer. It will also lead to shorter residence times as the mixture will have a higher overall velocity.

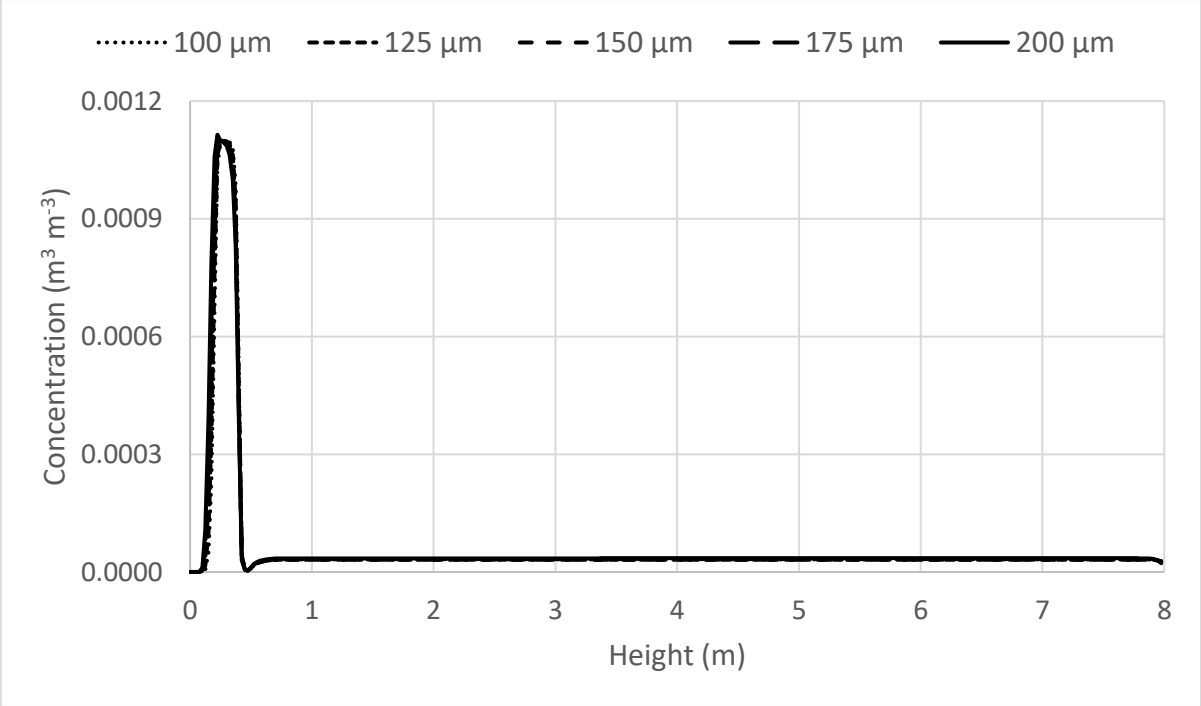

Figure 81: Solids concentrations at the wall of the reactor for a side inlet

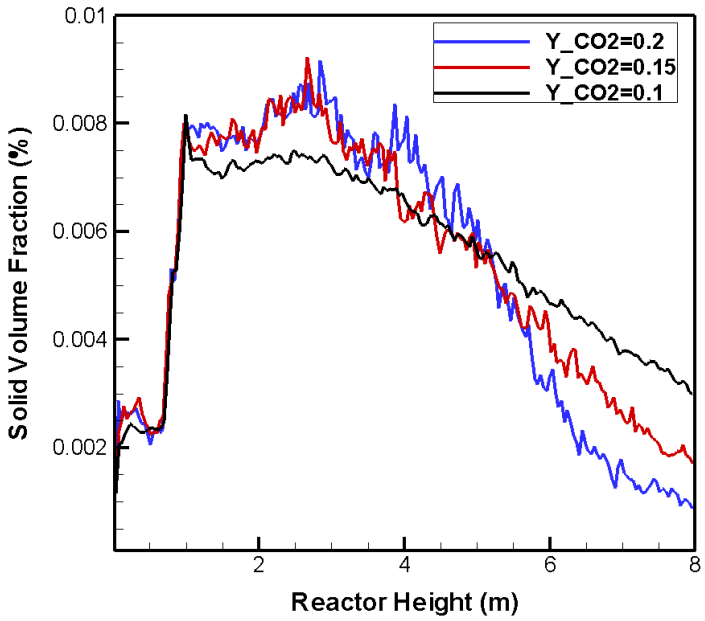

Figure 82: Solids concentration profiles for different CO_2 levels from Molaei

8.4 Molaei with lower gas density

8.4.1 Two dimensional

Some experiments based on Molaei's [26] work were performed in two dimensions with the reduced densities from Equations (118) and (119).

Molaei modelled the column as a bubbling bed using a Lagrangian formulation which allowed the particles residence times up to 30 s. This model is more akin to pneumatic conveying, as it required convection to the dominant vector of transportation, so the residence times will be less: in the region of 10 s. This will lead to lower particle conversions for the same inlet solid concentrations, as seen above.

In order to increase the reaction rates, the mixture velocity was lowered to 1 m s^{-1}, but with gas:solid ratios based on the ratio of the lower levels used by Molaei [26], and the residence time kept to 10 s. Particles with 100 μm diameter were used.

The calculated equivalent flowrates used are given in Table 19. The mesh was also altered slightly from 10 x 400 to 20 x 270 cells.

Table 19: Equivalent values used by Molaei [26] and in this work

	Molaei		This work	
	Mass flux (kg m^{-2} s^{-1})	u_{gas} (m s^{-1})	Volume flux (m^3 m^{-2} s^{-1})	u_{mix} (m s^{-1})
Solid mass flow	0.064	2.15	0.00015	1.1
Gas mass flow	0.84		0.1	

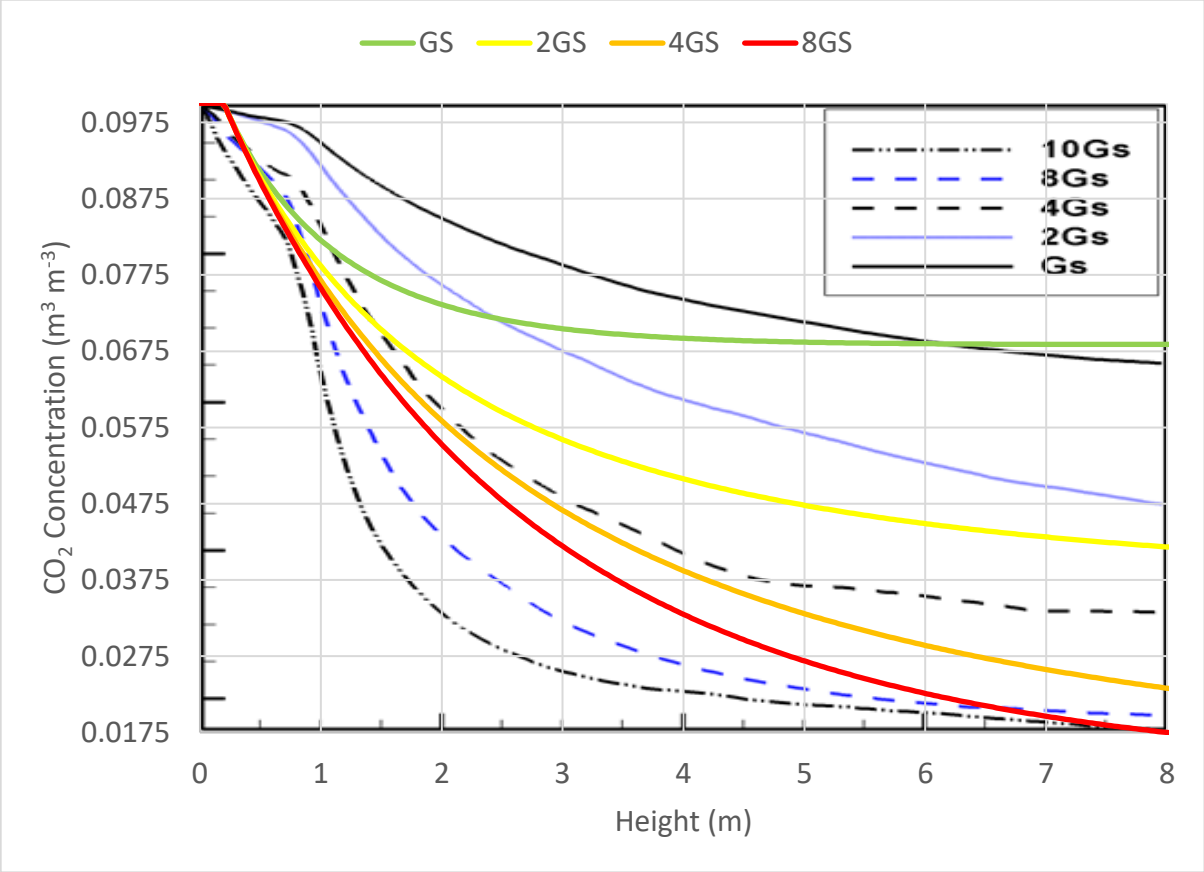

Figure 83: Comparison of CO_2 concentrations in Molaei [26] and algebraic slip model

Figure 83 shows some of the results obtained by Molaei for different solids flow rates compared to simulations done with the algebraic slip model.

The initial reaction profiles for the algebraic slip model follow each other more closely than Molaei. After a certain length, as they approach what appears to be a maximum conversion, the conversions for the algebraic slip model begin to diverge from this shared line.

As the solids concentrations are doubled, the effect on ultimate concentration is increased more so for the algebraic slip than for Molaei's Lagrangian model. The doubling of the initial flow rate doubles the CO_2 captured, with lesser increases as the concentrations is further increased.

The solids profiles for these runs and their comparison with Molaei are shown in Figure 78.

The most notable difference between the models is the mores smooth profile of the CO_2 conversion in the algebraic slip model. This is due to the more consistent equilibrium concentration of the solids in the algebraic slip, whereas in the Lagrangian model, most of the solids are near the bottom of the column, so most of the reaction occurs here also.

The lowest flowrate has completed reaction for the algebraic slip, whereas all higher concentrations are still reacting as they reach the outlet. All Molaei's experiments were still undergoing reaction as they exited the reactor.

8.4.2 Comparison between two and three dimensions

A series of runs were made with a view to compare data from two- and three-dimensional simulations. These were conducted in the same mesh as the earlier three-dimensional studies in Section 8.2, but with velocities and concentrations from the two-dimensional work in this section, to promote the rate of carbon capture. These results are shown in Figure 84.

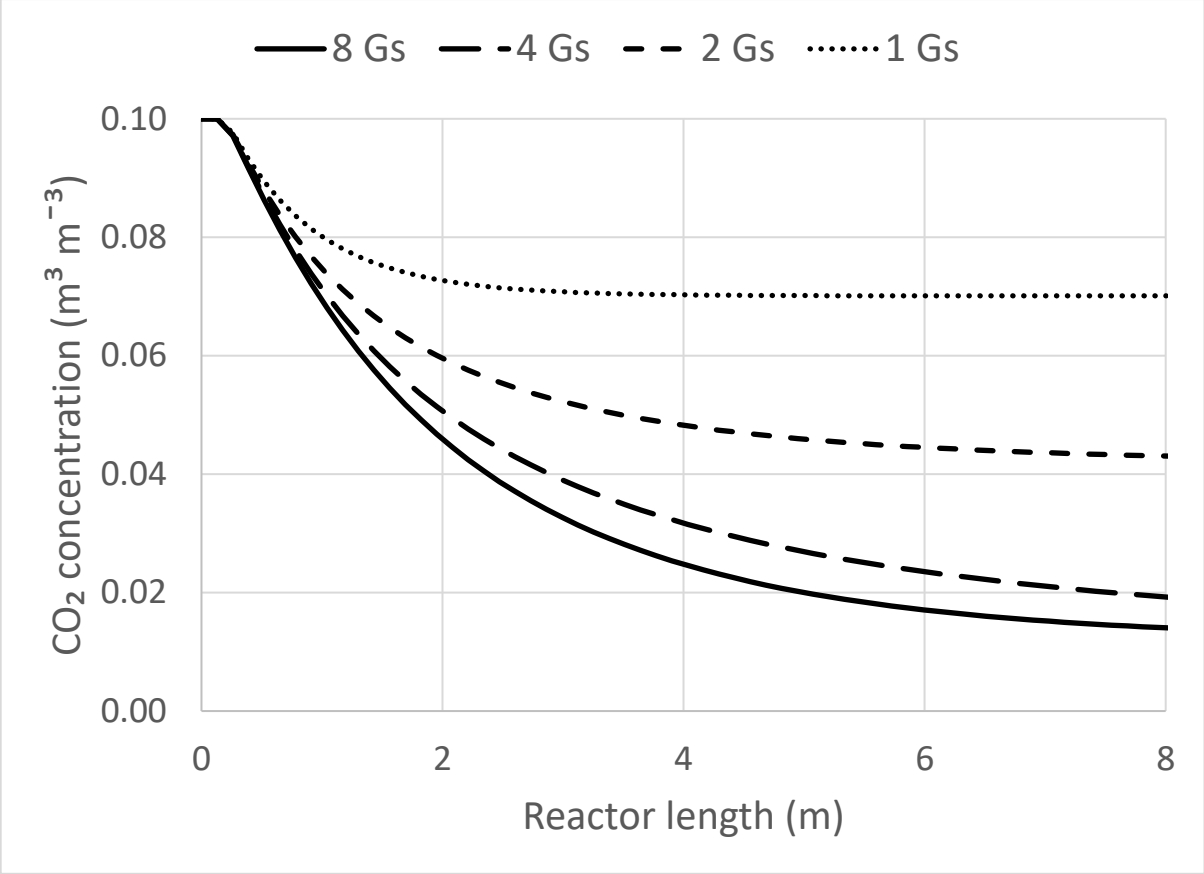

Figure 84: Runs in three dimensions

The results for two and three dimensions in Figure 83 and 84 are very similar, as would be expected for extension from simple two to three-dimensional flow. The reductions in CO_2 concentration are almost the same for each flow rate, although Gs performs better for three dimensions (reduction to 0.064 m^3 m^{-3} in two and 0.07 for three dimensions) while 8Gs performs the other way (reduces to 0.017 in two and 0.014 in three dimensions).

All reaction rates follow the same line at the start before diverging and settling on an equilibrium value.

The values obtained in these experiments at higher solids flows are very similar to those obtained by Molaei [26] despite the experimental setup being quite different.

8.4.3 Comparison between side and lower inlets

Further tests were performed based on the carbonator from Molaei [26], this time based on a side inlet at the lower gas densities. This inlet was 0.1 m tall with its base at the lower barrier. The results of these tests are shown in Figures 85 and 86.

Figure 85 shows a capture rate for the highest solid flow of over 80 %, which is comparable to the performance for 4Gs column with a lower inlet.

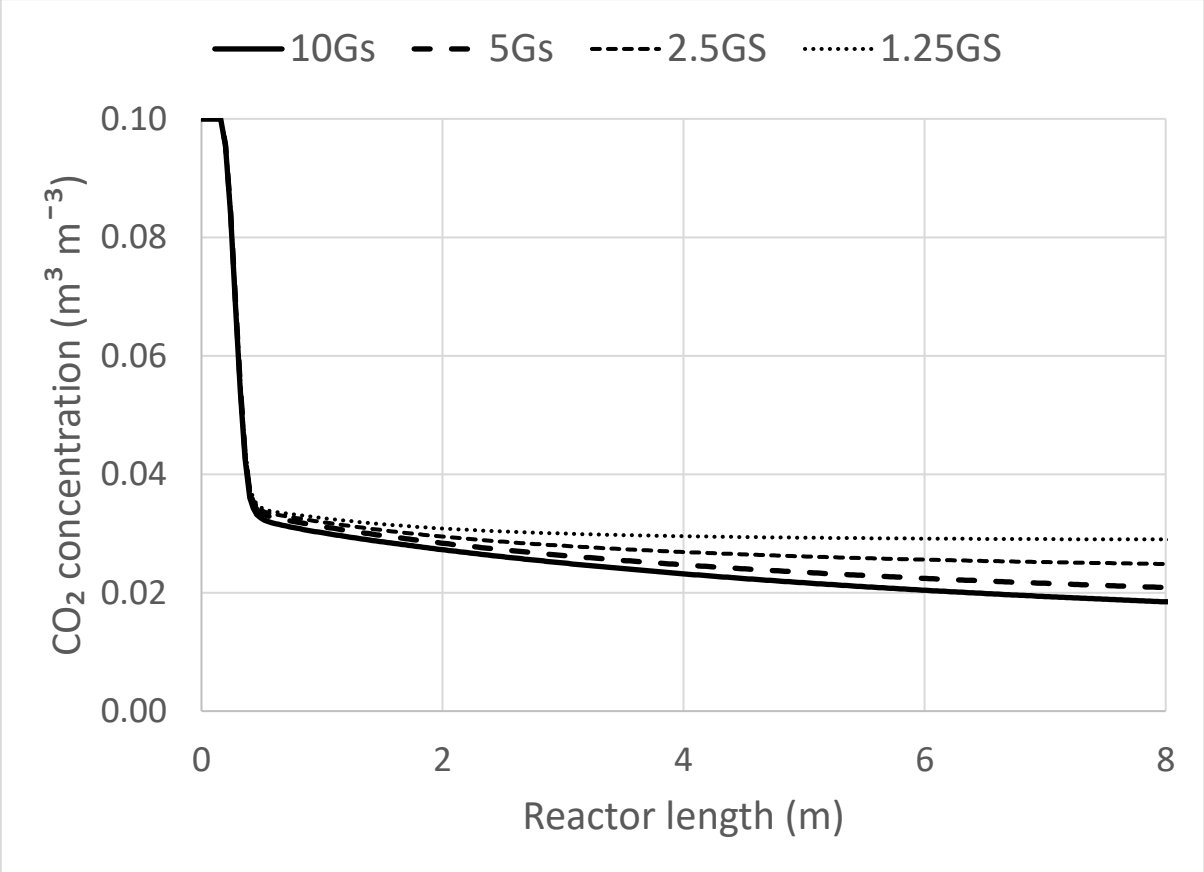

Figure 85: Concentrations profiles for solids flow from a side inlet at reduced gas density

As before, with flow from a side inlet, the particles do not behave naturally in the column, with the reactants not fully reaching the far side from the inlet, and the CO_2 remaining concentrated close to this side, as shown in Figure 86. A large amount of CO_2 is escaping, despite the positive results displayed in Figure 85.

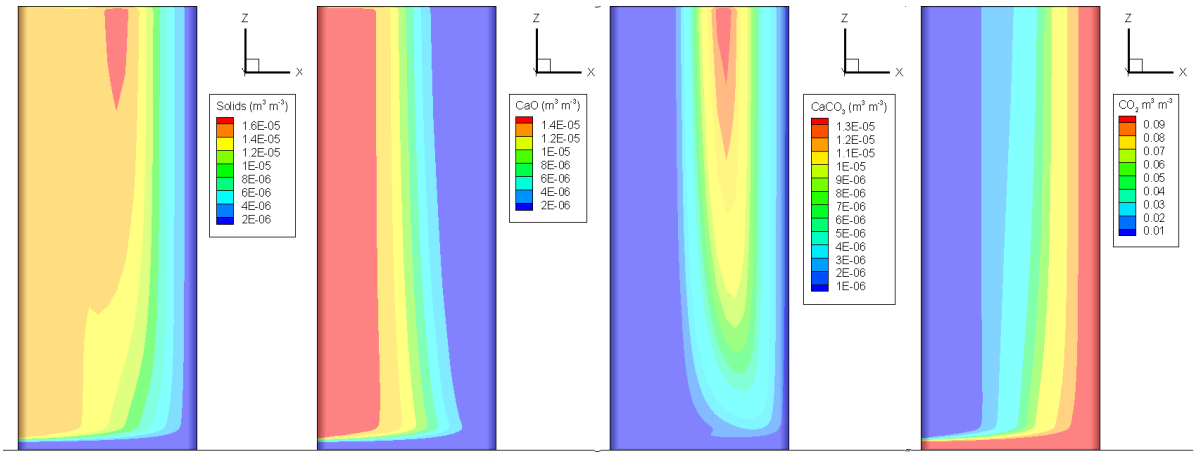

Figure 86: Concentration profiles for solids flow from a side inlet with reduced density

The capture rate for the side inlet flow with reduced gas densities is very good. Almost all the CO_2 is captured at the solids inlet for all solids inlet concentrations, down from 0.1 to around 0.03 $m^3\ m^{-3}$. This is not quite the target reduction in Molaei's work, but it is an improvement on the work in Section 8.2.

Molaei optimised his experiments to run quickly, although doesn't appear to have made any references to time. A 60 s simulation for the 2D version here too 5.5 hours on a dual core 3.6 GHz processer, which was running other simulations.

8.5 Carbonator replication

A carbonator was modelled based on experiments done by Duelli et al [78], Unterberger [90] and Charitos [70], with a view to repeating the results they obtained to give an idea of the accuracy of the algebraic slip model for carbonator simulation. They used a dual column 10 kW carbonation cycle in Stuttgart to perform parametric tests to evaluate larger scale systems in Stuttgart (0.25 MW) and La Pereda in Spain (1.7 MW) [78, 90, 121, 122]. A diagram of the lab cycle can be seen in Figure 87 with a breakdown of the individual streams shown in Figure 88 and Table 20.

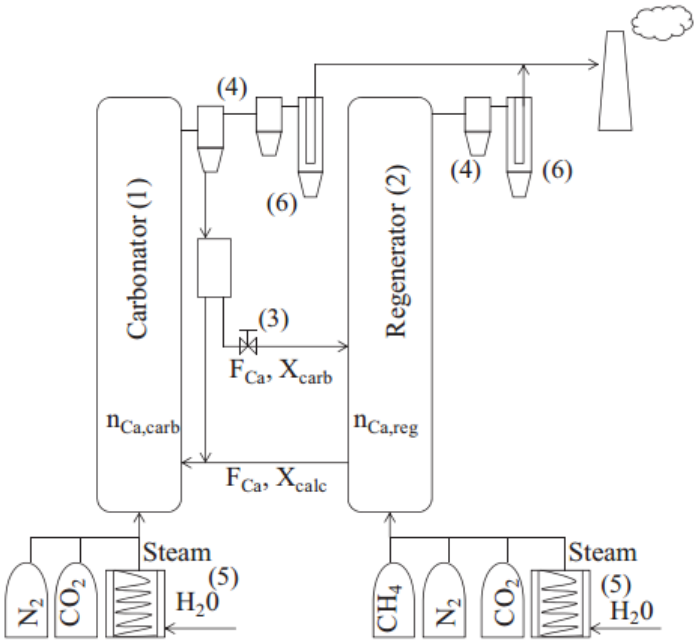

Figure 87: The experimental setup used by Duelli [78]

A 10-kW system ins Stuttgart which processed 150 kg of CO_2 per hour [70] was used as a preliminary investigation for an industrial scale 10 MW plant which would process 815 tonnes of CO_2 per hour. The 10-kW system had a carbonator operating in the fast-fluidised regime and a regenerator operating as a bubbling bed. The carbonator was 0.071 x 12.3 m and operated with a gas flow of around 4.5 m s^{-1}, while the calciner was smaller at 0.15 x 5 m and operated with a gas flow rate below 2 m s^{-1}. Both reactors used multiple passes of the gas streams.

A mass balance was performed based on values for the 10 MW system [90] and scaled down, based on boundary conditions and equipment used in the 10 kW studies [78]. A mass balance for the 10 MW system is given in Table 24, while Table 25 shows the volumetric balance for the 10 kW experiments. Both can be found in the Appendix.

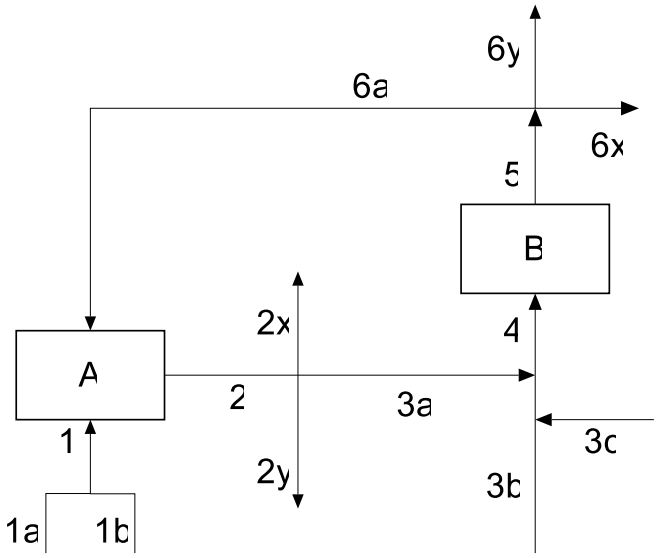

Figure 88: Flow diagram for the carbonation cycle in Figure 84 from [78] and [90]

For the simulation in PHYSICA, the inlet streams were split into two: solids from a side inlet and gas from a lower inlet. The lower air stream was set to maintain fluidisation velocity, while the inlet solids velocity and concentrations was specified to maintain the volumetric ratios of CaO to CO_2 from Unterberger [90].

Duelli and Charitos used flow ratios, defined as reactor space times, based on the reactor inventory of CaO and the molar flow of CO_2 for the carbonator which came to between 5 and 20 seconds, and a ratio of the time spent in the calciner over the incoming solids conversion in the carbonator, of between 0.4 and 1.2 hours for the calciner. These resulted in very disperse mixtures for the carbonator, and long residence times for the calciner. The space time (in hours) was given by:

$$\tau_s = \frac{n_{CaO}}{F_{CO_2}} \tag{123}$$

Where n_{CaO} is the molar amount of CaO (mol) in the carbonator and F_{CO2} is the molar flow of CO_2 to the carbonator (mol h^{-1}).

Table 20: Key for the plant in Figure 87

Item	Function
A	Carbonator
B	Calciner
Stream 1a	Gas to carbonator
Stream 1b	Solid feed to carbonator
Stream 1	Inlet to carbonator
Stream 2	Outlet from carbonator
Stream 2x	Gas to atmosphere
Stream 2y	Purge of solids
Stream 3a	Solids to calciner
Stream 3b	Gas to calciner
Stream 3c	Solid feed to calciner
Stream 4	Inlet to calciner
Stream 5	Outlet from calciner
Stream 6a	Solids to carbonator
Stream 6x	Gas to storage
Stream 6y	Purge of solids

A reactor space time of 10 s was chosen for the carbonator and the standard operating conditions used in the lab experiment are shown in Table 21. There were five particle sizes corresponding to diameters of 100 ,125, 150, 175 and 200 μm. The overall CaO inlet concentrations were $1.5x10^{-3}$ m^3 m^{-3} CaO at a velocity of 0.3 m s^{-1}, with no $CaCO_3$ in the side inlet stream. The velocity for this run was chosen to be 1.8 m s^{-1} to get a high enough residence time for most of the phases.

Table 21: Standard operating conditions from Duelli [78]

	Carbonator	Regenerator
Temperature in °C	600–680	880–930
Velocity in m/s	4.5–5.5	0.3–2.0
Fluidization regime	Fast	Bubbling/turbulent
Inlet CO_2 in vol.% d.b.	10–16	0–75
Inlet H_2O in vol.%	0–10	0–35
Space time	0.44–0.66	0.3–1.2
Looping ratio		2–15

8.5.1 Side inlet

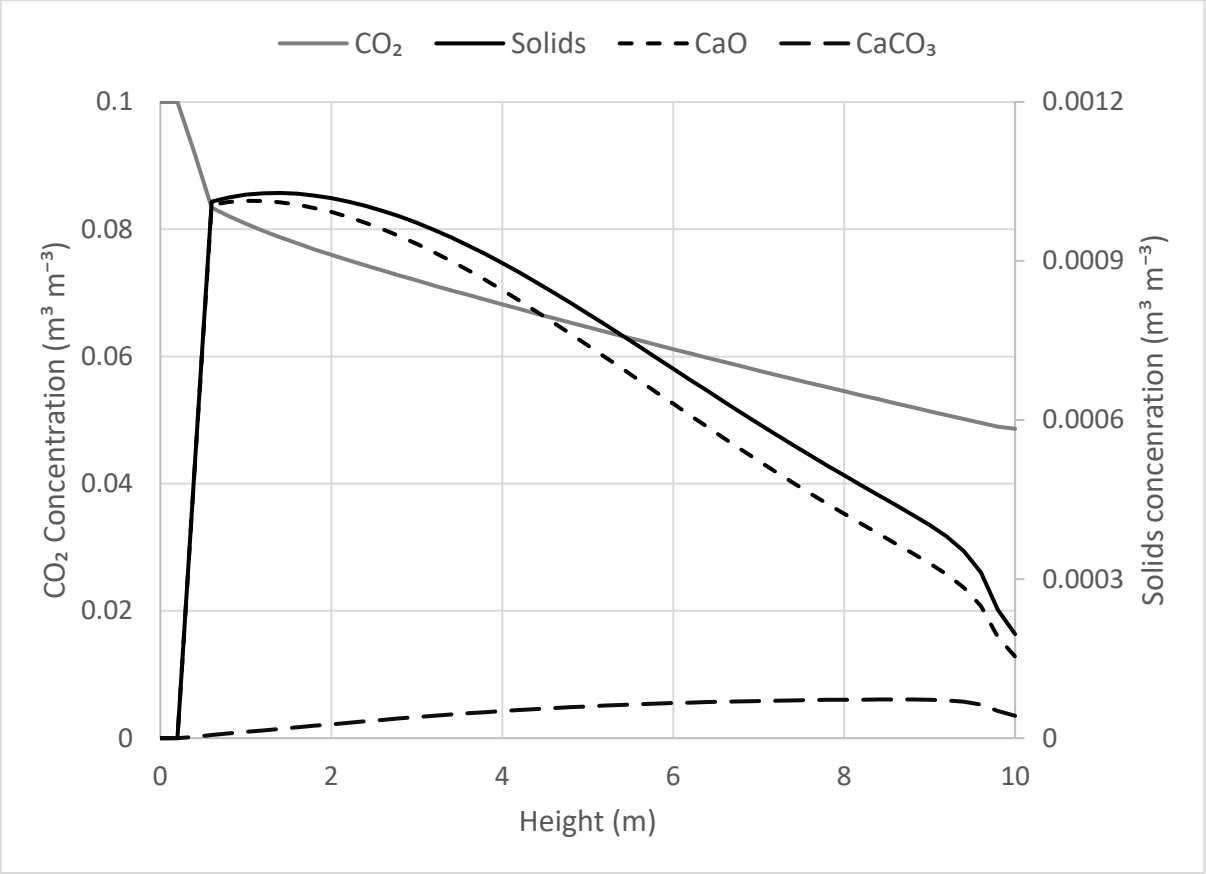

Figure 89: Overall concentration profiles for the carbonator after 10 s

Figure 89 shows the overall concentration profiles for the centre of the carbonator after 10 s. As this is a three-dimensional simulation, this does not fully capture the behaviour of the column but is a good indicator of the behaviour of the reaction and transport modules for the bulk of the flow.

Here, there is a rapid decline in CO_2 concentration coinciding with the solids inlet, followed by a gentler decrease up the column. The CO_2 falls from 0.1 to 0.08 $m^3\ m^{-3}$ as the solids enter and declines to 0.048 by the time it leaves. This is more akin to the gradual reduction in rate and conversion from Molaei's work [26] than earlier studies with higher velocities, such as in Figure 82 earlier in this report.

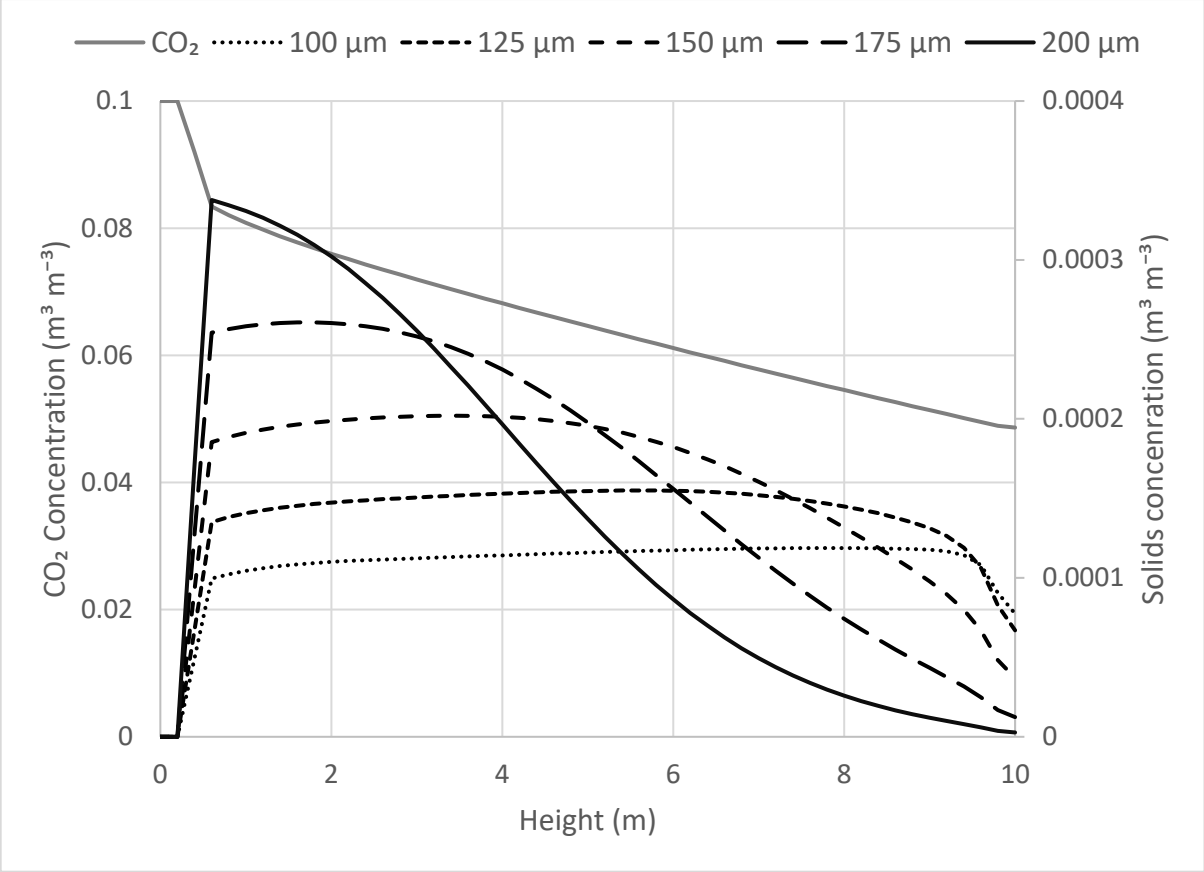

Figure 90: Solids and CO_2 concentration profiles through the centre of the column after 10 s

The solid profiles for the different diameter particles are shown in Figure 90. Here, there is a definite solid peak at the lower barrier, followed by a steady reduction for the phases with a higher slip velocity, and a slight increase in those with less drag towards a steady equilibrium level. This bears resemblance to the solid profiles of Molaei [26] in Figure 82.

The behaviour at the walls in Figure 91 is like that of the centre with a lower peak at the solid inlet of 0.1 m^3 m^{-3} followed by a steady decline up the column. At the walls the CO_2 is also reduced to near 0 at the solids inlet, before recovering slightly.

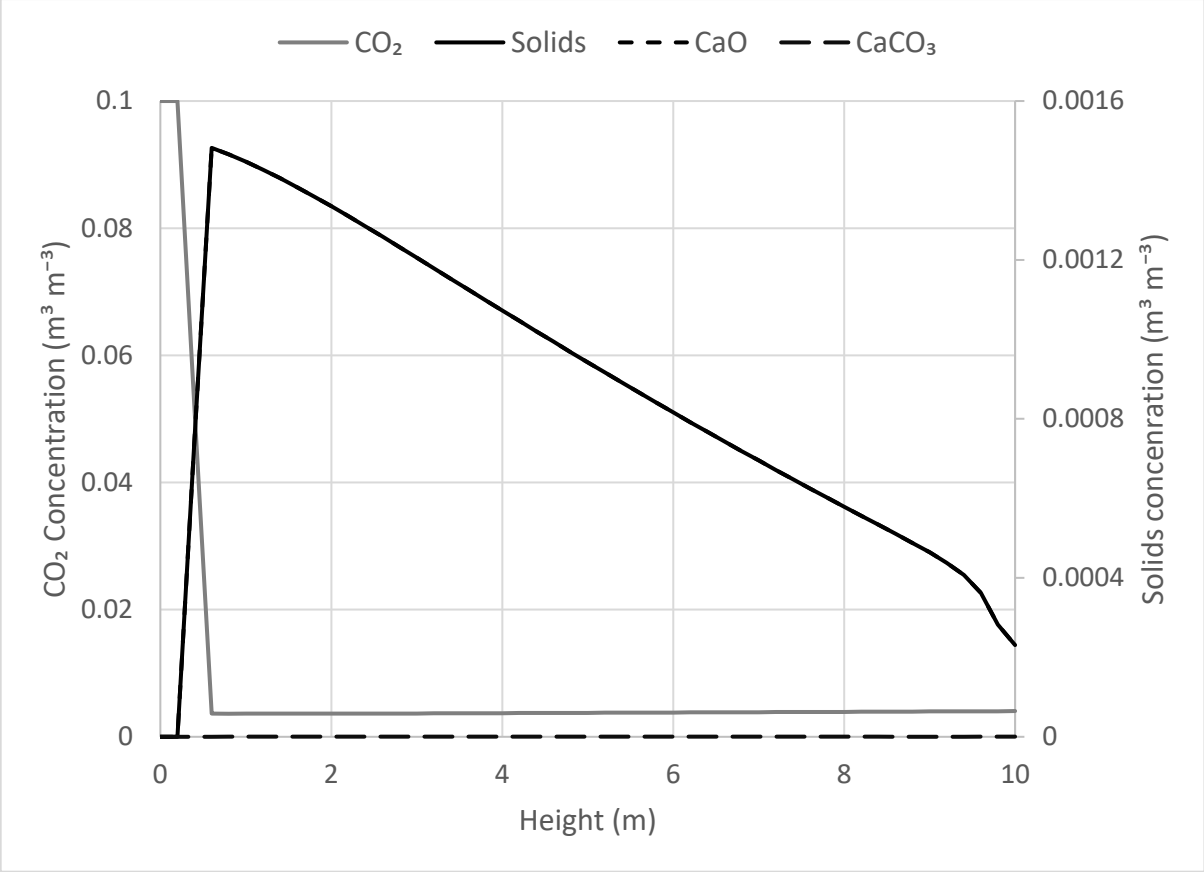

Figure 91: Solids and CO_2 profile at the walls for the carbonator after 10 s

The slices in Figure 92 show the evolution of the contents of the reactor from the lower and solids inlets to the top of the column. The CO_2 fraction is spread across the column initially, but stronger away from the solids inlet. The level of CO_2 reduces gradually on the solids side while remaining relatively constant on the other side, as with the work in Section 8.1, although the CaO is more spread out across the side of the column.

The solids are entering via an inlet just above the lowest slice, which corresponds to the onset of the lower barrier below which they cannot drop. The arrow indicates this location.

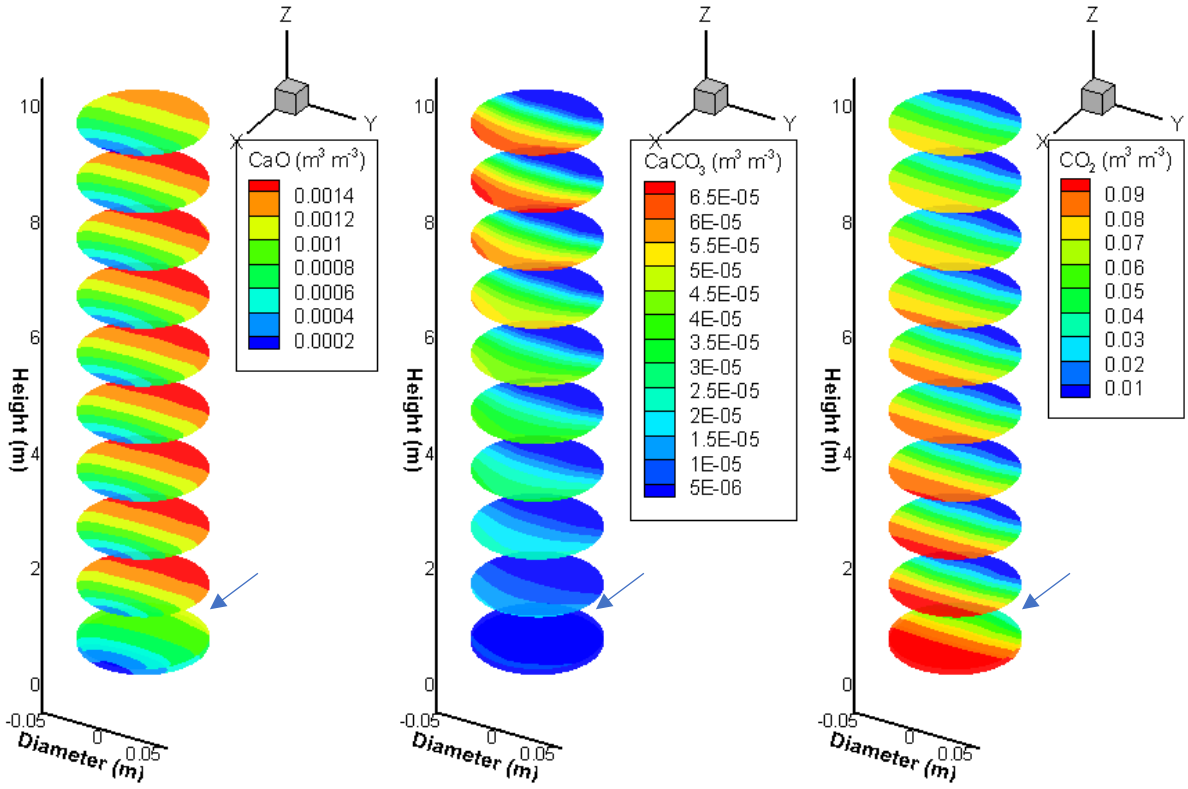

Figure 92: Horizontal slices of a carbonator with a side-inlet

The vertical slices of the column, shown in Figures 93 and 94, show the evolution of the solids concentrations and mixture velocity in the x and y dimensions.

Figure 93 shows the solids coming in from an inlet on the left and ascending the reactor. The CO_2 enters from below, and where the two streams meet, the solids are pushed upwards, creating an echelon of particles on the left-hand side and a stream of gas on the right. The higher diameter particles, which do not fluidise well are the only particles reaching the right-hand side, where they are settling above the lower barrier and moving upwards very slowly. The CO_2 is moving up the column in the gas stream, steadily reacting with the CaO to form $CaCO_3$, which is noticeable in the higher parts of the column.

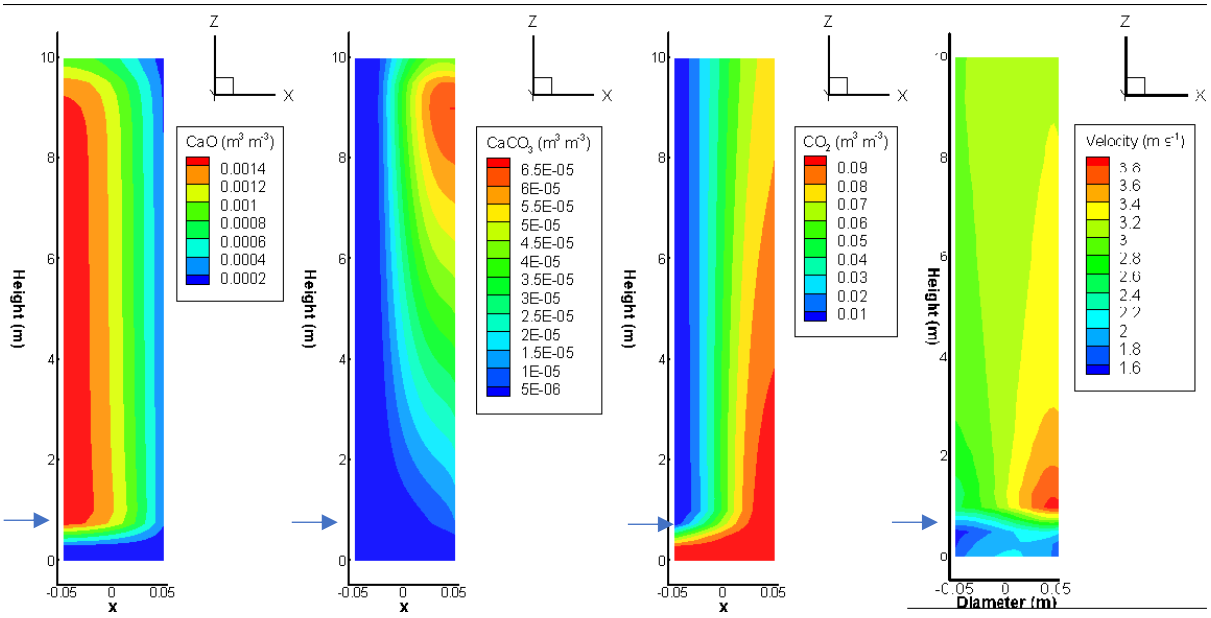

Figure 93: Vertical slices of a carbonator with a side-inlet taken perpendicular to the inlet stream

Reaction is mostly occurring up the right-hand side of the column, away from the solids inlet, where the CO_2 concentration is highest. Gas concentration and mixture velocity are also higher here, which reduces the residence time, due to the solids inlet velocity adding to the gas velocity from below.

Figure 94 shows the column from a view in line with the inlet, and here the evolution of the mixture up the column more closely resembles flow from below: CaO and CO_2 are reduced as the $CaCO_3$ concentration increases. Velocity peaks in the middle of the column, with steady reductions in the concentration of solids as we move up the reactor. This is like some of the two-dimensional results from Chapter 7. Solids are more concentrated at the walls of the reactor.

The inlet above the lower barrier is more obvious here, due to the dramatic changes in concentration occurring at the barrier.

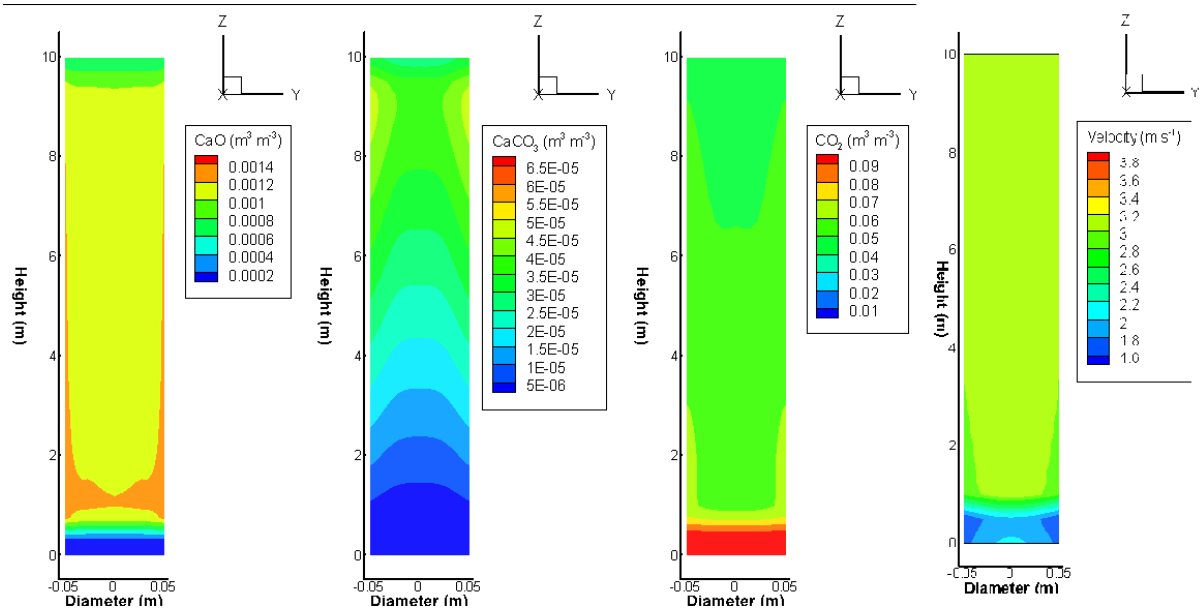

Figure 94: Vertical slices of a carbonator with a side-inlet taken in line with the inlet stream

Table 22 shows a balance for the carbonator. 38.5% of the CO_2 has been captured in this one pass. This could be improved by increasing the length of the reactor, reducing the diameter of the particles or by increasing the residence time. Although reducing the gas velocity would increase the residence time, it might leave the mixture unable to fluidise.

Table 22: Balance for the carbonator with a side inlet

Source	Q (m^3)
Inlet	1.16E-03
Outlet	-7.13E-04
carbonation	-4.47E-04
% captured	35.8

A further run was performed with reduced gas densities, to account for the higher temperatures. For this case, due to the reduction in mass and molar flowrate in the gas phase, as the density was reduced from 1.2 to around 0.38 kg m^{-3}, the solids concentrations were decreased to a third of their previous value.

This led to a higher capture rate through the centre of the column (over 80%), and the CaO conversion here reduced from 0.0004 to 0.00022 m^3 m^{-3} over the height of the column – a little under 50% conversion, which is somewhat more than the 33% reported in Unterberger [90]. Of course, the column displayed the behaviour of Figure 93, so this is an overestimate.

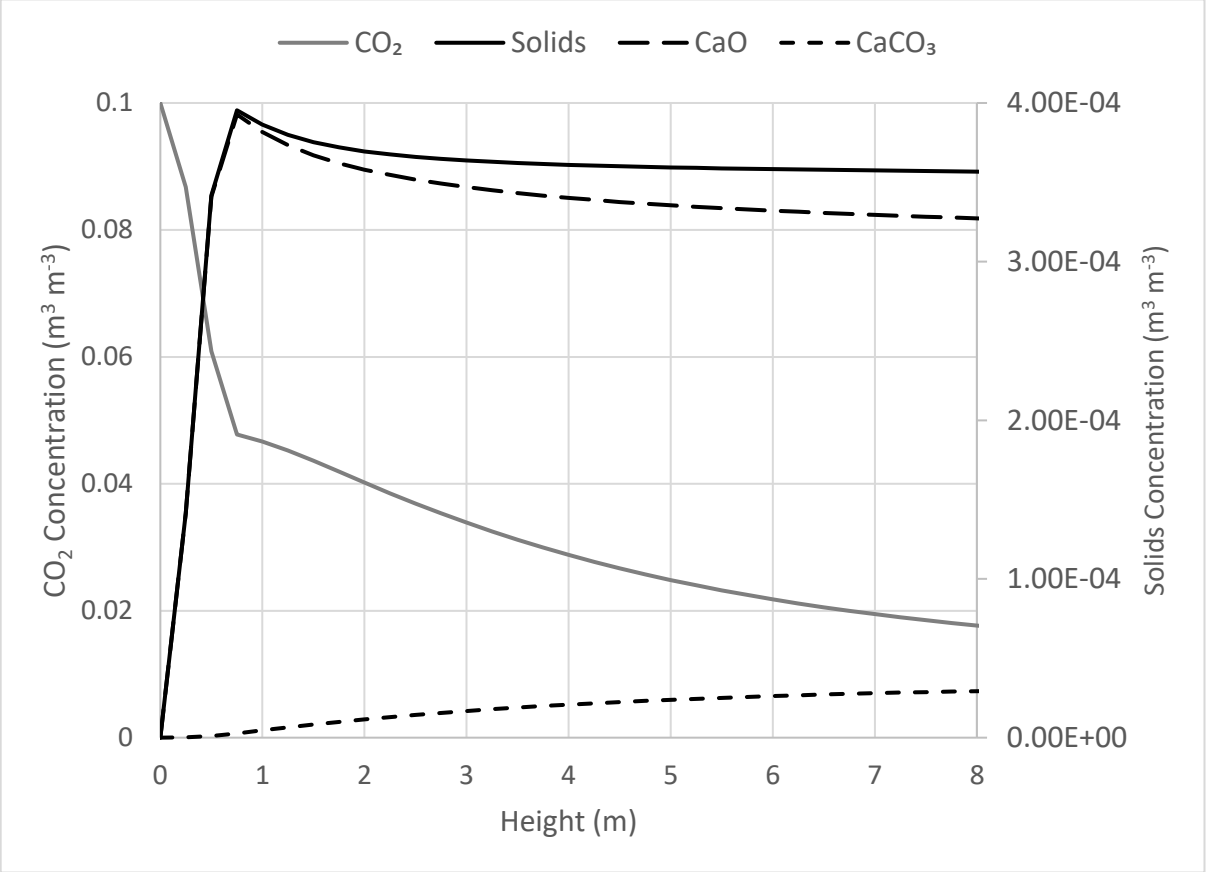

Figure 95: Carbonator with amended gas densities after 90 s

8.5.1 Lower inlet

Simulations were also performed without a side inlet, with the lower inlet acting as a boundary patch for solids and gases. The velocity was set to 2.15 m s^{-1} with concentrations of 0.1 m^3 m^{-3} for the CO_2 and a total solids level of $1.5x10^{-3}$ m^3 m^{-3}, which is a molar CaO:CO_2 ratio of 10:1, in keeping with the earlier work from the side

inlet. The initial enthalpy was set to 927 kJ m^{-3} with inlet enthalpy of 840 kJ m^{-2} s^{-1}, which assumes a temperature of 900 K, for initially pure air and the inlet mixture. The concentrations profiles for this experiment are shown in Figure 96.

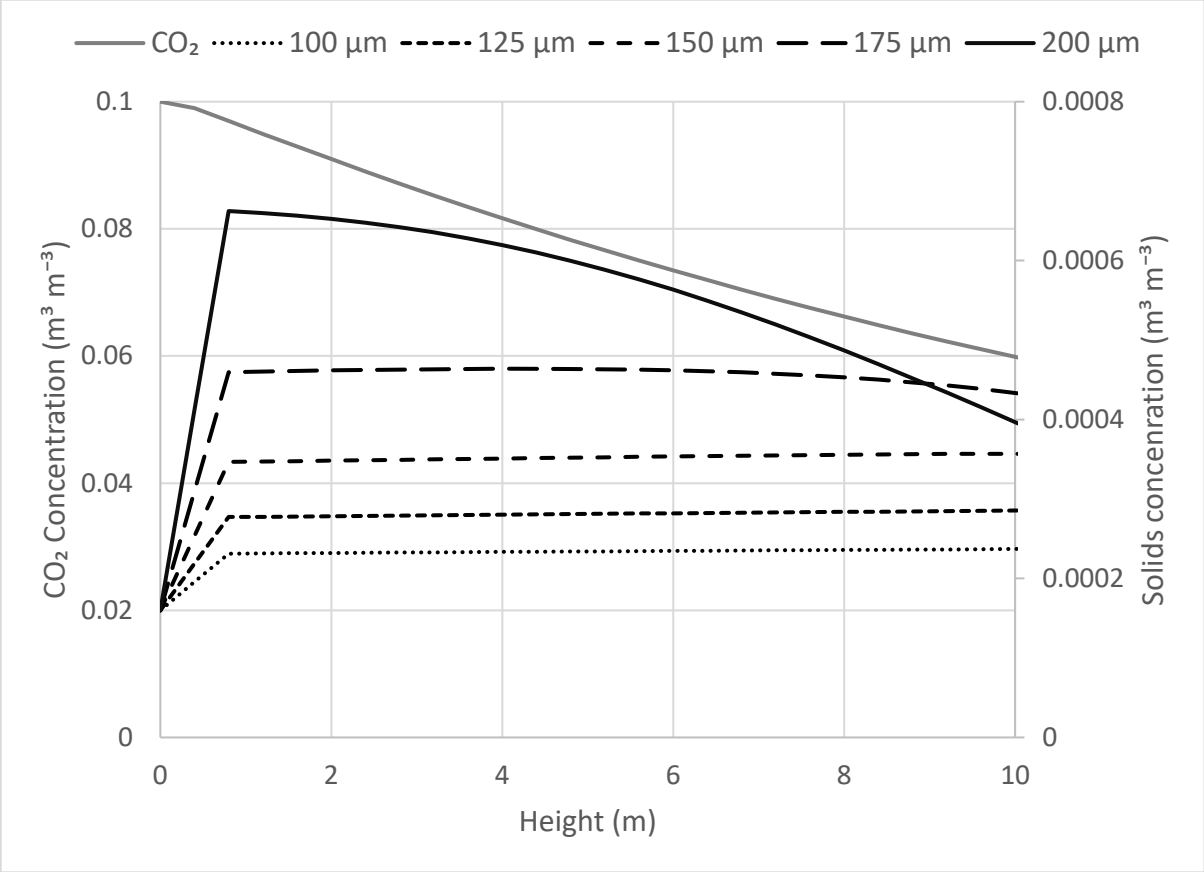

Figure 96: Solids concentration profiles with flow from below

Compared to the side inlet, the lower inlet gives an appearance much more in keeping with the earlier experiments in Section 8.1.1. The CO_2 has reduced only to 0.52, but this is a capture rate of 45%, twice that of the earlier run with the side inlet, suggesting that an improved way of mixing the fluids together with a side inlet would improve performance in that setup.

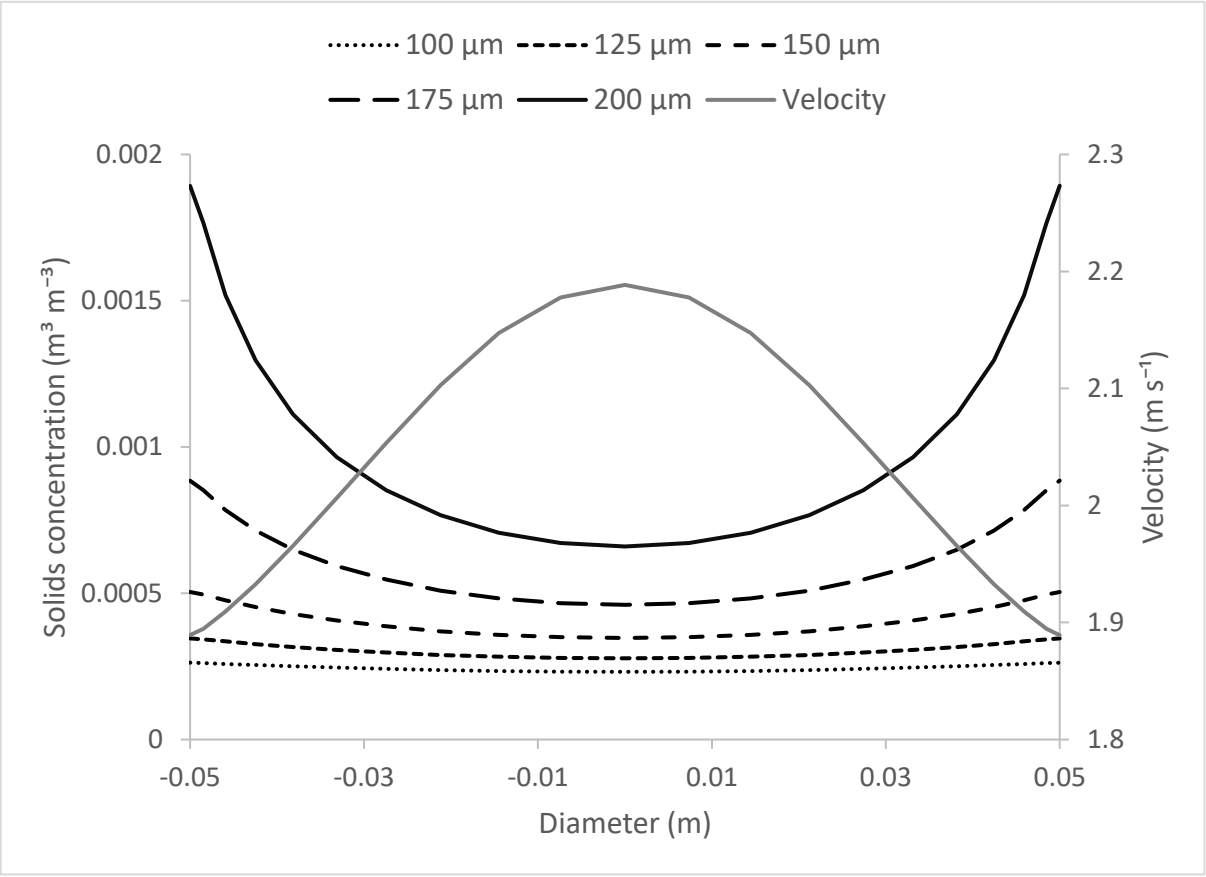

Figure 97: Solid concentrations and gas velocity at z=1 m

The velocity and concentration profiles at z=1 m in Figure 97 show a velocity peaking in the centre of the column, with higher solids concentrations at the walls. This corresponds with Figures 98 to 100, which show horizontal and vertical slices through the column. The solid phases remain close to the walls, while the gas passes up through the centre of the reactor, which is due to the reduced slip velocity near the boundaries, as there is a reduced mixture velocity due to the boundary layer at the wall. The balance for the reactor in Table 23 confirms that almost 56% of the CO_2 has been captured in one pass. This is an improvement on the side inlet by 20%, due predominantly to the pre-mixed state of the reactor contents as they entered.

Figures 98 and 99 show horizontal and vertical slices through the carbonator. In keeping with the earlier experiments in Section 8.3.1, there is a higher concentration of particles

around the wall, and the gas flows through the middle of the column where there is less resistance.

Most reaction occurs around the walls, where the CaO is highest in concentration. This results in higher levels of CO_2 and CaO in the centre with more $CaCO_3$ around the edges in the higher regions of the column. The reduction in CO_2 along the reactor length looks similar to the results for a lower gas inlet shown in Figure 94.

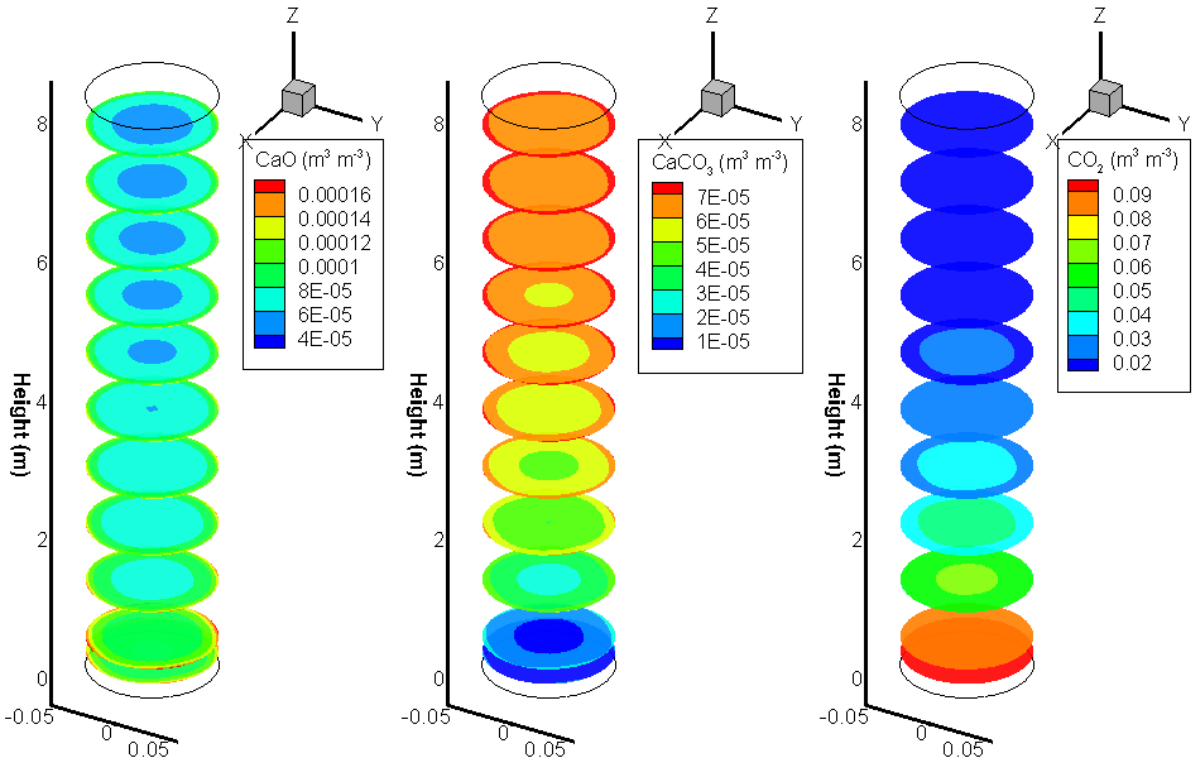

Figure 98: Horizontal slices of a carbonator with a lower inlet

Table 23: Balance for the column with a lower solids inlet

Source	Q (m^3)
Inlet	1.55E-03
Outlet	-6.88E-04
carbonation	-8.59E-04
% captured	55.6

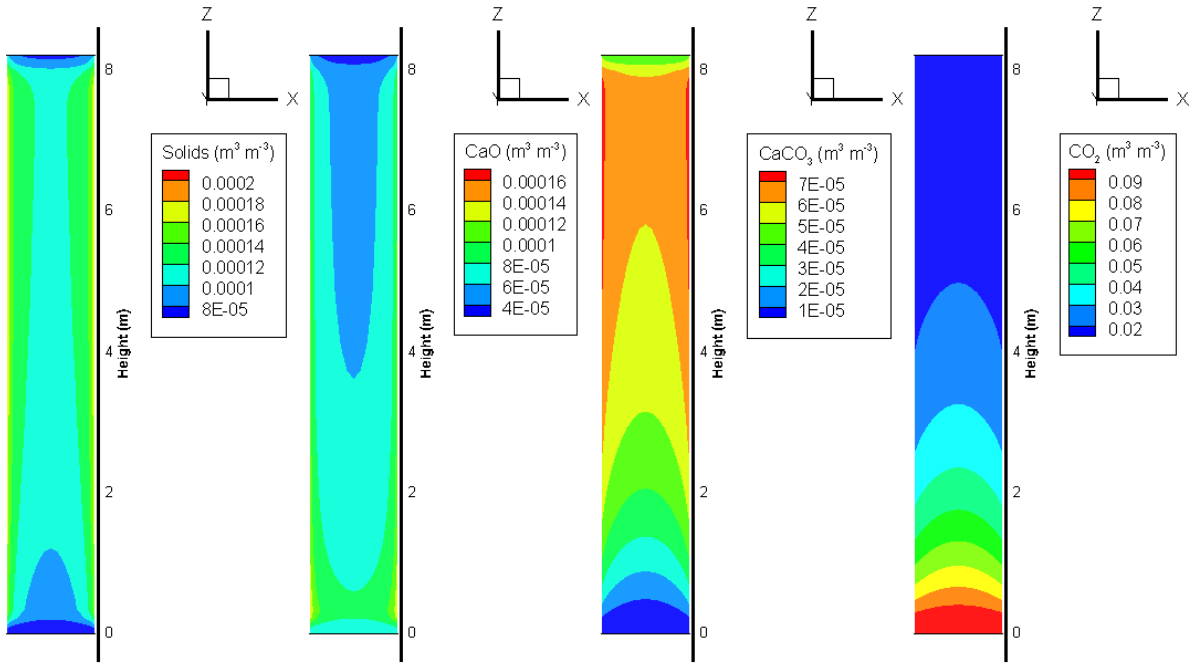

Figure 99: Vertical slices of a carbonator with a lower inlet

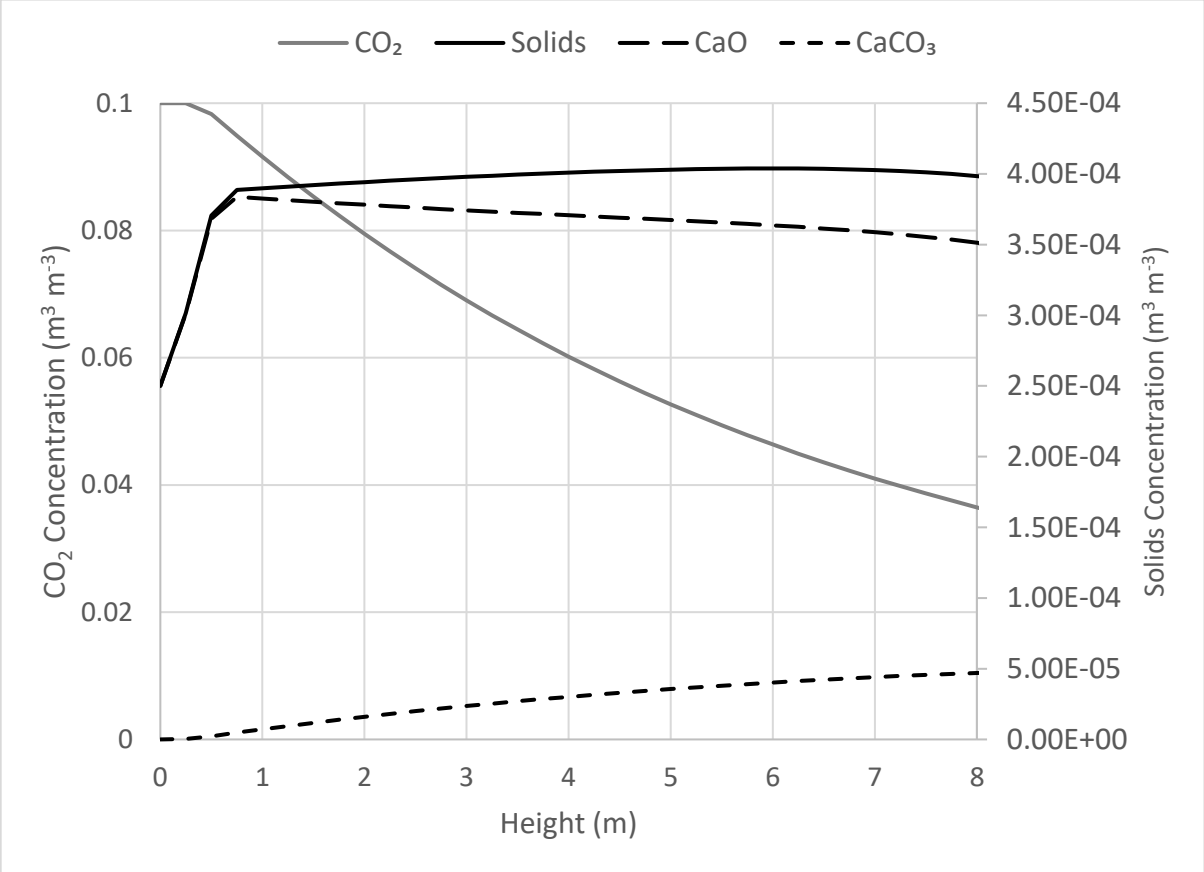

Figure 100: Carbonator with amended gas densities

An additional run was performed under the same conditions, but with reduced gas densities of 0.38 kg m^{-3} for air and 0.6 kg m^{-3} for CO_2 and is shown in Figure 100. As with the side inlet above, the solids flowrates were reduced by two thirds to account for the reduction in molar gas flow. This led to an improved capture rate of 64%, as the CO_2 left the reactor at a concentration of 0.36 m^3 m^{-3}. The CaO concentration is reduced from 0.0004 to 0.00035, a disappointing 12.5%. This is an improvement, but still short of the desired numbers.

A run without the reduced solids flow-rates is shown in Figure 101, in which the CO_2 outlet concentration is reduced to 0.13 m^3 m^{-3}, but this has a very solids flow-rate compared to the gas, which is suggestive of a higher recycle ratio than was suggested in the works of Duelli [78] and Unterberger [90].

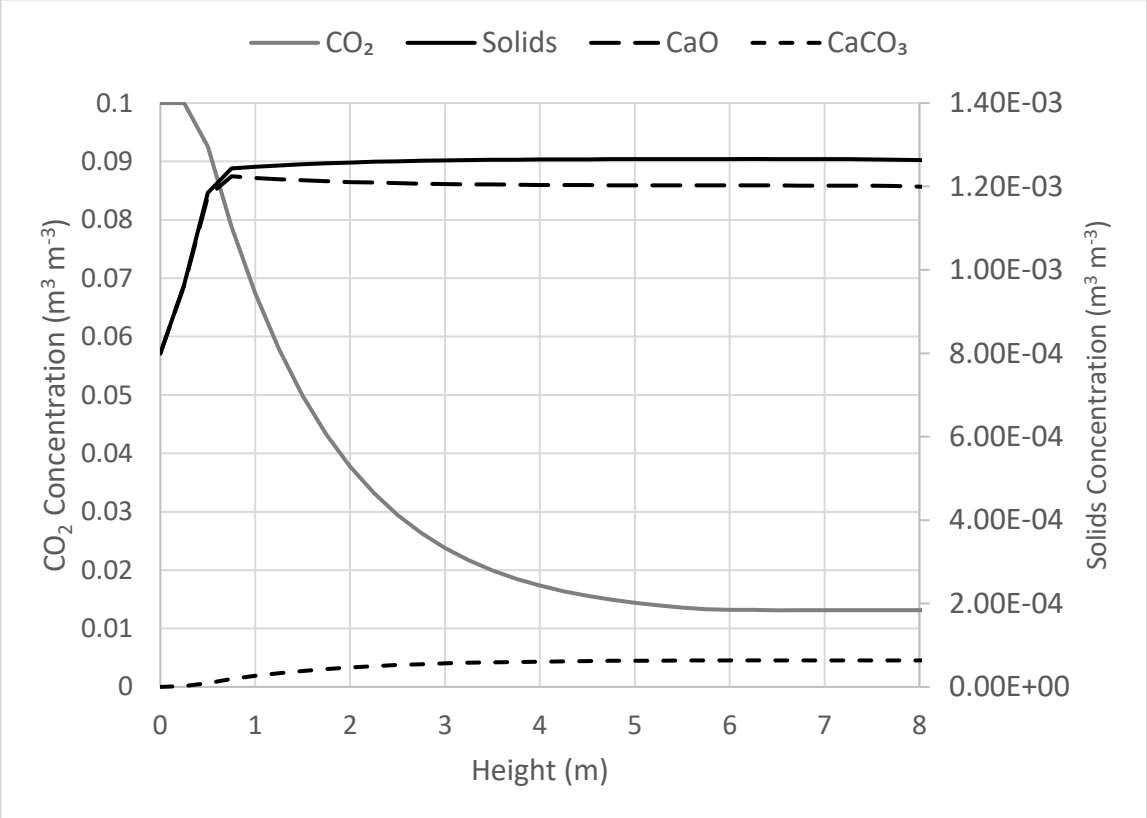

Figure 101: Carbonator with flow from a lower inlet and unmodified solids flow

In this section, the algebraic slip model has been extended to three dimensions. It has been used to simulated reactors based on designs by Molaei [26] and Unterberger [90].

It was found that the algebraic slip model captured the behaviour of the powders to a large extent, albeit not fully representing the mixing of the phases in the carbonator, which may have led to less reaction occurring, or being capable of simulating the bubbling conditions of the calciner, which required a taller reactor with gas flow at higher velocities, to approach a high enough residence time.

When using a side inlet, the solids were injected into the reactor as part of a gas stream with specified velocity to promote dispersion, whereas in a real-world scenario, they would have entered via a re-entry duct, which would have contributed much less to the overall gas velocity in the column and there would have been more mixing.

This use of a side inlet with additional gas velocity to disperse the solids across the column reduced the available time for reaction to occur, thereby reducing conversion, and the efficiency of the system.

Additional experiments were with gas density amended due to temperature, and these resulted in much greater carbon capture efficiency.

The simulations of the carbonator were very detailed with five particle sizes in two species. This led to a long simulation time of over 14 hours on a mesh containing 10240 elements on a dual core 3.6 GHz processor with 64 Mb of RAM.

CONCLUSIONS AND FUTURE WORK

9.1 Conclusions

The algebraic slip model has been adapted to and programmed to work in the in-house software PHYSICA. It has been used to predict the behaviour of gas-solid mixtures containing a range of solid phases.

The hydrodynamic model was based on a modification of an existing drift flux model, with additional terms and allied routines to account for changing mixture properties based on local concentrations. A reaction module was written based on a shrinking core mechanism, to account for carbonation, which was integrated with the hydrodynamic module, property modules and enthalpy module.

The performance of the hydrodynamic, reaction and enthalpy modules were tested and have been found to compare favourably with examples from the literature and to be representative of what one would expect for a fluidisation column operating in the fast-fluidisation regime.

The idea of an inlet flow from the side which could be fluidised was examined and it was found that in this implementation it did not fully represent the real-world scenario.

Due to the long relaxation times of the particles under consideration, the algebraic slip model is not appropriate a means to model bubbling beds, where diffusion and other factors become important. The relative lack of mixing created some problems for the reaction modules as the gases and solids required contact time and this was reduced due to the high momentum of the solid mixture and the low momentum of the gas phase, which preferred to avoid passing through the solids and travel around them.

Tests were performed with both a prescribed density, based on the material properties at 298 K, and with a reduced gas density, based on the ideal gas law at the temperature in the reactor. It was found that the reduced gas density lead to an improvement in CO_2 capture rates, but also, due to the way inlet conditions were specified, a reduced CO_2 inlet flow, so the increase in carbon capture were not as great as initially appeared to be.

The model was compared with Lagrangian code developed by Molaei [26], and although the solids behaviour was very different, a similar rate of carbon capture could be attained through the manipulation of the flow rate, temperature and inlet concentrations.

The model was used to compared with experiments at Stuttgart [78, 90] and found to underpredict carbon capture rates.

The performance of the model was compared for both two- and three-dimensional flows and was found to behave similarly for both, in terms of solid mass flow and carbon capture.

Although limited to fast fluidisation and other convection dominated regimes, the algebraic slip model does offer an additional option for the simulation of fluidisation columns at relatively low computational costs.

9.2 Recommendations for future work

Although preliminary investigations were completed, no detailed study was made of the performance of the calciner, particularly with regards to its relationship with the carbonator as part of a carbonation cycle. As the algebraic slip model is inappropriate for a bubbling bed, another multiphase method would have to be applied to the operation of the calciner, as a fast fluidising bed would require too much gas to produce a concentrated CO_2 stream.

A more detailed study of a full carbonation plant, with integration of other facilities including heating and utilities, and the economic assessment of this would results in a more complete project and would highlight how the carbonation cycle can be used to benefit the power generation industry.

The application of different turbulence models and viscosity correlations would be of interest, particularly with three-dimensional flow from the side, as this resulted in turbulent energy around where the two streams mixed. It might also be possible to

introduce the particles at lower velocities and still ensure mixing if a more forgiving correlation were applied.

It would be interesting to investigate the application of an algebraic slip model in different software and in other areas, including natural phenomena such as landslides, sandstorms and volcanic eruptions.

REFERENCES

1. Bhatia, S.K. and D.D. Perlmutter, *A random pore model for fluid-solid reactions: I. Isothermal, kinetic control.* AICheJ, 1980. **26**: p. 369.
2. *Climate Change 2007: Synthesis Report, Contribution of Working Groups I, II and III to the fourth assessment report of the intergovernmental panel on climate change*. 2007, Intergovernmental Panel on Climate Change: Geneva, Switzerland.
3. IPCC, *Carbon Dioxide Capture and Storage*. 2005, New York: Cambridge.
4. I.E.A., *CO_2 emissions from fuel combustion*. 2017, International Energy Agency.
5. *World Energy Outlook*. 2008, International Energy Agency.
6. OECD and IEA, *Energy Technology Perspectives -- Scenarios & Strategies to 2050*. 2006, IEA.
7. Fu, C. and T. Gundersen, *Carbon Capture and Storage in the Power Industry: Challenges and Opportunities.* Energy Procedia, 2012. **16**: p. 1806-1812.
8. Pires, J.C.M., et al., *Recent developments on carbon capture and storage: An overview.* Chemical Engineering Research and Design, 2011. **89**: p. 1446-1460.
9. Zhang, T. *Milestone Oxyfuel Plant Going Into Operation In Hubei, China*. 2016 [cited 2017 09/08/2017]; Available from: https://www.globalccsinstitute.com/insights/authors//2016/05/05/milestone-oxyfuel-plant-going-operation-hubei-china?author=MTY4OTg%3D.
10. *Guangdong Province, China - getting ready for CCUS development*. 2013; Available from: https://www.globalccsinstitute.com/insights/authors/dizhou/2013/10/21/guangdong-province-china-getting-ready-ccus-development.
11. Irlam, L., *Global Costs of Carbon Capture and Storage*. Global CCS Institute.
12. I.E.A., *Energy Technology Perspectives*. 2016, I.E.A.: Paris.
13. *Industrial Emissions Directive*, E.P. Council, Editor. 2010, European Union. p. 17-119.
14. Kittel, J., et al., *Corrosion in MEA units for CO_2 capture: pilot plant studies.* Energy Procedia, 2009. **1**: p. 791-797.
15. Blamey, J., et al., *The calcium looping cycle for large scale CO_2 capture.* Progress in Energy and Combustion, 2010. **36**: p. 260-279.
16. Shimizu, A., et al., *A twin fluid bed reactor for removal of CO_2 from combustion processes.* Chemical Engineering Research and Design, 1999. **77**.
17. Grace, J.R., A. Avidan, and T.M. Knowlton, *Circulating Fluidized Beds*. 1997: Blackie Academic and Professional.
18. *Final Report - CAOLING (Development of post-combustion CO_2 capture with CaO in a large testing facility: 'CaOLing'*. 2013, European Commission.
19. Meyer, D. *UK Power Plant Tests 'Negative Emission' Carbon Capture Technology*. 2019; Available from: http://fortune.com/2019/02/08/drax-biomass-carbon-capture/.

20. Foehringer Merchant, E. *With 43 Carbon-Capture Projects Lined Up Worldwide, Supporters Cheer Industry Momentum*. 2018; Available from: https://www.greentechmedia.com/articles/read/carbon-capture-gains-momentum#gs.f68cpw.
21. Rubin, E.S., et al., *The outlook for improved carbon capture technology.* Progress in Energy and Combustion Science, 2012. **38**: p. 630-671.
22. Pericleous, K., *Mathematical simulation of hydrocyclones.* Applied Mathematical Modelling, 1987. **11**: p. 242-255.
23. Noroozi, S. and S.H. Hashemabadi, *CFD analysis of inlet chamber body profile effects on de-oiling hydrocyclone efficiency.* Chemical Engineering Research and Design, 2011. **89**: p. 968-977.
24. Shang , Z., J. Lou, and H. Li, *CFD of dilute gas–solid two-phase flow using Lagrangian algebraic slip mixture model.* Powder Technology, 2014. **266**: p. 120-128.
25. *Multi-Physics Computational Modelling with PHYSICA*. University of Greenwich.
26. Molaei, M., *Fluidized Bed Process for the Capture of CO_2 from Fossil Fuel Combustion Sources*. 2013, University of Greenwich.
27. Pericleous, K. and S.N. Drake, *An Algebraic Slip Model of PHOENICS for Multiphase Applications*, in *Lecture Notes In Engineering*, N.C. Markatos, et al., Editors. 1986: Berlin.
28. Pericleous, K.A. and N. Rhodes, *The hydrocyclone classifier — A numerical approach.* International Journal of Mineral Processing, 1986. **17**(1-2): p. 23-43.
29. Khinast, J., et al., *Decomposition of limestone: the influence of CO_2 and particle size on the reaction rate.* Chemical Engineering Science, 1996. **51**: p. 623-634.
30. Symonds, R.T., et al., *CO_2 capture from syngas via cyclic carbonation/calcination for a naturally occurring limestone: Modelling and bench-scale testing.* Chemical Engineering Science, 2009. **64**: p. 3536-3543.
31. Pericleous, K.A. and M. Patel, *The modelling of tangential and axial agitators in chemical reactors.* Physicochemical Hydrodynamics, 1987. **8**(2): p. 105-123.
32. Pericleous, K., *Lecture 3: Conservation Equations*.
33. CHAM. *The Algebraic Slip Model*. 25/10/2017]; Available from: http://www.cham.co.uk/phoenics/d_polis/d_lecs/asmlec.htm.
34. Versteeg, H.K. and W. Malalasekera, *An Introduction to Computational Fluid Dynamics: The Finite Volume Method*. 2007: Pearson Education Limited.
35. Steeneveldt, R., B. Berger, and T.A. Torp, *CO_2 CAPTURE AND STORAGE: Closing the Knowing–Doing Gap.* Chemical Engineering Research and Design, 2006. **84**: p. 739-763.
36. Dean, C.C., et al., *Review: The calcium looping cycle for CO_2 capture from power generation, cement manufacture and hydrogen production.* Chemical Engineering Research and Design, 2011. **89**: p. 836-855.
37. Blomen, E., C. Hendriks, and F. Neele, *Capture technologies: improvements and promising developments.* Energy Procedia. **1**: p. 1505-1512.
38. Olajire, A.A., H. Mano, and Y. Fujioka, *CO_2 capture and separation technologies for end-of-pipe applications - a review.* Energy, 2008. **35**: p. 2610-2628.
39. Rubin, E.S., *CO_2 capture and transport.* Elements, 2008. **4**(5): p. 311-317.

40. Zanganeh, K.E., A. Shafeen, and S. Salvador, *CO_2 capture and development of an advanced pilot-scale cryogenic separation and decompression unit.* Energy Procedia, 2009. **1**: p. 247-252.
41. Bolland, O. and H. Undrum, *A novel methodology for comparing CO_2 capture options for natural gas-fired combined cycle plants.* Adv. Environ. Res., 2003. **7**: p. 901-911.
42. Knudsen, J.N., et al., *Experience with CO_2 capture from coal flue gas in pilot-scale: testing of different amine solvents.* Energy Procedia, 2009. **1**: p. 783-790.
43. Rao, A.B. and E.S. Rubin, *A technical, economic, and environmental assessment of amine-based CO_2 capture technology for power plant greenhouse gas control.* Environmental Science and Technology, 2002. **36**(20): p. 4467-4475.
44. Darde, V., et al., *Chilled ammonia process for CO_2 capture.* Int. J. Greenh. Gas Con., 2010. **4**: p. 131-136.
45. IPCC, *Special report on carbon capture and storage*, B. Metz, Editor. 2005, Intergovernmental Panel on Climate Change: New York.
46. Ho, M.T., G.W. Allinson, and D.E. Wiley, *Reducing the cost of CO_2 capture from flue gases using pressure swing adsorption.* Ind. Eng. Chem. Res., 2008. **47**: p. 4883-4890.
47. Damen, K., et al., *A comparison of electricity and hydrogen production systems with CO_2 capture and storage. Part A: Review and selection of promising conversion and capture technologies.* Prog. Energy. Combust., 2006. **32**: p. 215-246
48. Grande, C.A., et al., *Electric swing adsorption as emerging CO_2 capture technique.* Energy Procedia, 2009. **1**: p. 1219-1225.
49. Su, F.S., et al., *Capture of CO_2 from flue gas via multiwalled carbon nanotubes.* Sci. Total Environ., 2009. **47**(3017-3023).
50. Thiruvenkatachari, R., et al., *Post combustion CO_2 capture by carbon fibre monolithic adsorbents.* Prog. Energ. Combust., 2009. **35**(438-455).
51. An, H., B. Feng, and S. Su, *CO_2 capture capacities of activated carbon fibre-phenolic resin composites.* Carbon, 2009. **47**: p. 2396-2405.
52. Bertos, M.F., et al., *A review of accelerated carbonation technology in the treatment of cement-based materials and sequestration of CO_2.* Journal of Hazardous Materials, 2004. **B112**: p. 193-205.
53. Bukowski, J.M. and R.L. Berger *Reactivity and strength development of CO_2 activated non-hydraulic calcium silicates.* Cement And Concrete Research, 1979. **9**(57).
54. Shao, Y., et al., *Determination of minimum fluidization velocity in fluidized bed at elevated pressures and temperatures using CFD simulations.* Powder Technology, 2019. **350**: p. 81-90.
55. Lim, K.S., J.X. Zhu, and J.R. Grace, *Hydrodynamics of gas-solid fluidization.* International Journal of Multiphase Flow, 1995. **21**: p. 141-193
56. Howard, J.R., *Fluidized Bed Technology*. 1989, Bristol, UK: JW Arrowsmith Ltd.
57. Geldart, D., *The effect of particle size and size distribution on the behaviour of gas-fluidized beds.* Powder Technology, 1972. **6**: p. 201-215.

58. Yang, W.C., *A model for the dynamics of a circulating fluidized bed loop*, in *Circulating Fluidized Bed Technology II*, P. Basu and J.F. Large, Editors. 1988, Pergamon Press: Toronto.
59. Grace, J.R., *Contacting modes and behaviour classification of gas—solid and other two-phase suspensions.* The Canadian Journal of Chemical Engineering, 1986. **64**(3): p. 353-363.
60. Botterill, J.S.M., Y. Teoman, and K.R. Yüriger, *The effect of operating temperature on the velocity of minimum fluidization bed voidage and general behaviour.* Powder Technolgy, 1982. **31**: p. 101-110.
61. Davidson, J.F. and D.L. Keairns. *Fluidization*. in *Second Engineering Foundation Conference*. 1978. Cambridge: Cambridge University Press.
62. Ansys, *Ansys Fluent 12.1 Documentation*. 2009.
63. Ström, H., S. Sasic, and B. Andersson, *A novel multiphase DNS approach for handling solid particles in a rarefied gas.* International Journal of Multiphase Flow, 2011. **37**: p. 906-918.
64. Morvan, H., *Modelling multiphase flow using CFD*. 2005.
65. Spalding, D.B., *Numerical Computation of Multiphase Flow and Heat-transfer*, in *Recent Advances in Numerical Methods in Fluids*, D. Taylor and K. Morgan, Editors. 1980, Pineridge Press: Swansea.
66. Patel, M.K., K.A. Pericleous, and M. Cross, *Numerical modelling of circulating fluidized beds.* International Journal of Computational Fluid Dynamics, 1993. **1**(2): p. 161-176.
67. Oliver, X. and C. Agelet de Saracibar, *Continuum Mechanics for Engineers. Theory and Problems*. 2nd ed. 2017.
68. Wang, Y., et al., *CFD simulation methodology for gas-solid flow in bypass pneumatic conveying - A review.* Applied Thermal Engineering, 2017. **125**: p. 185-208.
69. Chen, L., et al., *Dynamic modelling of fluidisation in gas-solid bubbling fluidised beds.* Powder Technology, 2017. **322**: p. 461-470.
70. Charitos, A., et al., *Parametric investigation of the calcium looping process for CO_2 capture in a 10kW dual fluidised bed.* International Journal of Greenhouse Gas Control, 2010. **4**: p. 776-784.
71. Grasa, G.S., et al., *Reactivity of highly cycled particles of CaO in a carbonation/calcination loop.* Chemical Engineering Journal, 2008. **137**: p. 561-567.
72. Wang, K., et al., *High temperature capture of CO_2 on lithium-based sorbents from rice husk ash.* Journal of Hazardous Materials, 2011. **189**: p. 301-307.
73. Yi, C.-K., et al., *Continuous operation of a potassium-based dry sorbent CO_2 capture process with two fluidized-bed reactors.* International Journal of Greenhouse Gas Control, 2007. **1**: p. 31-36.
74. Stanmore, B.R. and P. Gilot, *Review-calcination and carbonation of limestone during thermal cycling for CO_2 sequestration.* Fuel Processing Technology, 2005. **86**: p. 1707-1743.
75. Abanades, J.C., *Calcium Sorbent Cycling for Simultaneous CO2 Capture and Clinker Production*. 2005, Spanish National Research Council.

76. Abanades, J.C., et al., *Cost structure of a postcombustion CO_2 capture system using CaO.* Environmental Science and Technology, 2007. **41**: p. 5523-5527.
77. David, J. and H. Herzog, *The cost of carbon capture*. 2011.
78. Duelli, G., et al., *Investigations at a 10 kWth calcium looping dual fluidized bed facility: Limestone calcination and CO_2 capture under high CO_2 and water vapor atmosphere.* International Journal of Greenhouse Gas Control, 2015. **33**: p. 103-122.
79. Gupta, H.S. and L.S. Fan, *Carbonation-calcination cycle using high reactivity calcium oxide for carbon dioxide separation from flue gas.* Industrial and Engineering Chemical Research, 2002. **41**: p. 4035-4042.
80. Lopez Pacheco, A., *Mill mods save money*, in *Canadian Institute of Mining Metallurgy and Petroleum*. 2012.
81. Kittipongvises, S., *Assessment of environmental impacts of limestone quarrying operations in Thailand.* Environmental and Climate Technologies, 2017. **20**: p. 67-83.
82. Pacyna, J.M., et al., *Lime Production*, in *EMEP/EEA emission inventory guidebook 2009*, J. Keunen, Editor. 2009.
83. Abanades, J.C., *The maximum capture efficiency of CO_2 using a carbonation/calcination cycle of $CaO/CaCO_3$.* Chemical Engineering Journal, 2002. **90**: p. 303-306.
84. Zeman, F., *Effect of steam hydration on performance of lime sorbent for CO_2 capture.* International Journal of Greenhouse Gas Control, 2008. **2**: p. 203-209.
85. Bryngelsson, M. and M. Wester, *CO_2 capture pilot test at a pressurized coal fired CHP plant.* Energy Procedia, 2009. **1**: p. 1403-1410.
86. Lee, D.K., *An apparent kinetic model for the carbonation of calcium oxide by carbon dioxide* Chemical Engineering Journal, 2004. **100**: p. 71-77.
87. Kunii, D. and O. Levenspiel, *Fluidization Engineering*. 1969, New York: Wiley.
88. *Heterogeneous Reaction: Shell and core model*. Indian Institute of Technology - Madras: Madras.
89. Bhatia, S.K. and D.D. Perlmutter, *The effect of product layer on the kinetics of the CO_2-lime reaction.* AIChE Journal, 1983. **29**.
90. Unterberger, S. and A. Schuster, *Evaluation of Carbonate Looping for Post-Combustion CO_2-Capture from a Utility's Perspective*. 2011, EnBW.
91. Duelli, G., et al., *Calcium Looping Process: Experimental investigation of limestone performance regenerated under high CO_2 partial pressure and validation of a carbonator model.* Energy Procedia, 2013. **37**: p. 190-198.
92. Ingraham, T.R. and P. Marier, *Kinetic studies on the thermal decomposition of calcium carbonate.* Can. J. Chem. Eng., 1963. **41**: p. 170-173.
93. Satterfield, C.N. and F. Feakes, *Kinetics of thermal decomposition of calcium carbonate.* AICHE J., 1959. **5**: p. 115-122.
94. Koloberdin, V., V.N. Blinichev, and V.V. Strel'tsov, *The kinetics of limestone calcination.* Int. Chem. Eng., 1975. **15**: p. 101-104.
95. Ar, I. and G. Dogu, *Calcination kinetics of high purity limestone.* Chemical Engineering Journal, 2001. **83**: p. 131-137.

96. Shen, J. and J.M. Smith, *The mechanism of the thermal decomposition of calcium carbonate.* Ind. Eng. Chem. Fundam., 1965. **4**: p. 293-301.
97. Borgwardt, R.H., *Calcination kinetics and surface area of dispersed limestone particles.* AIChE J, 1985. **31**: p. 103-111.
98. Ohme, K., R. Schrader, and A. Mueller, *Kinetik der theimischen Dissoziation von Kalkstein und Zementrohmehl im Flugstaubreaktor.* Silikattechnik, 1975. **26**(12): p. 403-407.
99. Milne, C.R., et al., *Calcination and sintering models for application to high-temperature short-time sulfation of calcium-based sorbents.* Ind. Eng. Chem. Res., 1990. **29**: p. 139-149.
100. Bhatia, S.K. and D.D. Perlmutter, *Unified treatment of structural effects in fluid-solid reactions.* AICheJ, 1983. **29**: p. 281-289.
101. Porter, R.T.J., et al., *Cost and performance of some carbon capture technology options for producing different quality CO_2 product streams.* International Journal of Greenhouse Gas Control, 2017. **57**: p. 185-195.
102. Wang, W., S. Ramkumar, and L.-S. Fan, *Energy penalty of CO_2 capture for the carbonation-calcination reaction process - Parametric effects and comparisons with alternative processes.* Fuel, 2013. **104**: p. 561-574.
103. Han, J.-H., et al., *Optimal strategy for carbon capture and storage infrastructure: a review.* Korean Journal of Chemical Engineering, 2012. **29**(8): p. 975-984.
104. Bode, S. and M. Jung, *Carbon dioxide capture and storage—liability for non-permanence under the UNFCCC* International Environmental Agreements, 2006. **6**: p. 173-186.
105. Ishii, M. and N. Zumber, *Drag coefficient and relative velocity in bubbly, droplet or particulate flows.* AIChe Journal, 1979. **25**(5): p. 843-855.
106. Manninen, M., V. Taivassalo, and S. Kallio, *On the mixture method for multiphase flow*. 1996, Technical Research Centre of Finland: Espoo.
107. Thermtest. *Introducing the rule of mixtures calculator*. 2017; Available from: https://thermtest.com/rule-of-mixtures-calculator.
108. Clift, R., J.R. Grace, and M.E. Weber, *Bubbles, Drops and Particles*. 1978, London: Academic Press.
109. Pericleous, K., *Lecture 3 - CFD Conservation*. 2009.
110. Johansen, G., M. Massoudi, and J.R. Rajagopal, *Flow of a fluid-solid mixture between flat plates.* Chemical Engineering Science, 1991. **46**(7): p. 1713-1723.
111. Ungarish, M., *Hydrodynamics of suspensions: Fundamentals of centrifugal and gravity separation*. 1993, Berlin: Springer.
112. Baker, E.H., *The CaO-CO_2 system in the pressure range 1-300 atm.* Journal of the Chemical Society, 1962: p. 464-470.
113. Kuipers, J.A.M., et al., *A numerical model of gas-fluidized beds.* Chemical Engineering Science, 1992. **47**(8): p. 1913-1924.
114. Croft, T.N., *Unstructured Mesh - Finite Volume Algorithms for Swirling, Turbulent, Reacting Flows*, in *School of Computing and Mathematical Sciences*. 1998, University of Greenwich.

115. Spalding, D.B., *A Novel Finite Difference Formulation for Differential Expressions Involving both First and Second Derivatives. International Journal for Numerical Methods in Engineering*, 1972. **4**: p. 551-579.
116. Clare, J. *PHYSICA MBrick3 Beginner's Guide*. 2012 [cited 2017 04/12/2017]; Available from: http://bluecombats.blogspot.co.uk/2012/06/physica-mbrick3-beginners-guide.html.
117. Djambazov, G., *Zonal Method for Simultaneous Definition of Block-Structured Geometry and Mesh.* Journal of Algorithms and Computer Technology, 2012. **6**(1): p. 203-218.
118. Bhatia, S.K. and D.D. Perlmutter, *The effect of pore structure on fluid-solid reactions: application to the SO_2-lime reaction.* AIChE J., 1981. **27**: p. 226-234
119. Abanades, J.C. and D. Alvarez, *Conversion limits in the reaction of CO_2 with lime.* Energy & Fuels, 2003. **17**: p. 308-315.
120. MacKenzie, A., et al., *Economics of CO_2 capture using the calcium cycle with a pressurized fluidized bed combustor.* Energy & Fuels, 2007. **21**: p. 920-926.
121. Hawthorne, C., et al., *Simulation of the carbonate looping power cycle.* Energy Procedia, 2009. **1**: p. 1387-1394.
122. Alonso, M., et al., *Carbon dioxide capture from combustion flue gases with a calcium oxide chemical loop. Experimental results and process development.* International Journal of Greenhouse Gas Control, 2009. **4**: p. 167-173.

APPENDICES

Sample inform file

```
# Para\June\P5Flame4RHD3cextra
# Created 26/04/2018
# Modelled after the Stuttgart experiments
# Testing carbonation!
# Proper size reactor
# Replicating Excel work
# 5 solid phases - = really 10 solid phases!

GEOMETRY_MODULE
#   MESH  react1.mbl
   FILENAME  react1
        GRAVITY_Z   -9.81
END

PARALLEL_MODULE
 PARTITION_SOURCE  SEQUENTIAL
END

#GENERIC_MODULE
#        STEADY_STATE_RUN
#        MAX_SWEEPS  5000
#        USER_INTERVAL_SAVE  ON
#END

DATABASE_MODULE
#        INPUT_DATABASE           0001
        OUTPUT_DATABASE           0001
#        RESTART_SIMULATION_TIME     -1.0
#        RESTART_SWEEP_NUMBER       -1
#        RESTART_TIME_STEP_NUMBER    -1
        WRITE_DATABASE           ON
END

GENERIC_MODULE
        TRANSIENT_RUN
                DELTA_T
                        FOR_ALL_TIME_STEPS  0.01
                END
                END_TIME      20.
```

```
            SAVE_AT_EVERY_TIME_STEP -1
        END
        MAX_SWEEPS 1000
        USER_INTERVAL_SAVE OFF
END

USER_MODULE
        OUTPUT_INITIAL  ON
        OUTPUT_FREQUENCY 1.
END

MATERIAL_PROPERTY_MODULE
#       DYNAMIC_VISCOSITY ON
        DENSITY
#               MATERIAL 1 CONSTANT 1.206
                SAVE_PROPERTY TRANSIENT
                MATERIAL 1 USER_ROUTINE densy 4 1.2 3340. 2710. 1.98
        END

        VISCOSITY
#               MATERIAL 1 CONSTANT 1.5e-5
                SAVE_PROPERTY TRANSIENT
        MATERIAL 1 USER_ROUTINE viscy 1 1.5e-5
        END

        SPECIFIC_HEAT
#               MATERIAL 1 CONSTANT 1.005
                SAVE_PROPERTY TRANSIENT
                MATERIAL 1 USER_ROUTINE heaty 4 1.005 0.91 0.76 0.85
        END

        THERMAL_CONDUCTIVITY
                MATERIAL 1 CONSTANT 0.0257
        END

        THERMAL_EXPANSION_COEFFICIENT
                MATERIAL 1 CONSTANT 0.002
        END
END

FREE_SURFACE_MODULE
 GALA ON
 SOLVE_FREESURF
  INITIAL_VALUES ALL 0.
  BOUNDARY_CONDITIONS
   PATCH 5 FIXED_VALUE VALUE 0.
```

```
  END
 END
END

SCALAR_MODULE
        STORE_ESOL
                INITIAL_VALUES  ALL  0.
        END
        STORE_ESO1
                INITIAL_VALUES  ALL  0.
        END
        STORE_ESO2
                INITIAL_VALUES  ALL  0.
        END
        STORE_ESO3
                INITIAL_VALUES  ALL  0.
        END
        STORE_ESO4
                INITIAL_VALUES  ALL  0.
        END
        STORE_ESO5
                INITIAL_VALUES  ALL  0.
        END

        STORE_ECX0
                INITIAL_VALUES  ALL  0.
        END

        SOLVE_ECX1
     DIFFUSION_TERM  OFF
     TRANSIENT_COEFFICIENT
          ALL CONSTANT 1.
     END
     CONVECTION_COEFFICIENT
          ALL CONSTANT 1.
     END
                INITIAL_VALUES  ALL  0.
                USER_SOURCE_TERMS
                        extradv  3   1.2  3340.  0.0001
                        carbon1  3   -56.  3340.  0.0001
                END
                BOUNDARY_CONDITIONS
                        PATCH  5   FIXED_VALUE  VALUE  0.
                        PATCH  8   FIXED_VALUE  VALUE  1.e-3
                        PATCH  9   FIXED_VALUE  VALUE  0.
                END
```

```
   END

   SOLVE_ECX2
DIFFUSION_TERM  OFF
TRANSIENT_COEFFICIENT
     ALL CONSTANT 1.
END
CONVECTION_COEFFICIENT
     ALL CONSTANT 1.
END
           INITIAL_VALUES  ALL  0.
           USER_SOURCE_TERMS
                  extradv  3   1.2  3340.  0.000125
                  carbon2  3   -56.  3340.  0.000125
           END
           BOUNDARY_CONDITIONS
                  PATCH  5   FIXED_VALUE  VALUE  0.
                  PATCH  8   FIXED_VALUE  VALUE  1.e-3
                  PATCH  9   FIXED_VALUE  VALUE  0.
           END
   END

   SOLVE_ECX3
DIFFUSION_TERM  OFF
TRANSIENT_COEFFICIENT
     ALL CONSTANT 1.
END
CONVECTION_COEFFICIENT
     ALL CONSTANT 1.
END
           INITIAL_VALUES  ALL  0.
           USER_SOURCE_TERMS
                  extradv  3   1.2  3340.  0.00015
                  carbon3  3   -56.  3340.  0.00015
           END
           BOUNDARY_CONDITIONS
                  PATCH  5   FIXED_VALUE  VALUE  0.
                  PATCH  8   FIXED_VALUE  VALUE  1.e-3
                  PATCH  9   FIXED_VALUE  VALUE  0.
           END
   END

   SOLVE_ECX4
DIFFUSION_TERM  OFF
TRANSIENT_COEFFICIENT
     ALL CONSTANT 1.
```

```
END
CONVECTION_COEFFICIENT
     ALL CONSTANT 1.
END
          INITIAL_VALUES  ALL  0.
          USER_SOURCE_TERMS
                extradv  3   1.2  3340.  0.000175
                carbon4  3   -56.  3340.  0.000175
          END
          BOUNDARY_CONDITIONS
                PATCH  5   FIXED_VALUE  VALUE  0.
                PATCH  8   FIXED_VALUE  VALUE  1.e-3
                PATCH  9   FIXED_VALUE  VALUE  0.
          END
   END

   SOLVE_ECX5
DIFFUSION_TERM  OFF
TRANSIENT_COEFFICIENT
     ALL CONSTANT 1.
END
CONVECTION_COEFFICIENT
     ALL CONSTANT 1.
END
   INITIAL_VALUES  ALL  0.
          USER_SOURCE_TERMS
                extradv  3   1.2  3340.  0.0002
                carbon5  3   -56.  3340.  0.0002
          END
          BOUNDARY_CONDITIONS
                PATCH  5   FIXED_VALUE  VALUE  0.
                PATCH  8   FIXED_VALUE  VALUE  1.e-3
                PATCH  9   FIXED_VALUE  VALUE  0.
          END
   END

   STORE_ECR0
          INITIAL_VALUES  ALL  0.
   END

   SOLVE_ECR1
DIFFUSION_TERM  OFF
TRANSIENT_COEFFICIENT
     ALL CONSTANT 1.
END
CONVECTION_COEFFICIENT
```

```
     ALL CONSTANT 1.
END
   INITIAL_VALUES  ALL  0.
          USER_SOURCE_TERMS
                 extradv  3   1.2  2710.  0.0001
                 carbon1  3   100.  2710.  0.0001
          END
          BOUNDARY_CONDITIONS
                 PATCH  5   FIXED_VALUE  VALUE  0.
                 PATCH  8   FIXED_VALUE  VALUE  0.
                 PATCH  9   FIXED_VALUE  VALUE  0.
          END
   END

   SOLVE_ECR2
DIFFUSION_TERM  OFF
TRANSIENT_COEFFICIENT
     ALL CONSTANT 1.
END
CONVECTION_COEFFICIENT
     ALL CONSTANT 1.
END
   INITIAL_VALUES  ALL  0.
          USER_SOURCE_TERMS
                 extradv  3   1.2  2710.  0.000125
                 carbon2  3   100.  2710.  0.000125
          END
          BOUNDARY_CONDITIONS
                 PATCH  5   FIXED_VALUE  VALUE  0.
                 PATCH  8   FIXED_VALUE  VALUE  0.
                 PATCH  9   FIXED_VALUE  VALUE  0.
          END
   END

   SOLVE_ECR3
DIFFUSION_TERM  OFF
TRANSIENT_COEFFICIENT
     ALL CONSTANT 1.
END
CONVECTION_COEFFICIENT
     ALL CONSTANT 1.
END
   INITIAL_VALUES  ALL  0.
          USER_SOURCE_TERMS
                 extradv  3   1.2  2710.  0.00015
                 carbon3  3   100.  2710.  0.00015
```

```
        END
        BOUNDARY_CONDITIONS
                PATCH  5   FIXED_VALUE  VALUE  0.
                PATCH  8   FIXED_VALUE  VALUE  0.
                PATCH  9   FIXED_VALUE  VALUE  0.
        END
   END

   SOLVE_ECR4
DIFFUSION_TERM  OFF
TRANSIENT_COEFFICIENT
     ALL CONSTANT 1.
END
CONVECTION_COEFFICIENT
     ALL CONSTANT 1.
END
   INITIAL_VALUES  ALL  0.
        USER_SOURCE_TERMS
                extradv  3   1.2  2710.  0.000175
                carbon4  3   100.  2710.  0.000175
        END
        BOUNDARY_CONDITIONS
                PATCH  5   FIXED_VALUE  VALUE  0.
                PATCH  8   FIXED_VALUE  VALUE  0.
                PATCH  9   FIXED_VALUE  VALUE  0.
        END
   END

   SOLVE_ECR5
DIFFUSION_TERM  OFF
TRANSIENT_COEFFICIENT
     ALL CONSTANT 1.
END
CONVECTION_COEFFICIENT
     ALL CONSTANT 1.
END
   INITIAL_VALUES  ALL  0.
        USER_SOURCE_TERMS
                extradv  3   1.2  2710.  0.0002
                carbon5  3   100.  2710.  0.0002
        END
        BOUNDARY_CONDITIONS
                PATCH  5   FIXED_VALUE  VALUE  0.
                PATCH  8   FIXED_VALUE  VALUE  0.
                PATCH  9   FIXED_VALUE  VALUE  0.
        END
```

```
   END

   SOLVE_ECO2
DIFFUSION_TERM  OFF
TRANSIENT_COEFFICIENT
                ALL CONSTANT 1.
END
CONVECTION_COEFFICIENT
                ALL CONSTANT 1.
END
          INITIAL_VALUES  ALL  0.
          USER_SOURCE_TERMS
                carbong  3   -44.  1.98  1.
          END
          BOUNDARY_CONDITIONS
                PATCH  5   FIXED_VALUE  VALUE  0.1
                PATCH  8   FIXED_VALUE  VALUE  0.
                PATCH  9   FIXED_VALUE  VALUE  0.
          END
   END

   STORE_EAIR
          INITIAL_VALUES  ALL  0.
   END

   STORE_CSOL
          INITIAL_VALUES  ALL  0.
   END
   STORE_CSO1
          INITIAL_VALUES  ALL  0.
   END
   STORE_CSO2
          INITIAL_VALUES  ALL  0.
   END
   STORE_CSO3
          INITIAL_VALUES  ALL  0.
   END
   STORE_CSO4
          INITIAL_VALUES  ALL  0.
   END
   STORE_CSO5
          INITIAL_VALUES  ALL  0.
   END
   STORE_CCX0
          INITIAL_VALUES  ALL  0.
   END
```

```
STORE_CCX1
       INITIAL_VALUES ALL 0.
END
STORE_CCX2
       INITIAL_VALUES ALL 0.
END
STORE_CCX3
       INITIAL_VALUES ALL 0.
END
STORE_CCX4
       INITIAL_VALUES ALL 0.
END
STORE_CCX5
       INITIAL_VALUES ALL 0.
END
STORE_CCR0
       INITIAL_VALUES ALL 0.
END
STORE_CCR1
       INITIAL_VALUES ALL 0.
END
STORE_CCR2
       INITIAL_VALUES ALL 0.
END
STORE_CCR3
       INITIAL_VALUES ALL 0.
END
STORE_CCR4
       INITIAL_VALUES ALL 0.
END
STORE_CCR5
       INITIAL_VALUES ALL 0.
END
STORE_CCO2
       INITIAL_VALUES ALL 0.
END
STORE_CAIR
       INITIAL_VALUES ALL 0.
END

STORE_XCX0
       INITIAL_VALUES ALL 0.
END
STORE_XCX1
       INITIAL_VALUES ALL 0.
END
```

```
STORE_XCX2
       INITIAL_VALUES ALL 0.
END
STORE_XCX3
       INITIAL_VALUES ALL 0.
END
STORE_XCX4
       INITIAL_VALUES ALL 0.
END
STORE_XCX5
       INITIAL_VALUES ALL 0.
END
STORE_XCR0
       INITIAL_VALUES ALL 0.
END
STORE_XCR1
       INITIAL_VALUES ALL 0.
END
STORE_XCR2
       INITIAL_VALUES ALL 0.
END
STORE_XCR3
       INITIAL_VALUES ALL 0.
END
STORE_XCR4
       INITIAL_VALUES ALL 0.
END
STORE_XCR5
       INITIAL_VALUES ALL 0.
END
STORE_XCO2
       INITIAL_VALUES ALL 0.
END
STORE_XXXX
       INITIAL_VALUES ALL 0.
END

STORE_RCA1
       INITIAL_VALUES ALL 0.
END
STORE_RCA2
       INITIAL_VALUES ALL 0.
END
STORE_RCA3
       INITIAL_VALUES ALL 0.
END
```

```
        STORE_RCA4
                INITIAL_VALUES ALL 0.
        END
        STORE_RCA5
                INITIAL_VALUES ALL 0.
        END
END

FLUID_FLOW_MODULE

        MOMENTUM_FALSE_TIMESTEP 0.001

        BUOYANCY
                BOUSSINESQ_APPROXIMATION OFF
        END

        SOLVE_U-MOMENTUM
        INITIAL_VALUES ALL 0.
                BOUNDARY_CONDITIONS
                        PATCH 3 WALL COEFF 1. VALUE 0.0
                        PATCH 8 FIXED_VALUE VALUE 0.5
                        PATCH 9 FIXED_VALUE VALUE 0.5
                END
        END

        SOLVE_V-MOMENTUM
        INITIAL_VALUES ALL 0.
                BOUNDARY_CONDITIONS
                        PATCH 3 WALL COEFF 1. VALUE 0.0
                END
        END

        SOLVE_W-MOMENTUM
    INITIAL_VALUES ALL 2.35
                BOUNDARY_CONDITIONS
      PATCH 3 WALL COEFF 1. VALUE 0.0
                        PATCH 5 FIXED_VALUE VALUE 2.35
                END
        END

        SOLVE_PRESSURE
        INITIAL_VALUES ALL 0.
        UNDER_RELAXATION 0.25
                BOUNDARY_CONDITIONS
                        PATCH 6 FIXED_VALUE VALUE 0.
                END
```

```
        END
END

TURBULENCE_MODULE
        SOLVE_KINETIC_ENERGY
        INITIAL_VALUES ALL  0.01
                BOUNDARY_CONDITIONS
                        PATCH  5   FIXED_VALUE   VALUE  0.01
                        PATCH  2   FIXED_VALUE   VALUE  0.027
                END
                FALSE_TIMESTEP  0.001
        END
                        !  enut = 0.09 * k^2 / eps
        SOLVE_DISSIPATION_RATE
        INITIAL_VALUES ALL  0.011
                BOUNDARY_CONDITIONS
                        PATCH  5   FIXED_VALUE   VALUE  0.011
                        PATCH  2   FIXED_VALUE   VALUE  0.017
                END
                FALSE_TIMESTEP  0.001
        END
END

HEAT_TRANSFER_MODULE
# MAYBE EDIT THIS LIKE COMBUSTION MODULE
        SOLVE_ENTHALPY
        INITIAL_VALUES  ALL  927.
                USER_SOURCE_TERMS
                        extrahn  1   1782.
                END
                BOUNDARY_CONDITIONS
                        PATCH  5   FIXED_VALUE   VALUE  907.
                        PATCH  8   FIXED_VALUE   VALUE  840.
                        PATCH  9   FIXED_VALUE   VALUE  840.
                END
        END
END

LINEAR_SOLVER_MODULE
  MAX_ITERATIONS  500
END

MONITOR_MODULE
        OUTPUT_INTERVAL  100
        WRITE_TO_FILE  RUN
END
```

```
GENERAL_EQUATION_MODULE
        PRINT_SOURCES  ON
#      NUMERICAL_ZERO_VALUE  1.e-10
END

POST-PROCESSING_MODULE
  TECPLOT_FORMAT
                WRITE_INITIAL_VALUES  ON
                TECPLOT_FILE_NAME A
                TIME_FREQUENCY   0.1
  END
END

STOP
```

Mass and volume balances for the carbonator

Table 24: Mass balance for 815 t h^{-1} CO_2 capture (all t h^{-1})

Air	CO_2 into carbonator from flue	CO_2 into calciner from CCS	CO_2 into system	CO_2 Out of carbonator	CO_2 Reacted in carbonator	CaO required	$CaCO_3$ produced	CaO into carbonator	CaO out of carbonator	$CaCO_3$ out of carbonator	Into carbonator	Out of carbonator	Net gain
4116	815	502	1317	198	1119	1425	2544	4420	2995	2544	5737	5737	0
Air	CaO into calciner	$CaCO_3$ into calciner from carbonator	$CaCO_3$ into calciner from makeup	CaO out of calciner to carbonator	CaO out of calciner	Outcast lime	extra CO_2 from fuel	extra coal/O_2 for CCS	extra water?	CO_2 out of calciner (to storage)	Into calciner	Out of calciner	Net gain
	2995	2544	55	4420	4451	31	502	638	136	1119	5570	5570	0

Table 25: Volumetric mass balance for 120 kg/h CO_2 capture (all m^3 s^{-1})

Air	CO_2 into carbonator from flue	CO_2 into calciner from CCS	CO_2 into system	CO_2 Out of carbonator	CO_2 Reacted in carbonator	CaO required	$CaCO_3$ produced	CaO into carbonator	CaO out of carbonator	$CaCO_3$ out of carbonator	Into carbonator	Out of carbonator	Net gain
1.5E-01	1.7E-02	1.0E-02	2.7E-02	4.1E-03	2.3E-02	1.7E-05	3.8E-05	5.4E-05	3.7E-05	3.8E-05	2.7E-02	4.2E-03	-2.3E-02
Air	CaO into calciner	$CaCO_3$ into calciner from carbonator	$CaCO_3$ into calciner from makeup	CaO out of calciner to carbonator	CaO out of calciner	Outcast lime	extra CO_2 from fuel	extra coal/O_2 for CCS	extra water?	CO_2 out of calciner (to storage)	Into calciner	Out of calciner	Net gain
9.3E-02	3.7E-05	3.8E-05	8.3E-07	5.4E-05	7.6E-05	2.2E-05	1.0E-02	1.3E-02	2.8E-03	2.3E-02	1.3E-02	3.6E-02	2.3E-02